Numerical methods for advection-diffusion-reaction equations and medical applications

Gino Ignacio Montecinos Gúzman
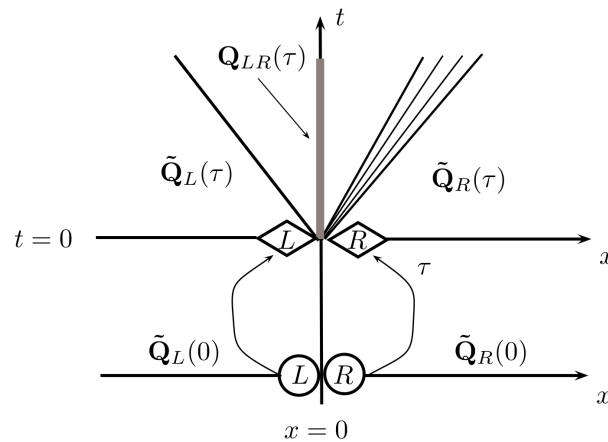
Abstract

The purpose of this thesis is twofold, firstly, the study of a relaxation procedure for numerically solving advection-diffusion-reaction equations, and secondly, a medical application.

Concerning the first topic, we extend the applicability of the Cattaneo relaxation approach to reformulate time-dependent advection-diffusion-reaction equations, that may include stiff reactive terms, as hyperbolic balance laws with stiff source terms. The resulting systems of hyperbolic balance laws are solved by extending the applicability of existing high-order ADER schemes, including well-balanced and non-conservative schemes. Moreover, we also present a new locally implicit version of the ADER method to solve general hyperbolic balance laws with stiff source terms. The relaxation procedure depends on the choice of a relaxation parameter ϵ. Here we propose a criterion for selecting ϵ in an optimal manner, relating the order of accuracy r of the numerical scheme used, the mesh size Δx and the chosen ϵ. This results in considerably more efficient schemes than some methods with the parabolic restriction reported in the current literature. The resulting present methodology is validated by applying it to a blood flow model for a network of viscoelastic vessels, for which experimental and numerical results are available. Convergence-rates assessment for some selected second-order model equations, is carried out, which also validates the applicability of the criterion to choose the relaxation parameter.

The second topic of this thesis concerns the numerical study of the haemodynamics impact of stenoses in the internal jugular veins. This is motivated by the recent discovery of a range of extra cranial venous anomalies, termed Chronic CerbroSpinal Venous Insufficiency (CCSVI) syndrome, and its potential link to neurodegenerative diseases, such as Multiple Sclerosis. The study considers patient specific anatomical configurations obtained from MRI data. Computational results are compared with measured data.

Acknowledgements

Contents

List of Figures

List of Tables

Publications

The main results presented in this thesis are based on the following works:

1. L. O. Müller, **G. I. Montecinos** and E. F. Toro. Some Issues in Modelling Venous Haemodynamics. Proceeding of Numerical Methods for Hyperbolic Equations: Theory and Applications. Santiago de Compostela, Spain, July 2012, pp 347-354.

2. E. F. Toro and **G. I. Montecinos.** Advection-diffusion-reaction equations: hyperbolisation and high-order ADER discretizations. *SIAM Journal on Scientific Computing.* Under review, 2014.

3. **G. I. Montecinos** and E. F. Toro. Reformulations for general advection-diffusion-reaction equations and locally implicit ADER schemes. *Jourrnal of Computational Physics.* Under review, 2014.

4. **G. I. Montecinos**, L. O. Müller and E. F. Toro. Hyperbolic reformulation of a 1D viscoelastic blood flow model and ADER finite volume schemes. *Jourrnal of Computational Physics.* In press, 2014. This work was also published as:
   G. I. Montecinos, L. O. Müller and E. F. Toro. Hyperbolic reformulation of a 1D viscoelastic blood flow model and ADER finite volume schemes. Preprint NI14014-NPA, Isaac Newton Institute for Mathematical Sciences, University of Cambridge, UK, 2014.

5. A. Caiazzo, **G. I. Montecinos**, L. O. Müller, E. M. Haacke and E. F. Toro. Computational Haemodynamics in Stenotic Internal Jugular Veins. *Journal of Mathematical Biology.* Under review, 2014. This work was also published as:
   A. Caiazzo, **G. I. Montecinos**, L. O. Müller, E. M. Haacke and E. F. Toro. Computational haemodynamics in stenotic internal jugular veins. *WIAS Berlin.* No 1793, 2013.

Chapter 1

Introduction

1.1 Motivation of the thesis

Advection-Diffusion-Reaction Partial Differential Equations (adrPDEs) arise in a wide range of scientific disciplines. These include astrophysics, biology, aerospace sciences, industrial and environmental problems. Specific examples of our interest here include, heat conduction [12, 14, 109], haemodynamics [34, 130, 136], dynamics of blood coagulation [16, 120], cardiac arrhythmias [29, 131] and atherosclerosis [48, 68].

Of particular interest in this thesis are the ardPDEs of parabolic type [53, 78]. These equations contain second-order spatial derivatives (diffusive terms) and present several challenging difficulties. For example, at the physical/mathematical level, the heat equation presents the phenomenon of infinite speed of propagation of information [107]. The heat equation is based on the Fourier law. Cattaneo [25] and Vernotte [160], independently, proposed a modification of the Fourier law, which avoided the instantaneous propagation of information, leading to the reformulation of the heat equation as a hyperbolic system with a stiff source term. This is today recognised as a major achievement. Extensions of this reformulation have been possible for more general advection-diffusion-reaction equations. A consequence of these reformulations, however, is that all possible problems associated with second-order terms are replaced by other difficulties, namely that of solving hyperbolic balance laws with stiff source terms. Therefore, in order to fully exploit the Cattaneo approach, we need to develop numerical methodology capable of solving, efficiently, hyperbolic balance laws with stiff source terms.

Given the above considerations, we will first extend the Cattaneo relaxation approach, so that general, time-dependent adrPDEs can be reformulated as hyperbolic balance laws with stiff source terms. In addition, we shall exploit existing methods and develop new ones for tackling hyperbolic balance laws with stiff source terms.

In this thesis, we also study some applications of current medical interest, in which some of the mathematical/numerical advances reported in this thesis are applied. One of these applications concerns the Chronic CerbroSpinal Venous Insufficiency (CCSVI) syndrome, characterized by the presence of stenoses in internal jugular veins and azygous veins [166]. Stenoses are diagnosed by following some criteria as; i) measurements of the cross-sectional area below a prescribed value, ii) the assessments of mechanical properties like velocity ratio between inlet and outlet velocities. However, in these diagnosis criteria no patient specific features are considered. The investigation of the effects of stenoses in a patient specific context is an issue which can be studied.

1.2   State of the art

A first order system with a reactive source term can be associated with an advection-diffusion-reaction equation in the limiting of a small reactive scale [69, 70, 95, 122, 123], in this range the source term is stiff. On the other hand, the procedure to obtain a first order system from an advection-reaction-diffusion equation is named *relaxation procedure*. The original idea of Cattaneo [25] and Vernotte [160] provide a relaxation procedure for the heat equation. Other relaxation procedures are for example, the relaxation of Liu [94], see also [95, 122], and that implemented by Gómez et al. [58, 59].

There are several investigations devoted to the study of the behaviour of first-order systems with reactive source terms [9, 93, 94, 128]. However, the number of works dealing with the relaxation as an alternative solution for advection-diffusion-reactions, is small. See for example the works of Nishikawa [111–113] where steady state solutions are obtained using the Cattaneo relaxation procedure. See Jin and Liu [75], Jin and Levermore [74] and the works of Gómez et al. [58, 59] where unsteady solutions were obtained.

The relaxation procedures associated to Liu [94] and Gómez [58] have some features which are different from that of Cattaneo; i) these relaxations require to satisfy the so-called *sub-characteristic condition*, see Liu [94], ii) these relaxations modify the original governing advection-diffusion-reaction equation by including the advective term as a source term in the new first-order system.

Numerical schemes for solving the direct advection-diffusion-reaction equations range from; i) finite difference methods [5, 28, 84, 97, 97, 98, 102], ii) finite element methods [7, 8, 52, 71], iii) mixtures of methods as given by splitting schemes [56, 83, 135, 169] and iv) finite volume methods. Of particular interest to us are the class of high-order finite volume ADER (Arbittrary accuracy DERivative Riemann problem) methods, [144, 150,

154]. See [22, 100] and chapters 19 and 20 of [147] for a review and the many relevant references therein.

Titarev and Toro [145, 153] first applied ADER to solve the model advection-reaction-diffusion equation. Hidalgo and Toro applied ADER to a purely diffusion equation in [149]; Dumbser [46], Hidalgo and Dumbser [67] applied ADER to solve the compressible Navier-Stokes equations to very high order of accuracy. Hidalgo et al. [68] also applied ADER to a system of time-dependent diffusion-reaction equations that model atherosclerosis. However, a disadvantage of such direct approach to solve advection-diffusion-reaction equations is the parabolic-like time stability constraint, of the type Δx^2. An extension of ADER that is able to overcome the parabolic limitations was proposed by Zambra et al. [168] for solving the Richards equation. The scheme is globally implicit, see also [158, 159].

The solution of a first order system as the solution approximation of an advection-diffusion-reaction equation can be found in the works of Boscarino and collaborators [17, 18] following the Implicit-Explicit (IMEX) methods and Nishikawa [111, 112] based on residual-distribution numerical methodologies [126, 127] for steady computations and Gómez et al [58, 59] for unsteady computations and based on discontinuous Galerkin methods.

In recent years, computational haemodynamics has become a valuable, non-invasive alternative tool for gaining additional insight on patient haemodynamics, in terms of flow patterns, pressure, wall shear stress (see [82, 87, 156, 164]), as well as for computing clinically relevant indicators [62, 85]. However, the feasibility of detailed computer simulation is still limited by the prohibitive computational cost, especially when considering a large number of blood vessels and complex topologies. This issue is particularly important when modelling the haemodynamics in veins, as small vessels and minor collaterals might be determinant for the physiological flow conditions. In order to reduce the model complexity, 3D models are often used in combination with reduced one-dimensional (1D) models, to simulate haemodynamics in large vessel networks (see [15, 49, 50, 92, 119]), and *lumped parameter* or zero-dimensional (0D) models, which are introduced to take into account the influence of smaller and terminal vessels (see [161, 162]).

1.3 Research aims of the thesis

The purpose of this thesis is twofold, firstly, the study of a relaxation procedure for numerically solving advection-diffusion-reaction equations, and secondly, some medical applications.

Regarding the first topic, in this thesis only the one-dimensional case is studied. However, there exists evidence that the relaxation approach of Cattaneo can be extended to the two-dimensional case, see for example [112], where the steady case was studied.However we note that the extension of the methodology proposed in this thesis to multiple space dimensions poses several challenges. Obviously, a solid starting point is a thorough study of the one-dimensional case, which is done here. This topic is divided into the objectives listed below:

- Investigation of the relaxation approach of Cattaneo and Vernotte, called here the *Cattaneo* relaxation approach. The investigation includes the comparison with another relaxation approach for advective and diffusive regimes.

- Study the limitation of the applicability of the proposed methodology to third-order partial differential equations.

- Present two extensions of the relaxation approach of Cattaneo and provide the respective sufficiency criteria for hyperbolicity.

- Provide a theoretical result to choose the optimal relaxation parameter, such that stability and accuracy are ensured for the hyperbolic reformulations.

- Illustrate how ADER schemes able to solve hyperbolic balance laws with stiff source terms, can efficiently be applied to solve advection-diffusion-reaction equations with a suitable choice of the relaxation parameter.

- Introduce a new, locally-implicit solver for the generalised Riemann problem that includes stiff source terms. The resulting ADER schemes, with the new local solver, is then able to deal with the general initial-boundary value problem for hyperbolic balance laws with stiff source terms and is thus able to compute approximate solutions to general, time-dependent advection-diffusion-reaction equations.

- Provide theoretical and empirical results, which show that the relaxation approach presented in this thesis is an efficient, simple and powerful alternative for solving general time-dependent advection-diffusion-reaction equations.

Another topic of this thesis concerns the study of the haemodynamics influence of a stenosis in the internal jugular veins. Here the objectives are:

- Implementation of a multi-scale model where a three-dimensional geometry is obtained from MRI imaging and it is coupled with a one-dimensional network accounting for major cerebral veins.

- Numerical assessment of diagnosis criteria of stenoses. Using the multi scale model, the haemodynamics impact of a stenosis it is studied in terms of measurements of pressure drops, velocity ratios and estimations of the wall shear stress patterns.

1.4   Contents of the thesis

In chapter 2 the ADER type method reported in [41] is introduced. The Cattaneo's relaxation approach is presented and compared with another used relaxation approach. A criterion to choose the relaxation parameters, which ensures the accuracy of hyperbolic reformulations is obtained and empirical convergence rate assessments are presented. The issues of parabolic time step constraints as well as limitations to apply the Cattaneo relaxation to partial differential equations of third order, are discussed.

In chapter 3 extensions of the relaxation of Cattaneo for general advection-diffusion-reaction equations are presented. These reformulations are applied to the one-dimensional compressible Navier-Stokes equations and sufficiency criteria that ensure the hyperbolicty of new reformulations are presented. A brief review of ADER method is done, as that following the Toro-Titarev philosophy [150] as well as that of Harten et al. [66]. A new locally-implicit gneralized Riemann solver based on the previous work of Montecinos and Toro [101], is presented.

In chapter 4 a blood flow model is introduced and its hyperbolic reformulation is presented. The ADER methodology used for that model is reviewed. A numerical evidence that confirms the applicability of the criterion to choose the relaxation parameter introduced in chapter 2, is provided. The proposed methodology is validated by comparing our numerical results with experimental measurements and numerical results reported in the literature a for one-dimensional blood flow model in a network of viscoelastic vessels.

In chapter 5 we describe the setup of our *in-silico* stenotic vein model and the methodologies for the numerical simulations of stenotic jugular veins are described. The computational results are presented.

In chapter 6 global conclusions are done.

Chapter 2

Advection-diffusion-reaction equations: hyperbolisation and high-order ADER discretizations

2.1 Introduction

In this chapter we are interested in hyperbolization, via a relaxation approach, of time-dependent Advection-Diffusion-Reaction Partial Differential Equations (adrPDEs) and high-order numerical discretizations. The relaxation approach appears to have first been put forward by Cattaneo [24, 25] as applied to the heat equation. See also Vernotte [160] who, independently, reported the same approach, and the paper by Nagy and collaborators [107] who review quite in detail Cattaneo's approach. The heat equation is the canonical equation for diffusion-type problems. One of the first relaxation approaches arises naturally from a reformulation of Fourier law's, by introducing a term governed by a relaxation time, in order to resolve the unphysical phenomenon of instantaneous wave propagation. This provided the motivation for the work of Cattaneo and Vernotte. Following the reformulation of Cattaneo, a hyperbolic system is obtained. Indeed, the resulting first order system is known as the hyperbolic heat equation. Subsequently, Roetzel et al. [129] proved that the new reformulation in fact governs heat conduction for finite relaxation times. In the present chapter we consider the constitutive equation proposed by Cattaneo and Vernote, which is similar to the augmented Fourier law, to remove second-order terms. We name this procedure the *Cattaneo's relaxation approach.*

At this stage, it is appropriate to mention that another relaxation approach has been studied by Jin and Xin [77] to solve hyperbolic equations numerically. In this approach, the augmented, reformulated hyperbolic systems are linear but with stiff non-linear

source terms. Subsequently, Jin and Levermore [74] and Jin et al. [76] extended such approach to solve adrPDEs. See, for example, Pember [122, 123], Lowrie and Morel [95]. The approach was first studied theoretically by Liu [94] and subsequently an entropy conditions was obtained by Chen *et al.* [26]. We note that the relaxation approach in [74, 76] is related to Cattaneo's approach. However in the former the augmented Fourier law contains additional, convective, terms. Both relaxation approaches when applied to homogeneous (no reaction terms) purely diffusion equations, produce hyperbolic systems with stiff source terms. There are however, substantial differences between both approaches. The relaxation approach of Jin an collaborators [74, 76] imposes relaxation of sub-characteristics, see [94], whereas Cattaneo's approach does not require such condition. Abgrall and Karni [1] have confirmed the need to impose such sub-characteristics condition, in a numerical context. On the other hand, in the relaxation approach of Cattaneo, one carries out a relaxation of spatial gradients and the structure of the original equations does do not change significantly. This is quite different to the relaxation approach of Jin et al. [74, 76] in which the structure of the original equations does change appreciably.

In this chapter we investigate the relaxation approach in the sense of Cattaneo to solve numerically non-linear, time-dependent advection-diffusion-reaction equations, including stiff reaction terms. In addition, we identify the limitation of this approach, as applied to third-order partial differential equations. This kind of relaxation approach was first applied to simplified advection-diffusion equations by Gomez et al. [58]. They solved a two-dimensional linear problem with a numerical scheme of second-order accuracy, based on the finite element method. Nishikawa [111, 112], has investigated residual-distribution numerical methodologies [126, 127] to compute steady-state solutions of model, advection-diffusion equations, with emphasis on the steady-state case. Here, time-dependent advection-diffusion equations with stiff reaction terms are transformed to hyperbolic equations with stiff source terms. The stiff nature of such source terms is independent of the nature of the reaction terms in the original equations. In fact, even if the original equations are homogeneous (no source terms), the reformulated equations will still have stiff source terms.

Here we implement a numerical methodology in the frame of the high-order finite volume ADER scheme, [144, 150, 154]. See [22, 100] and chapters 19 and 20 of [147] for a review and the many relevant references therein. ADER schemes have already been implemented to solve adrPDEs in a straightforward manner. Titarev and Toro [145, 153] first applied ADER to solve the model advection-reaction-diffusion equation. Hidalgo and Toro applied ADER to a purely diffusion equation in [149]; Dumbser [37] and Hidalgo and Dumbser [67] applied ADER to solve the compressible Navier-Stokes equations to very high order of accuracy. Hidalgo et al. [68] also applied ADER to a

system of time-dependent diffusion-reaction equations that model atherosclerosis. However, a disadvantage of such direct approach to solve adrPDEs is the parabolic-like time stability constraint, of the type Δx^2. An extension of ADER that is able to overcome the parabolic limitations was proposed by Zambra et al. [168] for solving the Richards equation. The scheme is globally implicit, see also [158, 159]. With the relaxation approach in the sense of Cattaneo, we expect to relax such restriction. From the numerical point of view, which is one of the main motivations of the present chapter, the challenge is to reconcile stiffness and high accuracy, requirements that tend to be contradictory. For overcoming this difficulty we solve the associated generalised Riemann problem (GRP) by a locally implicit methodology due to Dumbser, Enaux and Toro in [41]. A systematic assessment of the reported numerical schemes is carried out, which includes comparison with existing methodologies. It is shown that our approach exhibits considerable gains in terms of CPU times, due to a generous stability restriction when choosing the time step.

The remaining part of this chapter is organised as follows. Sec. 2.2 gives a brief introduction to the finite volume and ADER methods. In Sec. 2.3 we introduce Cattaneo's relaxation approach to reformulate adrPDEs as hyperbolic systems with stiff source terms. A comparison of this relaxation procedure with other commonly used approaches is carried out. A theoretical result to choose the relaxation parameter, which ensures the accuracy of hyperbolic reformulations and an empirical convergence rate assessment is carried out in Sec. 2.4. The issue of parabolic time step limitation is discussed in Sec. 2.5. Our reformulated adrPDEs are solved numerically; comparisons with exact solutions are made and convergence rates are studied. In Sec. 2.6 we apply the developed ADER methods to solve a system of reaction-diffusion equations associated to a model for atherosclerosis. In section 2.7 we prove that partial differential equations of third order cannot be reduced to hyperbolic systems, following the Cattaneo approach. Concluding remarks are found in Sec. 2.8.

2.2   The ADER approach for hyperbolic equations

We first recall the finite volume method and then succinctly review the a variant of the ADER approach, which will be extended here to solve advection-diffusion-reaction equations.

2.2.1 The finite volume framework

We are interested in solving the general initial-boundary value problem

$$
\left.\begin{array}{rl}
PDE: & \partial_t q(x,t) + \partial_x f(q(x,t)) = s(q(x,t)) , \quad x \in [a,b] , \ t > 0 , \\[2mm]
IC: & q(x,0) = h(x) , \\[2mm]
BCs: & q(a,t) = q_L(t) , \ q(b,t) = q_R(t) ,
\end{array}\right\} \tag{2.1}
$$

where $q(x,t)$ is the conserved quantity, $f(q(x,t))$ is a prescribed physical flux function and $s(q(x,t))$ is the source term, also prescribed. The initial condition is $h(x)$, while $q_L(t)$ and $q_R(t)$ are the boundary conditions. The finite volume method results from integrating the PDE in (2.1), in space and time, in the control volume $[x_{i-\frac{1}{2}}, x_{i+\frac{1}{2}}] \times [t^n, t^{n+1}]$ of dimensions $\Delta x = x_{i+\frac{1}{2}} - x_{i-\frac{1}{2}}$ and $\Delta t = t^{n+1} - t^n$. One obtains

$$
q_i^{n+1} = q_i^n - \frac{\Delta t}{\Delta x}[f_{i+\frac{1}{2}} - f_{i-\frac{1}{2}}] + \Delta t s_i , \tag{2.2}
$$

where q_i^n is the spatial-integral average at time $t = t^n$

$$
q_i^n = \frac{1}{\Delta x} \int_{i-\frac{1}{2}}^{i+\frac{1}{2}} q(x,t^n) dx , \tag{2.3}
$$

$f_{i+\frac{1}{2}}$ is the time-integral average

$$
f_{i+\frac{1}{2}} = \frac{1}{\Delta t} \int_{t^n}^{t^{n+1}} f(q(x_{i+\frac{1}{2}},t)) dt \tag{2.4}
$$

and s_i is the space-time integral average

$$
s_i = \frac{1}{\Delta t}\frac{1}{\Delta x} \int_{t^n}^{t^{n+1}} \int_{x_{i-\frac{1}{2}}}^{x_{i+\frac{1}{2}}} s(q(x,t)) dx dt . \tag{2.5}
$$

Formula (2.2) is exact if definitions (2.3)-(2.5) are adhered to. The finite volume scheme begins by interpreting (2.2) in an approximate manner, as a numerical formula to update in time, approximations to cell integral averages (2.3). Let us denote by $I_i = [x_{i-\frac{1}{2}}, x_{i+\frac{1}{2}}]$ a cell, or volume, in the discretised domain $[a,b]$. A finite volume method is determined once approximations to $f_{i+\frac{1}{2}}$ and s_i are proposed. These are respectively termed the *numerical* flux and the *numerical source*. There are many ways of constructing finite volume methods. Next we briefly review the ADER methodology.

2.2.2 ADER finite volume schemes

The ADER finite volume approach computes high-order approximations to the integral averages (2.4) and (2.5), to obtain an ADER numerical flux and an ADER numerical source. The ADER methodology is an extension of the second-order method of Ben-Artzi and Falcoviz [10]. The extension concerns the generalised Riemann problem (GRP) to evaluate the numerical flux, and is twofold: (a) the initial condition for the GRP is piece-wise polynomials of any degree, and (b) the equations preserve their source terms, if present originally. We also remark that ADER is akin to the method proposed by Harten et al. [66], as noted by Castro and Toro [22]. The ADER approach was first put forward by Toro et al. [150] for linear problems on Cartesian meshes, see also [132]. Several extensions have been done to non-linear problems on Cartesian meshes [144, 146, 154] and on non Cartesian meshes [21, 79, 80], to mention but a few. Extension of the ADER approach in the framework of discontinuous Galerkin finite element methods is due to Dumbser; see [35, 36, 45], for instance. The ADER methods are one-step schemes, fully discrete, containing two main ingredients to determine the numerical flux, namely (i) a high-order, non-linear spatial reconstruction procedure and (ii) solution of a generalised, or high order, Riemann problem at each cell interface. If source terms are present, an additional, analogous step is required. Reconstructions should be non-linear, to circumvent Godunov's theorem [55, 147]. Concerning the GRP, in this chapter we use the solver due to Dumbser et al. [41], that allows the treatment of stiff source terms in a way that the usually contradictory requirements of high accuracy and stiffness are reconciled. For a review of ADER see [22, 100] and chapters 19 and 20 of [147].

2.2.3 Generalised Riemann problem, flux and source

The ADER approach requires a high-order representation of the solution in each volume, or cell, at any given time t^n, typically via spatial polynomials of high degree. We use a WENO interpolation procedure to circumvent Godunov's theorem and control spurious oscillations.

The Generalized Riemann Problem (GRP) for (2.1) is the Cauchy problem

$$\left. \begin{array}{ll} \text{PDE:} & \partial_t q + \partial_x f(q) = s(q) \ , \\[2em] \text{IC :} & q(x,0) = \left\{ \begin{array}{ll} p_i(x) & \text{if} \quad x < 0 \ , \\[1em] p_{i+1}(x) & \text{if} \quad x > 0 \ . \end{array} \right. \end{array} \right\} \qquad (2.6)$$

Here $p_i(x)$ and $p_{i+1}(x)$ are polynomials of arbitrary degree resulting from a reconstruction procedure. The solution of (2.6) at the fixed interface position $x_{i+\frac{1}{2}}$, or $x = 0$ in local coordinates, denoted by $q_{i+\frac{1}{2}}(\tau)$, is a function of time and will be available once the GRP (2.6) is solved. The first practical solver for the GRP is due to Toro and Titarev [154]. A review of GRP solvers is found in [100]. The numerical flux $f_{i+\frac{1}{2}}$ results from the evaluation of

$$f_{i+\frac{1}{2}} = \frac{1}{\Delta t} \int_0^{\Delta t} f(q_{i+\frac{1}{2}}(\tau)) d\tau \ . \tag{2.7}$$

In the presence of source terms we construct an approximation $q_i(x, t)$ of the solution of the Cauchy problem

$$\left. \begin{array}{ll} \text{PDE:} & \partial_t q + \partial_x f(q) = s(q) \ , \quad x \in [x_{i-\frac{1}{2}}, x_{i+\frac{1}{2}}] \ , \ t > 0 \ , \\[2ex] \text{IC :} & q(x, 0) = p_i(x) \ . \end{array} \right\} \tag{2.8}$$

Then the numerical source is

$$s_i = \frac{1}{\Delta t} \frac{1}{\Delta x} \int_0^{\Delta t} \int_{x_{i-\frac{1}{2}}}^{x_{i+\frac{1}{2}}} s(q_i(x, t)) dx dt \ . \tag{2.9}$$

For the rest of this chapter we assume that the function $q_{i+\frac{1}{2}}(\tau)$ is computed by using the DET solver [41] for the GRP, to be briefly described in the next subsection.

2.2.4 The Dumbser-Enaux-Toro (DET) solver for the GRP

Here we briefly outline the two mains steps of the procedure to solve the GRP using the method proposed by Dumbser et al. [41]: (i) evolution of the initial conditions to the left and right of the interface and (ii) interaction of the evolved data at the interface, at any specified time, by solving a classical Riemann problem.

2.2.4.1 Data evolution

The data-evolution step first defines two space-time control volumes, namely $I_L = [-\Delta x, 0] \times [0, \Delta t]$ to the left of the interface and $I_R = [0, \Delta x] \times [0, \Delta t]$ to the right of the interface. Then, in each of these domains one defines the Cauchy problem

$$\left. \begin{array}{ll} \text{PDE:} & \partial_t q + \partial_x f(q) = s(q) \ , \\[2ex] \text{IC :} & q(x, 0) = p_k(x) \ , \end{array} \right\} \tag{2.10}$$

where $k = i$ for I_L and $k = i+1$ for I_R. For convenience we transform I_L and I_R into the reference domain $[0,1] \times [0,1]$ using

$$x(\xi) = (\xi - 1)\Delta x \,, \quad t(\tau) = \tau \Delta t \,, \quad \text{for } (x,t) \in I_L \tag{2.11}$$

and

$$x(\xi) = \xi \Delta x \,, \quad t(\tau) = \tau \Delta t \,, \quad \text{for } (x,t) \in I_R \,. \tag{2.12}$$

In $\xi - \tau$ coordinates the Cauchy problem (2.10) becomes

$$\left.\begin{aligned}
\text{PDE:} \quad & \partial_\tau r(\xi, \tau) + \partial_\xi g(r(\xi, \tau)) = z(r(\xi, \tau)) \,, \\[2mm]
\text{IC :} \quad & r(\xi, 0) = p_k(x(\xi)) \,,
\end{aligned}\right\} \tag{2.13}$$

where

$$r(\xi, \tau) = q(x(\xi), t(\tau)) \,, \quad g(r) = \frac{\Delta t}{\Delta x} f(r) \,, \quad z(r) = \Delta t s(r) \,. \tag{2.14}$$

Problem (2.13) is now solved using a space-time discontinuous Galerkin method. Consider a space $\mathbf{V}$ formed by nodal space-time polynomials $\theta_p(\xi, \tau)$ defined in $[0,1] \times [0,1]$, whose basis is $\{\theta_1, ..., \theta_m\}$. Here $m = (K+1)^2$, with K the degree of the reconstruction polynomials $p_k(x)$, with $K+1$ degrees of freedom. Note that $K+1$ will also be the order of accuracy of the resulting ADER numerical scheme.

We seek solutions of the form

$$r(\xi, \tau) = \sum_{p=1}^{m} \theta_p(\xi, \tau) \hat{r}_p \tag{2.15}$$

and introduce the following operators for any two functions $\phi(\xi, \tau)$ and $\psi(\xi, \tau)$, namely

$$[\phi, \psi]_\tau = \int_0^1 \phi(\xi, \tau)\psi(\xi, \tau)d\xi \,, \quad \langle \phi, \psi \rangle = \int_0^1 \int_0^1 \phi(\xi, \tau)\psi(\xi, \tau)d\xi d\tau \,. \tag{2.16}$$

Then, multiplying (2.13) by a test function $\theta_l \in V$ and integrating the first term on the left hand side by parts, in time τ, yields

$$[r, \theta_l]_1 - \langle r, \partial_\tau \theta_l \rangle + \langle \partial_\xi g(r), \theta_l \rangle = \langle z(r), \theta_l \rangle + [p_k, \theta_l]_0 \,, \tag{2.17}$$

with

$$[p_k, \theta_l]_0 = \int_0^1 p_k(x(\xi))\theta_l(\xi, 0)d\xi \,. \tag{2.18}$$

We now define matrices

$$\left.\begin{aligned} \mathbf{K}_{k,l}^1 &= [\theta_k, \theta_l]_1 - \langle \theta_k, \partial_\tau \theta_l \rangle \ , \\[2ex] \mathbf{K}_{k,l}^\xi &= \langle \partial_\xi \theta_k, \theta_l \rangle \ , \\[2ex] \mathbf{M}_{k,l} &= \langle \theta_k, \theta_l \rangle \ , \\[2ex] \mathbf{W}_l &= [p_k, \theta_l]_0 \end{aligned}\right\} \tag{2.19}$$

and vectors

$$\mathcal{R} = \begin{bmatrix} \hat{r}_1 \\ \vdots \\ \hat{r}_m \end{bmatrix} \ , \quad \mathcal{G}(\mathcal{R}) = \begin{bmatrix} g(\hat{r}_1) \\ \vdots \\ g(\hat{r}_m) \end{bmatrix} \ , \quad \mathcal{Z}(\mathcal{R}) = \begin{bmatrix} z(\hat{r}_1) \\ \vdots \\ z(\hat{r}_m) \end{bmatrix} . \tag{2.20}$$

Then, as the polynomial basis is nodal, (4.54) can be written as

$$\mathbf{K}^1 \mathcal{R} + \mathbf{K}^\xi \mathcal{G}(\mathcal{R}) - \mathbf{M} \mathcal{Z}(\mathcal{R}) = \mathbf{W} \ . \tag{2.21}$$

This is a system of non-linear algebraic equations for $\mathcal{R}$. Standard fix-point iteration methods can be used. Here we suggest that proposed in [23], namely

$$\mathbf{K}^1 \mathcal{R}^{n+1} + \mathbf{K}^\xi \mathcal{G}(\mathcal{R}^n) - \mathbf{M} \mathcal{Z}(\mathcal{R}^{n+1}) = \mathbf{W}, \tag{2.22}$$

where n stands for the Newton iteration step. Once $\mathcal{R}$ is known, the sought coefficients are known and the polynomial representations of the form (4.56) for the evolved data on both sides of the interface are available, which are denoted by r_i and r_{i+1} respectively.

2.2.4.2 Data interaction for flux evaluation

To compute the numerical flux we need to determine a function $q_{i+\frac{1}{2}}(\tau)$. This is achieved by solving the following *classical Riemann problem*

$$\left.\begin{aligned} \text{PDE:} \quad &\partial_t q(x,t) + \partial_x f(q(x,t)) = 0 \ , \\[2ex] \text{IC:} \quad &q(x,0) = \begin{cases} r_i(1,\tau) & if \quad x < 0 \ , \\ r_{i+1}(0,\tau) & if \quad x > 0 \ . \end{cases} \end{aligned}\right\} \tag{2.23}$$

In local coordinates, denote by $u(\hat{x}/\hat{t})$ the self-similar solution of (2.23), then $q_{i+\frac{1}{2}}(\tau) = u(0)$. To evaluate the numerical flux we only require to compute the function $q_{i+\frac{1}{2}}(\tau)$ at
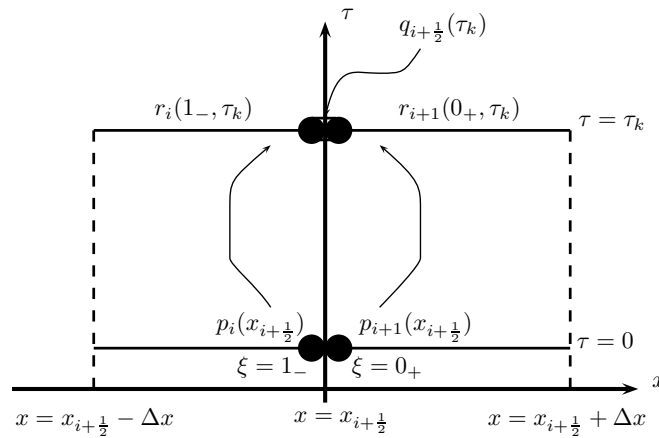
FIGURE 2.1: Illustration of the DET solver for the GRP at the interface, at a given time τ_k.

selected integration points τ_k, as illustrated in Fig. 2.1. The evaluation of the numerical source is very simple, one just proceeds to evaluate the space-time integral (2.9) using the evolved data $r_i(\xi, \tau)$ in I_L for cell i. In the next section we deal with reformulations of adrPDEs in terms of hyperbolic problems with stiff source terms.

2.3 Advection-diffusion-reaction equations

In this section we formulate the family of advection-diffusion-reaction partial differential equations as *hyperbolised equations* with stiff source terms, following the Cattaneo's relaxation approach, as used in [111] and [112], for example. First we deal with the linear scalar case.

2.3.1 The linear scalar case

Consider the time-dependent, advection-diffusion-reaction equation, with stiff or non-stiff reaction term

$$\partial_t q_1(x,t) + \hat{\lambda}\partial_x q_1(x,t) = \alpha\partial_x^2 q_1(x,t) + \beta q_1(x,t) . \tag{2.24}$$

Here the unknown function is $q_1(x,t)$, $\hat{\lambda}$ is the characteristic speed, $\alpha > 0$ is the diffusion coefficient and $\beta \leq 0$ is the reaction coefficient. We allow for stiff reaction, for which $|\beta| >> 1$. Note that the formulation works equally well for non-stiff source terms, or no source term.

We introduce a relaxation time ε, with $0 < \varepsilon << 1$, and an auxiliary function $q_2(x,t)$ such that

$$q_2(x,t) \to \partial_x q_1(x,t) \quad as \quad \varepsilon \to 0 . \tag{2.25}$$

Then we consider the following additional partial differential equation

$$\partial_t q_2(x,t) = (\partial_x q_1(x,t) - q_2(x,t)) \frac{1}{\varepsilon} . \tag{2.26}$$

Equations (2.24) and (2.26) constitute a relaxation system

$$\left.\begin{array}{rcl} \partial_t q_1(x,t) + \hat{\lambda}\partial_x q_1(x,t) - \alpha\partial_x q_2(x,t) & = & \beta q_1(x,t) , \\[2mm] \partial_t q_2(x,t) - \frac{1}{\varepsilon}\partial_x q_1(x,t) & = & -q_2(x,t)\frac{1}{\varepsilon} , \end{array}\right\} \tag{2.27}$$

whose solutions approximates those of the original equation (2.24).

2.3.2 Comparison between Cattaneo's and commonly used relaxation approaches

The constitutive equation (2.26) is equivalent to the original, augmented Fourier law proposed by Cattaneo [25] and Vernotte [160]. See [107] for a detailed review of the hyperbolic heat equation and how it is obtained from the modified Fourier law.

At this point, we remark that there exist other relaxation approaches, which are characterised by different constitutive equations but still able to reproduce (2.25). Examples include [74–76, 108], whose origin can be traced to the theoretical work of Liu [94]. This approach [74], which we refer to as the *Jin and Levermore* relaxation procedure, is different from Cattaneo's original ideas. The constitutive equation is given by

$$\partial_t q_2(x,t) = \left(\hat{\lambda}q_1(x,t) - \alpha\partial_x q_1(x,t) - q_2(x,t)\right)\frac{1}{\varepsilon} . \tag{2.28}$$

Note however, that in contrast to relaxation (2.27), the constitutive equation (2.28) completely modifies the governing equation (2.24). Now, convective terms become source terms in (2.28). This relaxation approach reads

$$\left.\begin{array}{rcl} \partial_t q_1(x,t) + \partial_x q_2(x,t) & = & \beta q_1(x,t) , \\[2mm] \partial_t q_2(x,t) + \frac{\alpha}{\varepsilon}\partial_x q_1(x,t) & = & \left(\hat{\lambda}q_1(x,t) - q_2(x,t)\right)\frac{1}{\varepsilon} . \end{array}\right\} \tag{2.29}$$

Motivated by the analysis reported in [128], we have carried out a dispersive analysis of the relaxation approaches (2.27) and (2.29), and the original equation (2.24). In what

follows, we briefly describe this procedure. Let us consider the Fourier modes

$$q_1 = Q_1 exp(Iwt - \xi x) \ ,$$
$$q_2 = Q_2 exp(Iwt - \xi x) \ ,$$
(2.30)

with $I^2 = -1$. Assume the expression $w = w_R + w_I I$, where w_R is a wave speed and w_I is a damping rate. Then we substitute (2.30) into equations (2.24), (2.27) and (2.29). In order to study just advection and diffusion, source terms have been neglected in all equations. Thus, for each case we obtain algebraic equations for w_R and w_I as functions of the parameter $\tau = \xi \varepsilon^{\frac{1}{2}}$.

For a comparison, the important quantities are the dimensionless wave speed $a(\xi) := \frac{w_R}{\xi}$ and damping $e^{\tau b(\xi)}$, where $b(\xi)$ is the dimensionless damping rate defined as $b(\xi) := \frac{w_I}{\xi^2}$.

Fig 2.2 shows the behaviour of the dimensionless wave speed as function of τ for two regimes. The top frame shows the diffusion-dominated case, while the bottom frame shows the advection-dominated case.

The figure illustrates the fact that both relaxations (2.31) and (2.29) have similar wave speeds for the range of small values of τ. However, this is not so, for the range of larger values of τ. This difference is more evident for the advection-dominated case, see bottom frame. For the diffusion-dominated case, both approaches cease to work for values of τ greater than approximately 0.5, see top frame. For the advection-dominated case, Cattaneo's approach correctly follows the parabolic wave speed, while the approach of Jin and Levermore [74–76, 108] fails to do so, stating from a relatively small value of τ of approximately between 10^{-2} and 5×10^{-2}. Note that $\tau = \xi \varepsilon^{\frac{1}{2}}$ and thus the discussion regarding its range is relevant when it comes to the choice of the relaxation parameter ε.

2.3.3   Hyperbolic reformulation of the linear scalar problem

System (2.24) and (2.26) can be written in the form of a system of hyperbolic balance laws with source terms, namely

$$\partial_t \mathbf{Q} + \partial_x \mathbf{F}(\mathbf{Q}) = \mathbf{S}(\mathbf{Q}) \ ,$$
(2.31)

with

$$\mathbf{Q} = \begin{bmatrix} q_1 \\ q_2 \end{bmatrix} \ , \ \mathbf{F} = \begin{bmatrix} f_1 \\ f_2 \end{bmatrix} = \begin{bmatrix} \hat{\lambda} q_1 - \alpha q_2 \\ -q_1/\varepsilon \end{bmatrix} \ , \ \mathbf{S} = \begin{bmatrix} s_1 \\ s_2 \end{bmatrix} = \begin{bmatrix} \beta q_1 \\ -q_2/\varepsilon \end{bmatrix} \ .$$
(2.32)
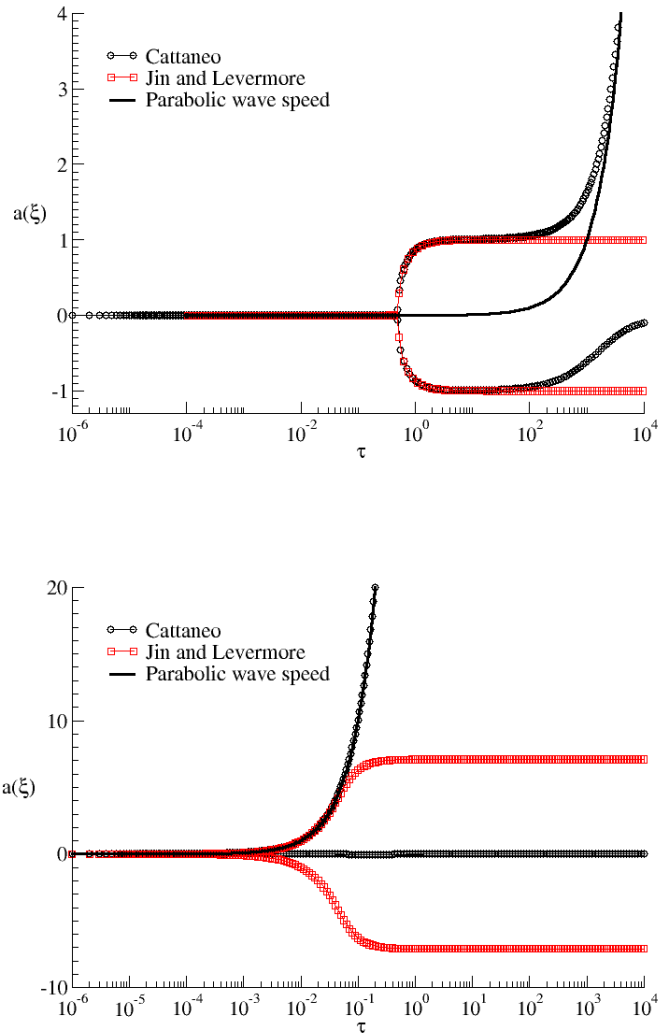
FIGURE 2.2: Comparison of relaxation approaches. Behaviour of the dimensionless wave speed as function of τ for two regimes: Top frame shows the diffusion-dominated case, while the bottom frame shows the advection-dominated case.

Note that irrespectively of the nature of the source term $s(q_1)$ in the original equation, the relaxation system is stiff due to the new source term $-q_2/\varepsilon$.

Below we prove hyperbolicty of system (2.31), a result that the reader can also find in [112]. However, for the sake of completeness we provide full details, here.

Proposition 2.1. *The relaxation system (2.31) is strictly hyperbolic for all nonzero values of the relaxation parameter ε.*

Proof. Written in quasilinear form, system (2.31) reads

$$\partial_t \mathbf{Q} + \mathbf{A} \partial_x \mathbf{Q} = \mathbf{S}(\mathbf{Q}) \,, \tag{2.33}$$

in which the Jacobian matrix is

$$\mathbf{A} = \frac{\partial \mathbf{F}}{\partial \mathbf{Q}} = \begin{bmatrix} \partial f_1/\partial q_1 & \partial f_1/\partial q_2 \\ \\ \partial f_2/\partial q_1 & \partial f_2/\partial q_2 \end{bmatrix} = \begin{bmatrix} \hat{\lambda} & -\alpha \\ \\ -\frac{1}{\varepsilon} & 0 \end{bmatrix} . \tag{2.34}$$

The eigenvalues of $\mathbf{A}$ are the roots of the characteristic polynomial $|\mathbf{A} - \lambda \mathbf{I}| = 0$, where $\mathbf{I}$ is the identity matrix and λ is a parameter. The eigenvalues are both real and distinct, given as

$$\lambda_1 = \frac{1}{2}\hat{\lambda} - \sqrt{\left(\frac{1}{2}\hat{\lambda}\right)^2 + \frac{\alpha}{\varepsilon}} \,, \quad \lambda_2 = \frac{1}{2}\hat{\lambda} + \sqrt{\left(\frac{1}{2}\hat{\lambda}\right)^2 + \frac{\alpha}{\varepsilon}} \,. \tag{2.35}$$

Note that the associated wave pattern satisfies

$$\lambda_1 < \hat{\lambda} < \lambda_2 \,. \tag{2.36}$$

The right eigenvectors, for appropriate scalings, are

$$\mathbf{R}_1 = \begin{bmatrix} \varepsilon \lambda_1 \\ -1 \end{bmatrix} \,, \quad \mathbf{R}_2 = \begin{bmatrix} \varepsilon \lambda_2 \\ -1 \end{bmatrix} \,, \tag{2.37}$$

which for $\lambda_1 \neq \lambda_2$ are linearly independent. Therefore the relaxation system (2.31) is strictly hyperbolic and Proposition 2.3.3 is thus proved.

□

Next we find exact solutions to the relaxation system.

Proposition 2.2. *For all values of ε and β satisfying*

$$\beta = -1/\varepsilon \,, \tag{2.38}$$

the general initial value problem for system (2.31) with initial conditions

$$\mathbf{Q}^{(0)}(x) = \mathbf{Q}(x,0) = \begin{bmatrix} q_1^{(0)}(x) \\ q_2^{(0)}(x) \end{bmatrix} \,, \tag{2.39}$$

has exact solution

$$
\begin{aligned}
q_1(x,t) \;=\;& \frac{e^{-\frac{1}{\varepsilon}t}}{(\lambda_2-\lambda_1)}\lambda_1[-q_1^{(0)}(x-\lambda_1 t)-\varepsilon\lambda_2 q_2^{(0)}(x-\lambda_1 t)] \\[2mm]
&+\frac{e^{-\frac{1}{\varepsilon}t}}{(\lambda_2-\lambda_1)}\lambda_2[q_1^{(0)}(x-\lambda_2 t)+\varepsilon\lambda_1 q_2^{(0)}(x-\lambda_2 t)]\,,
\end{aligned}
\tag{2.40}
$$

and

$$
\begin{aligned}
q_2(x,t) \;=\;& -\frac{e^{-\frac{1}{\varepsilon}t}}{\varepsilon(\lambda_2-\lambda_1)}[q_1^{(0)}(x-\lambda_1 t)+\varepsilon\lambda_2 q_2^{(0)}(x-\lambda_1 t)] \\[2mm]
&+\frac{e^{-\frac{1}{\varepsilon}t}}{\varepsilon(\lambda_2-\lambda_1)}[q_1^{(0)}(x-\lambda_2 t)+\varepsilon\lambda_1 q_2^{(0)}(x-\lambda_2 t)]\,.
\end{aligned}
\tag{2.41}
$$

Proof. The matrix of right eigenvectors is

$$
\mathbf{R}=\begin{bmatrix} \varepsilon\lambda_1 & \varepsilon\lambda_2 \\ -1 & -1 \end{bmatrix}
\tag{2.42}
$$

and the characteristic are variables

$$
\mathbf{C}=\begin{bmatrix} c_1 \\ c_2 \end{bmatrix}=\mathbf{R}^{-1}\mathbf{Q}\,.
\tag{2.43}
$$

We can express system (2.31) in characteristic variables as

$$
\partial_t\mathbf{C}+\mathbf{\Lambda}\partial_x\mathbf{C}=\hat{\mathbf{S}}\,,
\tag{2.44}
$$

with diagonal coefficient matrix

$$
\mathbf{\Lambda}=\begin{bmatrix} \lambda_1 & 0 \\ 0 & \lambda_2 \end{bmatrix}
\tag{2.45}
$$

and transformed source term as

$$
\hat{\mathbf{S}}=\begin{bmatrix} \hat{s}_1 \\ \hat{s}_2 \end{bmatrix}=\mathbf{R}^{-1}\mathbf{S}\,.
\tag{2.46}
$$

Now, under assumption (2.38) it is shown that

$$
\hat{s}_1=-\frac{1}{\varepsilon}c_1\,,\quad \hat{s}_1=-\frac{1}{\varepsilon}c_1\,,
\tag{2.47}
$$

so that system (2.44) becomes decoupled and the exact solutions for $c_1(x,t)$ and $c_2(x,t)$ can be computed as

$$
\left.
\begin{aligned}
c_1(x,t) &= c_1^{(0)}(x - \lambda_1 t)e^{\frac{1}{\varepsilon}t} \ , \\[2ex]
c_2(x,t) &= c_2^{(0)}(x - \lambda_2 t)e^{-\frac{1}{\varepsilon}t} \ .
\end{aligned}
\right\}
\tag{2.48}
$$

Transforming back to the original variables we obtain the solution for the initial value problem for (2.31) with initial condition (2.39), given in (2.40)-(2.41), as claimed.

$\square$

The exact solution to the relaxation system just constructed will be used to assess the performance of numerical methods. Next we deal with the non-linear case.

2.3.4 The non-linear case

We consider the initial-value problem for a general non-linear advection-diffusion-reaction equation

$$
\left.
\begin{aligned}
\partial_t q(x,t) + \partial_x f(q(x,t)) &= \partial_x(\alpha(q(x,t)\partial_x q(x,t)) + s(q(x,t)) \ , \\[2ex]
q(x,0) &= h(x) \ ,
\end{aligned}
\right\}
\tag{2.49}
$$

with $f(q)$ the flux function, $s(q)$ the source function and $\alpha(q)$ the diffusion coefficient, a non-negative function of q. We propose the relaxation formulation for (2.49) as

$$
\left.
\begin{aligned}
\partial_t q_1(x,t) + \partial_x f(q_1(x,t)) &= \partial_x(\alpha(q_1(x,t)q_2(x,t)) + s(q_1(x,t)) \ , \\[2ex]
\partial_t q_2(x,t) - \tfrac{1}{\varepsilon}\partial_x q_1(x,t) &= -\tfrac{1}{\varepsilon}q_2(x,t) \ .
\end{aligned}
\right\}
\tag{2.50}
$$

In conservative form the system reads

$$
\partial_t \mathbf{Q} + \partial_x \mathbf{F}(\mathbf{Q}) = \mathbf{S}(\mathbf{Q}) \ ,
\tag{2.51}
$$

where

$$
\mathbf{Q} = \begin{bmatrix} q_1 \\ q_2 \end{bmatrix} \ , \quad
\mathbf{F} = \begin{bmatrix} f(q_1) - \alpha(q_1)q_2 \\ -\tfrac{1}{\varepsilon}q_1 \end{bmatrix} \quad
\mathbf{S} = \begin{bmatrix} s(q_1) \\ -\tfrac{1}{\varepsilon}q_2 \end{bmatrix} \ .
\tag{2.52}
$$

Written in quasilinear form, system (2.51) reads

$$
\partial_t \mathbf{Q} + \mathbf{A}(\mathbf{Q})\partial_x \mathbf{Q} = \mathbf{S}(\mathbf{Q}) \ ,
\tag{2.53}
$$

where $\mathbf{A}$ is the Jacobian matrix

$$\mathbf{A} = \begin{bmatrix} \eta(q_1, q_2) & -\alpha(q_1) \\ -\frac{1}{\varepsilon} & 0 \end{bmatrix} . \tag{2.54}$$

Here

$$\eta(q_1, q_2) = \hat{\lambda}(q_1) - \alpha'(q_1)q_2 \ , \quad \hat{\lambda}(q) = f'(q) \ . \tag{2.55}$$

The eigenvalues of $\mathbf{A}$ are

$$\lambda_1 = \frac{\eta}{2} - \sqrt{\left(\frac{\eta}{2}\right)^2 + \frac{\alpha}{\varepsilon}} \ , \quad \lambda_2 = \frac{\eta}{2} + \sqrt{\left(\frac{\eta}{2}\right)^2 + \frac{\alpha}{\varepsilon}} \ . \tag{2.56}$$

As we have assumed α to be non-negative, the eigenvalues are always real and distinct. The corresponding eigenvectors are

$$\mathbf{R}_1 = \begin{bmatrix} \varepsilon\lambda_1 \\ -1 \end{bmatrix} \ , \quad \mathbf{R}_2 = \begin{bmatrix} \varepsilon\lambda_2 \\ -1 \end{bmatrix} . \tag{2.57}$$

The eigenvectors are linearly independent and thus the relaxation system (2.51) is, strictly, hyperbolic. Note in addition that the associated wave patterns for the system always satisfy $\lambda_1 \leq \eta \leq \lambda_2$, for η positive. This is defined as the *sub-characteristic* condition [94] and also occurs for the relaxation approaches in [74, 76, 95]. But for the present work this feature is not a requirement for stability and well posedness.

2.4 Relaxation system versus the original equation

Note that the relaxation system (2.31) approaches the original advection-diffusion-reaction equation (2.24), in the limit as ε tends to zero. For finite values of ε solutions of the relaxation system differ from those of the original equation, giving rise to an error due to the formulation. When solving the relaxation system numerically, there will be an additional error, a numerical error that depends on the mesh and on the order of accuracy of the numerical method used. In order to illustrate these issues we perform some numerical calculations. Consider (2.24) with the initial condition

$$q_1(x, 0) = h(x) = sin(\pi x) \ , \tag{2.58}$$

whose exact solution is

$$q_1(x, t) = exp((-\alpha\pi^2 + \beta) \, t)sin(\pi(x - \lambda t)) \ . \tag{2.59}$$

The corresponding relaxation hyperbolic system (2.33) for the particular case $\beta = \frac{-1}{\varepsilon}$ has exact solution given by (2.40) and (2.41). We now carry out some numerical experiments, for which we introduce the Péclet number

$$Pe = \frac{\lambda L}{\alpha} \tag{2.60}$$

to assess the relative importance of advection and diffusion. Figure 2.3 shows the results of computations performed for a fixed mesh of $M = 64$ cells and $Pe = 10$. The figure shows L_1 errors as functions of $1/\varepsilon$ for schemes of 3rd, 5th and 7th order of accuracy. The L_1 errors are measured with reference to the exact solution of the original advection-diffusion-reaction equation. For large ε the error will be large, mainly due to the error in the relaxation formulation. The message is that in practical computations, specially if high-order methods are used, the error in the hyperbolised formulation must be reduced by taking suitably small values of ε. For large ε we see that changing the accuracy of the numerical method has no effect. As ε decreases, the error begins to decrease, as the relaxation system begins to get closer to the original equation. The error decreases for all methods used, but up to a point. At a certain value of ε the third order scheme can no longer decrease the error, as it is constrained by the fixed mesh of 64 cells. Due to their higher accuracy, the errors for the other methods continue to decrease, but again we see that the fifth order method reaches a point beyond which it cannot longer decrease its error. The error for the seventh order method continues to decrease. The general observation here is that the accuracy of the numerical method and the value of the relaxation parameter are intimately linked.

A key issue in our hyperbolic formulation of advection-diffusion-reaction equations, is the choice of the relaxation parameter ε. Clearly as ε tends to zero, the hyperbolic formulation recovers the original equations. A sufficiently small ε guarantees a small formulation error. In addition, small values of ε imply a more stringent CFL stability condition, resulting in smaller-than-necessarily time steps, which does scarifies efficiency. Large values of ε would imply larger time steps, but, this would also imply a larger formulation error. Moreover, in this range of larger values of ε, it could well happen that the use of fine meshes or high accurate methods is wasted due to the fact that the formulation error dominates. Below we state a theoretical result that resolves this problem.

2.4.1 A sufficiency criterion for ensuring theoretically expected accuracy

From Nagy *et al.* [107] the solution of the hyperbolized problem, u_h, and the solution of the original ADR problem, u_p, are related by

$$u_p = u_h + O(\varepsilon) \, , \tag{2.61}$$

where $O(\varepsilon)$ represents the formulation error in the relaxation approach. If we consider a numerical scheme able to solve a hyperbolic problem with an accuracy of order q, then, taking into account the cfl stability condition, we can write

$$\tilde{u} = u_h + O(\Delta x^q) \, , \tag{2.62}$$

where $\tilde{u}$ represents the numerical solution and Δx is the mesh size. Thus $O(\Delta x^q)$ represents the numerical error for the hyperbolic problem. The following result summarizes a sufficiency condition which guarantees that the adrPDE problem is solved with accuracy q.

Proposition 2.3. *The solution of the adrPDE by means of the hyperbolic reformulation, is approximated with accuracy q for all ε and Δx satisfying*

$$\triangle_q := \frac{\varepsilon}{(\Delta x)^q} K_q(q) = O(1) \, , \tag{2.63}$$

where

$$K_q(q) = \frac{1 - 2^{-\frac{1}{2}}}{2^{q - \frac{1}{2}} - 1} \, .$$

Proof. From (2.61) and (2.62) we obtain

$$\tilde{u} - u_p = u_h - u_p + O(\Delta x^q) \, , \tag{2.64}$$

which allows us to relate the formulation error and the numerical error as

$$O(\Delta x^r) = O(\varepsilon) + O(\Delta x^q) \, , \tag{2.65}$$

where r is the order of accuracy by which the numerical scheme approximates the solution of original adrPDE. Note that the numerical error can be expressed as

$$O(\Delta x^r) = C\Delta x^r \, , \tag{2.66}$$

with C depending on the problem to be solved, but is independent of the mesh spacing Δx.

We denote by $\tilde{u}_k$ the numerical solution obtained with a mesh of length Δx_k. Therefore, from (2.65) and (2.66), on two successive meshes with lengths Δx_k, Δx_{k+1}, we obtain

$$\left(\frac{\Delta x_k}{\Delta x_{k+1}}\right)^r = \frac{O(\varepsilon) + O(\Delta x_k^q)}{O(\varepsilon) + O(\Delta x_{k+1}^q)} \ , \tag{2.67}$$

yielding after manipulations

$$\left(\frac{\Delta x_k}{\Delta x_{k+1}}\right)^r = \left(\frac{\Delta x_k}{\Delta x_{k+1}}\right)^q \theta \ , \tag{2.68}$$

with

$$\theta = \frac{\dfrac{O(\varepsilon)}{O(\Delta x_k^q)} + O(1)}{\dfrac{O(\varepsilon)}{O(\Delta x_{k+1}^q)} + O(1)} \ . \tag{2.69}$$

Without loss of generality, we assume $\Delta x_k = 2\Delta x_{k+1}$. Taking logarithm in (2.68), we obtain

$$r = q + \log(\theta)/\log(2) \ . \tag{2.70}$$

Let us now assume that given an expected order of accuracy q, we consider that the numerical scheme yields this accuracy if

$$r \geq q - \frac{1}{2} \ .$$

Therefore, the order of accuracy for the adrPDE attains that of the hyperbolic problem when

$$-\tfrac{1}{2} < \log(\theta)/\log(2) \ . \tag{2.71}$$

From the monotonicity of the logarithm, (2.71) is equivalent to

$$\frac{1}{\sqrt{2}} < \theta \ , \tag{2.72}$$

which yields

$$\frac{1}{\sqrt{2}}\left(2^q \frac{O(\varepsilon)}{O(\Delta x_k^q)} + O(1)\right) < \frac{O(\varepsilon)}{O(\Delta x_k^q)} + O(1) \ , \tag{2.73}$$

or

$$\frac{O(\varepsilon)}{O(\Delta x_k^q)} < O(1) \left(\frac{1 - 2^{-\frac{1}{2}}}{2^{q-\frac{1}{2}} - 1} \right) . \tag{2.74}$$

Moreover, we assume that

$$\frac{O(\varepsilon)}{O(\Delta x_k^q)} = O\left(\frac{\varepsilon}{\Delta x_k^q} \right) = K \frac{\varepsilon}{\Delta x_k^q} , \tag{2.75}$$

with K to be determined. Therefore, we impose that

$$K \frac{\varepsilon}{\Delta x_k^q} = O(1) , \tag{2.76}$$

or

$$K \varepsilon 2^{\bar{n}q} = O(1) , \tag{2.77}$$

noting that it is possible to set $\Delta x = 2^{-\bar{n}}$, where $\bar{n} = \log_2(1/\Delta x)$. So, inspired by (2.74), for all $\bar{n} \geq 0$ we set

$$K\varepsilon \leq \frac{1}{2^{\bar{n}q}} \left(\frac{1 - 2^{-\frac{1}{2}}}{2^{q-\frac{1}{2}} - 1} \right) \leq \left(\frac{1 - 2^{-\frac{1}{2}}}{2^{q-\frac{1}{2}} - 1} \right) . \tag{2.78}$$

For convenience we take $K \leq \varepsilon^{-1} K_{max}$, as to maintain order $O(1)$. Thus, we have

$$K_{max} := \varepsilon \frac{1 - 2^{-\frac{1}{2}}}{2^{q-\frac{1}{2}} - 1} . \tag{2.79}$$

In this manner, a sufficiency condition to maintain accuracy solving the adrPDE problem for a given mesh of size Δx is given by

$$\frac{\varepsilon}{(\Delta x)^q} K_q(q) = O(1) , \tag{2.80}$$

where $K_q(q) := \varepsilon^{-1} K_{max}$.

□

Remark 2.4. Note that if in equation (2.63) the left-hand side is greater than $O(1)$, the formulation error dominates over the numerical one. From the right hand side in (2.65), a mesh refinement reduces the numerical error whereas the formulation error remains, becoming the barrier for the accuracy of the numerical scheme.

Remark 2.5. In this thesis we assume $O(1) = 15$, which is the sum of the maximum magnitude accepted as $O(1)$, plus its rounding error. We observe that given a relaxation

parameter ε it is possible to predict the maximum number of cells such that the sought accuracy is attained.

Proposition 2.6. *Given a mesh spacing Δx and a numerical method of order q for solving hyperbolic formulations of advection-diffusion-reaction equations, then the optimal choice ε_r of the relaxation parameter ε obeys*

$$\varepsilon_q := \frac{O(1)\Delta x^q}{K_q(q)} \ . \tag{2.81}$$

Proof. It is directly obtained from the proposition 2.6. □

Remark 2.7. Note that (2.81) provides a practical and optimal way of choosing the relaxation time. For $\varepsilon < \varepsilon_q$, the numerical error dominates over the formulation error and for $\varepsilon > \varepsilon_q$, the formulation error dominates over the numerical error. This provides an explanation for the results shown in Figure 2.3.

2.4.2 Convergence rates study

Given two successive meshes $\mathcal{M}_n$ and $\mathcal{M}_{n+1}$ with respective mesh sizes h_n and h_{+1}, the empirical convergence rate r is

$$r = log\left(\frac{E_n^p}{E_{n+1}^p}\right)/log\left(\frac{h_n}{h_{n+1}}\right) , \tag{2.82}$$

where E_n^p denotes the error for mesh $\mathcal{M}_n$ measured with an L_p norm.

Table 2.1 shows convergence rates for $\varepsilon = 0.1$ at output time $t_{out} = 0.5$, with $Pe = 10$, $\alpha = 0.2$, $\beta = -1$ and $C_{cfl} = 0.9$. Here the error is measure against the exact solution of the relaxation system, for a large value of the relaxation parameter, $\varepsilon = 0.1$. Note that convergence rates attained are those theoretically expected. Had the error been measured against the exact solution of original equations, then we would have not expected the convergence rates to match those theoretically expected. In fact this is verified by our computations, not shown here.

Errors between the numerical solution from the relaxation procedure and the exact solution of the original advection-diffusion-reaction equation are evaluated at output time $t_{out} = 0.1$, for parameters $Pe = 10$, $\alpha = 0.2$, $\beta = -1$ and $C_{cfl} = 0.9$. Results are shown in tables 2.2 to 2.5, for $\varepsilon = 10^{-6}$, $\varepsilon = 10^{-5}$, $\varepsilon = 10^{-4}$ and $\varepsilon = 10^{-3}$, respectively. We also vary the value of relaxation parameter ε. Recall that from proposition 2.6, see (2.63), we can predict the range of mesh sizes for which the formulation error becomes dominant; in such case we cannot compute numerical solution with the expected order of accuracy.
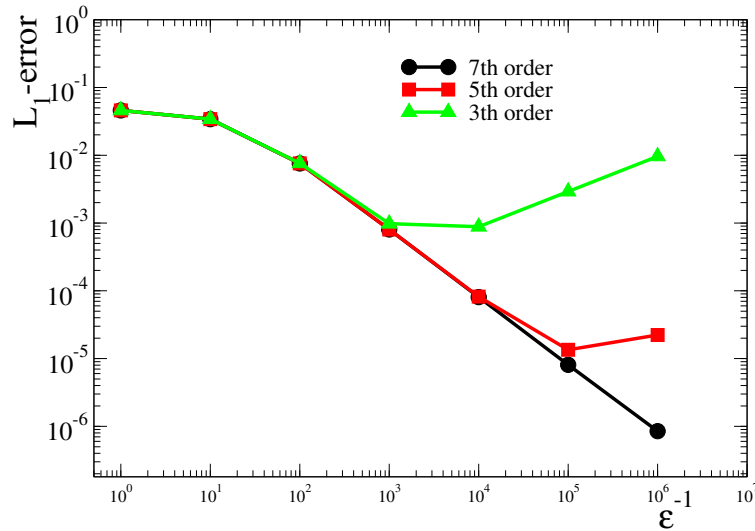
FIGURE 2.3: Influence of ε on the accuracy of the hyperbolised system. Error in the L_1 norm is measured with respect to the original advection-diffusion-reaction equation using $M = 64$ cells and $Pe = 10$, for schemes of 3rd, 5th and 7th order.

The highlighted rows in Tables 2.2 to 2.5 show the results for finest predicted meshes that correspond to the optimal predicted choice of the relaxation parameter ($\Delta_r > 15$). The use of finer meshes, see rows below the highlighted ones, does no longer make sense. The last column of each table shows the corresponding CPU times.

2.5 Discussion on stability restrictions

This section regards a discussion of stability for advection-diffusion and diffusion-reaction regimes. We compare the efficiency of our scheme with respect to numerical schemes with parabolic restrictions.

2.5.1 Stability for diffusion-reaction regimes

Time step Δt_h for numerical implementation of our schemes applied to hyperbolic balance laws is subject to a hyperbolic type condition computed according to

$$\Delta t_h = C_{cfl} \frac{\Delta x}{\lambda^n_{max}} \, , \tag{2.83}$$

where $\lambda^n_{max} = max\{|\lambda_1|, |\lambda_2|, \ldots, |\lambda_m|\}$ with λ_i denoting the eigenvalues of the Jacobian matrix. For a model problem, we shall quantify the efficiency of our scheme as compared to a scheme subject to a parabolic-type stability restriction. Our method has a clear

Theoretical order : 3

Mesh	L_∞ - err	L_∞- ord	L_1 - err	L_1 - ord	L_2 - err	L_2 - ord
8	4.27e-04	0.00	6.00e-04	0.00	4.60e-04	0.00
16	4.75e-05	3.17	6.15e-05	3.29	4.80e-05	3.26
32	5.10e-06	3.22	6.51e-06	3.24	5.11e-06	3.23
64	5.86e-07	3.12	7.46e-07	3.13	5.86e-07	3.12

Theoretical order : 5

Mesh	L_∞ - err	L_∞- ord	L_1 - err	L_1 - ord	L_2 - err	L_2 - ord
8	4.83e-05	0.00	6.43e-05	0.00	4.98e-05	0.00
16	1.28e-06	5.23	1.67e-06	5.27	1.30e-06	5.25
32	3.43e-08	5.23	4.38e-08	5.25	3.44e-08	5.25
64	9.80e-10	5.13	1.25e-09	5.13	9.80e-10	5.13

Theoretical order : 7

Mesh	L_∞ - err	L_∞- ord	L_1 - err	L_1 - ord	L_2 - err	L_2 - ord
8	5.82e-06	0.00	7.73e-06	0.00	5.99e-06	0.00
16	3.97e-08	7.19	5.16e-08	7.22	4.03e-08	7.21
32	2.86e-10	7.12	3.68e-10	7.13	2.88e-10	7.13
64	3.82e-11	2.91	1.88e-11	4.29	1.60e-11	4.17

TABLE 2.1: Convergence rates for the hyperbolised system at output time $t_{out} = 0.5$, with $\alpha = 0.2$, $Pe = 10$ and $C_{cfl} = 0.9$. The error is measure against the exact solution of the relaxation system, for a large value of the relaxation parameter, namely $\varepsilon = 0.1$. Note that convergence rates are those theoretically expected.

advantage when the adrPDE's contain stiff reactive terms. In order to highlight how our scheme works in this regime, we consider the model problem

$$\partial_\tau q = \alpha \partial_\xi^{(2)} q + \beta q \,, \tag{2.84}$$

with $\beta < 0$ and $\alpha > 0$. In order to assess stability criteria in both diffusive and reactive regimes, we introduce the dimensionless variables $\xi = Lx$ and $\tau = |\beta|^{-1}t$, which produce the dimensionless equation

$$\partial_t q = \tfrac{1}{P}\partial_x^{(2)} q - q \,, \tag{2.85}$$

where $P = \frac{|\beta|L^2}{\alpha}$ is a dimensionless number. Note that $P \to 0$ implies a diffusive regime whereas $P \to \infty$ means a reactive (stiff) regime. Thus, if we implement a finite volume scheme for this equation we obtain

$$q_i^{n+1} = q_i^n + \tfrac{\Delta t}{\Delta x}[g_{i+\frac{1}{2}} - g_{i-\frac{1}{2}}] + \Delta t s_i \,, \tag{2.86}$$

Theoretical order : 3

Mesh	L_∞ - err	L_∞- ord	L_1 - err	L_1 - ord	L_2 - err	L_2 - ord	Δ_3	CPU time(s)
8	$7.18e-01$	0.00	$8.94e-01$	0.00	$7.20e-01$	0.00	$3.31e-06$	0.04
16	$3.66e-01$	0.97	$4.71e-01$	0.93	$3.68e-01$	0.97	$2.65e-05$	0.13
32	$6.21e-02$	2.56	$7.90e-02$	2.57	$6.21e-02$	2.57	$2.12e-04$	0.48
64	$8.02e-03$	2.95	$1.02e-02$	2.95	$8.02e-03$	2.95	$1.70e-03$	1.84
128	$9.87e-04$	3.02	$1.26e-03$	3.02	$9.87e-04$	3.02	$1.36e-02$	7.15
256	$1.19e-04$	3.05	$1.52e-04$	3.05	$1.19e-04$	3.05	$1.09e-01$	28.33
512	$1.43e-05$	3.05	$1.82e-05$	3.05	$1.43e-05$	3.05	$8.69e-01$	112.44
1024	$2.08e-06$	2.78	$2.64e-06$	2.79	$2.08e-06$	2.79	$6.95e-00$	447.17
2048	$7.72e-07$	1.43	$9.79e-07$	1.43	$7.66e-07$	1.44	$55.59e-00$	1785.64
4096	$6.49e-07$	0.25	$8.24e-07$	0.25	$6.44e-07$	0.25	$444.76e-00$	7126.93

Theoretical order : 5

Mesh	L_∞ - err	L_∞- ord	L_1 - err	L_1 - ord	L_2 - err	L_2 - ord	Δ_5	CPU time(s)
8	$3.26e-01$	0.00	$4.07e-01$	0.00	$3.27e-01$	0.00	$1.33e-05$	0.33
16	$1.52e-02$	4.42	$1.96e-02$	4.37	$1.53e-02$	4.41	$4.24e-04$	0.89
32	$4.98e-04$	4.94	$6.33e-04$	4.95	$4.98e-04$	4.95	$1.36e-02$	2.61
64	$1.59e-05$	4.97	$2.02e-05$	4.97	$1.59e-05$	4.97	$4.34e-01$	8.62
128	$1.02e-06$	3.97	$1.29e-06$	3.97	$1.01e-06$	3.98	$1.39e+01$	31.07
256	$6.44e-07$	0.66	$8.17e-07$	0.66	$6.39e-07$	0.66	$4.45e+02$	101.14

Theoretical order : 7

Mesh	L_∞ - err	L_∞- ord	L_1 - err	L_1 - ord	L_2 - err	L_2 - ord	Δ_7	CPU time(s)
8	$1.70e-02$	0.00	$2.13e-02$	0.00	$1.71e-02$	0.00	$5.30e-04$	0.64
16	$1.62e-04$	6.72	$2.07e-04$	6.68	$1.63e-04$	6.72	$6.79e-02$	1.49
32	$7.27e-06$	4.48	$9.29e-06$	4.48	$7.28e-06$	4.48	$8.69e-00$	3.76
64	$6.35e-06$	0.19	$8.10e-06$	0.20	$6.36e-06$	0.20	$1.11e+02$	10.97
128	$6.35e-06$	0.00	$8.08e-06$	0.00	$6.34e-06$	0.00	$1.42e+05$	35.91
256	$6.35e-06$	0.00	$8.08e-06$	0.00	$6.34e-06$	0.00	$1.82e+07$	110.00

TABLE 2.2: Convergence rates for $\varepsilon = 10^{-6}$ at output time $t_{out} = 0.1$, with $Pe = 10$, $\alpha = 0.2$, $\beta = -1$ and $C_{cfl} = 0.9$. The error is measured against the original advection-diffusion-reaction equation. Theoretically expected convergence rates are attained. The highlighted row corresponds to the largest number of cells N for which, predicted by proposition 2.3, the theoretical convergence rate is expected to be achieved.

with the numerical flux, generally defines as

$$g_{i+\frac{1}{2}} = \frac{1}{\Delta t} \int_0^{\Delta t} \alpha \partial_x q(x_{i+\frac{1}{2}}, t) dt \ . \tag{2.87}$$

Let us consider the simple numerical flux

$$g_{i+\frac{1}{2}} = \frac{1}{P} \left(\frac{q_{i+1}^n - q_i^n}{\Delta x} \right) \ . \tag{2.88}$$

For the numerical source term the simplest evaluation of the volume integral (2.9) gives

$$s_i = -q_i^n \ . \tag{2.89}$$

Therefore, introducing the quantity

$$d = P^{-1} \frac{\Delta t}{\Delta x^2} \ , \tag{2.90}$$

Theoretical order : 3

Mesh	L_∞ - err	L_∞- ord	L_1 - err	L_1 - ord	L_2 - err	L_2 - ord	Δ_3	CPU time(s)
8	$5.83e-01$	0.00	$7.27e-01$	0.00	$5.85e-01$	0.00	$3.31e-05$	0.01
16	$1.43e-01$	2.03	$1.84e-01$	1.98	$1.44e-01$	2.02	$2.65e-04$	0.04
32	$1.98e-02$	2.85	$2.52e-02$	2.87	$1.98e-02$	2.86	$2.12e-03$	0.16
64	$2.44e-03$	3.02	$3.11e-03$	3.02	$2.44e-03$	3.02	$1.70e-02$	0.60
128	$2.93e-04$	3.06	$3.73e-04$	3.06	$2.93e-04$	3.06	$1.36e-01$	2.37
256	$3.80e-05$	2.95	$4.84e-05$	2.95	$3.80e-05$	2.95	$1.09e-00$	9.33
512	$9.40e-06$	0.00	$1.20e-05$	0.00	$9.39e-06$	0.00	$8.69e-00$	36.60
1024	$6.66e-06$	0.50	$8.47e-06$	0.50	$6.65e-06$	0.50	$69.49e-00$	147.11
2048	$6.38e-06$	0.06	$8.12e-06$	0.06	$6.37e-06$	0.06	$555.95e-00$	589.29

Theoretical order : 5

Mesh	L_∞ - err	L_∞- ord	L_1 - err	L_1 - ord	L_2 - err	L_2 - ord	Δ_5	CPU time(s)
8	$1.25e-01$	0.00	$1.56e-01$	0.00	$1.26e-01$	0.00	$1.33e-04$	0.10
16	$4.81e-03$	4.70	$6.18e-03$	4.66	$4.84e-03$	4.70	$4.24e-03$	0.28
32	$1.58e-04$	4.93	$2.00e-04$	4.95	$1.58e-04$	4.94	$1.36e-01$	0.83
64	$1.01e-05$	3.96	$1.29e-05$	3.96	$1.01e-05$	3.96	$4.34e-00$	2.75
128	$6.44e-06$	0.65	$8.19e-06$	0.65	$6.43e-06$	0.65	$1.39e+01$	9.80
256	$6.34e-06$	0.02	$8.08e-06$	0.02	$6.34e-06$	0.02	$4.45e+02$	36.09

Theoretical order : 7

Mesh	L_∞ - err	L_∞- ord	L_1 - err	L_1 - ord	L_2 - err	L_2 - ord	Δ_7	CPU time(s)
8	$1.70e-02$	0.00	$2.13e-02$	0.00	$1.71e-02$	0.00	$5.30e-04$	0.66
16	$1.62e-04$	6.72	$2.07e-04$	6.68	$1.63e-04$	6.72	$6.79e-02$	1.53
32	$7.27e-06$	4.48	$9.29e-06$	4.48	$7.28e-06$	4.48	$8.69e-00$	3.80
64	$6.35e-06$	0.19	$8.10e-06$	0.20	$6.36e-06$	0.20	$1.11e+02$	11.14
128	$6.35e-06$	0.00	$8.08e-06$	0.00	$6.34e-06$	0.00	$1.42e+05$	34.59
256	$6.35e-06$	0.00	$8.08e-06$	0.00	$6.34e-06$	0.00	$1.82e+07$	107.97

TABLE 2.3: Convergence rates for $\varepsilon = 10^{-5}$ at output time $t_{out} = 0.1$, with $Pe = 10$, $\alpha = 0.2$, $\beta = -1$ and $C_{cfl} = 0.9$. The error is measured against the original advection-diffusion-reaction equation. Theoretically expected convergence rates are attained. The highlighted row corresponds to the largest number of cells N for which, predicted by proposition 2.3, the theoretical convergence rate is expected to be achieved.

the scheme becomes

$$q_i^{n+1} = dq_{i-1}^n + (1 - 2d - \Delta t)q_i^n + dq_{i+1}^n \; . \tag{2.91}$$

A simple exercise provides the stability requirement

$$2d - \Delta t < 1 \; , \tag{2.92}$$

which gives the parabolic constraint for Δt as

$$\Delta t < \frac{\Delta x^2}{2P^{-1} + \Delta x^2} \; . \tag{2.93}$$

Thus the time step for this scheme is assumed to be computed as

$$\Delta t_p = C_{cfl} \frac{\Delta x^2}{2P^{-1} + \Delta x^2} \; . \tag{2.94}$$

Theoretical order : 3

Mesh	L_∞ - err	L_∞- ord	L_1 - err	L_1 - ord	L_2 - err	L_2 - ord	Δ_3	CPU time(s)
8	$2.94e-01$	0.00	$3.67e-01$	0.00	$2.95e-01$	0.00	$3.31e-04$	0.00
16	$4.74e-02$	2.63	$6.10e-02$	2.59	$4.77e-02$	2.63	$2.65e-03$	0.02
32	$5.99e-03$	2.99	$7.61e-03$	3.00	$5.99e-03$	3.00	$2.12e-02$	0.05
64	$7.41e-04$	3.01	$9.43e-04$	3.01	$7.41e-04$	3.01	$1.70e-01$	0.19
128	$1.32e-04$	2.49	$1.68e-04$	2.49	$1.32e-04$	2.49	$1.36e-00$	0.75
256	$7.01e-05$	0.91	$8.93e-05$	0.91	$7.01e-05$	0.91	$1.09e+01$	2.98
512	$6.42e-05$	0.00	$8.17e-05$	0.00	$6.42e-05$	0.00	$8.69e+01$	11.36
1024	$6.35e-05$	0.02	$8.08e-05$	0.02	$6.35e-05$	0.02	$6.95e+02$	45.68

Theoretical order : 5

Mesh	L_∞ - err	L_∞- ord	L_1 - err	L_1 - ord	L_2 - err	L_2 - ord	Δ_5	CPU time(s)
8	$4.22e-02$	0.00	$5.29e-02$	0.00	$4.24e-02$	0.00	$1.33e-03$	0.03
16	$1.52e-03$	4.79	$1.95e-03$	4.76	$1.53e-03$	4.79	$4.24e-02$	0.09
32	$9.97e-05$	3.93	$1.27e-04$	3.93	$9.99e-05$	3.94	$1.36e-00$	0.26
64	$6.42e-05$	0.63	$8.19e-05$	0.64	$6.43e-05$	0.64	$4.34e+01$	0.87
128	$6.34e-05$	0.02	$8.07e-05$	0.02	$6.34e-05$	0.02	$1.39e+02$	3.13
256	$6.34e-05$	0.00	$8.07e-05$	0.00	$6.34e-05$	0.00	$4.45e+03$	11.74

Theoretical order : 7

Mesh	L_∞ - err	L_∞- ord	L_1 - err	L_1 - ord	L_2 - err	L_2 - ord	Δ_7	CPU time(s)
8	$5.46e-03$	0.00	$6.85e-03$	0.00	$5.49e-03$	0.00	$5.30e-03$	0.21
16	$1.02e-04$	5.74	$1.30e-04$	5.72	$1.02e-04$	5.74	$6.79e-01$	0.49
32	$6.36e-05$	0.69	$8.07e-05$	0.69	$6.35e-05$	0.69	$8.687e+01$	1.26
64	$6.33e-05$	0.01	$8.07e-05$	0.00	$6.34e-05$	0.00	$1.11e+03$	3.42
128	$6.33e-05$	0.00	$8.07e-05$	0.00	$6.34e-05$	0.00	$1.42e+06$	11.17
256	$6.33e-05$	0.00	$8.07e-05$	0.00	$6.34e-05$	0.00	$1.82e+08$	35.79

TABLE 2.4: Convergence rates for $\varepsilon = 10^{-4}$ at output time $t_{out} = 0.1$, with $Pe = 10$, $\alpha = 0.2$, $\beta = -1$ and $C_{cfl} = 0.9$. The error is measured against the original advection-diffusion-reaction equation. Theoretically expected convergence rates are attained. The highlighted row corresponds to the largest number of cells N for which, predicted by proposition 2.3, the theoretical convergence rate is expected to be achieved.

On the other hand, the numerical scheme of the present chapter for the hyperbolic reformulation of (2.85) has the stability restriction

$$\Delta t_h = C_{cfl} \frac{\Delta x}{\sqrt{\dfrac{P^{-1}}{\varepsilon}}} \ . \tag{2.95}$$

Thus the efficiency of our schemes relative to the parabolic-type restriction can be measured in terms of the ratio

$$r_{ph} := \frac{\Delta t_p}{\Delta t_h} \ , \tag{2.96}$$

thus, the present methodology is more efficient than the other one if $r_{ph} < 1$, which is equivalent to

$$\Delta x < \sqrt{P^{-1}\varepsilon}\left(2 + \Delta x^2 P\right) . \tag{2.97}$$

Theoretical order : 3

Mesh	L_∞ - err	L_∞- ord	L_1 - err	L_1 - ord	L_2 - err	L_2 - ord	Δ_3	CPU time(s)
8	$1.07e-01$	0.00	$1.35e-01$	0.00	$1.08e-01$	0.00	$3.31e-03$	0.00
16	$1.51e-02$	2.82	$1.93e-02$	2.81	$1.52e-02$	2.83	$2.65e-02$	0.00
32	$2.20e-03$	2.78	$2.80e-03$	2.79	$2.20e-03$	2.79	$2.12e-01$	0.02
64	$7.81e-04$	1.50	$9.95e-04$	1.49	$7.81e-04$	1.49	$1.70e-00$	0.06
128	$6.47e-04$	0.27	$8.24e-04$	0.27	$6.47e-04$	0.27	$1.36e+01$	0.24
256	$6.33e-04$	0.03	$8.06e-04$	0.03	$6.33e-04$	0.03	$1.09e+02$	0.94

Theoretical order : 5

Mesh	L_∞ - err	L_∞- ord	L_1 - err	L_1 - ord	L_2 - err	L_2 - ord	Δ_5	CPU time(s)
8	$1.35e-02$	0.00	$1.72e-02$	0.00	$1.36e-02$	0.00	$1.33e-02$	0.01
16	$9.89e-04$	3.77	$1.25e-03$	3.79	$9.89e-04$	3.78	$4.24e-01$	0.03
32	$6.39e-04$	0.63	$8.11e-04$	0.62	$6.39e-04$	0.63	$1.36e+01$	0.09
64	$6.30e-04$	0.02	$8.03e-04$	0.01	$6.31e-04$	0.02	$4.34e+02$	0.29
128	$6.30e-04$	0.00	$8.03e-04$	0.00	$6.31e-04$	0.00	$1.39e+03$	1.02

Theoretical order : 7

Mesh	L_∞ - err	L_∞- ord	L_1 - err	L_1 - ord	L_2 - err	L_2 - ord	Δ_7	CPU time(s)
8	$2.03e-03$	0.00	$2.78e-03$	0.00	$2.14e-03$	0.00	$5.30e-02$	0.07
16	$6.33e-04$	1.68	$8.13e-04$	1.78	$6.37e-04$	1.75	$6.79e-00$	0.16
32	$6.30e-04$	0.01	$8.00e-04$	0.02	$6.30e-04$	0.02	$8.67e+02$	0.42
64	$6.30e-04$	0.00	$8.00e-04$	0.00	$6.30e-04$	0.00	$1.11e+04$	1.12
128	$6.30e-04$	0.00	$8.00e-04$	0.00	$6.30e-04$	0.00	$1.42e+07$	3.60

TABLE 2.5: Convergence rates for $\varepsilon = 10^{-3}$ at output time $t_{out} = 0.1$, with $Pe = 10$, $\alpha = 0.2$, $\beta = -1$ and $C_{cfl} = 0.9$. The error is measured against the original advection-diffusion-reaction equation. Theoretically expected convergence rates are attained. The highlighted row corresponds to the largest number of cells N for which, predicted by proposition 2.3, the theoretical convergence rate is expected to be achieved.

We consider the optimal ε, which provides the inequality

$$\frac{\Delta x}{2} < a_1 \Delta x^{\frac{r}{2}} + a_2 \Delta x^{\frac{r}{2}+2} \tag{2.98}$$

or

$$\frac{1}{2} < a_1 \Delta x^{\frac{r}{2}-1} + a_2 \Delta x^{\frac{r}{2}+1} \, , \tag{2.99}$$

with $a_1 = \left(\frac{O(1)P^{-1}}{K_r(r)}\right)^{\frac{1}{2}}$ and $a_2 = \left(\frac{O(1)}{4K_r(r)P^{-1}}\right)^{\frac{1}{2}}$. Let us consider the function

$$\Psi(\Delta x) = -\frac{1}{2} + a_1 \Delta x^{\frac{r}{2}-1} + a_2 \Delta x^{\frac{r}{2}+1} \, . \tag{2.100}$$

Note that the necessary condition for efficiency given by (2.98) is recovered for $\Psi > 0$. Additionally

$$\Psi'(\Delta x) = \left(\frac{r}{2}-1\right)a_1 \Delta x^{\frac{r}{2}-2} + \left(\frac{r}{2}+1\right)a_2 \Delta x^{\frac{r}{2}} \, . \tag{2.101}$$

Thus if $r > 2$, Ψ is an increasing function in $[0, \infty]$, with $\Psi(0) = -\frac{1}{2}$. Therefore, there exists Δx^* such that $\Psi(\Delta x^*) = 0$, $\Psi'(\Delta x*) > 0$ and $\Psi(\Delta x) > 0$ for all $\Delta x > \Delta x^*$. Now, we look for an estimate of Δx^*. Note that we can write

$$\Delta x \Psi'(\Delta x) = (\tfrac{r}{2} + 1)(\Psi(\Delta x) + \tfrac{1}{2}) - 2a_1 \Delta x^{\frac{r}{2} - 1} , \tag{2.102}$$

and hence

$$0 \leq \tfrac{1}{2}(\tfrac{r}{2} + 1) - 2a_1 (\Delta x^*)^{\frac{r}{2} - 1} , \tag{2.103}$$

which yields

$$\Delta x^* \leq \Delta x^*_{max} := \left(\tfrac{1}{4a_1}(1 + \tfrac{r}{2}) \right)^{\frac{2}{r-2}} . \tag{2.104}$$

Note that if $r = 2$ then

$$\Delta x^* = \Delta x^*_{max} := \left(\tfrac{1}{a_2} max\{\tfrac{1}{2} - a_1, 0\} \right)^{\frac{1}{2}} . \tag{2.105}$$

For $r = 1$, $\Psi(\Delta x) > 0$ for all Δx satisfying

$$\Delta x^*_{max} := \left(\frac{1}{2a_2} \right)^{\frac{2}{3}} \leq \Delta x . \tag{2.106}$$

Therefore, with these choices of Δx^*_{max}, we have that $\Psi(\Delta x) > 0$ for all $\Delta x > \Delta x^*_{max} \geq \Delta x^*$ and thus $r_{ph} < 1$.

Table 2.6 shows the ratio r_{ph}, time steps Δt_p and Δt_h, and Δ^*_{max} for regimes ranging from stiff reaction up to stiff diffusion. Though we are considering dimensionless quantities, the analysis illustrates the behaviour of the efficiency of the relaxation procedure for diffusive and reactive regimes. We observe that the present method is more efficient for reactive and diffusive regimes for coarse meshes, which determine large enough optimum relaxation parameters. For stiff reactive terms the efficiency of present method is up to three orders of magnitude more efficient than that of the standard parabolic restriction, while for stiff diffusive processes the present method is up to one order of magnitude more efficient.

2.5.2 Stability for advection-diffusion regimes

We now carry out a comparison of the time efficiency of our schemes following a different approach, that is by comparing our approach to that of the family of PNPM schemes

$P = 1e+03$		(stiff reaction)	
r	r_{ph}	Δt_p	Δt_h	Δx^*_{max}
2	$1.00e+00$	$3.88e-01$	$3.88e-01$	$3.56e-02$
3	$5.96e-04$	$9.99e-01$	$1.68e+03$	$1.64e+00$
5	$1.46e-03$	$9.97e-01$	$6.84e+02$	$8.84e-01$
7	$1.48e-03$	$9.97e-01$	$6.72e+02$	$7.73e-01$

$P = 1e+01$		(reaction)	
r	r_{ph}	Δt_p	Δt_h	Δx^*_{max}
2	$1.63e-01$	$3.27e-13$	$2.00e-12$	$2.56e-07$
3	$7.99e-01$	$1.34e-03$	$1.68e-03$	$1.64e-02$
5	$4.84e-01$	$1.54e-01$	$3.18e-01$	$1.90e-01$
7	$3.02e-01$	$3.21e-01$	$1.07e+00$	$3.08e-01$

$P = 1.00e+00$		(intermediate)	
r	r_{ph}	Δt_p	Δt_h	Δx^*_{max}
2	$5.17e-02$	$1.03e-13$	$2.00e-12$	$4.55e-07$
3	$8.00e-01$	$1.34e-06$	$1.68e-06$	$1.64e-03$
5	$5.69e-01$	$3.89e-03$	$6.84e-03$	$8.84e-02$
7	$4.36e-01$	$1.85e-02$	$4.24e-02$	$1.94e-01$

$P = 1.00e-01$		(diffusion)	
r	r_{ph}	Δt_p	Δt_h	Δx^*_{max}
2	$1.63e-02$	$3.27e-14$	$2.00e-12$	$8.08e-07$
3	$8.00e-01$	$1.34e-09$	$1.68e-09$	$1.64e-04$
5	$5.71e-01$	$8.42e-05$	$1.47e-04$	$4.10e-02$
7	$4.44e-01$	$7.50e-04$	$1.69e-03$	$1.23e-01$

$P = 1.00e-03$		(stiff diffusion)	
r	r_{ph}	Δt_p	Δt_h	Δx^*_{max}
2	$1.63e-03$	$3.27e-15$	$2.00e-12$	$2.56e-06$
3	$8.00e-01$	$1.34e-15$	$1.68e-15$	$1.64e-06$
5	$5.71e-01$	$3.91e-08$	$6.84e-08$	$8.84e-03$
7	$4.44e-01$	$1.19e-06$	$2.68e-06$	$4.88e-02$

TABLE 2.6: Efficiency for model diffusion-reaction equation measured for diffusive and reactive regimes.

proposed by Dumbser et al. [38]. See also [37]. The extension of these schemes, originally developed for hyperbolic equations, to parabolic equations is *conventional*, in that the discretisation of advection-diffusion-reaction equations is direct and straightforward. We shall focus on advection-diffusion type problems, as the treatment of reactive terms is similar in both methodologies. We consider the scheme with N=M, whose stable time step is given by

$$\Delta t_{dg} = C_{cfl} \frac{\Delta x}{(2r - 1)\left(\hat{\lambda} + 2\frac{\alpha}{\Delta x}(2r - 1)\right)} \ . \tag{2.107}$$

Here $\hat{\lambda}$ is the maximum eigenvalue associated with the advection terms, exclusively; α is the maximum eigenvalue associated with the diffusion terms, exclusively. The time step of our scheme in this case has the form

$$\Delta t_{h} = C_{cfl} \frac{\Delta x}{\frac{\hat{\lambda}}{2} + \sqrt{(\frac{\hat{\lambda}}{2})^2 + \frac{\alpha}{\varepsilon}}} \ . \tag{2.108}$$

The *efficiency* assessment of both schemes can be done in terms of the ratio defined as

$$r_{dgh} := \frac{\Delta t_{dg}}{\Delta t_{h}} \ . \tag{2.109}$$

For $r_{dgh} < 1$, the present approach will be more efficient than the direct discretization scheme of [37]. For the empirical comparison we take $\alpha = 1$ and $\hat{\lambda} = 1$.

Results are displayed in Figs. 2.4, 2.5 and 2.6, for $\Delta x = 5 \times 10^{-2}$, $\Delta x = 1 \times 10^{-2}$ and $\Delta x = 1 \times 10^{-3}$, respectively. The optimal relaxation parameter values ε_r are computed for the corresponding orders of accuracy and these are depicted as vertical lines in the figures. Recall that for each order of accuracy r there corresponds an optimal relaxation parameter value ε_r. For relaxation parameters $T > T_r$ the formulation error dominates over the numerical error, whereas the opposite occurs for $\varepsilon \leq \varepsilon_r$, where the numerical schemes attain the expected order of accuracy.

Figure 2.4 shows results for a coarse mesh and a corresponding range of large relaxation parameters. Results tell us that the present methods have efficiency gains for all values of ε. From our calculations we note the following: the third order scheme attains its order of accuracy for $\varepsilon \leq \varepsilon_3 = 2.98 \times 10^{-2}$; the fifth order scheme attains its order of accuracy for $\varepsilon \leq \varepsilon_5 = 3.46 \times 10^{-4}$ and the seventh order scheme does it for $\varepsilon \leq \varepsilon_7 = 3.58 \times 10^{-6}$.

Figure 2.5 shows results for an intermediate mesh and a corresponding range of intermediate relaxation parameters. Results show that for example, the third order version of the present method has efficiency gains for $\varepsilon > 2 \times 10^{-8}$ and its order of accuracy is expected for $\varepsilon < \varepsilon_3 = 2.38 \times 10^{-4}$, whereas the accuracy should be sub-optimal for
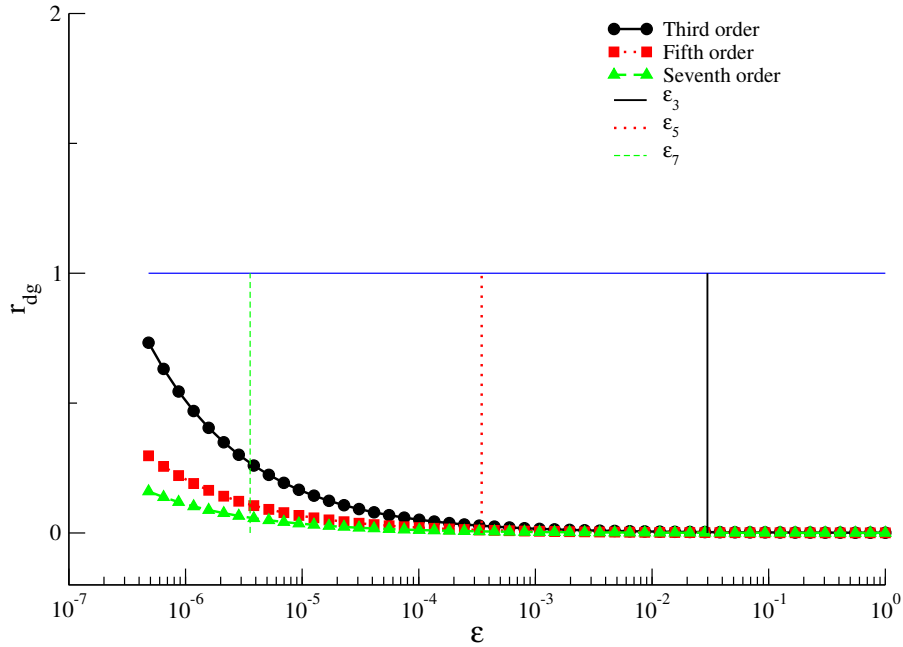
FIGURE 2.4: Time-efficiency gains for fixed $\Delta x = 5 \times 10^{-2}$. Time step ratio r_{dgh}, as function of the relaxation parameter ε, reveals the time efficiency of the present schemes as compared with the state-of-the art $PNPM$ schemes [38], [37].

$\varepsilon > \varepsilon_3$. The fifth order scheme has efficiency gains, with the expected order of accuracy, for ε in the range $3 \times 10^{-9} \leq \varepsilon \leq \varepsilon_5 = 1.11 \times 10^{-7}$; however for $\varepsilon > \varepsilon_5$, the fifth order scheme is efficient but the accuracy is sub-optimal. The seventh order scheme has efficiency gains but the accuracy is sub-optimal for $\varepsilon > 9 \times 10^{-10}$.

Figure 2.6 shows results for a fine mesh and a corresponding range of small relaxation parameters. Note that the scheme of third order is more efficient, with expected order of accuracy, for ε in the range $2 \times 10^{-10} \leq \varepsilon \leq \varepsilon_3 = 2.38 \times 10^{-7}$ and it is more efficient but the accuracy is sub-optimal for $\varepsilon > \varepsilon_3 = 2.38 \times 10^{-7}$. The fifth order scheme is efficient but its accuracy is sub-optimal for $\varepsilon > 4 \times 10^{-11}$. The seventh order scheme is more efficient but also its accuracy is sub-optimal for $\varepsilon > 8 \times 10^{-12}$.

In following section we illustrated the performance of our methods through computations for a viscous shock wave, as modelled by the viscous Burgers equation. Results are compared with those obtained from the method reported in [37].
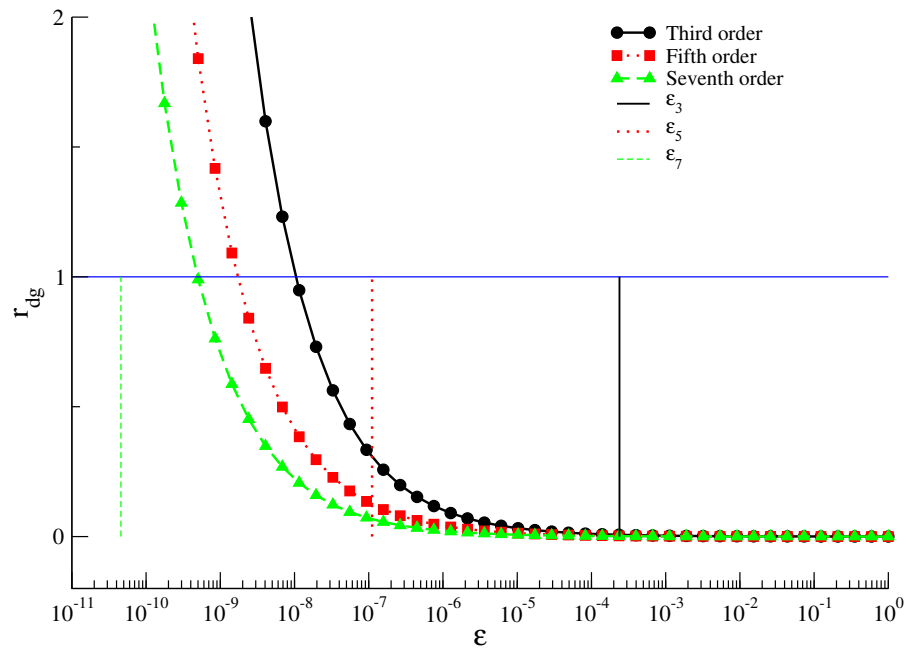
FIGURE 2.5: Time-efficiency gains for fixed $\Delta x = 1 \times 10^{-2}$. Time step ratio r_{dgh}, as function of the relaxation parameter ε, reveals the time efficiency of the present schemes as compared with the state-of-the art $PNPM$ schemes [38], [37].
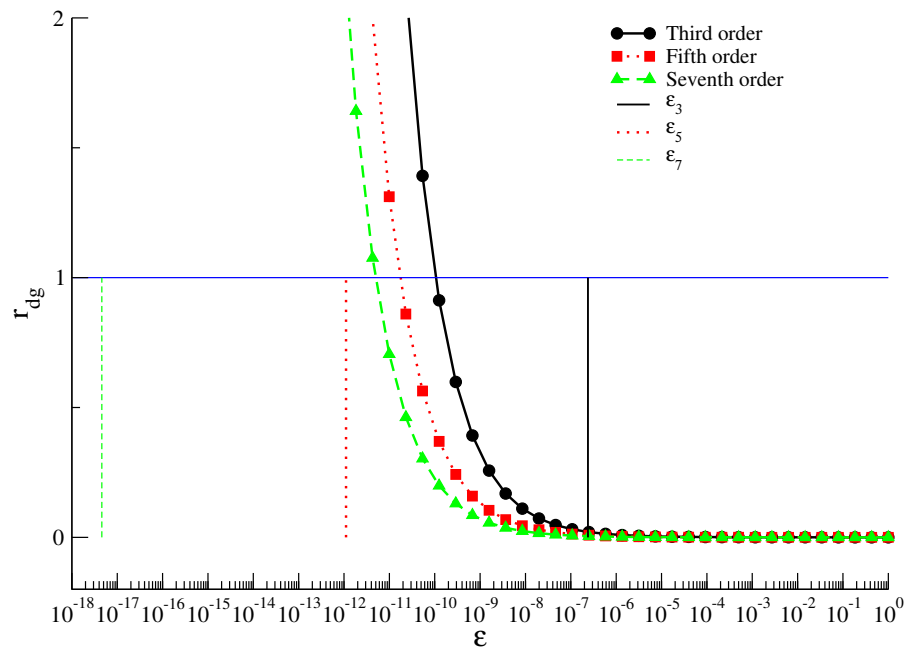
FIGURE 2.6: Time-efficiency gains for fixed $\Delta x = 1 \times 10^{-3}$. Time step ratio r_{dgh}, as function of the relaxation parameter ε, reveals the time efficiency of the present schemes as compared with the state-of-the art $PNPM$ schemes [38], [37].

Orders	Δt			CPU time		
	Ord 3	Ord 5	Ord 7	Ord 3	Ord 5	Ord 7
Present scheme, $\varepsilon = 10^{-3}$	$1.2e{-}02$	$1.2e{-}02$	$1.2e{-}02$	$1.2e{-}02$	$5.6e{-}02$	$2.4e{-}01$
Scheme of Ref. [37]	$3.6e{-}03$	$4.9e{-}04$	$2.4e{-}04$	$5.6e{-}02$	2.8	33.1

TABLE 2.7: Computations for the viscous Burgers equation. Comparison of time step size and CPU time between the present approach and that of Ref. [37]. The comparison is carried out for schemes of 3rd, 5th and 7th order of accuracy in space and time.

2.5.3 Computational results for the viscous Burgers' equation

We consider the viscous Burgers' equation

$$\partial_t q(x,t) + \partial_x f(q(x,t)) = \alpha \partial_x^{(2)} q(x,t) \; , \tag{2.110}$$

$$\tag{2.111}$$

with physical flux $f(q) = \frac{1}{2}q^2$ and α a constant. The initial condition considered is

$$h(x) = \begin{cases} q_L = 2, & x < 0 \; , \\ q_R = 1, & x > 0 \; . \end{cases} \tag{2.112}$$

As $q_L > q_R$, the solution is a (viscous) shock wave given as

$$q(x,t) = q_R + \tfrac{1}{2}(q_L - q_R)\left[1 - tanh((q_L - q_R)(x - st)/4\alpha)\right] \; , \tag{2.113}$$

with $s = \frac{1}{2}(q_L + q_R)$ being the shock speed. We solve (2.49), (2.112) numerically in the domain $[-3.0, 3.0]$, with $\varepsilon = 10^{-3}$ using the present finite volume ADER schemes of 3rd, 5th and 7th order of accuracy. Figure 2.7 shows computed results for physical viscosity $\alpha = 0.2$, at time $t_{out} = 0.2$, with $C_{cfl} = 0.9$ and mesh $M = 30$ cells. The choice of $\varepsilon = 10^{-3}$ for the relaxation parameter ε ensures that the numerical error dominates over the formulation error. Computed results (empty symbols) are compared to the exact solution (full line). Also shown are results obtained from the scheme of [37] (filled symbols). Table 2.7 shows time steps and the CPU times for both schemes for orders of accuracy 3rd, 5th and 7th. We observe that the present approach is significantly more efficient, particularly for the higher-order range. For example, for 7th order of accuracy the present scheme is more than two orders of magnitude more efficient than its counterpart.
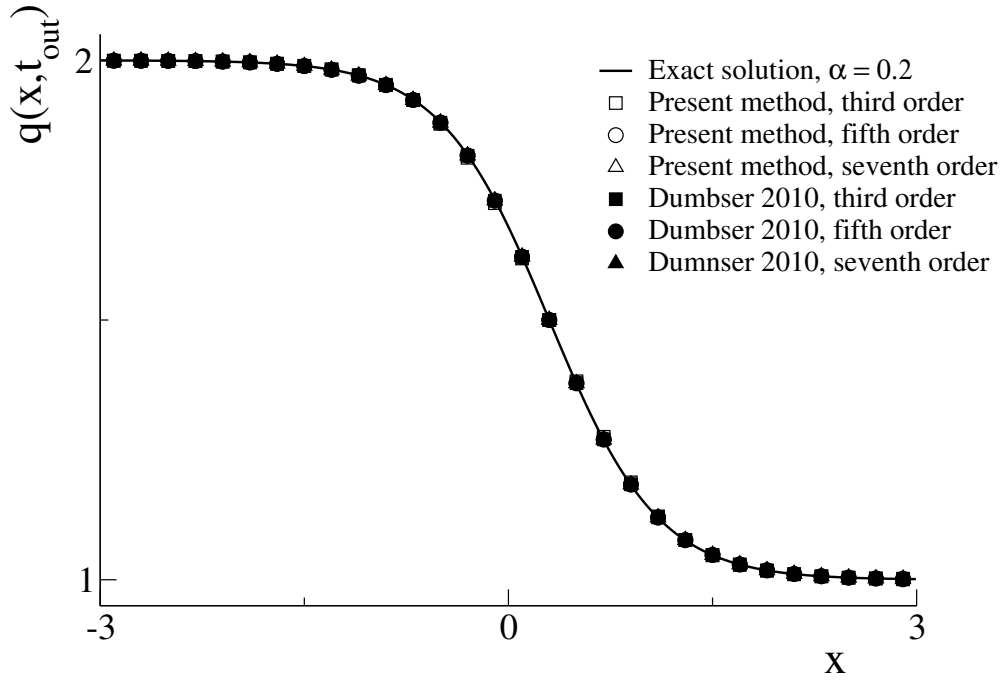
FIGURE 2.7: Viscous shock. Computed (blank symbols) and exact (line) solutions to Burgers' equation with $\varepsilon = 10^{-3}$, at $t_{out} = 0.2$, using ADER schemes and ADER-DG (fill symbols) reported in [37]. Mesh used: 30 cells.

2.6 Application to an atherosclerosis model

Here we illustrate the applicability of the ADER high-order numerical methodology presented in this chapter by solving a system of time-dependent diffusion-reaction equations associated with a model for atherosclerosis. For background on the physiopathological aspects of atherosclerosis, see [91]. For details on the mathematical model see [48] and [68].

2.6.1 The mathematical model

The mathematical model of interest here consists of a system of diffusion-reaction equations, put forward by El Khatib et al. [48]. The equations are

$$\left. \begin{array}{l} \partial_t M = \alpha_1 \partial_x^2 M + f_1(A) - \gamma_1 M \ , \\[2mm] \partial_t A = \alpha_2 \partial_x^2 A + f_2(A)M - \gamma_2 A \ , \end{array} \right\} \tag{2.114}$$

in the spatial domain $0 < x < L$, for time $t > 0$. Boundary conditions are

$$\partial_x M(0,t) = 0 \ , \quad \partial_x M(L,t) = 0 \ , \quad \partial_x A(0,t) = 0 \ , \quad \partial_x A(L,t) = 0 \tag{2.115}$$

and initial conditions are

$$M(x,0) = M_0(x) , \quad A(x,0) = A_0(x) . \tag{2.116}$$

Here $M(x,t)$ is density of immune cells (monocytes, macrophages); $A(x,t)$ is density of cytokines secreted by immune cells. The function $f_1(A)$ accounts for the recruitment of immune cells from the blood stream and function $f_2(A)$ is the cytokine production rate. The functions $f_1(A)$ and $f_2(A)$ are given as

$$f_1(A) = \frac{\delta_1 + \beta A}{1 + A/\tau_1} , \quad f_2(A) = \frac{\delta_2 A}{1 + A/\tau_2} . \tag{2.117}$$

All parameters of the model δ_1, δ_2, α_1, α_2, τ_1, τ_2, γ_1, γ_2, β are positive. For further details on the physiological meaning of the model and its parameters see [48] and [68].

2.6.2 Hyperbolisation of the equations

First, we re-write equations (2.114) as

$$\left. \begin{aligned} \partial_t M_1 &= \alpha_1 \partial_x^2 M_1 + f_1(A_1) - \gamma_1 M_1 , \\[2mm] \partial_t A_1 &= \alpha_2 \partial_x^2 A_1 + f_2(A_1) M_1 - \gamma_2 A_1 , \end{aligned} \right\} \tag{2.118}$$

with $M \equiv M_1$, $A \equiv A_1$ and source terms

$$S_{11} = f_1(A_1) - \gamma_1 M_1 , \quad S_{21} = f_2(A_1) M_1 - \gamma_2 A_1 . \tag{2.119}$$

Introducing two new functions $A_2(x,t)$ and $M_2(x,t)$ such that

$$A_2(x,t) \to \partial_x A_1(x,t) , \quad M_2(x,t) \to \partial_x M_1(x,t) , \quad \text{as} \quad \varepsilon \to 0 \tag{2.120}$$

we express system (2.118) as

$$\partial_t \mathbf{Q} + \mathbf{A} \partial_x \mathbf{Q} = \mathbf{S}(\mathbf{Q}) , \tag{2.121}$$

where

$$\mathbf{Q} = \begin{bmatrix} M_1 \\ M_2 \\ A_1 \\ A_2 \end{bmatrix} , \quad \mathbf{A} = \begin{bmatrix} 0 & -\alpha_1 & 0 & 0 \\ -1/\varepsilon & 0 & 0 & 0 \\ 0 & 0 & 0 & -\alpha_2 \\ 0 & 0 & -1/\varepsilon & 0 \end{bmatrix} \tag{2.122}$$

and

$$\mathbf{S} = \begin{bmatrix} s_{11} \\ s_{12} \\ s_{21} \\ s_{22} \end{bmatrix} = \begin{bmatrix} f_1(A_1) - \delta 1 M_1 \\ -M_2/\varepsilon \\ f_2(A_1)M_1 - \delta 2 A_1 \\ -A_2/\varepsilon \end{bmatrix}. \tag{2.123}$$

The eigenvalues of $\mathbf{A}$ are

$$\lambda_1 = -\sqrt{\frac{\alpha_1}{\varepsilon}}, \quad \lambda_2 = -\sqrt{\frac{\alpha_2}{\varepsilon}}, \quad \lambda_3 = \sqrt{\frac{\alpha_2}{\varepsilon}}, \quad \lambda_4 = \sqrt{\frac{\alpha_1}{\varepsilon}}. \tag{2.124}$$

They are all real and distinct. The corresponding right eigenvectors are

$$\mathbf{R_1} = \begin{bmatrix} 1 \\ -\frac{\lambda_1}{\alpha_1} \\ 0 \\ 0 \end{bmatrix}, \quad \mathbf{R_2} = \begin{bmatrix} 0 \\ 0 \\ 1 \\ -\frac{\lambda_2}{\alpha_2} \end{bmatrix}, \quad \mathbf{R_3} = \begin{bmatrix} 0 \\ 0 \\ 1 \\ -\frac{\lambda_3}{\alpha_2} \end{bmatrix}, \quad \mathbf{R_4} = \begin{bmatrix} 1 \\ -\frac{\lambda_4}{\alpha_1} \\ 0 \\ 0 \end{bmatrix}.$$

They are linearly independent. Hence the relaxation system (2.122) is hyperbolic and the associated wave pattern is always subsonic, that is $\lambda_{min} < 0 < \lambda_{max}$, with $\lambda_{min} = \min\{\lambda_i\}$, $\lambda_{max} = \max\{\lambda_i\}$.

2.6.3   Numerical Results

We solve system (2.121) numerically for one of the three test problems proposed in [68]. The initial conditions are

$$\begin{aligned} M_1(x) &= 2 + \bar{\epsilon}e^{-(3(x-5))^2}, \\ M_2(x) &= -6(x-5)\bar{\epsilon}e^{-(3(x-5))^2}, \\ A_1(x) &= \bar{\epsilon}e^{-(3(x-5))^2}, \\ A_2(x) &= -6(x-5)\bar{\epsilon}e^{-(3(x-5))^2}. \end{aligned} \right\} \tag{2.125}$$

Here $\bar{\epsilon} = 0.2$ is a perturbation parameter. We consider a test problem, which is defined by the parameters given in Table 2.9. Figure 2.8, shows the space-time distribution of the computed solution up to time $t_{out} = 20$. In the computations we use $C_{cfl} = 0.9$ and a mesh of 200 cells. This test shows the evolution of the initial perturbation of a healthy state to a steady-state solution that corresponds to an inflammatory state.

We compare our numerical solutions at the fixed time $t_{out} = 0.5s$, for the optimal $\varepsilon_3 = 2.9 \times 10^{-2}$, with those reported in [68] and with those obtained with the scheme of [37]. Results are displayed in Figure 2.9 for $M(x, t_{out})$. Excellent agreement is observed. Table 2.8 contains detailed information concerning the computations performed. CPU

Scheme	CPU time ($t_{out} = 0.5s$)	CPU time ($t_{out} = 20s$)	Δt
Scheme of Ref. [68]	$1.20e - 01$	$4.37e + 00$	$1.20e{-}02$
Present method, $\varepsilon = 2.9 \times 10^{-2}$	$1.10e - 01$	$5.62e + 00$	$2.42e{-}02$
Present method, $\varepsilon = 1.0 \times 10^{-2}$	$1.70e - 01$	$9.22e + 00$	$1.42e{-}02$
Present method, $\varepsilon = 1.0 \times 10^{-3}$	$5.00e - 01$	$2.79e + 01$	$4.50e{-}03$
Scheme of Ref. [37], $N = M = 3$	$5.71e + 00$	$2.27e + 02$	$3.00e{-}04$

TABLE 2.8: CPU times and time steps for schemes of third order of accuracy, as applied to system (2.114).

α_1	α_2	β	δ_1	δ_2	γ_1	γ_2	τ_1	τ_2
0.01	0.1	8	2	1	1	1	1	42/43

TABLE 2.9: Parameters for the atherosclerosis model.
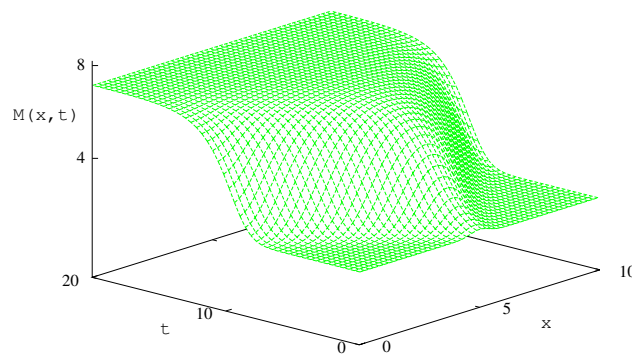
FIGURE 2.8: Evolution in space and time of density of immune cells $M(x, t)$. Simulation carried out up to $t_{out} = 20s$, with 200 cells, $\varepsilon = 2.9 \times 10^{-2}$ and $C_{cfl} = 0.9$.

times and time steps Δt are shown for all three schemes and at two output times, $t_{out} = 0.5s$ and $t_{out} = 20s$.

In the next section we address the question of the applicability of the relaxation approach to higher-order partial differential equations.

2.7 Limitations of Cattaneo's relaxation approach

In this section we show that the Cattaneo relaxation approach adopted in this thesis cannot be directly applied to third-order partial differential equations. In particular, the methodology as applied to generalized Korteweg-deVries equations, leads to systems with complex eigenvalues, and hence not hyperbolic.
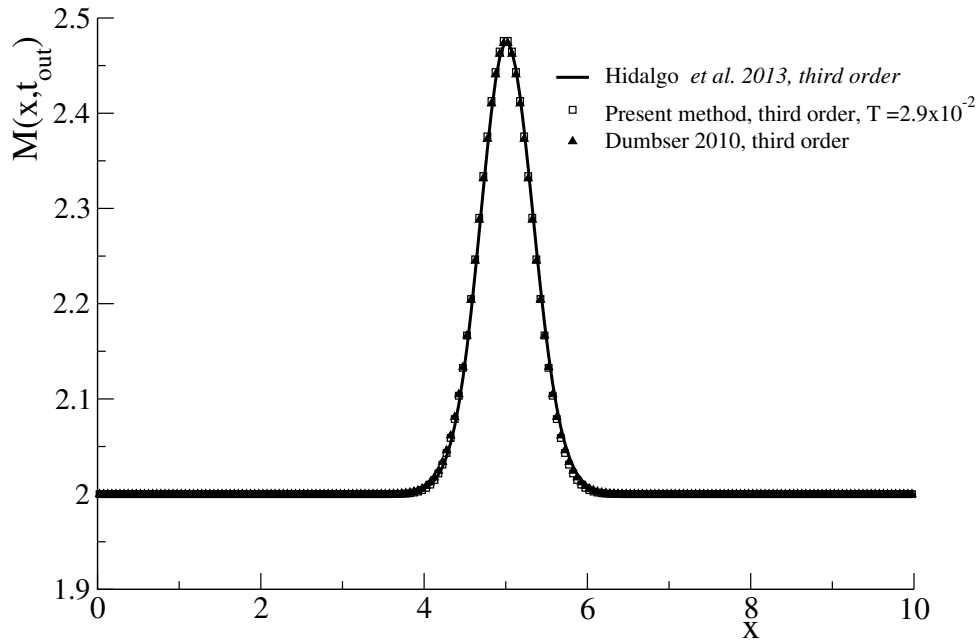
FIGURE 2.9: Results for function $M(x,t)$. Comparisons amongst 3rd order numerical solutions. Present scheme with $\varepsilon = 2.9 \times 10^{-2}$ (empty square), the numerical solution from [37] (filled triangle) and the reference solution from [68] (full line) at time $t_{out} = 0.5s$. Computational parameters are: 200 cells and $C_{cfl} = 0.9$.

2.7.1 The governing equation

Let us consider partial differential equations written in the general form

$$\partial_t q = \partial_x G(q, \partial_x q, \partial_x^{(2)} q) + s(q, \partial_x q, \partial_x^{(2)} q) , \qquad (2.126)$$

where $G(q, \partial_x q, \partial_x^{(2)} q)$ and $s(q, \partial_x q, \partial_x^{(2)} q)$ are two functionals. For convenience we define

$$\left. \begin{aligned} \partial_q G(q, \partial_x q, \partial_x^{(2)} q) &= -\alpha_1(q, \partial_x q, \partial_x^{(2)} q) , \\[2mm] \partial_{(\partial_x q)} G(q, \partial_x q, \partial_x^{(2)} q) &= \alpha_2(q, \partial_x q, \partial_x^{(2)} q) , \\[2mm] \partial_{(\partial_x^{(2)} q)} G(q, \partial_x q, \partial_x^{(2)} q) &= \alpha_3(q, \partial_x q, \partial_x^{(2)} q) . \end{aligned} \right\} \qquad (2.127)$$

We impose $\alpha_3 \neq 0$ to ensure a third order partial differential equation. By virtue of the chain rule and definitions (2.127) we can express (2.126) as

$$\partial_t q + \alpha_1 \partial_x q = \alpha_2 \partial_x^{(2)} q_1 + \alpha_3 \partial_x^{(3)} q + s(q, \partial_x q, \partial_x^{(2)} q) . \qquad (2.128)$$

Following the direct application of the original idea of Cattaneo's, we sequentially replace high-order spatial derivatives by functions $q_2(x,t)$ and $q_3(x,t)$, such that $q_2 \to \partial_x q_1$ and

$q_3 \to \partial_x q_2 \equiv \partial_x^{(2)} q_1$, and which, more formally, satisfy the following partial differential equations

$$\partial_t q_2 = \frac{1}{\varepsilon} \left(\partial_x q_1 - q_2 \right) \ , \quad \partial_t q_3 = \frac{1}{\varepsilon} \left(\partial_x q_2 - q_3 \right) \ . \tag{2.129}$$

Note that when $\varepsilon \to 0$ above, $q_1 \to q$, $q_2 \to \partial_x q_1$ and $q_3 \to \partial_x q_2 \equiv \partial_x^{(2)} q_1$. The resulting relaxation system written in quasilinear form is

$$\partial_t \mathbf{Q} + \mathbf{A} \partial_x \mathbf{Q} = \mathbf{S}(\mathbf{Q}) \ , \tag{2.130}$$

with

$$\mathbf{Q} = \begin{bmatrix} q_1 \\ q_2 \\ q_3 \end{bmatrix} , \quad \mathbf{A} = \begin{bmatrix} \alpha_1 & -\alpha_2 & -\alpha_3 \\ -\dfrac{1}{\varepsilon} & 0 & 0 \\ 0 & -\dfrac{1}{\varepsilon} & 0 \end{bmatrix} , \quad \mathbf{S} = \begin{bmatrix} s(q_1, q_2, q_3) \\ -\dfrac{q_2}{\varepsilon} \\ -\dfrac{q_3}{\varepsilon} \end{bmatrix} . \tag{2.131}$$

Note that (2.129) provides two functions whose limiting behaviour is that of the spatial gradients. The original governing equation (2.128) can be represented in several forms. Equations (2.130)-(2.131) represent all possible forms. Now the task is to determine the nature of the system. To this end we study its eigenvalues, which are the roots of the characteristic polynomial

$$p(\lambda) = \lambda^3 - \alpha_1 \lambda^2 - \frac{\alpha_2}{\varepsilon} \lambda + \frac{\alpha_3}{\varepsilon^2} = 0 \ . \tag{2.132}$$

From Cardano's formula, we know that all roots of a third order polynomial

$$\lambda^3 + a\lambda^2 + b\lambda + c = 0 \tag{2.133}$$

are real if and only if the discriminant Δ satisfies

$$\Delta := \left(\frac{2a^3}{27} - \frac{ab}{3} + c \right)^2 + \frac{4}{27} \left(b - \frac{a^2}{3} \right)^3 \leq 0 \ . \tag{2.134}$$

Therefore, identifying terms between (2.132) and (2.133), we note that two roots of $p(\lambda) = 0$ will be complex if only if the discriminant Δ satisfies

$$27\Delta = -\frac{\alpha_1 \, \alpha_3 \left(\frac{18 \, \alpha_2}{\varepsilon} + 4 \, \alpha_1{}^2 \right)}{\varepsilon^2} + \frac{\alpha_2{}^2 \left(-\frac{4 \, \alpha_2}{\varepsilon} - \alpha_1{}^2 \right)}{\varepsilon^2} + \frac{27 \, \alpha_3{}^2}{\varepsilon^4} > 0 \ . \tag{2.135}$$

The dominant term in (2.135), for small values of ε, is $27\alpha_3^2$. Then $\Delta > 0$ for sufficiently small ε. This claim is proved below.

Proposition 2.8. *The first-order system (2.130) has complex eigenvalues under the following condition on the relaxation parameter ε*

$$\frac{\sqrt{3}|\alpha_3|}{M\sqrt{15M + 22}} > \varepsilon , \quad M = \frac{\alpha_1^2 + \alpha_2 + \alpha_3^2}{3} . \tag{2.136}$$

Consequently, system (2.130) is not hyperbolic.

Proof. First note that (2.135) can be written as

$$27\Delta = \frac{F(\varepsilon)}{\varepsilon^4} , \tag{2.137}$$

with

$$F(\varepsilon) = 27\alpha_3^2 - \varepsilon r_1 - \varepsilon^2 r_2 \tag{2.138}$$

and

$$r_1 = 18\alpha_1\alpha_2\alpha_3 + 4\alpha_2^3 , \quad r_2 = 4\alpha_1^3\alpha_3 + \alpha_1^2\alpha_2^2 . \tag{2.139}$$

Since

$$|\alpha_1| \le \sqrt{3M} , \quad \alpha_2 \le 3M , \quad |\alpha_3| \le \sqrt{3M} \tag{2.140}$$

and $\varepsilon < 1$, after some manipulations, the claimed result follows. $\square$

2.7.2 Special cases

Here we illustrate the above result for more specific equations, in particular equations of Korteweg-deVries type and Korteweg-deVries-Burgers type. A more detailed study of the nature of eigenvalues of $\mathbf{A}$ can be carried out by noting that cubic polynomials contain two local critical points (maximum and minimum), which are solutions of $p'(\lambda) = 0$, denoted here as λ_- and λ_+. If $\lambda_- \ne \lambda_+$ then the roots of $p(\lambda) = 0$ are all real if and only if $p(\lambda_-)$ and $p(\lambda_+)$ have the same sign. The critical points in this case are

$$\lambda_\pm = \frac{\alpha_1 \pm \sqrt{\alpha_1^2 + 3\dfrac{\alpha_2}{\varepsilon}}}{3} . \tag{2.141}$$

For the particular case in which $s = 0$ and G has the form

$$G(q, \partial_x^{(2)} q) = G_1(q) + G_2(q, \partial_x^{(2)} q) \,, \tag{2.142}$$

then

$$\alpha_2 = 0 \,. \tag{2.143}$$

If in addition we assume $\alpha_3 < 0$ we obtain the generalized Korteweg-deVries equations [31] and for $\alpha_1(q_1) = q_1$ we have the Korteweg-deVries-Burgers equations [99]. Therefore, the characteristic polynomial becomes

$$\frac{p(\lambda_-)}{p(\lambda_+)} = -\frac{4\,\alpha_1{}^3\,\varepsilon^2 - 27\,\alpha_3}{27\,\alpha_3} \,. \tag{2.144}$$

If $\alpha_1 > 0$ the polynomial has two complex roots; this is because $p(\lambda_-)$ and $p(\lambda_+)$ have the same sign and $\lambda_- \neq \lambda_+$. On the other hand, if $\alpha_1 < 0$, then for

$$\frac{3\sqrt{3|\alpha_3|}}{2|\alpha_1|^{\frac{3}{2}}} > \varepsilon \,, \tag{2.145}$$

we again have that $p(\lambda_-)$ and $p(\lambda_+)$ have the same sign; therefore the polynomial has complex roots and hence the formulation cannot be hyperbolic.

Note that the Korteweg-deVries-Burgers equation can be written as

$$G(q, \partial_x q, \partial_x^{(x)} q) = G(\partial_x^{(2)} q) \,, \quad s(q, \partial_x q, \partial_x^{(x)} q) = -q \partial_x q \,. \tag{2.146}$$

We reformulate the system as

$$\left.\begin{array}{c} \partial_t q_1 - \alpha_3(q_1)\partial_x q_3 = -q_1 q_2 \,, \\[2mm] \partial_t q_2 - \dfrac{1}{\varepsilon}\partial_x q_1 = -\dfrac{1}{\varepsilon}q_2 \,, \\[2mm] \partial_t q_3 - \dfrac{1}{\varepsilon}\partial_x q_2 = -\dfrac{1}{\varepsilon}q_3 \,. \end{array}\right\} \tag{2.147}$$

In conservative form this can be written as (2.130), with

$$
\mathbf{Q} = \begin{bmatrix} q_1 \\ q_2 \\ q_3 \end{bmatrix} , \quad
\mathbf{A} = \begin{bmatrix} 0 & 0 & -\alpha_3 \\ -\dfrac{1}{\varepsilon} & 0 & 0 \\ 0 & -\dfrac{1}{\varepsilon} & 0 \end{bmatrix} , \quad
\mathbf{S} = \begin{bmatrix} -q_1 q_2 \\ -\dfrac{q_2}{\varepsilon} \\ -\dfrac{q_3}{\varepsilon} \end{bmatrix} .
\tag{2.148}
$$

The eigenvalues are

$$
\lambda_1 = -\frac{\left(\sqrt{3}\,i - 1\right) \alpha_3^{\frac{1}{3}}}{2\,\varepsilon^{\frac{2}{3}}} , \quad
\lambda_2 = \frac{\left(\sqrt{3}\,i + 1\right) \alpha_3^{\frac{1}{3}}}{2\,\varepsilon^{\frac{2}{3}}} , \quad
\lambda_3 = -\frac{\alpha_3^{\frac{1}{3}}}{\varepsilon^{\frac{2}{3}}} ,
\tag{2.149}
$$

with $i^2 = -1$. Therefore, this reformulation does not yield a hyperbolic system.

2.8 Conclusions

In this chapter we have first extended the applicability of the Cattaneo relaxation approach to reformulate time-dependent advection-diffusion-reaction equations, that may include stiff reactive terms, as hyperbolic balance laws with stiff source terms. The procedure has been shown to be successful for second order PDEs but not so for third-order PDEs, such as the Korteweg-deVries-Burgers type. Additionally, we have extended the applicability of existent high-order numerical schemes to approximate numerically advection-diffusion-reaction partial differential equations. Next, we defined a criterion for selecting the relaxation time which depends only on the order of accuracy of the numerical scheme used to solve the hyperbolic system and the mesh spacing. We have studied linear and non-linear problems and have applied the methodologies to a diffusion-reaction system modelling atherosclerosis. The proposed hyperbolisation procedures turn out to give a generous stability range for the choice of the time step. This results in considerably more efficient schemes than some methods subject to the parabolic restriction reported in the current literature. Implementations of our numerical schemes and convergence-rates assessment are carried out for methods of up to 7-th order of accuracy in both space and time.

Chapter 3

Reformulations for general advection-diffusion-reaction equations and locally implicit ADER schemes

3.1 Introduction

Advection-Diffusion-Reaction Partial Differential Equations (adrPDEs) govern many physical phenomena, the heat equation being one of the simplest examples. Cattaneo, in his pioneering work [24, 25], attempted to resolve the paradox of infinite speed of wave propagation in the heat equation. He did so by extending Fourier's law by including a transient term dominated by a relaxation time. As a consequence, a first order system with stiff source terms arises. See also the work of Vernotte [160] and the more recent work of Nagy et al. [107] for a review of the subject. In this chapter we pursue the relaxation approach of Cattaneo but first note that this is different to the relaxation framework introduced by Jin and Xin [77] to transform non-linear hyperbolic systems into enlarged linear hyperbolic systems with stiff source terms. The present approach is also different to that introduced later by Jin et al. [73] to solve diffusive problems. See also the related work of Liu [94].

The relaxation approach in the sense of Cattaneo has already been employed to approximate numerically adrPDEs problems via hyperbolic reformulations. See, for example, Gómez and collaborators [58, 59], who solved time-dependent, linear advection-diffusion equations in two space dimensions, in the frame of finite element methods. Nishikawa

[111] solved the steady heat equation, reformulated as a hyperbolic system, using residual distribution methods [126, 127]. Later, Nishikawa [112] extended his methods to solve steady, linear advection-diffusion equations in two space dimensions.

In the present chapter, following Cattaneo's philosophy, we propose two classes of relaxation, whereby time-dependent, non-linear systems of advection-diffusion-reaction equations are reformulated as time-dependent, non-linear hyperbolic balance laws with stiff source terms. The first type of relaxation, named *Canonical Relaxation Formulation*, applies Cattaneo's law to all variables, ending up with an enlarged system of double the number of variables of the original adrPDE system. The second method, called *Ad Hoc Relaxation Formulation*, depends on particular features of the problem at hand. In both formulations, spatial gradients of the original variables are relaxed. In both cases the original adrPDE system is recovered, as the relaxation parameter tends to zero.

There are two main issues to be considered. The first concerns the formulation at the analytical level, that is the mathematical analysis of the resulting first-order inhomogeneous systems. Here we prove, in fairly general terms, necessary conditions for the resulting systems to have real eigenvalues. The second crucial issue is that of devising suitable numerical methods to solve the reformulated systems. In this chapter, we adopt the ADER high order approach, first put forward by Toro et al. [150]. The ADER finite volume scheme for solving simple adrPDEs has already been investigated, see for example the work of Titarev and Toro [145], Toro and Hidalgo [149] and Hidalgo et al. [68]. The compressible Navier-Stokes equations were solved by Dumbser and collaborators [37, 67]. In all of these cases, solutions were computed to high-order of accuracy in space and time. However, the schemes reported were subject to the stability restriction $O(\Delta x^2)$.

The ADER approach was first put forward by Toro et al. [150] for linear hyperbolic problems, see also [132]. This methodology has been extended to non-linear hyperbolic systems on Cartesian and unstructured meshes, see for example [21, 79–81, 141, 144, 146, 154, 155]. ADER has also been extended in the framework of discontinuous Galerkin finite element methods by Dumbser and collaborators, see for example [35, 36, 43–45]. ADER methods are one-step, fully discrete schemes, containing two main ingredients, namely (i) a high-order, non-linear spatial reconstruction procedure and (ii) solution of a generalised Riemann problem at each cell interface to compute the numerical flux to high accuracy. In the presence of source terms, local Cauchy problems inside the volumes are used to compute the numerical source. Note that the spatial reconstruction could also be linear (fixed stencil), but the non-linearity is required to circumvent Godunov's theorem [55, 147]. There are two types of generalised Riemann solvers: In the first type, the solution at any time $\hat{\tau}$ is obtained from the time evolution of the boundary

extrapolated values of the reconstructed data, interacted at time $\hat{\tau}$, by the solution of a classical Riemann problem at the cell interface [41, 66]. In the second type, the solution is obtained at the cell interface from a time Taylor series expansion, whose coefficients are determined from the solution of a classical non-linear Riemann problem, the use of the Cauchy-Kowaleski procedure and the solution of a sequence of classical linear Riemann problems for spatial derivatives [154]. See reviews [22, 100] and chapters 19 and 20 of [147].

In this chapter we present a new, locally implicit solver for generalised Riemann problem, which is able to handle stiff source terms. The solver is an extension of that first put forward by Montecinos and Toro for the scalar, linear case [101] and is inspired by the work of Scott [133] who used the idea of implicit Taylor expansions to develop methods to solve stiff ordinary differential equations. This new method can deal with hyperbolic balance laws with stiff source terms, reconciling stiffness and high accuracy, unlike the original solver of Toro and Titarev [154] that is unable to deal with stiff source terms. The method is an alternative to that of Dumbser et al. [41]. In this chapter we apply the proposed relaxation formulations and the new ADER-type numerical method to solve the compressible Navier-Stokes equations. We systematically assess the computed results and compare numerical solutions against accurate reference solutions for a range of viscosity values. The results are very satisfactory. In addition we carry out a convergence rates study to verify that that the theoretically expected accuracy is actually obtained in practice.

The rest of this chapter is structured as follows. In Section 3.2 we state the form of general advection-diffusion-reaction equations and introduce the relaxation approaches. We also present theoretical results that ensure that all eigenvalues of the relaxation systems are real. In Section 3 we apply the formulations to the compressible Navier-Stokes equations and obtain a theoretical result for the Ad Hoc Relaxation Formulation to ensure real eigenvalues. In section 3.4 we reviewed the ADER methodology, with the focus on the Toro-Titarev solver and that of Harten et al. [66]. In addition, the reconstruction procedure, Cauchy-Kowalewski procedure and the solution strategy for the GRP via classical Riemann problems are illustrated. In section 3.5 we present the newly proposed method. The methodology is assessed with scalar problems with stiff source terms. In section 3.6 we present numerical results for the one-dimensional compressible Navier-Stokes equations and convergence rates are empirically assessed. In Section 3.7 conclusions and remarks are drawn.

3.2 Advection-Diffusion-Reaction Equations

We consider systems of m non-linear advection-diffusion-reaction equations

$$\partial_t \mathbf{Q} + \partial_x \mathbf{F}(\mathbf{Q}) = \partial_x \mathbf{G}(\mathbf{Q}, \partial_x \mathbf{Q}) + \mathbf{S}(\mathbf{Q}) \ . \tag{3.1}$$

Here $\mathbf{Q} \in \mathbf{R}^m$ is the vector of unknowns; $\mathbf{F}(\mathbf{Q})$ is the inviscid flux; $\mathbf{G}(\mathbf{Q}, \partial_x \mathbf{Q})$ represents the viscous flux and $\mathbf{S}(\mathbf{Q})$ is the reaction term, a function of the unknown. For later use we introduce the following matrices

$$\mathbf{A}(\mathbf{Q}) = \frac{\partial \mathbf{F}(\mathbf{Q})}{\partial \mathbf{Q}} \ , \quad \mathbf{B}(\mathbf{Q}, \partial_x \mathbf{Q}) = \frac{\partial \mathbf{G}(\mathbf{Q}, \partial_x \mathbf{Q})}{\partial \mathbf{Q}} \ , \quad \mathbf{D}(\mathbf{Q}, \partial_x \mathbf{Q}) = \frac{\partial \mathbf{G}(\mathbf{Q}, \partial_x \mathbf{Q})}{\partial (\partial_x \mathbf{Q})} \ , \tag{3.2}$$

and for convenience, we shall often drop their arguments. In this section, inspired by the works of Cattaneo [24, 25] we introduce reformulations of adrPDEs (3.1), written as first order systems. See also the work of Nishikawa [111].

3.2.1 Reformulations for advection-diffusion-reaction equations

The key step of the approach is to replace the spatial gradient $\partial_x \mathbf{Q}$ in the viscous flux by a new vector of unknowns. Formally, we introduce the vector $\mathbf{U} \in \mathbf{R}^m$ and a small parameter $\varepsilon > 0$, such that

$$\mathbf{U} \to \partial_x \mathbf{Q} \ , \quad as \quad \varepsilon \to 0 \ . \tag{3.3}$$

In addition, we introduce the following system of evolution equations

$$\partial_t \mathbf{U} = \frac{\partial_x \mathbf{Q} - \mathbf{U}}{\varepsilon} \ . \tag{3.4}$$

Now the original adrPDE system (3.1) of m equations is replaced by an enlarged first order system of $2m$ equations

$$\left. \begin{aligned} \partial_t \mathbf{Q} + \partial_x \mathbf{F}(\mathbf{Q}) &= \partial_x \mathbf{G}(\mathbf{Q}, \mathbf{U}) + \mathbf{S}(\mathbf{Q}) \\[2mm] \partial_t \mathbf{U} - \partial_x \left(\frac{\mathbf{Q}}{\varepsilon} \right) &= -\frac{\mathbf{U}}{\varepsilon} \ . \end{aligned} \right\} \tag{3.5}$$

Equations (3.5) are called a relaxation system, with relaxation parameter ε. This general formulation will be referred to as *Canonical Relaxation Formulation*, whose number of unknown is double that of the original system.

It is also possible to consider reduced, ad hoc, formulations which exploit the particular features of the original adrPDE system of interest, so that the number of unknowns of the extra equations n is less than that of the original system m. We introduce a vector of new unknowns

$$\tilde{\mathbf{Q}} = [\tilde{q}_1, \tilde{q}_2, ..., \tilde{q}_n]^T \ . \tag{3.6}$$

with $\tilde{q}_k \in \{q_1, q_2, ..., q_m\}$, $\tilde{\mathbf{Q}} \in \mathbb{R}^n$ and $n < m$. The non-linear adrPDE system (3.1) has now viscous flux given as

$$\mathbf{G}(\mathbf{Q}, \partial_x \mathbf{\Phi}(\tilde{\mathbf{Q}})) \ , \tag{3.7}$$

with $\mathbf{\Phi} : \mathbb{R}^n \to \mathbb{R}^r$ differentiable and $r \geq 1$. In an analogous manner as for the canonical relaxation formulation we introduce a function $\mathbf{\Psi}$, of the same dimensions as $\mathbf{\Phi}$, and a small parameter $\varepsilon > 0$ such that

$$\mathbf{\Psi} \to \partial_x \mathbf{\Phi}(\tilde{\mathbf{Q}}) \ , \quad as \quad \varepsilon \to 0 \ . \tag{3.8}$$

We also introduce the evolutions

$$\partial_t \mathbf{\Psi} = \frac{\partial_x \mathbf{\Phi}(\tilde{\mathbf{Q}}) - \mathbf{\Psi}}{\varepsilon} \tag{3.9}$$

so that the enlarged new system becomes

$$\left.\begin{aligned} \partial_t \mathbf{Q} + \partial_x \mathbf{F}(\mathbf{Q}) &= \partial_x \mathbf{G}(\mathbf{Q}, \mathbf{\Psi}) + \mathbf{S}(\mathbf{Q}) \\[2mm] \partial_t \mathbf{\Psi} - \partial_x \left(\frac{\mathbf{\Phi}(\tilde{\mathbf{Q}})}{\varepsilon} \right) &= -\frac{\mathbf{\Psi}}{\varepsilon} \ . \end{aligned}\right\} \tag{3.10}$$

Equations (3.10) will be called the *Ad Hoc Relaxation Formulation*. Next we study conditions for the hyperbolicity of both formulations.

3.2.2   Hyperbolicity of the relaxation formulations

Ensuring hyperbolicity of the formulations is a challenging task. For the general *Canonical Relaxation Formulation* we identify conditions under which the system has real eigenvalues. Unfortunately this falls short of proving hyperbolicity, for which in addition one needs to show the existence of a complete set of linearly independent eigenvectors. For

the *Ad Hoc Relaxation Formulation* the nature of the eigenstructure depends on the particular system of interest and the analysis must be carried out case by case.

Both formulations can be written as

$$\partial_t \mathbf{W} + \partial_x \mathbf{H}(\mathbf{W}) = \mathbf{L}(\mathbf{W}) \ . \tag{3.11}$$

For the *Canonical Relaxation Formulation*

$$\mathbf{W} = \begin{bmatrix} \mathbf{Q} \\ \mathbf{U} \end{bmatrix} \ , \quad \mathbf{L}(\mathbf{W}) = \begin{bmatrix} \mathbf{0} \\ -\frac{1}{\varepsilon}\mathbf{U} \end{bmatrix} \ , \quad \mathbf{H}(\mathbf{W}) = \begin{bmatrix} \mathbf{F}(\mathbf{Q}) - \mathbf{G}(\mathbf{Q},\mathbf{U}) \\ -\frac{1}{\varepsilon}\mathbf{Q} \end{bmatrix} \ , \tag{3.12}$$

with $\mathbf{W} \in \mathbb{R}^{2m}$. For the *Ad Hoc Relaxation Formulation* we have

$$\mathbf{W} = \begin{bmatrix} \mathbf{Q} \\ \boldsymbol{\Psi} \end{bmatrix} \ , \quad \mathbf{L}(\mathbf{W}) = \begin{bmatrix} \mathbf{0} \\ -\frac{1}{\varepsilon}\boldsymbol{\Psi} \end{bmatrix} \ , \quad \mathbf{H}(\mathbf{W}) = \begin{bmatrix} \mathbf{F}(\mathbf{Q}) - \mathbf{G}(\mathbf{Q},\boldsymbol{\Psi}) \\ -\frac{1}{\varepsilon}\boldsymbol{\Phi}(\tilde{\mathbf{Q}}) \end{bmatrix} \ , \tag{3.13}$$

with $\mathbf{W} \in \mathbb{R}^{m+r}$.

For later use we introduce the Jacobian matrix

$$\mathbf{J}(\mathbf{W}) = \frac{\partial \mathbf{H}(\mathbf{W})}{\partial \mathbf{W}} \ . \tag{3.14}$$

Lemma 3.1. *Let $\mathbf{M}_1$ and $\mathbf{M}_2$ be two real square matrices, with $\mathbf{M}_2$ a semi-positive definite matrix. Then there exists a positive real number ε_0 such that $\mathbf{M}_1 + \frac{1}{\varepsilon}\mathbf{M}_2$ is semi-positive definite for all $\varepsilon < \varepsilon_0$.*

Proof. We prove this by contradiction. We suppose that there exists a vector $\mathbf{v} \in \mathbb{R}^m$, with $\mathbf{v} \neq \mathbf{0}$, such that

$$\mathbf{v}^T\mathbf{M}_1\mathbf{v} + \frac{1}{\varepsilon}\mathbf{v}^T\mathbf{M}_2\mathbf{v} < 0 \ , \quad \forall \varepsilon \neq 0 \ , \tag{3.15}$$

which requires $\mathbf{v}^T\mathbf{M}_1\mathbf{v} \neq 0$. Then, as $\mathbf{v}$ is fixed, if we take $\varepsilon = \bar{\varepsilon} := \frac{\mathbf{v}^T\mathbf{M}_2\mathbf{v}}{|\mathbf{v}^T\mathbf{M}_1\mathbf{v}|}$ in (3.15) we obtain $\left(\mathbf{v}^T\mathbf{M}_1\mathbf{v} + |\mathbf{v}^T\mathbf{M}_1\mathbf{v}|\right) < 0$. This is a contradiction. Then there exists a positive ε_0 given as $\varepsilon_0 = \bar{\varepsilon}$. As $\frac{1}{\varepsilon} \geq \frac{1}{\varepsilon_0}$ for all $0 < \varepsilon \leq \varepsilon_0$ the result holds. $\square$

Lemma 3.2. *Let $\mathbf{A}_1$ and $\mathbf{A}_2$ be square matrices, with $\mathbf{A}_2$ semi-positive definite. Then, there exists a positive real number ε_0, such that the quadratic matrix problem for $\boldsymbol{\Sigma}$*

$$\boldsymbol{\Sigma}^2 = \mathbf{A}_1^2 + \frac{1}{\varepsilon}\mathbf{A}_2 + [\mathbf{A}_1, \boldsymbol{\Sigma}] \ , \tag{3.16}$$

with $[\mathbf{A}_1, \mathbf{\Sigma}] = \mathbf{A}_1\mathbf{\Sigma} - \mathbf{\Sigma}\mathbf{A}_1$ *the commutator operator, is solvable for all* $\varepsilon < \varepsilon_0$.

Proof. This quadratic matrix problem in the sense of Shurbet et al. [140] corresponds to a nonlinear algebraic-Riccati-equation type [63, 88]. Then, from Guo and Laub [64] there exists a solution which is a positive definite matrix, if the Hamiltonian given by

$$H = \begin{bmatrix} -\mathbf{A}_1 & -\mathbf{I} \\ -\left(\mathbf{A}_1^2 + \frac{1}{\varepsilon}\mathbf{A}_2\right) & -\mathbf{A}_1 \end{bmatrix} , \tag{3.17}$$

can be decomposed as $\alpha\mathbf{I} - \mathbf{N}$, where $\mathbf{N}_{i,j} \geq 0$, $\alpha > \rho(\mathbf{N})$, with $\rho(\mathbf{N})$ the spectral radius of $\mathbf{N}$. From Lemma 3.1 we take

$$\mathbf{M}_1 = \mathbf{A}_1^2 , \quad \mathbf{M}_2 = \mathbf{A}_2 . \tag{3.18}$$

Then there exists ε_0 such that $\mathbf{A}_1^2 + \frac{1}{\varepsilon}\mathbf{A}_2$ is semi-positive definite for all $\varepsilon < \varepsilon_0$, then as for all $\alpha > -\mathbf{A}_{i,j}$ the matrix

$$\mathbf{N} = \begin{bmatrix} \alpha\mathbf{I} + \mathbf{A}_1 & \mathbf{I} \\ \left(\mathbf{A}_1^2 + \frac{1}{\varepsilon}\mathbf{A}_2\right) & \alpha\mathbf{I} + \mathbf{A}_1 \end{bmatrix} \tag{3.19}$$

satisfies the requirements [64] for all α and $\varepsilon < \varepsilon_0$. The result follows. $\square$

Proposition 3.3. *If* $\mathbf{D}$ *in (3.2) is similar to a semi-positive definite and all eigenvalues of* $\mathbf{A}-\mathbf{B}$ *from (3.2) are real. Then, there exists* $\varepsilon_0 > 0$ *such that for* $\varepsilon < \varepsilon_0$ *all eigenvalues of the Jacobian (3.14) of the Canonical Formulation (3.11)-(3.12) are real.*

Proof. The eigenvalues of $\mathbf{J}$ in (3.14) for (3.11)-(3.12) are the roots of the characteristic polynomial

$$0 = p(\lambda) = det\left(\lambda^2\mathbf{I} - \lambda(\mathbf{A} - \mathbf{B}) - \frac{1}{\varepsilon}\mathbf{D}\right) , \tag{3.20}$$

with $\mathbf{I}$ the identity matrix. Moreover, there exist matrices $\bar{\mathbf{M}}_1$ and $\bar{\mathbf{M}}_2$ such that

$$\bar{\mathbf{M}}_1 + \bar{\mathbf{M}}_2 = \mathbf{A} - \mathbf{B} , \quad \bar{\mathbf{M}}_1\bar{\mathbf{M}}_2 = \frac{-1}{\varepsilon}\mathbf{D} . \tag{3.21}$$

Therefore

$$\left(\lambda\mathbf{I} - \bar{\mathbf{M}}_1\right)\left(\lambda\mathbf{I} - \bar{\mathbf{M}}_2\right) = \left(\lambda^2\mathbf{I} - \lambda(\mathbf{A} - \mathbf{B}) + \frac{-1}{\varepsilon}\mathbf{D}\right) \tag{3.22}$$

and so the eigenvalues of $\mathbf{J}$ are the eigenvalues of $\bar{\mathbf{M}}_1$ or $\bar{\mathbf{M}}_2$. Note from (3.21) that $\bar{\mathbf{M}}_1$ satisfies

$$\bar{\mathbf{M}}_1^2 + \tfrac{-1}{\varepsilon}\mathbf{D} = \bar{\mathbf{M}}_1\left(\mathbf{A} - \mathbf{B}\right) . \tag{3.23}$$

We denote by δ_i eigenvalues of $\mathbf{D}$, by μ_i the eigenvalues of $\mathbf{A} - \mathbf{B}$ and by λ_i the eigenvalues of $\mathbf{J}$. Then from

$$\left(\bar{\mathbf{M}}_1^2 + \tfrac{-1}{\varepsilon}\mathbf{D}\right)\mathbf{v}_i = \bar{\mathbf{M}}_1\left(\mathbf{A} - \mathbf{B}\right)\mathbf{v}_i \tag{3.24}$$

we obtain

$$\left(\lambda_i^2 - \lambda_i\mu_i - \tfrac{1}{\varepsilon}\delta_i\right)\mathbf{v}_i = \mathbf{0} . \tag{3.25}$$

Therefore the sought eigenvalues have the form

$$\lambda_i^\pm = \tfrac{1}{2}\left(\mu_i \pm \sqrt{\mu_i^2 + \tfrac{4}{\varepsilon}\delta_i}\right) . \tag{3.26}$$

Note, that the same result is obtained if we consider $\bar{\mathbf{M}}_2$ with the relation

$$\tfrac{-1}{\varepsilon}\mathbf{D} + \bar{\mathbf{M}}_2^2 = \left(\mathbf{A} - \mathbf{B}\right)\bar{\mathbf{M}}_2 \tag{3.27}$$

obtained from (3.21). On the other hand, as $\mathbf{D}$ is similar to a semi-positive matrix we assume that there exist matrices $\mathbf{\Lambda}$ and $\mathbf{P}$ such that

$$\mathbf{\Lambda} = \mathbf{P}^{-1}\mathbf{D}\mathbf{P} .$$

Then, motivated by Lemma 3.2 with

$$\mathbf{A}_1 = \mathbf{P}^{-1}\left(\mathbf{A} - \mathbf{B}\right)\mathbf{P} , \quad \mathbf{A}_2 = 4\mathbf{\Lambda} , \tag{3.28}$$

there exists a ε_0 such that

$$\tilde{\mathbf{\Sigma}}^2 = \left(\tilde{\mathbf{A}} - \tilde{\mathbf{B}}\right)^2 + \tfrac{4}{\varepsilon}\mathbf{\Lambda} + \left[\tilde{\mathbf{A}} - \tilde{\mathbf{B}}, \tilde{\mathbf{\Sigma}}\right] \tag{3.29}$$

is solvable for all $\varepsilon < \varepsilon_0$. Note that for a given matrix $\mathbf{C}$ we have adopted the notation $\tilde{\mathbf{C}} := \mathbf{P}^{-1}\mathbf{C}\mathbf{P}$. Therefore, $\bar{\mathbf{M}}_1$ and $\bar{\mathbf{M}}_2$ are defined as

$$\bar{\mathbf{M}}_1 = \tfrac{1}{2}\left(\left(\mathbf{A} - \mathbf{B}\right) - \mathbf{P}\tilde{\mathbf{\Sigma}}\mathbf{P}^{-1}\right) ,$$

$$\bar{\mathbf{M}}_2 = \tfrac{1}{2}\left(\left(\mathbf{A} - \mathbf{B}\right) + \mathbf{P}\tilde{\mathbf{\Sigma}}\mathbf{P}^{-1}\right) . \tag{3.30}$$

Hence the claimed result holds.

$\square$

Remark 3.4. For very small values $\varepsilon > 0$ we observe that the eigenvalues $\lambda_i^\pm$ behave as

$$\lambda_i^{\pm,\infty} = \pm\sqrt{\frac{\delta_i}{\varepsilon}} \ . \tag{3.31}$$

This means that if $\mathbf{D}$ is a semi-positive definite matrix, then there exists a dominant eigenvalue $\sqrt{\frac{\delta}{\varepsilon}}$, where δ the largest of all eigenvalues of $\mathbf{D}$.

3.3 The One-Dimensional Compressible Navier-Stokes Equations

The one-dimensional compressible Navier-Stokes equations are given as

$$\left.\begin{aligned}
\partial_t \rho + \partial_x (\rho u) &= 0 \ , \\[2mm]
\partial_t (\rho u) + \partial_x (\rho u^2 + p) &= \tfrac{4}{3}\partial_x^{(2)}(\eta u) \ , \\[2mm]
\partial_t E + \partial_x ((E+p)u) &= \tfrac{4}{3}\partial_x (\eta u \partial_x u) - \partial_x (\kappa \partial_x T) \ .
\end{aligned}\right\} \tag{3.32}$$

Here ρ is density, u is velocity, E is total energy, p is pressure, T is temperature, η is viscosity coefficient, κ is the heat transfer coefficient. The total energy is given as

$$E = \rho \left(\tfrac{1}{2}u^2 + e(p,\rho)\right) \ , \tag{3.33}$$

where $e(p,\rho)$ is the specific internal energy. For ideal gases $e(p,\rho)$ is given by the equation of state

$$e(p,\rho) = \frac{p}{(\gamma-1)\rho} \ , \tag{3.34}$$

with γ the ratio of specific heats. Here we take $\gamma = 1.4$. When written as (3.1), system (3.32) has

$$\mathbf{Q} = \begin{bmatrix} \rho \\ \rho u \\ E \end{bmatrix}, \quad \mathbf{F} = \begin{bmatrix} \rho u \\ \rho u^2 + p \\ u(E+p) \end{bmatrix}, \quad \mathbf{G} = \begin{bmatrix} 0 \\ \tfrac{4}{3}\eta\partial_x u \\ \tfrac{4}{3}\left(\eta u \partial_x u\right) - (\kappa\partial_x T) \end{bmatrix}. \tag{3.35}$$

In what follows we take

$$\alpha = \tfrac{4}{3}\eta \, , \quad \kappa = 0 \, . \tag{3.36}$$

3.3.1   Canonical formulation

To apply the canonical formulation following (3.11) and (3.12) we take $\mathbf{U} = [\psi_1, \psi_2, \psi_3]^T$, such that

$$\psi_1 \to \partial_x \rho \, , \quad \psi_2 \to \partial_x(\rho u) \, , \quad \psi_3 \to \partial_x E \, , \quad \text{as } \varepsilon \to 0 \, . \tag{3.37}$$

This behaviour is achieved by the evolution equations

$$
\left.
\begin{aligned}
\partial_t \psi_1 &= (\partial_x \rho - \psi_1) \frac{1}{\varepsilon} \, , \\[2mm]
\partial_t \psi_2 &= (\partial_x(\rho u) - \psi_2) \frac{1}{\varepsilon} \, , \\[2mm]
\partial_t \psi_3 &= (\partial_x E - \psi_3) \frac{1}{\varepsilon} \, .
\end{aligned}
\right\}
\tag{3.38}
$$

Therefore, the canonical formulation of (3.35) is

$$
\left.
\begin{aligned}
\partial_t \rho + \partial_x(\rho u) &= 0 \, , \\[2mm]
\partial_t (\rho u) + \partial_x \left(\rho u^2 + p - \alpha \left(\frac{\psi_2}{\rho} - u \frac{\psi_1}{\rho} \right) \right) &= 0 \, , \\[2mm]
\partial_t E + \partial_x \left(u \left(E + p - \alpha \left(\frac{\psi_2}{\rho} - u \frac{\psi_1}{\rho} \right) \right) \right) &= 0 \, , \\[2mm]
\partial_t \psi_1 + \partial_x \left(\tfrac{-1}{\varepsilon} \rho \right) &= -\tfrac{1}{\varepsilon} \psi_1 \, , \\[2mm]
\partial_t \psi_2 + \partial_x \left(-\tfrac{1}{\varepsilon} \rho u \right) &= -\tfrac{1}{\varepsilon} \psi_2 \, , \\[2mm]
\partial_t \psi_3 + \partial_x \left(-\tfrac{1}{\varepsilon} E \right) &= -\tfrac{1}{\varepsilon} \psi_3 \, .
\end{aligned}
\right\}
\tag{3.39}
$$

When (3.39) is written as in (3.11), the matrices (3.2) become

$$
\left.
\begin{aligned}
\mathbf{A} &= \begin{bmatrix}
0 & 1 & 0 \\
\frac{1}{2}(\gamma-3)u^2 & (3-\gamma)u & \gamma-1 \\
\frac{1}{2}(\gamma-2)u^3 - \frac{c^2 u}{\gamma-1} & \frac{(3-2\gamma)}{2}u^2 - \frac{c^2}{\gamma-1} & \gamma u
\end{bmatrix}, \\[2em]
\mathbf{B} &= \begin{bmatrix}
0 & 0 & 0 \\
-\frac{\alpha}{\rho^2}\left(\psi_2 - 2\frac{\psi_1 u}{\rho}\right) & -\frac{\alpha\psi_1}{\rho^3} & 0 \\
-\frac{\alpha u}{\rho^2}\left(2\psi_2 - 3\frac{\psi_1 u}{\rho}\right) & \frac{\alpha}{\rho^2}\left(\psi_2 - 2\frac{\psi_1 u}{\rho}\right) & 0
\end{bmatrix}, \\[2em]
\mathbf{D} &= \frac{\alpha}{\rho}\begin{bmatrix}
0 & 0 & 0 \\
-u & 1 & 0 \\
-u^2 & u & 0
\end{bmatrix}.
\end{aligned}
\right\}
\tag{3.40}
$$

Note that $\mathbf{D} = \mathbf{P}\mathbf{\Lambda}\mathbf{P}^{-1}$ where $\mathbf{\Lambda}$ is a diagonal matrix containing the eigenvalues of $\mathbf{D}$

$$
\delta_1 = \delta_2 = 0 , \quad \delta_3 = \frac{\alpha}{\rho}
\tag{3.41}
$$

and $\mathbf{P}$ is given by

$$
\mathbf{P} = \begin{bmatrix}
1 & 0 & 0 \\
u & 0 & 1 \\
0 & 1 & u
\end{bmatrix}.
\tag{3.42}
$$

The eigenvalues of matrix $\mathbf{A}$ are

$$
a_1 = u - c , \quad a_2 = u , \quad a_3 = u + c ,
\tag{3.43}
$$

with

$$
c = \sqrt{\frac{\gamma p}{\rho}}
\tag{3.44}
$$

being the sound speed. The eigenvalues of $\mathbf{B}$ are

$$b_1 = -\frac{\alpha\psi_1}{\rho^2} \;, \quad b_2 = b_3 = 0 \;. \tag{3.45}$$

Remark 3.5. We cannot give a closed form for the eigenvalues μ_i of $\mathbf{A}-\mathbf{B}$. However, from Cardano's formula [110], we known that all eigenvalues of $\mathbf{A} - \mathbf{B}$ are real. Numerically, we have verified that eigenvalues are always real, confirming the theory.

3.3.2 Ad Hoc relaxation formulation

System (3.35) allows an ad hoc relaxation formulation with

$$\tilde{\mathbf{Q}} = \begin{bmatrix} \rho \\ \rho u \end{bmatrix} \equiv \begin{bmatrix} q_1 \\ q_2 \end{bmatrix}, \quad \Phi(\tilde{\mathbf{Q}}) = \frac{q_2}{q_1} = u, \quad \mathbf{\Psi} = \psi \;. \tag{3.46}$$

In this case $\tilde{\mathbf{Q}} \in \mathbb{R}^2$ and $\mathbf{\Psi} \in \mathbb{R}$. Introducing

$$\psi \to \tfrac{\partial u}{\partial x} \;, \text{ as } \varepsilon \to 0 \tag{3.47}$$

the *Ad Hoc Formulation*, written in full, becomes

$$\left. \begin{aligned} \partial_t \rho + \partial_x(\rho u) &= 0 \;, \\[2mm] \partial_t\left(\rho u\right) + \partial_x\left(\rho u^2 + p - \alpha\psi\right) &= 0 \;, \\[2mm] \partial_t E + \partial_x(u(E + p - \alpha\psi)) &= 0 \;, \\[2mm] \partial_t \psi &= (\partial_x u - \psi)\tfrac{1}{\varepsilon} \;. \end{aligned} \right\} \tag{3.48}$$

Proposition 3.6. *If*

$$\frac{\alpha(\gamma - 1)\psi}{\rho} < c^2 \;, \tag{3.49}$$

then all the eigenvalues of the Ad Hoc Formulation (3.48) are real, for ε satisfying

$$\varepsilon < \frac{\alpha}{\rho|\bar{\kappa}|}\left(\frac{\sqrt{3} + 2}{2\sqrt{3} - 2}\right) \;, \tag{3.50}$$

with

$$\bar{\kappa} = \frac{\alpha\psi(\gamma - 1)}{\rho} - c^2 \;. \tag{3.51}$$

Proof. System (3.48), written as (3.11), (3.13), but in physical variables and in quasi-linear form becomes

$$\partial_t \mathbf{W} + \mathbf{J}(\mathbf{W})\partial_x \mathbf{W} = \mathbf{S}(\mathbf{W}) \,, \tag{3.52}$$

with

$$\mathbf{W} = \begin{bmatrix} \rho \\ u \\ p \\ \psi \end{bmatrix} \,, \quad \mathbf{S}(\mathbf{W}) = \begin{bmatrix} 0 \\ 0 \\ 0 \\ \frac{-\psi}{\varepsilon} \end{bmatrix} \,, \quad \mathbf{J}(\mathbf{W}) = \begin{bmatrix} u & \rho & 0 & 0 \\ 0 & u & \frac{1}{\rho} & \frac{-\alpha}{\rho} \\ 0 & c^2\rho - \alpha\psi(\gamma - 1) & u & 0 \\ 0 & \frac{-1}{\varepsilon} & 0 & 0 \end{bmatrix} \tag{3.53}$$

The characteristic polynomial of $\mathbf{J}(\mathbf{W})$ has the form

$$p(x) = (u - x)\left(-\frac{\alpha\,(u - x)}{\rho\,\varepsilon} - (u - x)^2\,x + \frac{\left(c^2\,\rho - \alpha\,(\gamma - 1)\,\psi\right)\,x}{\rho} \right) \,, \tag{3.54}$$

of which clearly u is an eigenvalue. To find the other eigenvalues we should find the roots of the reduced polynomial of third degree

$$p_3(x) = \frac{\alpha\,(u - x)}{\rho\,\varepsilon} + (u - x)^2\,x - \frac{\left(c^2\,\rho - \alpha\,(\gamma - 1)\,\psi\right)\,x}{\rho} \,, \tag{3.55}$$

which can be written as

$$p_3(x) = x^3 + c_1 x^2 + c_2 x + c_3 \,. \tag{3.56}$$

The roots of this polynomial can be found using the Cardano's formula [110], which in order to have real roots has the constraint

$$D \leq 0 \,, \tag{3.57}$$

where

$$D = Q^3 + R^2 \tag{3.58}$$

and

$$Q = \frac{3c_2 - c_1^2}{9} \,, \quad R = \frac{9c_1c_2 - 27c_3 - 2c_1^3}{54} \,. \tag{3.59}$$

The strategy will consist in writing D as function of u and look for conditions on parameters in order to satisfy $D \leq 0$ for all u. Note that we can express Q and R as

$$Q = L_1 - \frac{u^2}{9} \ , \quad R = u\left(L_2 - \frac{u^2}{27}\right) \ , \tag{3.60}$$

with

$$\begin{aligned}
L_1 &= -\frac{\alpha}{3\,\rho\,\varepsilon} + \frac{\alpha\,\psi}{3\,\rho}(\gamma-1) - \frac{c^2}{3} = -\frac{\alpha}{3\rho\varepsilon} + \frac{\bar{\kappa}}{3} \ , \\
L_2 &= -\frac{\alpha}{6\,\rho\,\varepsilon} - \frac{\alpha\,\psi}{3\,\rho}(\gamma-1) + \frac{c^2}{3} = -\frac{\alpha}{6\rho\varepsilon} - \frac{\bar{\kappa}}{3} \ .
\end{aligned} \tag{3.61}$$

Therefore

$$D(u) = L_1^3 + u^2\left(L_2^2 - \frac{L_1^2}{3}\right) + \frac{u^4}{27}\left(L_1 - 2L_2\right) \ , \tag{3.62}$$

or

$$D(u) = d_0 + u^2 d_1 + \frac{u^4}{27}d_2 \ , \tag{3.63}$$

where

$$d_0 := L_1^3 \ , \quad d_1 := L_2^2 - L_1^2/3 \ , \quad d_2 := L_1 - 2L_2 \ . \tag{3.64}$$

As $\bar{\kappa} < 0$ then $d_0 < 0$ and as ε satisfies

$$\varepsilon < \frac{\alpha}{\rho|\bar{\kappa}|}\left(\frac{\sqrt{3}+2}{2\sqrt{3}-2}\right) \ , \tag{3.65}$$

then $d_1 < 0$ and $d_2 = \bar{\kappa} < 0$ by definition. So $D(u) < 0$ for all u. Therefore the solutions can be found as

$$\left. \begin{aligned}
\lambda_1 &= S_1 + S_2 - \frac{a_1}{3} \ , \\
\lambda_2 &= -\frac{S_1+S_2}{2} - \frac{a_1}{3} + i\frac{\sqrt{3}}{2}(S_1 - S_2) \ , \\
\lambda_3 &= -\frac{S_1+S_2}{2} - \frac{a_1}{3} - i\frac{\sqrt{3}}{2}(S_1 - S_2) \ ,
\end{aligned} \right\} \tag{3.66}$$

where

$$S_1 = \sqrt[3]{R + \sqrt{D}} \quad , S_2 = \sqrt[3]{R - \sqrt{D}} \ . \tag{3.67}$$

$\square$

Remark: The above proposition imposes a strong restriction on variable ψ, which is undesirable. Next, we improve upon this result.

Proposition 3.7. *The Ad Hoc Relaxation Formulation (3.48) has real eigenvalues for sufficiently small relaxation parameter ε satisfying*

$$\varepsilon \leq \frac{\alpha}{3\rho M^*} \, , \tag{3.68}$$

with

$$M^* = \frac{160}{3}\left(\frac{u^2 + |K|}{2}\right) \, , \quad K = \frac{\bar{\kappa}}{3} = \frac{1}{3}\left[\frac{\psi\alpha(\gamma - 1)}{\rho} - c^2\right] . \tag{3.69}$$

Proof. We note that L_1 and L_2 in (3.61) can be written as

$$L_1 = M + K \, , \quad L_2 = \frac{M}{2} - K \, , \tag{3.70}$$

with

$$M = -\frac{\alpha}{3\rho\varepsilon} \, . \tag{3.71}$$

Thus from (3.62) we obtain

$$D = M^3 + p_2(M) \, , \tag{3.72}$$

with

$$p_2(M) \;=\; M^2\left(3\,K - \frac{u^2}{12}\right) + M\left(3\,K^2 - \frac{5\,u^2\,K}{2}\right) + \left(K^3 + \frac{2\,u^2\,K^2}{3} + 3\,u^4\,K\right) \tag{3.73}$$

Note that we need the range of $M < 0$ such that $D \leq 0$, which is equivalent to the range of $M > 0$ such that

$$p_2(-M) < M^3 \, . \tag{3.74}$$

In such a case we observe that

$$-M\left(3K^2 - \frac{5u^2K}{2}\right) \leq \frac{5}{2}Mu^2|K| \, , \tag{3.75}$$

for all K and $M > 0$ and thus

$$p_2(-M) \leq 3M^2\,K + M\frac{5}{2}|K|u^2 + \left(K^3 + \frac{2\,u^2\,K^2}{3} + 3\,u^4\,K\right) \, . \tag{3.76}$$

On the other hand we define $\tilde{L} = \frac{160}{3}$ and $\tilde{M}$ such that

$$u^2 \leq 2\tilde{M}, \quad |K| \leq 2\tilde{M} . \tag{3.77}$$

Therefore (3.76) satisfies

$$p_2(-M) \leq M^2 \tilde{M} 6 + M \tilde{M}^2 10 + \tilde{M}^3 \left(\frac{112}{3} \right) . \tag{3.78}$$

By considering M in the range $\tilde{M}\tilde{L} \leq M$, then $\tilde{M}^2 \leq \tilde{M}M$ and $\tilde{M}^3 \leq \tilde{M}^2 M$. Therefore

$$p_2(-M) \leq M^2 \tilde{M} \left(\frac{160}{3} \right) \leq M^3 . \tag{3.79}$$

Hence (3.74) is satisfied for $M > \tilde{M}\tilde{L}$ and the result holds, with $\tilde{M} = \frac{u^2 + |K|}{2}$. $\qquad \square$

Remark 3.8. With above results we have demonstrated a necessary condition for systems resulting from relaxation formulation of (3.1), (3.35) to be hyperbolic. We are also in a position to give the form of the eigenvalues, as shown in appendix A. From a numerical point of view, with this information, we are able to improve upon existing strategies, whereby eigenvalue are estimated on splitting between viscous and inviscid operators [39, 67, 113]. In appendix A we consider a linear problem and we make a comparison of the splitting technique and our approach.

The following section is devoted to recall a new methodology to solve hyperbolic systems with stiff source terms.

3.4 ADER Finite Volume Schemes for Advection-Reaction Equations. Brief Review

Consider the hyperbolic balance laws

$$\partial_t \mathbf{Q} + \partial_x \mathbf{F}(\mathbf{Q}) = \mathbf{S}(\mathbf{Q}) . \tag{3.80}$$

By integrating (3.80) in the control volume $V = [x_{i-\frac{1}{2}}, x_{i+\frac{1}{2}}] \times [t^n, t^{n+1}]$ we obtain

$$\mathbf{Q}_i^{n+1} = \mathbf{Q}_i^n - \frac{\Delta t}{\Delta x} \left[\mathbf{F}_{i+\frac{1}{2}} - \mathbf{F}_{i-\frac{1}{2}} \right] + \Delta t \mathbf{S}_i , \tag{3.81}$$

with

$$
\left.
\begin{aligned}
\mathbf{Q}_i^n &= \frac{1}{\Delta x} \int_{x_{i-\frac{1}{2}}}^{x_{i+\frac{1}{2}}} \mathbf{Q}(x, t^n) dx \, , \\[2ex]
\mathbf{F}_{i+\frac{1}{2}} &= \frac{1}{\Delta t} \int_{t^n}^{t^{n+1}} \mathbf{F}(\mathbf{Q}(x_{i+\frac{1}{2}}, t)) dt \, , \\[2ex]
\mathbf{S}_i &= \frac{1}{\Delta t \Delta x} \int_{x_{i-\frac{1}{2}}}^{x_{i+\frac{1}{2}}} \int_{t^n}^{t^{n+1}} \mathbf{S}(\mathbf{Q}(x, t)) dt dx \, .
\end{aligned}
\right\}
\tag{3.82}
$$

Here $\Delta x = x_{i+\frac{1}{2}} - x_{i+\frac{1}{2}}$ and $\Delta t = t^{n+1} - t^n$. Note that (3.81) is exact whenever integrals in (3.82) are satisfied exactly.

Finite volume methods are based on reinterpreting formula (3.81) approximately. In this manner, an approximation to $\mathbf{F}_{i+\frac{1}{2}}$ becomes the *numerical flux* and and approximation to $\mathbf{S}_i$ becomes the *numerical source*. There are many ways of constructing finite volume methods.

Next we briefly review the ADER methodology based on the one-step finite volume formula (3.81). For background on ADER see Chaps. 19 and 20 of [147] and references therein. ADER has two main steps: (1) non-linear spatial reconstruction and (2) solution of the generalised Riemann problem to compute $\mathbf{F}_{i+\frac{1}{2}}$ and $\mathbf{S}_i$ to high order of accuracy.

3.4.1 Generalized Riemann Problem

The Generalized Riemann Problem (GRP) is a particular Cauchy problem with piecewise smooth initial data, namely

$$
\left.
\begin{aligned}
\partial_t \mathbf{Q} + \partial_x \mathbf{F}(\mathbf{Q}) &= \mathbf{S}(\mathbf{Q}) \, , \\[2ex]
\mathbf{Q}(x, 0) &=
\begin{cases}
\mathbf{Q}_L(x) & x < 0 \, , \\[1ex]
\mathbf{Q}_R(x) & x > 0 \, .
\end{cases}
\end{aligned}
\right\}
\tag{3.83}
$$

Here $\mathbf{Q}_L(x)$ and $\mathbf{Q}_R(x)$ are, for example, polynomials of degree M resulting from a reconstruction procedure. We are interested in the solution at the interface position, as function of time, denoted by $\mathbf{Q}_{LR}(\tau)$. Next we briefly review two existent solvers for the GRP based on the Cauchy-Kowalewski procedure, illustrated below.

3.4.2 The Cauchy-Kowalewski procedure

We can express time derivatives in term of spatial derivatives by using the governing equations. To illustrate the procedure we consider the scalar hyperbolic balance law

$$\partial_t q + \partial_x f(q) = s(q) \ . \tag{3.84}$$

We define functionals $G^{(1)}, G^{(2)}, \ldots, G^{(k)}$ as

$$\partial_t q = G^{(1)}(q, \partial_x q) \ , \ \ \partial_t^{(2)} q = G^{(2)}(q, \partial_x q, \partial_x^{(2)} q) \ , \ \ \partial_t^{(k)} q = G^{(k)}(q, \partial_x q, \ldots, \partial_x^{(k)} q) \ . \tag{3.85}$$

In particular

$$\left.\begin{aligned}
G^{(1)}(q, \partial_x q) \quad &:= \quad s(q) - \lambda(q)\partial_x q \ , \\[2mm]
G^{(2)}(q, \partial_x q, \partial_x^{(2)} q) \quad &:= \quad [s(q) - \lambda(q)\partial_x q]\left[\mu(q) - \lambda(q)'\partial_x q\right] \\[2mm]
&\quad -\lambda(q)\left(\mu(q)\partial_x q - \lambda(q)'(\partial_x q)^2 - \lambda(q)\partial_x^{(2)} q\right) \ ,
\end{aligned}\right\} \tag{3.86}$$

with

$$\lambda(q) = \frac{df(q)}{dq} \ . \tag{3.87}$$

For the spacial case $f(q) = \lambda q$ and $s(q) = \beta q$, with λ and β constant

$$G^{(k)}(q, \partial_x q, ..., \partial_x^{(k)} q) := \sum_{l=0}^{k-l} \beta^{k-l} \lambda^l \frac{k!}{(k-l)!l!} \partial_x^{(l)} q \ , \tag{3.88}$$

where $\partial_x^{(0)} q = q$ and $n! = n(n-1)!$, with notation $0! = 1$.

The same procedure applies for systems, but symbolic manipulators may be needed for the calculations. The Cauchy-Kowalewski procedure replaces time derivatives by a functional of spatial derivatives

$$\partial_t^{(k)} \mathbf{Q}(x,t) = \mathbf{G}^{(k)}(\mathbf{Q}(x,t), ..., \partial_x^{(k)} \mathbf{Q}(x,t)) \ . \tag{3.89}$$

$\mathbf{G}^{(k)}$ will be called Cauchy-Kowalewski functional, whose arguments will often be omitted.

Next we review two solvers based on Taylor expansions and the Cauchy-Kowalewski procedure. Two more solvers are found in [22] and [41]. For a thorough review of GRP solvers see [100].

3.4.3 The Toro-Titarev solver (TT)

Following [154] the solution of $\mathbf{Q}_{LR}(\tau)$ at the interface is assumed to have the Taylor series expansion

$$\mathbf{Q}_{LR}(\tau) = \mathbf{Q}(0, 0_+) + \sum_{k=1}^{M} \frac{\tau^k}{k!} \partial_t^{(k)} \mathbf{Q}(0, 0_+) , \qquad (3.90)$$

with

$$\mathbf{Q}(0, 0_+) = \lim_{t \to 0_+} \mathbf{Q}(0, t) . \qquad (3.91)$$

Following (3.89), time derivatives $\partial_t^{(k)} \mathbf{Q}$ are replaced by their respective Cauchy-Kowalewski functionals $\mathbf{G}^{(k)}$

$$\partial_t^{(k)} \mathbf{Q}(0, 0_+) = \mathbf{G}^{(k)}(\mathbf{Q}(0, 0_+), ..., \partial_x^{(k)} \mathbf{Q}(0, 0_+)) . \qquad (3.92)$$

The leading term $\mathbf{Q}(0, 0_+)$ is found as the self-similar solution of the classical Riemann problem

$$\partial_t \mathbf{Q} + \partial_x \mathbf{F}(\mathbf{Q}) = \mathbf{0} ,$$

$$\mathbf{Q}(x, 0) = \begin{cases} \mathbf{Q}_L(0_-) = \lim_{x \to 0_-} \mathbf{Q}_L(x) & x < 0 , \\ \\ \mathbf{Q}_R(0_+) = \lim_{x \to 0_+} \mathbf{Q}_R(x) & x > 0 . \end{cases} \qquad (3.93)$$

Spatial derivatives are found as self-similar solutions of the following derivative, classical Riemann problems

$$\partial_t \left(\partial_x^{(k)} \mathbf{Q} \right) + \mathbf{A}(\mathbf{Q}(0, 0_+)) \partial_x \left(\partial_x^{(k)} \mathbf{Q} \right) = \mathbf{0} ,$$

$$\partial_x^{(k)} \mathbf{Q}(x, 0) = \begin{cases} \mathbf{Q}_L^{(k)}(0_-) = \lim_{x \to 0_-} \frac{d^k}{dx^k} \mathbf{Q}_L(x) & x < 0 , \\ \\ \mathbf{Q}_R^{(k)}(0_+) = \lim_{x \to 0_+} \frac{d^k}{dx^k} \mathbf{Q}_R(x) & x > 0 , \end{cases} \qquad (3.94)$$

where $\mathbf{A}(\mathbf{Q})$ is the Jacobian. Details on the evolution equations in (3.94) for spatial derivatives can be found in [154].

Note that this solver requires (a) the solution of one non-linear classical Riemann problem for the leading term and (b) the solution of a sequence of linear classical Riemann problems for spatial derivatives.

3.4.4 The Harten-Engquist-Osher-Chakravarthy (HEOC) solver

Here we review the re-interpretation of Castro and Toro [22] of the Harten et al. method [66]. The GRP solution $\mathbf{Q}_{LR}(\tau)$ at each time τ is found as the self-similar solution of the associated classical Riemann problem

$$
\left.
\begin{aligned}
\partial_t \mathbf{Q} + \partial_x \mathbf{F}(\mathbf{Q}) = \mathbf{0} \, , \\[2mm]
\mathbf{Q}(x,0) =
\begin{cases}
\hat{\mathbf{Q}}_L(\tau) & x < 0 \, , \\[4mm]
\hat{\mathbf{Q}}_R(\tau) & x > 0
\end{cases}
\end{aligned}
\right\}
\tag{3.95}
$$

evaluated at the interface $x/t = 0$, where

$$
\left.
\begin{aligned}
\hat{\mathbf{Q}}_L(\tau) &= \mathbf{Q}_L(0) + \sum_{k=1}^{M} \frac{\tau^k}{k!} \mathbf{G}^{(k)}\left(\mathbf{Q}_L(0), ..., \partial_x \mathbf{Q}_L(0)\right) , \\[4mm]
\hat{\mathbf{Q}}_R(\tau) &= \mathbf{Q}_R(0) + \sum_{k=1}^{M} \frac{\tau^k}{k!} \mathbf{G}^{(k)}\left(\mathbf{Q}_R(0), ..., \partial_x \mathbf{Q}_R(0)\right) .
\end{aligned}
\right\}
\tag{3.96}
$$

Note that this solver generally requires (a) the solution of K non-linear, classical Riemann problems at the interface and (b) the evaluation of two Taylor series expansions (3.96) at each integration time τ_k, for $k = 1, 2, \ldots, K$, where K is the number of integration points in the evaluation of the time integral to find the numerical flux in (3.82).

3.5 A New Locally Implicit Solver for the GRP

It is possible to solve the GRP by means of an implicit Taylor series expansion, as shown below. Such implicit form allows us to develop an alternative to solver, still based on Taylor series expansion and the Cauchy-Kowalewski procedure. This solver has the advantage of being able to handle stiff source terms and therefore is directly applicable to the hyperbolic reformulations of advection-diffusion-reaction equations, as presented in Sect. 3.2.1. The methodology was first communicated in [101] for the scalar case. We call the solver the MT solver (for Montecinos and Toro).

3.5.1 Implicit Taylor series expansion

A key aspect of the Montecinos-Toro Implicit Solver results from the following, simple observation.

Lemma 3.9. *Let* $\mathbf{Q}(x, \tau)$ *be an analytical function of* τ, *then* $\mathbf{Q}(x, \tau)$ *can be expressed in terms of the implicit Taylor series in time*

$$\mathbf{Q}(x, \tau) = \mathbf{Q}(x, 0_+) - \sum_{k=1}^{\infty} \frac{(-\tau)^k}{k!} \partial_t^{(k)} \mathbf{Q}(x, \tau) \ . \tag{3.97}$$

Proof.

$$
\begin{aligned}
\mathbf{Q}(x, 0_+) &= \lim_{\epsilon \to 0} \mathbf{Q}(x, 0 + \epsilon) \\
&= \lim_{\epsilon \to 0} \mathbf{Q}(x, \tau - \tau + \epsilon) \\
&= \lim_{\epsilon \to 0} \left\{ \mathbf{Q}(x, \tau) + \sum_{k=1}^{\infty} \frac{(-\tau + \epsilon)^k}{k!} \partial_t^{(k)} \mathbf{Q}(x, \tau) \right\} \\
&= \mathbf{Q}(x, \tau) + \sum_{k=1}^{\infty} \frac{(-\tau)^k}{k!} \partial_t^{(k)} \mathbf{Q}(x, \tau) \ .
\end{aligned}
\tag{3.98}
$$

Note that from the analyticity of $\mathbf{Q}(x, \tau)$ the Taylor series is uniformly convergent for ε, so the limiting operation can be interchanged with the summation. Therefore solving for $\mathbf{Q}(x, \tau)$ gives the sought result. $\qquad\square$

This result will be used both for computing the numerical flux, for which we need $\mathbf{Q}(0, \tau)$, and for computing the source term within the control volume.

The result just proved will be used to construct an alternative GRP solver to that of Toro and Titarev based on the explicit Taylor expansion (3.90). The present solver is based on the implicit expansion (3.97) at $x = 0$, truncated after M terms, that is

$$\mathbf{Q}(0, \tau) = \mathbf{Q}(0, 0_+) - \sum_{k=1}^{M} \frac{(-\tau)^k}{k!} \partial_t^{(k)} \mathbf{Q}(0, \tau) \ , \tag{3.99}$$

where the Cauchy-Kowalewski functionals are used to evaluate time derivatives as in (3.92) but now done implicitly

$$\partial_t^{(k)} \mathbf{Q}(0, \tau) = \mathbf{G}^{(k)}(\mathbf{Q}(0, \tau), ..., \partial_x^{(k)} \mathbf{Q}(0, \tau)) \ . \tag{3.100}$$

Then expansion (3.99) becomes

$$\mathbf{Q}(0, \tau) = \mathbf{Q}(0, 0_+) - \sum_{k=1}^{M} \frac{(-\tau)^k}{k!} \mathbf{G}^{(k)}(\mathbf{Q}(0, \tau), ..., \partial_x^{(k)} \mathbf{Q}(0, \tau)) \ . \tag{3.101}$$

In [101], only the source term was considered implicitly; spatial derivatives were dealt with explicitly resulting in a useful scheme but with a much reduced stability range.

The present formulation overcomes that problem, restoring stability in the expected full range of explicit ADER schemes for non-stiff problems, unity for the model equation.

For the present formulation, for each time τ, we have M algebraic problems for spatial derivatives

$$\partial_x^{(l)}\mathbf{Q}(0,\tau) = \partial_x^{(l)}\mathbf{Q}(0,0_+) - \sum_{k=1}^{M-l} \frac{(-\tau)^k}{k!} \partial_t^{(k)}(\partial_x^{(l)}\mathbf{Q}(0,\tau)) , \quad l = 1, ..., M , \quad (3.102)$$

which by virtue of (3.100) becomes

$$\partial_x^{(l)}\mathbf{Q}(0,\tau) = \partial_x^{(l)}\mathbf{Q}(0,0_+) - \sum_{k=1}^{M-l} \frac{(-\tau)^k}{k!} \partial_x^{(l)}\mathbf{G}^{(k)}(\mathbf{Q}(0,\tau), ..., \partial_x^{(k)}\mathbf{Q}(0,\tau)) . \quad (3.103)$$

In the next section we present a second-order version of this scheme, though the approach is capable of producing schemes of any order.

3.5.2   Second-order MT solver for GRP

We consider the problem (3.83), with $\mathbf{Q}_L(x)$ and $\mathbf{Q}_R(x)$ polynomials of degree one. We denote by $\mathbf{A}$ the Jacobian of $\mathbf{F}$ with respect to $\mathbf{Q}$ and by $\mathbf{B}$ the Jacobian of $\mathbf{S}$ with respect to $\mathbf{Q}$.

3.5.2.1   The MT-TT approach

Here we present an extension of the TT approach for solving the GRP, whereby a locally implicit approach is used. For the second order scheme one has

$$\mathbf{Q}(0,\tau) = \mathbf{Q}(0,0_+) + \tau\partial_t\mathbf{Q}(0,\tau) . \quad (3.104)$$

Using the Cauchy-Kowalewski procedurewe have

$$\mathbf{Q}(0,\tau) = \mathbf{Q}(0,0_+) + \tau\left[-\mathbf{A}(\mathbf{Q}(0,\tau))\partial_x\mathbf{Q}(0,\tau) + \mathbf{S}(\mathbf{Q}(0,\tau))\right] . \quad (3.105)$$

To evaluate spatial derivatives we use again the implicit Taylor series

$$\partial_x\mathbf{Q}(0,\tau) = \partial_x\mathbf{Q}(0,0_+) + \tau\partial_t(\partial_x\mathbf{Q}(0,\tau)) . \quad (3.106)$$

which after using the Cauchy-Kowalewski procedure becomes

$$\partial_x\mathbf{Q}(0,\tau) = \partial_x\mathbf{Q}(0,0_+) + \tau\partial_x\left[-\mathbf{A}(\mathbf{Q}(0,\tau))\partial_x\mathbf{Q}(0,\tau) + \mathbf{S}(\mathbf{Q}(0,\tau))\right] . \quad (3.107)$$

At this stage we linearise $\mathbf{A}(\mathbf{Q})$ by evaluating it at the leading term $\mathbf{Q}(0, 0_+)$. Then

$$\partial_x \mathbf{Q}(0, \tau) = \partial_x \mathbf{Q}(0, 0_+) + \tau \partial_x \left[-\mathbf{A}(\mathbf{Q}(0, 0_+)) \partial_x \mathbf{Q}(0, \tau) + \mathbf{S}(\mathbf{Q}(0, \tau)) \right] . \quad (3.108)$$

Since $\mathbf{Q}_L(x)$ and $\mathbf{Q}_R(x)$ are of degree one

$$\partial_x \mathbf{Q}(0, \tau) = \partial_x \mathbf{Q}(0, 0_+) + \tau \mathbf{B}(\mathbf{Q}(0, \tau)) \partial_x \mathbf{Q}(0, \tau) , \quad (3.109)$$

from which

$$\partial_x \mathbf{Q}(0, \tau) = [\mathbf{I} - \tau \mathbf{B}(\mathbf{Q}(0, \tau))]^{-1} \partial_x \mathbf{Q}(0, 0_+) , \quad (3.110)$$

where $\mathbf{I}$ denotes the identity matrix. By substituting (3.110) into (3.105) and denoting $\mathbf{Q}(0, \tau)$ by $\mathbf{Q}_{LR}$, we obtain a non-linear algebraic system for $\mathbf{Q}_{LR}$, at a specified time τ, namely

$$\mathbf{Q}_{LR} = \mathbf{Q}(0, 0_+) + \tau \left[-\mathbf{A}(\mathbf{Q}_{LR}) [\mathbf{I} - \tau \mathbf{B}(\mathbf{Q}_{LR})]^{-1} \partial_x \mathbf{Q}(0, 0_+) + \mathbf{S}(\mathbf{Q}_{LR}) \right] . \quad (3.111)$$

Then, by solving (3.111) we obtain the solution of the GRP at given the time τ. We use a nested Newton method, written as fixed point iteration

$$\mathbf{Q}_{LR}^{r+1} = \mathbf{Q}(0, 0_+) + \tau \left[-\mathbf{A}(\mathbf{Q}_{LR}^{r+1}) [\mathbf{I} - \tau \mathbf{B}(\mathbf{Q}_{LR}^r)]^{-1} \partial_x \mathbf{Q}(0, 0_+) + \mathbf{S}(\mathbf{Q}_{LR}^{r+1}) \right] . \quad (3.112)$$

Note that in this formulation the leading term $\mathbf{Q}(0, 0_+)$ and the derivative $\partial_x \mathbf{Q}(0, 0_+)$ are computed as in the Toro-Titarev scheme, by solving (3.93) and (3.94) respectively.

3.5.2.2   The MT-HEOC approach

The HEOC approach for solving the GRP can also be extended by resorting to a locally implicit approach. The solution $\mathbf{Q}_{LR}(\tau)$ is found as the self-similar solution of the classical Riemann problem

$$\partial_t \mathbf{Q} + \partial_x \mathbf{F}(\mathbf{Q}) = \mathbf{0} ,$$

$$\mathbf{Q}(x, 0) = \left\{ \begin{array}{ll} \hat{\mathbf{Q}}_L(\tau) & x < 0 , \\ \\ \hat{\mathbf{Q}}_R(\tau) & x > 0 , \end{array} \right\} \quad (3.113)$$

with initial condition obtained from two implicit Taylor series expansions, namely

$$\left.\begin{array}{l} \hat{\mathbf{Q}}_L(\tau) = \mathbf{Q}_L(0) + \tau\left[-\mathbf{A}(\hat{\mathbf{Q}}_L(\tau))\left[\mathbf{I} - \tau\mathbf{B}(\hat{\mathbf{Q}}_L(\tau))\right]^{-1}\partial_x\mathbf{Q}_L(0) + \mathbf{S}(\hat{\mathbf{Q}}_L(\tau))\right], \\ \\ \hat{\mathbf{Q}}_R(\tau) = \mathbf{Q}_R(0) + \tau\left[-\mathbf{A}(\hat{\mathbf{Q}}_R(\tau))\left[\mathbf{I} - \tau\mathbf{B}(\hat{\mathbf{Q}}_R(\tau))\right]^{-1}\partial_x\mathbf{Q}_R(0) + \mathbf{S}(\hat{\mathbf{Q}}_R(\tau))\right]. \end{array}\right\} \quad (3.114)$$

Next we illustrate the second order scheme for a scalar case.

3.5.2.3 Second-order scheme for the model advection-reaction equation

We illustrate the methodology by constructing a second-order scheme based on the solution to the Generalized Riemann problems via an implicit Taylor series, all as applied to the model scalar equation

$$\partial_t q(x,t) + \lambda\partial_x q(x,t) = \beta q(x,t), \quad \beta \leq 0. \tag{3.115}$$

We assume the solution of (3.115) to be computed with the one-step finite volume formula (3.81), on a computational domain consisting on M cells. To update the solution from time t^n to time t^{n+1} the ADER methodology requires (i) a reconstruction procedure and (ii) the solution of GRPs to compute the numerical flux and the numerical source.

3.5.2.4 ENO reconstruction

We adopt the ENO reconstruction procedure by constructing local, first-degree polynomials $p_i(x)$ in each cell $[x_{i-\frac{1}{2}}, x_{i+\frac{1}{2}}]$, of the form

$$p_i(x) = q_i^n + (x - x_i)\Delta_i, \tag{3.116}$$

with $x_i = (x_{i+\frac{1}{2}} + x_{i-\frac{1}{2}})/2$. Recall that in order to circumvent Godunov's Theorem [55], the reconstruction must be *non linear*. See Chap. 20 of [147] for background. Here the non-linearity of the scheme is ensured by taking the slope Δ_i as

$$\Delta_i = \left\{\begin{array}{ll} \dfrac{q_i^n - q_{i-1}^n}{\Delta x} & if \quad |q_i^n - q_{i-1}^n| < |q_{i+1}^n - q_i^n|, \\ \\ \dfrac{q_{i+1}^n - q_i^n}{\Delta x} & if \quad |q_i^n - q_{i-1}^n| \geq |q_{i+1}^n - q_i^n|. \end{array}\right\} \tag{3.117}$$

3.5.2.5 Generalized Riemann problem

For a second-order scheme the generalised Riemann problem for (3.115) has piecewise linear initial conditions. That is the GRP is

$$
\left.
\begin{aligned}
&\frac{\partial}{\partial t} q(x,t) + \lambda \frac{\partial}{\partial x} q(x,t) = \beta q(x,t) \,, \\[2mm]
&q(x,0) =
\begin{cases}
p_i(x) & if \quad x < x_{i+\frac{1}{2}} \,, \\
p_{i+1}(x) & if \quad x > x_{i+\frac{1}{2}} \,,
\end{cases}
\end{aligned}
\right\}
\tag{3.118}
$$

where $p_i(x)$ and $p_{i+1}(x)$ are reconstruction polynomials of degree one on the left and right sides of the interface $x = x_{i+\frac{1}{2}}$. We transform the problem (3.118) to local coordinates via $\xi = x - x_{i+\frac{1}{2}}$ and $\tau = t - t^n$. Let $q_{LR}(\tau)$ be the time-dependent solution of the generalised Riemann problem (3.118) at the interface in local reference coordinates; we express $q_{LR}(\tau)$ via the first-order implicit Taylor series in time as

$$
q_{LR}(\tau) = q(0,0_+) + \tau \partial_t q(0,\tau) \,.
\tag{3.119}
$$

The time derivative is evaluated using Cauchy-Kowalewski functional $G^{(1)}$ which depends on the data and its spatial derivative, which from (3.115) is given as

$$
G^{(1)}\left(q(0,\tau), \partial_x q(0,\tau)\right) := -\lambda \partial_x q(0,\tau) + \beta q(0,\tau) \,.
\tag{3.120}
$$

Recall that $q(0,\tau)$ is the sought solution at the interface position. The term $\frac{\partial}{\partial x} q(0,\tau)$ is found as

$$
\left.
\begin{aligned}
\partial_x q(0,\tau) &= \partial_x q(0,0_+) + \tau \partial_x \left[\beta q(0,\tau) - \lambda \partial_x q(0,\tau)\right] \,, \\[2mm]
\partial_x q(0,\tau) &= \partial_x q(0,0_+) + \beta \tau \partial_x q(0,\tau) \,, \\[2mm]
\partial_x q(0,\tau) &= \frac{\partial_x q(0,0_+)}{1 - \tau \beta} \,.
\end{aligned}
\right\}
\tag{3.121}
$$

By replacing the first spatial derivative in (3.120) and solving the implicit Taylor series (3.119) for $q_{LR}(\tau)$ we obtain

$$
q_{LR}(\tau) = \frac{q(0,0_+) - \dfrac{\tau \lambda}{1 - \tau \beta} \partial_x q(0,0_+)}{1 - \tau \beta} \,.
\tag{3.122}
$$

The leading term $q(0, 0_+)$ is computed as the self-similar solution, at the interface, of the classical Riemann problem

$$
\left. \begin{aligned}
&\partial_t q(x,t) + \lambda \partial_x q(x,t) = 0 \;, \\[2mm]
q(x,0) = &\begin{cases}
p_i(x_{i+\frac{1}{2}}) \equiv q_i^n + \dfrac{\Delta x}{2}\Delta_i, & x < 0 \;, \\[4mm]
p_{i+1}(x_{i+\frac{1}{2}}) \equiv q_{i+1}^n - \dfrac{\Delta x}{2}\Delta_{i+1}, & x > 0 \;.
\end{cases}
\end{aligned} \right\}
\tag{3.123}
$$

Analogously, the spatial derivative $\partial_x q(0, 0_+)$ is computed as the self-similar solution, at the interface, of the classical Riemann problem

$$
\left. \begin{aligned}
&\partial_t \left(\partial_x q(x,t) \right) + \lambda \partial_x \left(\partial_x q(x,t) \right) = 0 \;, \\[2mm]
\partial_x q(x,0) = &\begin{cases}
\dfrac{d}{dx} p_i(x_{i+\frac{1}{2}}) \equiv \Delta_i, & x < 0 \;, \\[4mm]
\dfrac{d}{dx} p_{i+1}(x_{i+\frac{1}{2}}) \equiv \Delta_{i+1}, & x > 0 \;.
\end{cases}
\end{aligned} \right\}
\tag{3.124}
$$

3.5.2.6 Numerical flux and numerical source

For $\lambda > 0$ the solutions of the classical Riemann problems (3.123) and (3.124) at the interface are

$$
q(0, 0_+) = q_i^n + \tfrac{\Delta x}{2}\Delta_i \;, \qquad \partial_x q(0, 0_+) = \Delta_i \;.
\tag{3.125}
$$

The sought GRP solution at the interface is

$$
q_{LR}(\tau) = \frac{q_i^n + \dfrac{\Delta x}{2}\Delta_i - \dfrac{\tau \lambda}{1 - \Delta t \beta}\Delta_i}{1 - \beta \tau} \;.
\tag{3.126}
$$

We are now able to evaluate the numerical flux. For second-order accuracy it is enough to use the mid-point integration rule for which one integration point is needed. We obtain

$$
f_{i+\frac{1}{2}} = \lambda \left(\frac{q_i^n + \frac{\Delta x}{2}\Delta_i - \dfrac{\frac{\Delta t}{2}\lambda}{1 - \frac{\Delta t}{2}\beta}\Delta_i}{1 - \beta \frac{\Delta t}{2}} \right) \;.
\tag{3.127}
$$

To compute the numerical source term we use the same methodology, but now we solve an initial value problem inside the cell, consisting of the governing equation (3.115) and

the function $p_i(x)$ as initial condition. Following (3.82) we need to evaluate a space-time integral, for which we again use the mid-point rule in space and time. Then we only need the solution in time, to the initial value problem at x_i, which is expressed with a Taylor series analogous to (3.119), but with leading term $q(0, 0_+) = p_i(x_i)$ and $\partial_x q(0, 0_+) = \frac{d}{dx} p_i(x_i)$. Then the numerical source is

$$s_i = \beta \left(\frac{q_i^n - \frac{\frac{\Delta t}{2} \lambda}{1 - \frac{\Delta t}{2} \beta} \Delta_i}{1 - \beta \frac{\Delta t}{2}} \right). \tag{3.128}$$

The second-order, locally implicit ADER scheme for the model advection-reaction equation is now complete. The numerical flux and the numerical source are inserted into the finite volume formula (3.81) to march the solution in time.

3.5.3 Numerical experiments for model advection-reaction equation

Here we assess the methodology with two classical test problems with stiff source terms.

3.5.3.1 Convergence rates study

We consider equation (3.115) with flux $f(q) = \lambda q$, source $s(q) = \beta q$, domain $[0, 1]$, initial condition

$$q(x, 0) = \sin(2\pi x) \tag{3.129}$$

and periodic boundary conditions. Table 3.1 shows convergence rates for this test, for $\beta = -10$, $C_{cfl} = 0.9$, at the output time $t_{out} = 1$. As expected, second-order accuracy is achieved.

3.5.3.2 LeVeque and Yee Test

We apply the scheme to the challenging LeVeque-Yee test [90]. The flux is $f(q) = \lambda q$ and the source term has the expression $s(q) = \beta q(q-1)(q - \frac{1}{2})$, with $\beta \leq 0$, constant. The computational domain is $[0, 1]$ and boundary conditions are transmissive. The initial condition is

$$q(x, 0) = \begin{cases} 1 & \text{if} \quad x < 0.3 \,, \\ \\ 0 & \text{if} \quad x > 0.3 \,. \end{cases} \tag{3.130}$$

Theoretical order : 2

Mesh	L_∞ - err	L_∞ - ord	L_1 - err	L_1 - ord	L_2 - err	L_2 - ord
32	$2.46e-05$	3.95	$9.43e-06$	3.53	$1.11e-05$	3.85
64	$2.59e-06$	3.25	$1.77e-06$	2.42	$1.83e-06$	2.61
128	$5.47e-07$	2.24	$4.06e-07$	2.12	$4.22e-07$	2.11
256	$1.45e-07$	1.92	$9.93e-08$	2.03	$1.04e-07$	2.02
512	$4.90e-08$	1.56	$2.47e-08$	2.01	$2.62e-08$	2.00

TABLE 3.1: Empirical convergence rates for linear advection-reaction equation at output time $t_{out} = 1$, with $\beta = -10$ and CFL number $C_{cfl} = 0.9$. Second-order accuracy is attained.
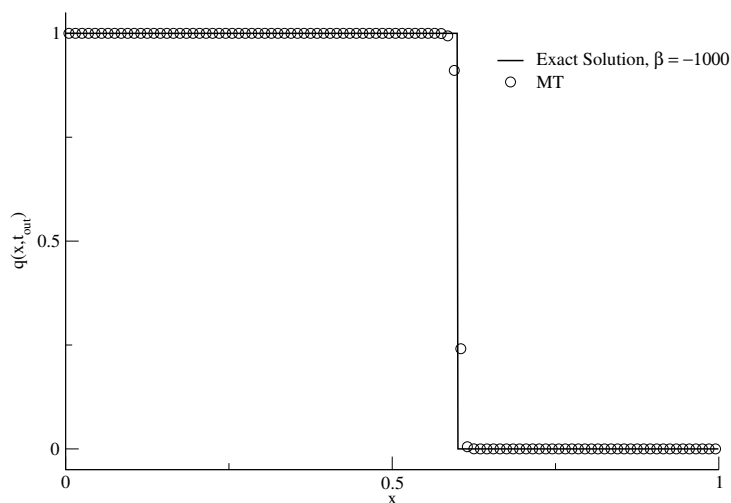
FIGURE 3.1: LeVeque-Yee Test. Numerical solution (symbols) compared against the exact solution (line) at the output time $t_{out} = 0.3$, for $\beta = -1000$. Computational parameters are: $M = 100$ cells and CFL number $C_{cfl} = 0.5$.

Figure 3.1 shows a comparison between exact (line) and numerical (symbols) solutions at time $t_{out} = 0.3$, for $\beta = -1000$, $M = 100$ cells and $C_{cfl} = 0.5$.

We remark that ADER-type schemes with conventional GRP solvers using explicit Taylor series expansions are unable to capture the correct solution, with the correct wave speed. In the next section we apply the proposed methodology to solve the compressible Navier-Stokes equations via two relaxation approaches, leading to stiff balance laws.

3.6 Application to the Compressible Navier-Stokes Equations

Here we implement the new MT solver in the HEOC framework, in which only one classical non-linear Riemann problem is solved at the cell interface but two implicit Taylor

expansions are required, one on each side of the interface. The other possibility is to use the solver MT in the Titarev-Toro framework (TT). For this one would need to solve one classical non-linear Riemann problem for the leading term and one linear, classical Riemann problem for the spatial derivative. If the eigenstructure of the equations were known, then an exact or approximate classical Riemann solver could be used to find the state $\mathbf{Q}(0, 0_+)$. See [147] and references therein. However, for the reformulated Navier-Stokes equations we do not know the complete eigenstructure and it is a pending, formidable task to find a state-Riemann solver. It is easier to find an approximate flux Riemann solver and this is why the MT-HEOC formulation is more attractive. Here we use the Dumbser-Osher-Toro (DOT) Riemann solver, [47] and the complete eigenstructure is computed numerically. See [104] for recent developments and a novel application to haemodynamics. Next, we briefly describe the DOT solver to evaluate the numerical flux in the finite volume formula (3.81) associated to (3.11).

3.6.1   Dumbser-Osher-Toro (DOT) Riemann solver: Numerical flux

Let $\mathbf{J}(\mathbf{W})$ be the Jacobian matrix of $\mathbf{H}(\mathbf{W})$ with respect to $\mathbf{W}$ in (3.11); let $\lambda_i(\mathbf{W})$ be the $i-th$ eigenvalue of $\mathbf{J}(\mathbf{W})$ and let $\mathbf{\Lambda}(\mathbf{W})$ be the diagonal matrix formed by all eigenvalues $\lambda_i(\mathbf{W})$. Then we denote by $\mathbf{R}(\mathbf{W})$ the matrix formed by the right eigenvectors of $\mathbf{J}(\mathbf{W})$ and define

$$\lambda_i(\mathbf{W})^+ = max\{\lambda_i(\mathbf{W}), 0\} \quad , \quad \lambda_i(\mathbf{W})^- = min\{\lambda_i(\mathbf{W}), 0\} . \tag{3.131}$$

Let $\mathbf{\Lambda}(\mathbf{W})^+$ be the diagonal matrix formed by $\lambda_i(\mathbf{W})^+$ and let $\mathbf{\Lambda}(\mathbf{W})^-$ be the diagonal matrix formed by $\lambda_i(\mathbf{W})^-$. Then we define the matrices $|\mathbf{\Lambda}|$ and $|\mathbf{J}|$ by

$$|\mathbf{\Lambda}(\mathbf{W})| = \mathbf{\Lambda}(\mathbf{W})^+ - \mathbf{\Lambda}(\mathbf{W})^- \tag{3.132}$$

and

$$|\mathbf{J}(\mathbf{W})| = \mathbf{R}(\mathbf{W})|\mathbf{\Lambda}(\mathbf{W})|\mathbf{R}(\mathbf{W})^{-1} . \tag{3.133}$$

Let us consider the interface $x_{i+\frac{1}{2}}$ where data on the left is denoted by $\mathbf{W}_L$ and that on the right is denoted by $\mathbf{W}_R$. Then the numerical flux at the interface is

$$\mathbf{H}_{i+\frac{1}{2}} = \tfrac{1}{2} \left(\mathbf{H}(\mathbf{W}_L) + \mathbf{H}(\mathbf{W}_R) \right) - \tfrac{1}{2} \left(\int_0^1 |\mathbf{J}(\mathbf{\Phi}(s))|ds \right) (\mathbf{W}_R - \mathbf{W}_L) . \tag{3.134}$$

By evaluating the integral numerically using a Gaussian quadrature of n_G points, with weights $\{\omega_j, s_j\}$, the numerical flux is

$$\mathbf{H}_{i+\frac{1}{2}} = \tfrac{1}{2}\left(\mathbf{H}(\mathbf{W}_L) + \mathbf{H}(\mathbf{W}_R)\right) - \tfrac{1}{2}\left(\sum_{j=1}^{n_G} \omega_j |\mathbf{J}(\mathbf{\Phi}(s_j))|\right)(\mathbf{W}_R - \mathbf{W}_L), \quad (3.135)$$

with the linear path defined as

$$\mathbf{\Phi}(s) = \mathbf{W}_L + s\left(\mathbf{W}_R - \mathbf{W}_L\right). \qquad (3.136)$$

We have used three Gaussian points to evaluate integrals. The time step Δt at time t^n is computed as

$$\Delta t = C_{cfl}\frac{\Delta x}{\lambda_{max}}, \qquad (3.137)$$

where

$$\lambda_{max} = max_{i=1,\dots,M}\left\{max_{j=1,\dots,m}\left\{|\lambda_j(\mathbf{W_i^n})|\right\}\right\}.$$

3.6.2   Convergence rates study

We assess empirically, the convergence rates of the present scheme as applied to the compressible Navier-Stokes equations. Following [37] we define the function

$$\tilde{\mathbf{Q}}(x,t) = \begin{bmatrix} \bar{\rho} + \rho_0 cos(kx - \omega t) \\ \bar{u} + u_0 sin(kx - \omega t) \\ \bar{p} + p_0 sin(kx - \omega t) \end{bmatrix} \qquad (3.138)$$

which we then introduce into the governing equations, resulting in the modified system

$$\partial_t\mathbf{Q} + \partial_x\mathbf{F}(\mathbf{Q}) = \partial_x\mathbf{G}(\mathbf{Q},\partial_x\mathbf{Q}) + \tilde{\mathbf{S}}(x,t). \qquad (3.139)$$

Here the source term $\tilde{\mathbf{S}}(x,t)$, which depends only on x and t, can be computed explicitly. We take $k = 2\pi/L$, $L = 2$, $\omega = 2\pi$, $\bar{\rho} = 1$, $\bar{p} = \bar{\rho}/\gamma$, $\bar{u} = 0$, $\rho_0 = p_0 = 1/2$ and $v_0 = 1/4$. In the numerical experiments we take $C_{CFL} = 0.7$, $\varepsilon = 10^{-4}$ and output time is $t_{out} = 0.5$. Periodic boundary conditions are applied.

Comparison of the canonical relaxation formulation and ad the hoc relaxation formulation against the exact solution (3.138) is shown in Figure 3.2 for density and pressure. Numerical results were obtained with $M = 128$ cells. Excellent agreement is observed.

Empirical convergence rates are depicted in table 3.2 for the ad hoc relaxation formulation, for the velocity, while Table 3.3 shows empirical convergence rates for the canonical

relaxation formulation, again for velocity. Second-order of accuracy is attained with both approaches. Note that for the value of ε used here, the associated hyperbolic relaxation problem is stiff. Thus conventional, explicit GRP solvers introduced in section 3.4 are unsuitable to solve this problem. This highlights the importance of the local, implicit formulation of the GRP solver presented in this chapter.

Theoretical order : 2

Mesh	L_∞ - err	L_∞- ord	L_1 - err	L_1 - ord	L_2 - err	L_2 - ord
16	$1.52e-01$	-	$1.86e-01$	-	$1.44e-01$	-
32	$6.90e-02$	1.14	$8.35e-02$	1.15	$6.33e-02$	1.19
64	$2.11e-02$	1.71	$2.29e-02$	1.87	$1.77e-02$	1.84
128	$5.55e-03$	1.93	$5.26e-03$	2.12	$4.44e-03$	2.00

TABLE 3.2: Compressible Navier-Stokes equations. Empirical convergence rates for the *Ad Hoc Relaxation Formulation*. Parameters are: $\varepsilon = 10^{-4}$, $\mu = 3/40Pa/s$, output time $t_{out} = 0.5s$ and $C_{cfl} = 0.7$. Second-order accuracy is attained.

Theoretical order : 2

Mesh	L_∞ - err	L_∞- ord	L_1 - err	L_1 - ord	L_2 - err	L_2 - ord
16	$1.53e-01$	-	$1.86e-01$	-	$1.45e-01$	-
32	$6.92e-02$	1.14	$8.38e-02$	1.15	$6.35e-02$	1.19
64	$2.12e-02$	1.71	$2.29e-02$	1.87	$1.77e-02$	1.84
128	$5.59e-03$	1.92	$5.26e-03$	2.12	$4.44e-03$	2.00

TABLE 3.3: Compressible Navier-Stokes equations. Empirical convergence rates for the *Canonical Relaxation Formulation*. Parameters are: $\varepsilon = 10^{-4}$, $\mu = 3/40Pa/s$, output time $t_{out} = 0.5s$ and $C_{cfl} = 0.7$. Second-order accuracy is attained.

3.6.3 Shock-tube problem

Here we assess the hyperbolic formulations and the numerical schemes presented in this chapter for a problem with discontinuous initial conditions so that the solution includes a shock wave, a contact surface and a rarefaction wave. The computational domain is $[-1, 1]$, with the initial discontinuity at $x = 0$. To the left of $x = 0$ the initial condition is: density $\rho_L = 1.29Kg/m^3$, velocity $u_L = 0m/s$, pressure $p_L = 2929.73Pa$. To the right of $x = 0$ the initial condition is: $\rho_R = 1.784Kg/m^3$, velocity $u_R = 0m/s$, pressure $p_R = 4349.31Pa$. See [89] for details about the range of physical parameters for gases. Here we simulate three cases with different viscosities. We show results for both relaxation formulations, the canonical and the ad hoc, and compare numerical results
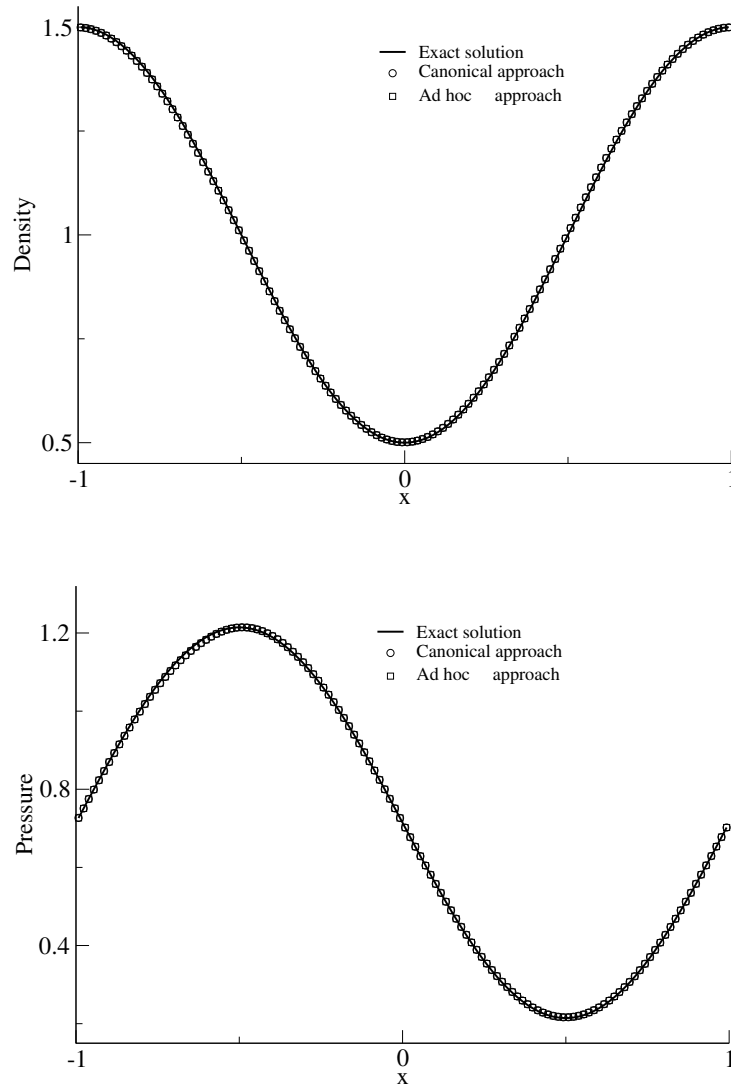
FIGURE 3.2: Compressible Navier-Stokes equations. Comparison between the exact (line) and numerical solutions using the *Canonical Formulation* (circles) and the *Ad Hoc Formulation* (squares). Parameters are: $\varepsilon = 10^{-4}$, $M = 128$ cells, $\mu = 3/40$, output time $t_{out} = 0.5$ and $C_{CFL} = 0.7$.

against a reference solution obtained numerically by solving (3.1), (3.35) with a splitting method, on a very fine mesh of $M = 10000$ cells.

Figure 3.3 depicts results for $\mu = 2Pa/s$, figure 3.4 shows the results for $\mu = 0.2Pa/s$ and figure 3.5 shows the results for $\mu = 0.001Pa/s$. In all simulations we took as output time $t_{out} = 0.02$, $M = 100$ cells, $C_{cfl} = 0.7$ and $\varepsilon = 10^{-4}$.

We have assessed our second-order method as applied to both hyperbolic relaxation formulations for the compressible Navier-Stokes equations. Results are very satisfactory.
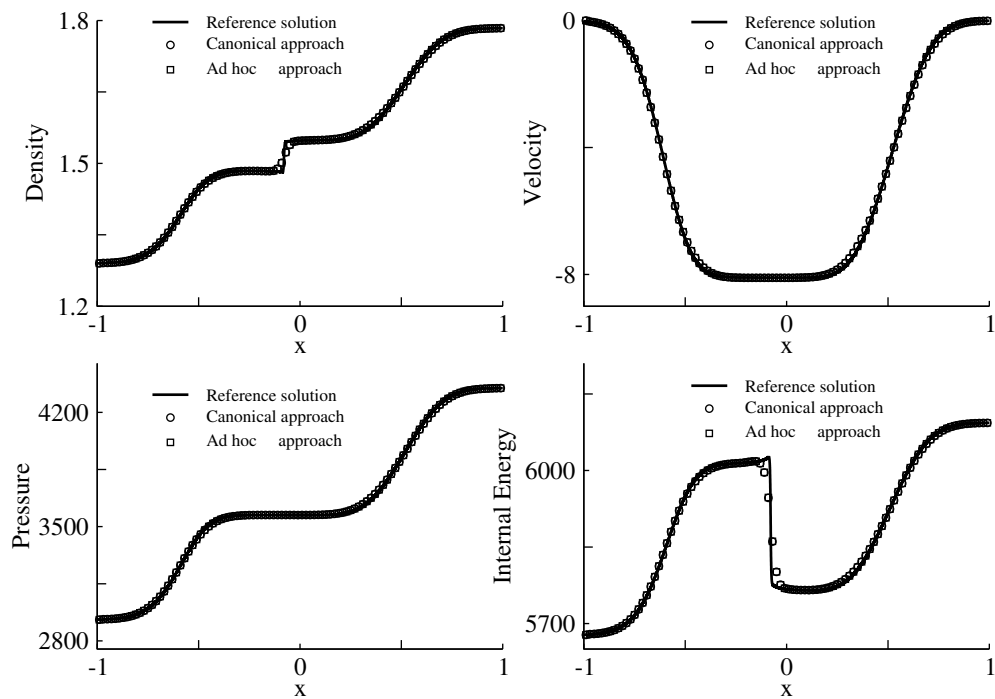
FIGURE 3.3: Compressible Navier-Stokes equations for $\mu = 2Pa/s$. Numerical (symbols) and reference (line) solutions at output time $t_{out} = 0.01s$, for $\varepsilon = 10^{-4}$, $M = 100$ cells and $C_{cfl} = 0.7$. *Canonical Relaxation Formulation* (circles) and *Ad Hoc Relaxation Formulation* (squares).
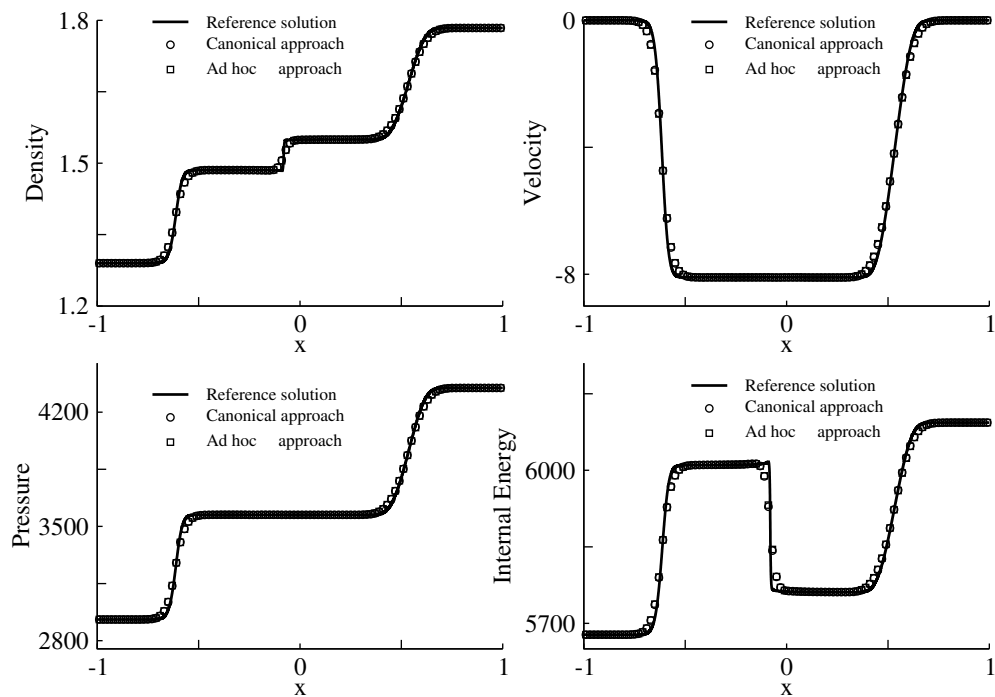
FIGURE 3.4: Compressible Navier-Stokes equations for $\mu = 0.2Pa/s$. Numerical (symbols) and reference (line) solutions at output time $t_{out} = 0.01s$, for $\varepsilon = 10^{-4}$, $M = 100$ cells and $C_{cfl} = 0.7$. *Canonical Relaxation Formulation* (circles) and *Ad Hoc Relaxation Formulation* (squares).
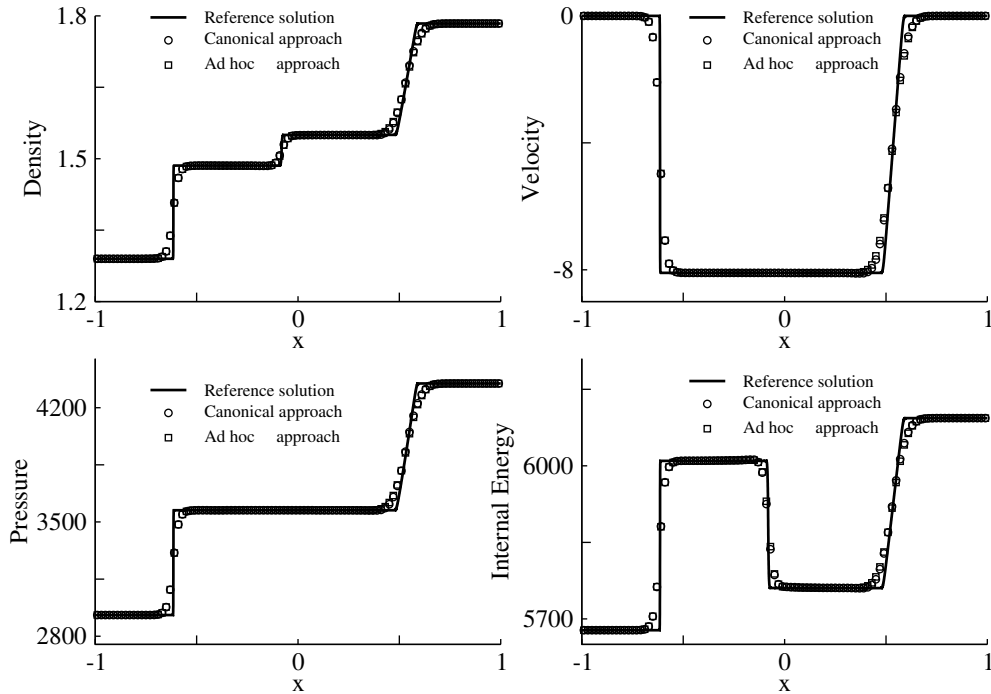
FIGURE 3.5: Compressible Navier-Stokes equations for $\mu = 0.001 Pa$. Numerical (symbols) and reference (line) solutions at output time $t_{out} = 0.01s$, for $\varepsilon = 10^{-4}$, $M = 100$ cells and $C_{cfl} = 0.7$. *Canonical Relaxation Formulation* (circles) and *Ad Hoc Relaxation Formulation* (squares).

3.7   Conclusions

In this chapter we have introduced and systematically assessed two approaches to solve advection-diffusion-reaction equations, the canonical relaxation and the ad hoc relaxation formulations. Such formulations convert advection-diffusion-reaction equations into hyperbolic systems with stiff source terms. The ad hoc relaxation formulation needs less variables than the canonical approach and depends on the specific problem. We have derived theoretical results which ensure real eigenvalues for both types of relaxation systems. In addition, we have proposed a new methodology for solving the generalised Riemann problem based on an implicit Taylor expansion and the Cauchy-Kowalewski procedure. Using this locally implicit GRP solver in the ADER approach, one is able to solve hyperbolic equations with stiff source terms. To illustrate the complete methodology we have solved the compressible Navier-Stokes equations. In this chapter we have restricted the presentation of the methodology to second order accuracy, but in principle, the approach can be generalised to any order of accuracy, in both space and time. Future work will include extensions of the relaxation approaches to multidimensional problems on unstructured meshes.

Chapter 4

Hyperbolic reformulation of a 1D viscoelastic blood flow model and ADER finite volume schemes

4.1 Introduction

The validity of one-dimensional blood flow models for reproducing pressure and flow rate waveforms in the cardiovascular system has been confirmed in multiple ways. It has been shown that these models well reproduce pressure and flow rate waves obtained using three-dimensional computational models in real vascular geometries using both, rigid boundaries, see Grinberg *et al.* [60] and fully three-dimensional Fluid-Structure-Interaction (FSI) models, see Xiao *et al.* [163]. One-dimensional blood flow models have also shown to reproduce measured pressure and flow rate wave patterns in animal arteries Steele *et al.* [139], human arteries Reymond *et al* [125] and human veins Müeller and Toro [105]. Moreover, these models have been used to study a variety of pathological conditions, like the assessment of variations and occlusions of the Circle of Willis, see Alastruey *et al.* [3] or the study of the influence of aortic valve stenosis in systemic circulation, see Liang *et al.* [92]. Another relevant application of one-dimensional models is to provide boundary conditions for three-dimensional FSI models, see Blanco *et al.* [15].

In this chapter we solve a time-dependent, one-dimensional system that is a model for blood flow in vessels with walls having viscoelastic properties. First, we reformulate the original Advection-Diffusion-Reaction Partial Differential Equations (adrPDE) problem via a relaxation technique introduced by Cattaneo [24, 25], obtaining a hyperbolic system

with stiff source terms. Then, we solve the resulting system using appropriate high-order accurate numerical methods.

Cattaneo [24] and Vernotte [160] are credited for having introduced a relaxation technique for the heat equation, as a strategy for resolving the paradox of instantaneous wave propagation. See also Nagy et al. [107]. The relaxation approach consists of augmenting the Fourier law with a transient term involving a relaxation time, a parameter, which recovers the original Fourier law for small relaxation times. Even though this relaxation technique was originally developed to avoid a non-physical description of instantaneous heat propagation, it is also appropriate for the construction of numerical schemes that transform adrPDE into hyperbolic systems which may be stiff for small relaxation parameters.

Relaxation in the sense of Cattaneo has been applied to solve adrPDEs, see for example Gómez and collaborators [57, 58], where two-dimensional implementations have been carried out for linear problems in the frame of finite element methods. Nishikawa and Roe [114, 115] and subsequently Nishikawa [112, 113] have implemented this approach in the frame of residual distribution schemes to find steady state solutions to parabolic partial differential equations.

We remark that there exist other relaxation approaches, as for example the one due to Jin *et al.* [76], which is an extension of the relaxation strategy presented by Jin and Xin [77], initially proposed to cast non-linear hyperbolic problems into linear hyperbolic systems with stiff source terms. However, this form of relaxation imposes a sub-characteristic condition for the derived hyperbolic systems and spurious oscillations appear when this condition is not ensured [1]. This relaxation approach also requires the sub-characteristic condition when applied to adrPDEs, requiring small relaxation parameters. Furthermore, the relaxation parameter for the adrPDE case is present in the advective components. Therefore, stability depends on the relaxation. In the context of implicit-explicit methods [17, 18, 118], the influence of these parameters on the stability has been reduced by introducing an artificial viscosity. However, the accuracy of these methods is reached in the parabolic limit of the adrPDEs, *i.e.* for very small relaxation parameters.

Here we make use of Cattaneo's relaxation technique because; i) avoids the sub-characteristic condition [76, 77] and therefore allows a large enough relaxation parameter suitable for numerical implementations; ii) allows selective relaxation of specific terms, in order to remove second order derivatives present in the original model requiring only minor changes in the mathematical formulation of the problem, maintaining the physical meaning of the

relaxed model and allowing for larger relaxation parameters in comparison to alternative approaches; iii) allows to compute accurate and efficient solutions by implementing numerical schemes able to handle stiff source terms.

The hyperbolic system obtained by relaxation of the original adrPDE system contains a stiff source term. The numerical methods implemented here make use of the methodology presented by Müller and Toro [104], which proposes high-order ADER (**A**rbitrary Accuracy **DER**ivative Riemann problem) schemes for one-dimensional blood flow models, which reconcile source term stiffness, well-balanced properties, accuracy and stability. The ADER approach was put forward by Toro *et al.* [150] for linear problems on Cartesian meshes. Nowadays ADER schemes can be implemented in both the finite volume and discontinuous Galerkin finite element frameworks. ADER schemes are arbitrarily accurate in both space and time and are applicable to general geometries in multiple space dimensions. ADER schemes have recently been implemented to solve one-dimensional blood flow models for elastic vessels with varying geometrical and mechanical properties [103, 104] in the context of non-conservative hyperbolic systems. Moreover, ADER schemes have been applied to adrPDEs. Titarev and Toro [145] extended the ADER methodology in a straightforward fashion to solve the model advection-diffusion equation. See also Toro and Hidalgo [148] and Hidalgo *et al.* [68] for applications of ADER to pure diffusion equations. ADER was applied to the compressible Navier-Stokes equations by Dumbser [37] and by Hidalgo and Dumbser in [67]. A disadvantage of the approach used in the above cited works is the time stability constraint that scales with Δx^2, instead of the classical scaling of ADER schemes for hyperbolic problems, which is Δx. In this chapter we relax this restriction exploiting the fact that ADER schemes can efficiently treat stiff source terms and are thus an excellent candidate to solve adrPDEs using the hyperbolisation approach. For an introduction to ADER schemes and a review of the literature see chapters 19 and 20 of [147].

This chapter is organised as follows. The governing equations, the relaxation procedure and the blood flow model and its hyperbolic reformulation are presented in section 4.2. In section 4.3 we briefly introduce the concepts of the ADER approach and the numerical methodology used in this chapter. In section 4.4 we provide numerical evidence that confirms the proposed criterion (Proposition 2.3) to choice the relaxation parameter ε. In section 4.5 we validate the proposed methodology by comparing our numerical results with experimental measurements and numerical results reported in the literature for one-dimensional blood flow in a network of viscoelastic vessels. Conclusions and remarks are drawn in section 5.7.

4.2 Governing equations

We consider non-linear advection-diffusion-reaction equations written in the form

$$\partial_t \mathbf{Q} + \mathbf{A}(\mathbf{Q})\partial_x \mathbf{Q} = \partial_x \mathbf{G}(\mathbf{Q}, \partial_x \mathbf{Q}) + \mathbf{S}(\mathbf{Q}) \, . \tag{4.1}$$

Here, $\mathbf{Q} \in \mathbb{R}^m$ is the vector of unknowns; $\mathbf{A}(\mathbf{Q})$ is a matrix; $\mathbf{G}(\mathbf{Q}, \partial_x \mathbf{Q})$ represents the viscous flux and $\mathbf{S}(\mathbf{Q})$ is the reaction term, a function of the unknown.

We introduce the following matrices

$$\mathbf{B}(\mathbf{Q}, \partial_x \mathbf{Q}) = \frac{\partial \mathbf{G}(\mathbf{Q}, \partial_x \mathbf{Q})}{\partial \mathbf{Q}} \, , \quad \mathbf{D}(\mathbf{Q}, \partial_x \mathbf{Q}) = \frac{\partial \mathbf{G}(\mathbf{Q}, \partial_x \mathbf{Q})}{\partial (\partial_x \mathbf{Q})} \, . \tag{4.2}$$

With these definitions we can write the governing equations as

$$\partial_t \mathbf{Q} + \Big(\mathbf{A}(\mathbf{Q}) - \mathbf{B}(\mathbf{Q}, \partial_x \mathbf{Q}) \Big) \partial_x \mathbf{Q} = \mathbf{D}(\mathbf{Q}, \partial_x \mathbf{Q}) \partial_x^{(2)} \mathbf{Q} + \mathbf{S}(\mathbf{Q}) \, . \tag{4.3}$$

4.2.1 General formulation

We will relax system (4.3) by following the constitutive Cattaneo's law [24],

$$\partial_t \mathbf{U} - \tfrac{1}{\varepsilon} \partial_x \mathbf{Q} = -\tfrac{1}{\varepsilon} \mathbf{U} \, , \tag{4.4}$$

where $\varepsilon > 0$ is a parameter. In practice, the strategy introduces the new variable $\mathbf{U}$ instead of gradients $\partial_x \mathbf{Q}$ for selected terms of the original adrPDEs. The evolution equation (4.4) for these new variables gives an asymptotic behaviour toward the original gradient. This allows to write (4.3) as

$$\partial_t \mathbf{Q} + \Big(\mathbf{A}(\mathbf{Q}) - \mathbf{B}(\mathbf{Q}, \mathbf{U}) \Big) \partial_x \mathbf{Q} = \mathbf{D}(\mathbf{Q}, \mathbf{U}) \partial_x \mathbf{U} + \mathbf{S}(\mathbf{Q}) \, . \tag{4.5}$$

We only consider components of $\mathbf{U}$ as the non-zero components i of $\partial_x \mathbf{Q}$ such that the i-th column of $\mathbf{D}$ in (4.2) is not null. If we consider $n \leq m$ columns of $\mathbf{D}$ to be not null then, we can consider $\mathbf{U} \in \mathbb{R}^n$ and

$$\begin{aligned} \partial_t \mathbf{Q} + \Big(\mathbf{A}(\mathbf{Q}) - \mathbf{B}(\mathbf{Q}, \mathbf{U}) \Big) \partial_x \mathbf{Q} &= \mathbf{D}(\mathbf{Q}, \mathbf{U}) \partial_x \mathbf{U} + \mathbf{S}(\mathbf{Q}) \, . \\ \partial_t \mathbf{U} - \tfrac{1}{\varepsilon} \partial_x \mathbf{Q} &= -\tfrac{1}{\varepsilon} \mathbf{U} \, . \end{aligned} \tag{4.6}$$

System (4.6) written in a semilinear form gives

$$\partial_t \mathbf{W} + \mathbf{J}(\mathbf{Q}) \partial_x \mathbf{W} = \mathbf{L}(\mathbf{W}) \, , \tag{4.7}$$

where

$$\mathbf{W} = \begin{bmatrix} \mathbf{Q} \\ \mathbf{U} \end{bmatrix} , \quad \mathbf{J}(\mathbf{W}) = \begin{bmatrix} \mathbf{A} - \mathbf{B} & -\bar{\mathbf{D}} \\ -\frac{1}{\varepsilon}\mathbf{I} & \mathbf{0} \end{bmatrix} , \quad \mathbf{L}(\mathbf{W}) = \begin{bmatrix} \mathbf{S}(\mathbf{Q}) \\ -\frac{1}{\varepsilon}\mathbf{U} \end{bmatrix} , \tag{4.8}$$

with matrix $\bar{\mathbf{D}} \in \mathbb{R}^{m \times n}$ containing only the n not null column vectors of $\mathbf{D}$, $\mathbf{I}$ is the identity matrix in $\mathbb{R}^{n \times n}$ and $\mathbf{0}$ is the null matrix in $\mathbb{R}^{n \times m}$.

4.2.2 One-dimensional blood flow model for viscoelastic vessels

Let us consider well-known equations that describe one-dimensional blood flow as in [104]

$$\left. \begin{aligned} \partial_t A(x,t) + \partial_x q(x,t) &= 0 , \\ \partial_t q(x,t) + \partial_x \left(\hat{\alpha} \frac{q(x,t)^2}{A(x,t)} \right) + \frac{A(x,t)}{\rho} \partial_x p(x,t) &= f(x,t) , \end{aligned} \right\} \tag{4.9}$$

where x is the axial coordinate along the vessel, t is time, $A(x,t)$ is the cross-sectional area, $q(x,t)$ is the flow rate, $\hat{\alpha} \equiv 1$, which indicates a blunt velocity profile, ρ is the fluid density, assumed as a constant, $p(x,t)$ is the average internal pressure and $f(x,t)$ is the friction force per unit length, given by

$$f(x,t) = -\gamma \pi \nu \frac{q}{A} , \tag{4.10}$$

where ν is the kinematic viscosity. Here, we take $\gamma = 22$, as specified in [2].

To close system (4.9) we introduce an additional equation known as tube law

$$p = p_e + \psi(A, A_0, K) + \varphi(A, A_0)\partial_t A , \tag{4.11}$$

where $p_e(x,t)$ is the external pressure and ψ is the transmural pressure given by

$$\psi(A(x,t), A_0(x), K(x)) = K(x)\phi(A(x,t), A_0(x)),$$

with

$$\phi(A(x,t), A_0(x)) = \left(\left(\frac{A(x,t)}{A_0(x)} \right)^m - \left(\frac{A(x,t)}{A_0(x)} \right)^n \right) . \tag{4.12}$$

$A_0(x)$ is the cross-sectional area at equilibrium, $K(x)$ is a positive function which depends on the Young modulus, the wall thickness and A_0, with $m > 0$ and $n \in (-2, 0]$. See [19] for details.

Moreover, the viscoelastic term $\varphi(A, A_0)\partial_t A$, taken as in [2], is

$$\varphi(A, A_0) = \frac{\Gamma}{A_0\sqrt{A}} \, , \tag{4.13}$$

where Γ is a constant related to the viscoelastic properties of the vessel wall.

From the governing equations we obtain $\partial_t A = -\partial_x q$, allowing us to write

$$p = p_e + \psi(A, A_0, K) - \varphi(A, A_0)\partial_x q \, . \tag{4.14}$$

The pressure gradient is thus

$$
\begin{aligned}
\partial_x p \;=\; & [1]\,\partial_x p_e + [\phi]\,\partial_x K + [K(\partial_A \phi) - (\partial_A \varphi)(\partial_x q)]\,\partial_x A \\
& + [K(\partial_{A_0}\phi) - (\partial_{A_0}\varphi)(\partial_x q)]\,\partial_x A_0 - [\varphi]\,\partial_x^{(2)} q \, .
\end{aligned}
\tag{4.15}
$$

4.2.3 Hyperbolic reformulation of the equations

Following Toro and Siviglia [152], we write system (4.9) with viscoelastic tube law (4.11) as

$$
\left.
\begin{aligned}
\partial_t A(x,t) + \partial_x q(x,t) \;&=\; 0 \, , \\[2mm]
\partial_t q(x,t) + \partial_x\left(\hat\alpha \frac{q(x,t)^2}{A(x,t)}\right) \;&=\; -\left[\tfrac{A}{\rho}\right]\partial_x p_e - \left[\tfrac{A}{\rho}\phi\right]\partial_x K \\
& \quad -\tfrac{A}{\rho}\left[K(\partial_A\phi) - (\partial_A\varphi)(\partial_x q)\right]\partial_x A \\
& \quad -\tfrac{A}{\rho}\left[K(\partial_{A_0}\phi) - (\partial_{A_0}\varphi)(\partial_x q)\right]\partial_x A_0 \\
& \quad +\tfrac{A}{\rho}\left[\varphi\right]\partial_x^{(2)} q + f \, , \\
\partial_t K \;&=\; 0 \, , \\
\partial_t A_0 \;&=\; 0 \, , \\
\partial_t p_e \;&=\; 0 \, ,
\end{aligned}
\right\}
\tag{4.16}
$$

which can be written as (4.1) with the following definitions

$$
\left.\begin{aligned}
\mathbf{Q} &= \begin{bmatrix} A & q & K & A_0 & p_e \end{bmatrix}^T , \\[2mm]
\mathbf{A} &= \begin{bmatrix}
0 & 1 & 0 & 0 & 0 \\
c^2 - u^2 + \frac{\varphi \partial_x q}{2\rho} & 2u & \frac{A}{\rho}\phi & \frac{A}{A_0}\left(\frac{\varphi \partial_x q}{\rho} - c^2\right) & \frac{A}{\rho} \\
0 & 0 & 0 & 0 & 0 \\
0 & 0 & 0 & 0 & 0 \\
0 & 0 & 0 & 0 & 0
\end{bmatrix} , \\[2mm]
\mathbf{S} &= \begin{bmatrix} 0 & f & 0 & 0 & 0 \end{bmatrix}^T , \\[2mm]
\partial_x \mathbf{G}(\mathbf{Q}, \partial_x \mathbf{Q}) &= \begin{bmatrix} 0 & \frac{\varphi A}{\rho}\partial_x^{(2)} q & 0 & 0 & 0 \end{bmatrix}^T .
\end{aligned}\right\} \tag{4.17}
$$

We introduce a new variable Ψ and a relaxation parameter $\varepsilon > 0$ such that

$$
\Psi \to \partial_x q , \quad \varepsilon \to 0 . \tag{4.18}
$$

In addition, we mimic the Cattaneo's law [24] with an evolution equation for Ψ given by

$$
\partial_t \Psi = \frac{1}{\varepsilon}\left(\partial_x q - \Psi\right) . \tag{4.19}
$$

Therefore, we can reformulate system (4.16) as

$$
\left.\begin{aligned}
\partial_t A(x,t) + \partial_x q(x,t) &= 0 , \\[2mm]
\partial_t q(x,t) + \partial_x\left(\hat{\alpha}\frac{q(x,t)^2}{A(x,t)}\right) &= -\left[\frac{A}{\rho}\right]\partial_x p_e - \left[\frac{A}{\rho}\phi\right]\partial_x K \\
&\quad -\frac{A}{\rho}\left[K(\partial_A \phi) - (\partial_A \varphi)\Psi\right]\partial_x A \\
&\quad -\frac{A}{\rho}\left[K(\partial_{A_0}\phi) - (\partial_{A_0}\varphi)\Psi\right]\partial_x A_0 \\
&\quad -\frac{A}{\rho}\left[\varphi\right]\partial_x \Psi + f , \\[2mm]
\partial_t K &= 0 , \\[2mm]
\partial_t A_0 &= 0 , \\[2mm]
\partial_t p_e &= 0 , \\[2mm]
\partial_t \Psi + \frac{-1}{\varepsilon}\partial_x q &= -\frac{1}{\varepsilon}\Psi ,
\end{aligned}\right\} \tag{4.20}
$$

which can be written in quasi-linear form (4.7) with

$$
\mathbf{W} = \begin{bmatrix} A & q & K & A_0 & p_e & \Psi \end{bmatrix}^T ,
$$

$$
\mathbf{J} = \begin{bmatrix}
0 & 1 & 0 & 0 & 0 & 0 \\
c^2 - u^2 + \frac{a_\Gamma}{2} & 2u & \frac{A}{\rho}\phi & \frac{A}{A_0}\left(a_\Gamma - c^2\right) & \frac{A}{\rho} & -\frac{A}{\rho}\varphi \\
0 & 0 & 0 & 0 & 0 & 0 \\
0 & 0 & 0 & 0 & 0 & 0 \\
0 & 0 & 0 & 0 & 0 & 0 \\
0 & -\frac{1}{\varepsilon} & 0 & 0 & 0 & 0
\end{bmatrix} ,
$$

$$
\mathbf{L} = \begin{bmatrix} 0 & f & 0 & 0 & 0 & -\frac{1}{\varepsilon}\Psi \end{bmatrix}^T ,
$$

(4.21)

where

$$
c^2 = \frac{A}{\rho} K \partial_A \phi , \quad u = \frac{q}{A} , \quad a_\Gamma = \frac{\varphi \Psi}{\rho} .
$$

(4.22)

4.2.4 Eigenstructure

In this section we study the eigenstructure for the first order system (4.7) with Jacobian (4.21).

Proposition 4.1. *System (4.7) with Jacobian (4.21) is hyperbolic provided that*

$$
\varepsilon^{-1} \geq -\frac{\Psi}{2A} - \frac{\rho c^2}{\varphi A} ,
$$

(4.23)

with eigenvalues

$$
\lambda_1 = u - \tilde{c} , \quad \lambda_2 = \lambda_3 = \lambda_4 = \lambda_5 = 0 , \quad \lambda_6 = u + \tilde{c},
$$

(4.24)

where

$$
\tilde{c} = \sqrt{c^2 + \omega} , \quad \omega = \frac{\varphi A}{\rho \varepsilon} + \frac{a_\Gamma}{2}
$$

(4.25)

and linear independent eigenvectors

$$
\mathbf{v}_1 = \begin{bmatrix} 1 \\ u - \tilde{c} \\ 0 \\ 0 \\ 0 \\ -\frac{1}{\varepsilon} \end{bmatrix} , \quad
\mathbf{v}_6 = \begin{bmatrix} 1 \\ u + \tilde{c} \\ 0 \\ 0 \\ 0 \\ -\frac{1}{\varepsilon} \end{bmatrix} , \quad
\mathbf{v}_2 = \begin{bmatrix} 1 \\ 0 \\ 0 \\ 0 \\ 0 \\ \frac{(c^2 + a_\Gamma/2) - u^2}{\varphi A} \rho \end{bmatrix} ,
$$

$$
\mathbf{v}_3 = \begin{bmatrix} 0 \\ 0 \\ 1 \\ 0 \\ 0 \\ \frac{\phi}{\varphi} \end{bmatrix} , \quad
\mathbf{v}_4 = \begin{bmatrix} 0 \\ 0 \\ 0 \\ 1 \\ 0 \\ \frac{(a_\Gamma - c^2)}{\varphi A_0} \rho \end{bmatrix} , \quad
\mathbf{v}_5 = \begin{bmatrix} 0 \\ 0 \\ 0 \\ 0 \\ 1 \\ \frac{1}{\varphi} \end{bmatrix} .
\tag{4.26}
$$

Proof. (omitted) . $\qquad\square$

Proposition 4.2. *Fields associated to eigenvectors* $\mathbf{v}_1$ *and* $\mathbf{v}_6$ *are genuinely non-linear.*

Proof. We denote $\lambda_1 = \lambda_-$ and $\lambda_6 = \lambda_+$. In a similar manner we redefine sub-indices of associated eigenvectors. The result follows by noting that

$$
\nabla_{\mathbf{W}} \lambda_\pm \cdot \mathbf{v}_\pm = -\frac{1}{q} \pm \frac{1}{\tilde{c}} \left(c \frac{\partial c}{\partial A} + \frac{\partial \omega}{\partial A} \right) - (u \pm \tilde{c}) \frac{A}{q^2} \pm \frac{1}{2\tilde{c}} \frac{\partial \omega}{\partial \Psi} \neq 0 .
\tag{4.27}
$$

$\qquad\square$

Proposition 4.3. *Fields associated to eigenvectors* $\mathbf{v}_2$ *to* $\mathbf{v}_5$ *are linearly-degenerated fields.*

Proof. The proof follows from the fact that for these eigenvectors, the associated eigenvalues are identically zero, so that

$$
\nabla_{\mathbf{W}} \lambda = \mathbf{0} .
\tag{4.28}
$$

$\qquad\square$

Proposition 4.4. *Let* $\mathcal{N}^1(\mathbf{W})$ *and* $\mathcal{N}^6(\mathbf{W})$ *be two functions of* $\mathbf{W}$. *Riemann invariants associated to genuinely non-linear fields for eigenvectors* $\mathbf{v}_1$ *and* $\mathbf{v}_6$ *satisfy*

$$
\mathcal{N}^1 := u - \int \frac{\tilde{c}}{A} dA = constant , \quad \mathcal{N}^6 := u + \int \frac{\tilde{c}}{A} dA = constant,
\tag{4.29}
$$

respectively.

Proof. From eigenvectors associated to genuinely non-linear fields, the significant Riemann invariant for non-linear fields is

$$\frac{1}{dA} = \frac{u \pm \tilde{c}}{dq} . \tag{4.30}$$

By considering $uA = q$ and manipulating the above expression we obtain

$$du = \pm \frac{\tilde{c}}{A} dA \tag{4.31}$$

and the result holds. □

Proposition 4.5. *Let $\mathcal{L}^1(\mathbf{W})$ and $\mathcal{L}^2(\mathbf{W})$ functions of $\mathbf{W}$. For p_e, A_0 and K constants, Riemann invariants associated to linearly degenerate fields for eigenvectors $\mathbf{v}_2$ to $\mathbf{v}_5$ satisfy*

$$\mathcal{L}^1 := \tilde{p} + \tfrac{1}{2}\rho u^2 = constant , \quad \mathcal{L}^2 := q = constant , \tag{4.32}$$

with $\tilde{p} = p_e + \psi - \varphi\Psi$.

Proof. We note that for constant values of p_e, A_0 and K we can consider a reduced system of the form (4.7) with

$$\left. \begin{array}{c} \mathbf{W} = \begin{bmatrix} A & q & \Psi \end{bmatrix}^T , \\[2mm] \mathbf{J} = \begin{bmatrix} 0 & 1 & 0 \\ c^2 - u^2 + \frac{a_\Gamma}{2} & 2u & -\frac{A}{\rho}\varphi \\ 0 & -\frac{1}{\varepsilon} & 0 \end{bmatrix} , \\[2mm] \mathbf{S} = \begin{bmatrix} 0 & f & -\frac{1}{\varepsilon}\Psi \end{bmatrix}^T . \end{array} \right\} \tag{4.33}$$

This system has eigenvalues

$$\lambda_1 = u - \tilde{c} , \quad \lambda_2 = 0 , \quad \lambda_3 = u + \tilde{c} . \tag{4.34}$$

Corresponding eigenvectors are

$$
\mathbf{v}_1 = \begin{bmatrix} 1 \\ u - \tilde{c} \\ -\frac{1}{\varepsilon} \end{bmatrix} , \quad
\mathbf{v}_2 = \begin{bmatrix} 1 \\ 0 \\ -\frac{\rho}{\varphi A}\left\{u^2 - (c^2 + a_\Gamma/2)\right\} \end{bmatrix} , \quad
\mathbf{v}_3 = \begin{bmatrix} 1 \\ u + \tilde{c} \\ -\frac{1}{\varepsilon} \end{bmatrix} . \quad (4.35)
$$

Riemann invariants associated to the stationary contact discontinuity (characteristic field associated to the eigenvalue λ_2) are

$$
\frac{1}{dA} = \frac{0}{dq} = \frac{-\frac{\rho}{\varphi A}\left\{u^2 - (c^2 + a_\Gamma/2)\right\}}{d\Psi} . \quad (4.36)
$$

Hence, we obtain $\mathcal{L}^2 = q = constant$ and

$$
M(A, \Psi)d\Psi + N(A, \Psi)dA = 0 , \quad (4.37)
$$

with

$$
M(A, \Psi) = \frac{A\varphi}{\rho} , \quad N(A, \Psi) = u^2 - c^2 + \frac{a_\Gamma}{\rho} . \quad (4.38)
$$

This ordinary differential problem is not exact because

$$
\frac{\partial M}{\partial A} \neq \frac{\partial N}{\partial \Psi} .
$$

However, it can be proved that an integrating factor for this problem is $F(A) = \frac{1}{A}$, *i.e.*

$$
\frac{\partial(FM)}{\partial A} = \frac{\partial(FN)}{\partial \Psi} .
$$

Moreover, (4.37) is equivalent to

$$
F(A)M(A, \Psi)d\Psi + F(A)N(A, \Psi)dA = 0 . \quad (4.39)
$$

Hence, the Riemann invariant is a function $\mathcal{L}^1(A, \Psi)$ which satisfies $d\mathcal{L}^1 = 0$ or

$$
\begin{aligned}
\partial_A \mathcal{L}^1(A, \Psi) &= F(A)N(A, \Psi) = \frac{1}{A}\left(u^2 - c^2 - \frac{a_\Gamma}{2}\right) , \\
\partial_\Psi \mathcal{L}^1(A, \Psi) &= F(A)M(A) = \frac{\varphi}{\rho} .
\end{aligned} \quad (4.40)
$$

To find $\mathcal{L}^1$ we first integrate $\partial_\Psi \mathcal{L}^1$ in (4.40) with respect to Ψ which yields

$$
\mathcal{L}^1(A, \Psi) = a_\Gamma + g(A) . \quad (4.41)
$$

Then, $g(A)$ is found by differentiating (4.41) with respect to A and using (4.40) to obtain

$$g'(A) = \frac{u^2 - c^2}{A} \,,$$

(4.42)

providing

$$\mathfrak{L}^1(A, \Psi) = a_\Gamma - \frac{\psi}{\rho} - \frac{u^2}{2} \,.$$

(4.43)

Since ρ is constant, from (4.37) and (4.39) we conclude that $\mathfrak{L}^1(A, \Psi)$ is constant across waves associated to linearly-degenerate fields. $\qquad\square$

4.3 Numerical methods

The ADER methodology [144, 150, 154] consists of two main building blocks: a spatial reconstruction procedure and the solution of a generalised Riemann problem at each interface. ADER is, effectively, an extension of the second-order method of Ben-Artzi and Falcovitz [10]. The extension relates to the generalised Riemann problem and is twofold: (i) initial conditions are piece-wise smooth, for example piece-wise polynomials of any degree and (ii) source terms in the equations are included, if present originally. We also remark that ADER is akin to the method proposed by Harten et al. [66], as noted by Castro and Toro [22]. The ADER approach was first put forward by Toro et al. [150] for linear problems on Cartesian meshes, see also [132]. Several extensions have been proposed for non-linear problems on Cartesian [146] and non Cartesian meshes [21, 79, 80], to mention but a few. Extension of the ADER approach in the framework of discontinuous Galerkin finite element methods is due to Dumbser and collaborators; see [35, 36, 45], for instance. Subsequently, the ADER approach was extended to non-conservative balance laws,[20, 40, 42, 46] to mention but a few. ADER methods are one-step schemes, fully discrete, containing two main ingredients: (i) a high-order spatial reconstruction procedure and (ii) the solution of a generalised, or high order, Riemann problem (GRP) at each cell interface. Reconstructions should be non-linear in order to circumvent Godunov's theorem [55, 147]. Concerning the GRP, in this chapter we use the solver due to Dumbser et al. [41], that allows the treatment of stiff source terms in such a way that the usually contradictory requirements of high accuracy and stiffness are reconciled. For a review of ADER see [22, 100] and chapters 19 and 20 of [147].

4.3.1 ADER framework

We discretize the computational domain by a set of intervals $I_i = [x_{i-\frac{1}{2}}, x_{i+\frac{1}{2}}]$ of length $\Delta x = x_{i+\frac{1}{2}} - x_{i-\frac{1}{2}}$. Then we integrate (4.7) on the space-time cell, or volume, $I_i^n :=$ $I_i \times [t^n, t^{n+1}]$ which as shown in [40, 46] yields

$$
\left.
\begin{aligned}
\mathbf{W}_i^{n+1} = \quad & \mathbf{W}_i^n + \frac{1}{\Delta x} \int_{t^n}^{t^{n+1}} \int_{x_{i-\frac{1}{2}}}^{x_{i+\frac{1}{2}}} \mathbf{J}(\mathbf{W}_i)\partial_x \mathbf{W}_i dx dt \\
+ \quad & \frac{1}{\Delta x} \int_{t^n}^{t^{n+1}} \int_{x_{i-\frac{1}{2}}}^{x_{i+\frac{1}{2}}} \mathbf{L}(\mathbf{W}_i) dx dt \\
- \quad & \frac{\Delta t}{\Delta x} \left[\mathbf{D}_{i+\frac{1}{2}}^- + \mathbf{D}_{i-\frac{1}{2}}^+ \right] ,
\end{aligned}
\right\}
\tag{4.44}
$$

with

$$
\left.
\begin{aligned}
\mathbf{D}_{i+\frac{1}{2}}^- = \frac{1}{\Delta t} \int_{t^n}^{t^{n+1}} \mathcal{D}_{i+\frac{1}{2}}^-(\mathbf{W}_{i+\frac{1}{2}}^-, \mathbf{W}_{i+\frac{1}{2}}^+) dt , \\
\mathbf{D}_{i-\frac{1}{2}}^+ = \frac{1}{\Delta t} \int_{t^n}^{t^{n+1}} \mathcal{D}_{i-\frac{1}{2}}^+(\mathbf{W}_{i-\frac{1}{2}}^-, \mathbf{W}_{i-\frac{1}{2}}^+) dt
\end{aligned}
\right\} .
\tag{4.45}
$$

Fluctuations $\mathcal{D}_{i+\frac{1}{2}}^\pm$ are defined by

$$
\mathcal{D}_{i+\frac{1}{2}}^\pm(\mathbf{W}_{i+\frac{1}{2}}^-, \mathbf{W}_{i+\frac{1}{2}}^+) = \frac{1}{2} \int_0^1 \left(\mathbf{J}(\mathbf{\Theta}(s)) \pm |\mathbf{J}(\mathbf{\Theta}(s))| \right) \frac{d\mathbf{\Theta}}{ds} ds,
\tag{4.46}
$$

with $\mathbf{\Theta}$ a Liptschitzian path in $[0,1]$ satisfying

$$
\mathbf{\Theta}(0) = \mathbf{W}_{i+\frac{1}{2}}^- , \quad \mathbf{\Theta}(1) = \mathbf{W}_{i+\frac{1}{2}}^+ .
$$

For more details see [33, 103, 117] and references therein.

4.3.2 The Dumbser-Enaux-Toro (DET) solver for the GRP

Here the generalized Riemann problem is the following Cauchy problem

$$
\left.
\begin{aligned}
\partial_t \mathbf{W} + \mathbf{J}\partial_x \mathbf{W} \quad = \quad & \mathbf{L}(\mathbf{W}) , \\
\mathbf{W}(x,0) \quad = \quad & \begin{cases} \mathbf{P}_i(x) , x < x_{i+\frac{1}{2}}, \\ \mathbf{P}_{i+1}(x) , x > x_{i+\frac{1}{2}}, \end{cases}
\end{aligned}
\right\}
\tag{4.47}
$$

where $\mathbf{P}_i(x)$ and $\mathbf{P}_{i+1}(x)$ are reconstruction polynomials defined in I_i and I_{i+1} respectively. In this chapter we use the WENO reconstruction procedure proposed in [104]. See also [72] and [40] for background on WENO reconstruction.

The solution of (4.47) allows us to approximate time integrals (4.45) with a required order of accuracy. Here we use the Dumbser-Enaux-Toro (DET) solver [41]. Data to the left and right of the interface $x_{i+\frac{1}{2}}$, necessary for the computation of numerical fluxes at quadrature points, are obtained by solving a local Cauchy problem in each element of the computational mesh. This solver yields $\mathbf{W}_i(x,t)$, that will be used to approximate integrals appearing in (4.44) by quadrature rules.

In the DET solver, we solve the local Cauchy problem in I_i^n, namely

$$\left.\begin{aligned} \partial_t \mathbf{W} + \mathbf{J}\partial_x \mathbf{W} &= \mathbf{L}(\mathbf{W}) , \\ \mathbf{W}(x,0) &= \mathbf{P}_i(x) . \end{aligned}\right\} \tag{4.48}$$

We transform the space-time interval I_i^n into $[0,1] \times [0,1]$, with reference variables $\xi - \tau$ given by the change of variables $x = x(\xi) = x_{i-\frac{1}{2}} + \xi \Delta x$ and $t = t(\tau) = t^n + \tau \Delta t$. The problem in $\xi - \tau$ variables reads

$$\left.\begin{aligned} \partial_\tau \mathcal{W} + \mathfrak{J}\partial_\xi \mathcal{W} &= \mathcal{L}(\mathcal{W}) , \\ \mathcal{W}(\xi,0) &= \mathbf{P}_i(x(\xi)) , \end{aligned}\right. \tag{4.49}$$

with $\mathfrak{J} = \frac{\Delta t}{\Delta x}\mathbf{J}$ and $\mathcal{L} = \Delta t \mathbf{L}$.

Problem (4.49) is now solved using a space-time discontinuous Galerkin method. Consider a space $\mathbf{V}$ formed by nodal space-time polynomials $\theta_p(\xi, \tau)$ defined in $[0,1] \times [0,1]$, whose basis is $\{\theta_1, ..., \theta_m\}$. Here $m = (K+1)^2$, with K the degree of the reconstruction polynomials in (4.48) and $K+1$ the degrees of freedom of the space-time basis. Note that $K+1$ will also be the order of accuracy of the resulting ADER numerical scheme.

Multiplying (4.49) by a test function $\theta_l \in V$ and integrating in $[0,1] \times [0,1]$ we have

$$\int_0^1 \int_0^1 [(\partial_\tau \mathcal{W})\theta_l + (\mathfrak{J}(\mathcal{W})\partial_\xi \mathcal{W})\theta_l] \, d\xi d\tau = \int_0^1 \int_0^1 \mathcal{L}(\mathcal{W})\theta_l d\xi d\tau . \tag{4.50}$$

Integrating by parts in time τ the first term on the left hand side yields

$$\left.\begin{aligned} \int_0^1 \int_0^1 \partial_\tau \mathcal{W}(\xi,\tau)\theta_l(\xi,\tau)d\xi d\tau &= \int_0^1 \mathcal{W}(\xi,1)\theta_l(\xi,1)d\xi \\ - \int_0^1 \mathbf{P}_i(x(\xi))\theta_l(\xi,0)d\xi &- \int_0^1 \int_0^1 \mathcal{W}(\xi,\tau)\partial_\tau \theta_l(\xi,\tau)d\xi d\tau . \end{aligned}\right\} \tag{4.51}$$

Substituting (4.51) into (4.50) gives

$$
\left.
\begin{aligned}
&\int_0^1 \mathcal{W}(\xi,1)\theta_l(\xi,1) - \int_0^1\int_0^1 \mathcal{W}(\xi,\tau)\partial_\tau\theta_l(\xi,\tau)d\xi d\tau \\[2mm]
&+ \int_0^1\int_0^1 \mathfrak{I}(\mathcal{W}(\xi,\tau))\partial_\xi\mathcal{W}(\xi,\tau)\theta_l(\xi,\tau)d\xi d\tau \\[2mm]
&= \int_0^1\int_0^1 \mathcal{L}(\mathcal{W}(\xi,\tau))\theta_l(\xi,\tau)d\xi d\tau + \int_0^1 \mathbf{P}_i(x(\xi))\theta_l(\xi,0)d\xi \; .
\end{aligned}
\right\}
\tag{4.52}
$$

We now introduce the following operators for any two functions $\phi(\xi,\tau)$ and $\psi(\xi,\tau)$, namely

$$
[\phi,\psi]_\tau = \int_0^1 \phi(\xi,\tau)\psi(\xi,\tau)d\xi \; , \qquad \langle\phi,\psi\rangle = \int_0^1\int_0^1 \phi(\xi,\tau)\psi(\xi,\tau)d\xi d\tau \; .
\tag{4.53}
$$

Introducing these definitions into (4.52) yields

$$
[\mathcal{W},\theta_l]_1 - \langle\mathcal{W},\partial_\tau\theta_l\rangle + \langle\mathfrak{I}(\mathcal{W})\partial_\xi\mathcal{W},\theta_l\rangle = \langle\mathcal{L}(\mathcal{W}),\theta_l\rangle + [\mathbf{P}_i,\theta_l]_0 \; ,
\tag{4.54}
$$

with

$$
[\mathbf{P}_i,\theta_l]_0 = \int_0^1 \mathbf{P}_i(x(\xi))\theta_l(\xi,0)d\xi \; .
\tag{4.55}
$$

We seek solutions of the form

$$
\mathcal{W}(\xi,\tau) = \sum_{p=1}^m \theta_p(\xi,\tau)\hat{\mathcal{W}}_p \; ,
\tag{4.56}
$$

with coefficients $\hat{\mathcal{W}}_k$ yet to be determined.

For convenience we define matrices

$$
\left.
\begin{aligned}
\mathbf{K}_{k,l}^1 &= [\theta_k,\theta_l]_1 - \langle\theta_k,\partial_\tau\theta_l\rangle \; , \\[2mm]
\mathbf{K}_{k,l}^\xi &= \langle\partial_\xi\theta_k,\theta_l\rangle \; , \\[2mm]
\mathbf{M}_{k,l} &= \langle\theta_k,\theta_l\rangle \; , \\[2mm]
\mathbf{V}_{rec,l} &= [\mathbf{P}_i,\theta_l]_0 \; .
\end{aligned}
\right\}
\tag{4.57}
$$

On the other hand, as we are considering a nodal base, then

$$
\mathfrak{I}(\mathcal{W})\partial_\xi\mathcal{W} = \mathfrak{I}\left(\sum_{p=1}^m \theta_p(\xi,\tau)\hat{\mathcal{W}}_p\right)\partial_\xi\left(\sum_{p=1}^m \theta_p(\xi,\tau)\hat{\mathcal{W}}_p\right) \approx \sum_{p=1}^m \partial_\xi\theta_p(\xi,\tau)\mathfrak{I}(\hat{\mathcal{W}}_p)\hat{\mathcal{W}}_p = \sum_{p=1}^m \theta_p(\xi,\tau)\hat{\mathcal{X}}_p
\tag{4.58}
$$

with $\hat{\mathcal{X}}_p$ coefficients directly computed on the polynomial space $\mathbf{V}$, *i. e.* solving

$$\mathbf{X} = \mathbf{M}^{-1}\mathbf{K}^{\xi}\mathbf{JW} \ , \tag{4.59}$$

with $\mathbf{X} = \left[\hat{\mathcal{X}}_1, ..., \hat{\mathcal{X}}_m\right]^T$ and $\mathbf{JW} = \left[\mathfrak{J}(\hat{\mathcal{W}}_1)\hat{\mathcal{W}}_1, ..., \mathfrak{J}(\hat{\mathcal{W}}_m)\hat{\mathcal{W}}_m\right]^T$. In the same manner by projection on the polynomial space we obtain

$$\mathcal{L}(\mathcal{W}) \approx \sum_{p=1}^{m} \theta_p(\xi, \tau)\mathcal{L}(\hat{\mathcal{W}}_p) \ . \tag{4.60}$$

Note that $\hat{\mathcal{X}}$ depends on coefficients $\hat{\mathcal{W}}$ so that we can define the vectors

$$\mathcal{R} = \begin{bmatrix} \hat{\mathcal{W}}_1 \\ \vdots \\ \hat{\mathcal{W}}_m \end{bmatrix}, \quad \mathcal{G}(\mathcal{R}) = \begin{bmatrix} \hat{\mathcal{X}}_1(\mathcal{R}) \\ \vdots \\ \hat{\mathcal{X}}_m(\mathcal{R}) \end{bmatrix}, \quad \mathcal{Z}(\mathcal{R}) = \begin{bmatrix} \mathcal{L}(\hat{\mathcal{W}}_1) \\ \vdots \\ \mathcal{L}(\hat{\mathcal{W}}_m) \end{bmatrix} . \tag{4.61}$$

Then, (4.54) can be written as

$$\mathbf{K}^1\mathcal{R} + \mathbf{M}\mathcal{G}(\mathcal{R}) - \mathbf{M}\mathcal{Z}(\mathcal{R}) = \mathbf{V}_{rec} \ . \tag{4.62}$$

This is a system of non-linear algebraic equations for $\mathcal{R}$ which can be solved by the fixed point iteration procedure proposed in [38], namely

$$\mathbf{K}^1\mathcal{R}^{n+1} - \mathbf{M}\mathcal{Z}(\mathcal{R}^{n+1}) = \mathbf{V}_{rec} - \mathbf{M}\mathcal{G}(\mathcal{R}^n), \tag{4.63}$$

where n stands for the iteration step. Once $\mathcal{R}$ is known, the sought coefficients are known and so the solution (4.56). We denote the solution to (4.49) by $\mathcal{W}_i(\xi, \tau)$ to clarify that it corresponds to the solution of the Cauchy problem in I_i^n.

Once that $\mathcal{W}_i(\xi, \tau)$ is available in all computational cells, integrals in (4.44) can be approximated by evaluating $\mathcal{W}_i(\xi, \tau)$ in selected quadrature points. Moreover, numerical fluctuations appearing in time integrals in (4.45) are obtained by using a first order classical Riemann solver at required quadrature points τ_k with $\mathcal{W}_i(1, \tau_k)$ and $\mathcal{W}_{i+1}(0, \tau_k)$. In the following section we introduce the first order Riemann solver used in the present chapter. Moreover, fluctuations in (4.45) can be evaluated by noting that

$$\mathbf{W}^-_{i+\frac{1}{2}} = \lim_{\xi \to 1^-} \mathcal{W}_i(\xi, 0), \quad \mathbf{W}^+_{i+\frac{1}{2}} = \lim_{\xi \to 0^+} \mathcal{W}_{i+1}(\xi, 0) \ .$$

To compute fluctuations we will use the DOT solver of Dumbser and Toro [47]. Let $\lambda_i(\mathbf{W})$ be the $i-th$ eigenvalue of $\mathbf{J}(\mathbf{W})$, then $\mathbf{\Lambda}(\mathbf{W})$ is the matrix formed by all eigenvalues $\lambda_i(\mathbf{W})$, and let $\mathbf{R}(\mathbf{W})$ be the matrix formed by the right eigenvectors of $\mathbf{J}(\mathbf{W})$.

We define

$$\lambda_i(\mathbf{W})^+ = max\{\lambda_i(\mathbf{W}), 0\} \quad , \quad \lambda_i(\mathbf{W})^- = min\{\lambda_i(\mathbf{W}), 0\} . \tag{4.64}$$

Let $\mathbf{\Lambda}(\mathbf{W})^+$ be the diagonal matrix formed by $\lambda_i(\mathbf{W})^+$ and let $\mathbf{\Lambda}(\mathbf{W})^-$ be the diagonal matrix formed by $\lambda_i(\mathbf{W})^-$. Then, we define the matrices $|\mathbf{\Lambda}|$ and $|\mathbf{J}|$ by

$$|\mathbf{\Lambda}(\mathbf{W})| = \mathbf{\Lambda}(\mathbf{W})^+ - \mathbf{\Lambda}(\mathbf{W})^- \tag{4.65}$$

and

$$|\mathbf{J}(\mathbf{W})| = \mathbf{R}(\mathbf{W})|\mathbf{\Lambda}(\mathbf{W})|\mathbf{R}(\mathbf{W})^{-1} . \tag{4.66}$$

Let us consider the interface $x_{i+\frac{1}{2}}$ where data on the left is denoted by $\mathbf{W}_L$ and data on the right is denoted by $\mathbf{W}_R$. The fluctuation at the interface is computed as

$$\mathcal{D}^{\pm}_{i+\frac{1}{2}}(\mathbf{W}_L, \mathbf{W}_R) = \tfrac{1}{2} \int_0^1 \left(\mathbf{J}(\mathbf{\Theta}(s)) \pm |\mathbf{J}(\mathbf{\Theta}(s))| \right) \frac{\partial \mathbf{\Theta}}{\partial s} ds , \tag{4.67}$$

where the integral is evaluated numerically. We consider a Gaussian quadrature of n points and weights $\{\omega_j, s_j\}$.

We still have to define the integration path $\mathbf{\Theta}$. If we choose the path

$$\mathbf{\Theta}(s) = \mathbf{W}_L + s\,(\mathbf{W}_R - \mathbf{W}_L) , \tag{4.68}$$

the fluctuations are

$$\mathcal{D}^{\pm}_{i+\frac{1}{2}}(\mathbf{W}_L, \mathbf{W}_R) = \tfrac{1}{2} \sum_{j=1}^{n} \omega_j \left(\mathbf{J}(\mathbf{\Theta}(s_j)) \pm |\mathbf{J}(\mathbf{\Theta}(s_j))| \right)(\mathbf{W}_R - \mathbf{W}_L) . \tag{4.69}$$

However, in order to preserve and guarantee well-balanced properties, the integration path $\mathbf{\Theta}(s)$ should be chosen as the parametrization in phase-space of the curve $\mathfrak{L}^1$ in proposition 4.5, defined by the Riemann invariants associated to linearly-degenerate fields as proposed by Müller *et al.* [103, 104]. In the next subsection we illustrate how path $\mathbf{\Theta}$ is constructed.

4.3.3 Integration path

As proposed in [104], to guarantee well-balanced properties we take the integration path as

$$
\Theta(s) =
\begin{bmatrix}
A(s) \\
q(s) = q^-_{i+\frac{1}{2}} + s\left(q^+_{i+\frac{1}{2}} - q^-_{i+\frac{1}{2}} \right) \\
K(s) = K^-_{i+\frac{1}{2}} + s\left(K^+_{i+\frac{1}{2}} - K^-_{i+\frac{1}{2}} \right) \\
A_0(s) = A^-_{0,i+\frac{1}{2}} + s\left(A^+_{0,i+\frac{1}{2}} - A^-_{0,i+\frac{1}{2}} \right) \\
p_e(s) = p^-_{e,i+\frac{1}{2}} + s\left(p^+_{e,i+\frac{1}{2}} - p^-_{e,i+\frac{1}{2}} \right) \\
\Psi(s) = \Psi^-_{i+\frac{1}{2}} + s\left(\Psi^+_{i+\frac{1}{2}} - \Psi^-_{i+\frac{1}{2}} \right)
\end{bmatrix} ,
\tag{4.70}
$$

where super index $-$ refers to the data immediately to the left of the interface and super index $+$ refers to the data immediately to the right of the interface. $A(s)$ is obtained from the arch joining two states $A^-_{i+\frac{1}{2}}$ and $A^+_{i+\frac{1}{2}}$, through the curve defined by Riemann invariants $\mathfrak{L}^1$ of the linearly degenerated field. To determine this curve, we first note that for the stationary state case, $q = 0$, we have

$$
\mathfrak{L}^1(A, A_0, K, p_e) = K\phi(A, A_0) + p_e .
\tag{4.71}
$$

Therefore, $A(s)$ can be obtained from the algebraic equation

$$
\phi(A(s), A_0(s)) = \frac{\bar{\mathfrak{L}}^1(s) - p_e(s)}{K(s)} ,
$$

with

$$
\bar{\mathfrak{L}}^1(s) = (1 - s)\, \mathfrak{L}^1(A^-_{i+\frac{1}{2}}, A^-_{0,i+\frac{1}{2}}, K^-_{i+\frac{1}{2}}, p^-_{e,i+\frac{1}{2}}) + s\, \mathfrak{L}^1(A^+_{i+\frac{1}{2}}, A^+_{0,i+\frac{1}{2}}, K^+_{i+\frac{1}{2}}, p^+_{e,i+\frac{1}{2}})
\tag{4.72}
$$

Finally, we define the time step at time t^n as

$$
\Delta t = C_{cfl} \frac{\Delta x}{\lambda_{max}} ,
\tag{4.73}
$$

where $\lambda_{max} = max_{i=1,...,m}|\lambda_i(\mathbf{W}^n)|$ and $\mathbf{W}^n$ is the corresponding data evaluated at time t^n.

4.4 Numerical accuracy of solutions to advecion-diffusion-reaction equations by hyperbolic reformulation

In order to solve numerically adrPDEs, we reformulate them as hyperbolic systems with stiff source terms. Subsequently, we implement a numerical scheme which solves the stiff hyperbolic problem with order of accuracy q. Proposition 2.3 is a result of sufficiency which ensures that the numerical solution approximates the solution to the original adrPDE with the same order of accuracy q. This result is independent of the specific adrPDE problem and depends only on the relaxation time ε, the convergence rate q and the mesh spacing Δx. In this section we provide further numerical evidence that supports this result.

4.4.1 Convergence rate study for an advection-diffusion-reaction problem via hyperbolic reformulation

Here, we provide numerical results that confirm proposition 2.3 for the particular case of the one-dimensional blood flow model (4.16). To assess empirically the accuracy of the high-order numerical scheme (4.44) and the ability of reformulation (4.20) to recover the solution of the original viscoelastic problem (4.16), we construct a modified problem with exact solution. This is achieved by prescribing a function to be inserted in (4.16). Here we choose such function as

$$
\hat{\mathbf{Q}}(x,t) = \begin{bmatrix} \hat{A}(x,t) \\ \hat{q}(x,t) \\ \hat{K}(x) \\ \hat{A}_0(x) \\ \hat{p}_e(x) \end{bmatrix} = \begin{bmatrix} \tilde{A} + \tilde{a}\,sin\left(\frac{2\pi}{L}x\right)cos\left(\frac{2\pi}{T_0}t\right) \\ \tilde{q} - \tilde{a}\,\frac{L}{T_0}cos\left(\frac{2\pi}{L}x\right)sin\left(\frac{2\pi}{T_0}t\right) \\ \tilde{K} \\ \tilde{A}_0 \\ \tilde{P}_e \end{bmatrix} . \tag{4.74}
$$

Inserting (4.74) in (4.16) leads to the modified system

$$
\partial_t \mathbf{Q} + \mathbf{A}(\mathbf{Q})\partial_x \mathbf{Q} = \partial_x \mathbf{G}(\mathbf{Q}, \partial_x \mathbf{Q}) + \mathbf{S}(\mathbf{Q}) + \hat{\mathbf{S}}(x,t) , \tag{4.75}
$$

where $\hat{\mathbf{S}}(x,t)$ results from the evaluation of (4.74) in (4.16) and is only a function of time t and space x variables. $\hat{\mathbf{S}}(x,t)$ may be found with an algebraic manipulator and is not reported here. For the present study we use the following parameters: $L = 1.0\,m$, $T_0 = 1.0\,s$, $\tilde{A} = \tilde{A}_0 = 4.0 \times 10^{-4}\,m^2$, $\tilde{a} = 4.0 \times 10^{-5}\,m^2$, $\tilde{q} = 0.0\,m^3\,s^{-1}$, $\tilde{K} = 50.0\,KPa$, $\tilde{P}_e = 0.0\,Pa$, $m = 1/2$ and $n = 0$. For this test we used a $CFL = 0.9$.

Tables 4.1 to 4.4 show the empirical convergence rates from second to fifth order ADER schemes with several relaxation times ε. The highlighted row corresponds to the largest number of cells N for which, according to proposition 2.3, the theoretical convergence rate is expected to be achieved. It can be seen that the expected empirical accuracy is achieved for all orders of accuracy, and at least up to the predicted maximum number of cells.

Another interesting aspect to be noted is that when the discretization error becomes smaller than the formulation error, the error norms become independent from further mesh refinement, as expected.

4.5 Computational results for a network of viscoelastic vessels

In this section we validate our numerical scheme in the context of an *in-vitro* model of the human arterial system.

4.5.1 Review of reference *in-vitro* model of the arterial system

An *in-vitro* model of the human arterial system was put forward by Matthys *et al.* [96]. Along with an accurate description of the physical model, the authors constructed the corresponding mathematical model for one-dimensional blood flow in elastic vessels and provided a wealth of measurements and numerical results. The vessel network is composed of 37 silicone tubes resembling major arteries, a pump acting as the heart and terminal resistances representing the peripheral circulation. We refer the reader to the above named reference for details on the topography of the network, the description of mechanical properties, geometry of the vessels, terminal resistances and flow rate measured at the root of the ascending aorta. In a subsequent publication, Alastruey *et al.* [2], a viscoelastic vessel wall model was used in order to improve computational results for specific portions of the network, where non-physical high amplitude oscillation were observed. This test constitutes an ideal benchmark for assessing the performance of the methodology proposed in this chapter in the context of a complex network of viscoelastic vessels.

4.5.2 Details on the settings of the network solver

Modelling the network of vessels proposed in [96] requires dealing with other aspects besides the solution of system (4.16) within the one-dimensional domain. In particular,

the flow rate has to be prescribed at the root of the aorta, terminal lumped parameter models have to be resolved and interface conditions at the junction between two or more vessels have to be given. Boundary conditions involving a prescribed flow rate or terminal resistances were treated as in [4]. For the treatment of junctions, the methodology proposed in [137] was used. Details on the treatment of boundary conditions and junctions are given in appendix B.

We adopted the spatial discretisation of [2]: vessels longer than 1.5 cm were divided in non-overlapping cells of a maximum length of 2 cm; for vessels shorter than 1.5 cm a single cell was used. Taking into account the results of proposition 2.3 and the fact that the characteristic mesh spacing is of order $\Delta x = 2 \, cm$ for almost all vessels, we used a relaxation time $\epsilon = 10^{-3} \, s$ over the entire network. This choice ensures that the formulation error will be smaller than the numerical error for all vessels, except for 3 vessels which would require a relaxation time of $\epsilon = 10^{-4} \, s$. As we shall see later, this choice will not have a significant impact on the numerical results.

Computations were performed using a $C_{cfl} = 0.9$, which combined with the chosen relaxation time results in an average time step of approximately $\Delta t = 400 \, \mu s$. Note that the time step Δt is computed at each time step, in order to advance as much as possible in time during each step, within the linear stability limit of unity of our explicit scheme.

4.5.3 Comparison of solutions obtained using elastic and viscoelastic vessel wall models

Our first validation regards a comparison among experimental measurements reported in [2], numerical results for elastic vessels reported in [104] and numerical results for the viscoelastic model (4.16) obtained with the methodology presented in section 4.3 of this chapter. We note that the one-dimensional model for elastic vessels results from taking $\Gamma = 0$ in (4.13).

Figure 4.1 shows experimental measurements and computational results for both the elastic and viscoelastic vessel wall models. It can be easily seen that the solution obtained with the elastic model presents abnormally large amplitude fluctuations, as compared to experiments, in the left renal and right carotid arteries during diastole. This phenomenon can be observed for both measured quantities, pressure and flow rate, being more evident for the later one. The viscoelastic formulation significantly increases the accuracy by which the numerical solution approximates experimental measurements, reducing non-physical oscillations for pressure and flow rate.

4.5.4 Comparison with published numerical results

Here, we compare numerical results obtained with the proposed formulation and numerical results previously reported in [2]. Figure 4.2 shows both numerical results, along with experimental measurements for several vessels. Agreement between numerical results obtained with the proposed methodology and those reported in [2] is excellent. We note that the time step of our explicit scheme is around 20 times larger than that in [2], where a time step of $\Delta t = 20\,\mu\,s$ was reported.

4.5.5 Sensitivity of the numerical solution to the relaxation time ε

In figure 4.3 we report numerical results for different relaxation times ε. As expected, there is a significant difference between results obtained using $\varepsilon = 10^{-2}\,s$ and $\varepsilon = 10^{-3}\,s$ for vessels which show high frequency oscillations (right carotid artery). This is due to the fact that in the first case the formulation error dominates over the discretization error, whereas for $\varepsilon = 10^{-3}\,s$ we are attaining the expected accuracy of the numerical scheme for almost all vessels. Further reduction of ε does not result in significant improvement of the numerical solution, since the discretization error remains dominant. Finally, the last row of figure 4.3 shows computational results for the shortest vessel of the network, which would require a relaxation time $\varepsilon = 10^{-4}\,s$. Improvements with respect to the numerical solution obtained using $\varepsilon = 10^{-3}\,s$ are negligible.

4.6 Conclusions

In this chapter we have reformulated a one-dimensional blood flow model for viscoelastic vessels in the form of a hyperbolic system with stiff source terms, via a relaxation approach. After carefully studying the mathematical properties of the resulting system we proposed a methodology for its numerical solution, ensuring high-order accuracy and well-balanced properties. The criterion for selecting the relaxation time presented in chapter 2, ensures that the formulation error will be smaller than the discretisation error. Moreover, the order of accuracy of the numerical scheme, as well as the proposed criterion for the definition of the relaxation time, were tested via an empirical convergence rate study up to fifth order of accuracy in space and time. Empirical results confirm the theory. Finally, we validated the proposed methodology by comparing our numerical results with experimental measurements, as well as with numerical results reported in the literature for a network of viscoelastic vessels. We showed that: the viscoelastic formulation improves the agreement between numerical results and experimental measurements, as compared to the results obtained considering elastic vessels;

numerical results obtained with the proposed methodology are in agreement with previously reported data. The choice of the relaxation time via the proposed criterion ensures an accurate numerical solution, also in the context of complex vessel networks.

ADER-O2

ε	N	L^1	L^2	L^∞	$\mathcal{O}(L^1)$	$\mathcal{O}(L^2)$	$\mathcal{O}(L^\infty)$	$t_{CPU}\,[s]$	$\triangle_2$
10^{-2}	4	1.08e-05	1.23e-05	2.46e-05	-	-	-	0.59	
	8	2.58e-06	3.02e-06	7.42e-06	2.1	2.0	1.7	0.92	1.03e-01
	16	5.58e-07	7.01e-07	2.11e-06	2.2	2.1	1.8	1.90	4.10e-01
	32	1.34e-07	1.70e-07	5.24e-07	2.1	2.0	2.0	4.49	1.64e+00
	64	3.50e-08	4.34e-08	1.19e-07	1.9	2.0	2.1	10.14	6.52e+00
	128	1.48e-08	1.87e-08	4.18e-08	1.2	1.2	1.5	25.22	2.62e+01
10^{-3}	4	1.05e-05	1.27e-05	2.86e-05	-	-	-	0.89	
	8	2.34e-06	3.07e-06	9.24e-06	2.2	2.0	1.6	1.17	1.03e-02
	16	5.39e-07	7.45e-07	2.45e-06	2.1	2.0	1.9	3.81	4.10e-02
	32	1.30e-07	1.83e-07	6.17e-07	2.1	2.0	2.0	8.10	1.64e-01
	64	3.17e-08	4.50e-08	1.55e-07	2.0	2.0	2.0	16.23	6.58e-01
	128	7.79e-09	1.08e-08	3.76e-08	2.0	2.1	2.0	39.74	2.62e+00
	256	2.06e-09	2.59e-09	7.64e-09	1.9	2.1	2.3	92.13	1.05e+01
	512	1.26e-09	1.53e-09	3.05e-09	0.7	0.8	1.3	276.16	4.20e+01
10^{-4}	4	1.14e-05	1.28e-05	2.18e-05	-	-	-	2.25	
	8	2.26e-06	3.29e-06	1.04e-05	2.3	2.0	1.1	2.32	1.03e-03
	16	5.65e-07	8.54e-07	2.82e-06	2.0	1.9	1.9	8.09	4.10e-03
	32	1.36e-07	2.03e-07	6.85e-07	2.1	2.1	2.0	21.26	1.64e-02
	64	3.31e-08	4.96e-08	1.69e-07	2.0	2.0	2.0	42.51	6.56e-02
	128	8.20e-09	1.23e-08	4.23e-08	2.0	2.0	2.0	89.87	2.62e-01
	256	2.02e-09	3.02e-09	1.04e-08	2.0	2.0	2.0	234.33	1.05e-00
	512	4.85e-10	6.96e-10	2.43e-09	2.1	2.1	2.1	738.74	4.20e+00
	1024	1.37e-10	1.69e-10	4.27e-10	1.8	2.0	2.5	2501.83	1.68e+01
	2048	1.29e-10	1.48e-10	2.70e-10	0.1	0.2	0.7	8757.74	6.72e+01
10^{-5}	4	1.95e-05	2.25e-05	3.33e-05	-	-	-	5.40	
	8	5.75e-06	6.97e-06	1.45e-05	1.8	1.7	1.2	9.50	1.03e-04
	16	1.04e-06	1.40e-06	3.40e-06	2.5	2.3	2.1	27.35	4.10e-04
	32	1.83e-07	2.57e-07	7.60e-07	2.5	2.4	2.2	59.42	1.64e-03
	64	3.74e-08	5.51e-08	1.81e-07	2.3	2.2	2.1	128.79	6.56e-03
	128	8.76e-09	1.33e-08	4.48e-08	2.1	2.1	2.0	279.25	2.62e-02
	256	2.15e-09	3.29e-09	1.12e-08	2.0	2.0	2.0	745.23	1.05e-01
	512	5.33e-10	8.17e-10	2.78e-09	2.0	2.0	2.0	2210.56	4.20e-01
	1024	1.29e-10	1.97e-10	6.78e-10	2.0	2.1	2.0	7216.78	1.68e+00
	2048	3.03e-11	4.30e-11	1.51e-10	2.1	2.2	2.2	25564.93	6.72e+00
	4096	1.07e-11	1.32e-11	2.78e-11	1.5	1.7	2.4	96751.62	2.69e+01

TABLE 4.1: Empirical convergence rates for a second order ADER scheme with several relaxation times ε. N is the number of cells. Errors are computed for variable A. CPU times are reported for all tests. The highlighted row corresponds to the largest number of cells N for which, predicted by proposition 2.3, the theoretical convergence rate is expected to be achieved.

ADER-O3

ε	N	L^1	L^2	L^∞	$\mathcal{O}(L^1)$	$\mathcal{O}(L^2)$	$\mathcal{O}(L^\infty)$	$t_{CPU}\,[s]$	$\triangle_3$
10^{-2}	4	4.31e-06	4.85e-06	8.38e-06	-	-	-	0.70	
	8	5.91e-07	7.16e-07	1.46e-06	2.9	2.8	2.5	1.34	3.22e-01
	16	7.43e-08	9.18e-08	2.03e-07	3.0	3.0	2.8	2.70	2.58e+00
	32	1.84e-08	2.07e-08	3.57e-08	2.0	2.2	2.5	5.54	2.06e+01
	64	1.54e-08	1.71e-08	2.52e-08	0.3	0.3	0.5	15.93	1.65e+02
10^{-3}	4	3.82e-06	4.59e-06	9.08e-06	-	-	-	0.94	
	8	5.46e-07	6.77e-07	1.47e-06	2.8	2.8	2.6	2.07	3.22e-02
	16	7.17e-08	8.94e-08	2.00e-07	2.9	2.9	2.9	4.14	2.58e-01
	32	9.06e-09	1.13e-08	2.60e-08	3.0	3.0	2.9	9.25	2.06e+00
	64	1.91e-09	2.16e-09	4.03e-09	2.2	2.4	2.7	24.20	1.65e+01
10^{-4}	4	3.82e-06	4.59e-06	9.10e-06	-	-	-	1.83	
	8	5.58e-07	6.90e-07	1.48e-06	2.8	2.7	2.6	5.14	3.22e-03
	16	7.35e-08	9.03e-08	1.99e-07	2.9	2.9	2.9	10.32	2.58e-02
	32	9.22e-09	1.14e-08	2.59e-08	3.0	3.0	2.9	25.53	2.06e-01
	64	1.15e-09	1.43e-09	3.39e-09	3.0	3.0	2.9	61.13	1.65e+00
	128	2.05e-10	2.37e-10	4.91e-10	2.5	2.6	2.8	161.16	1.32e+01
	256	1.53e-10	1.71e-10	2.65e-10	0.4	0.5	0.9	488.69	1.06e+02
10^{-5}	4	7.92e-06	9.24e-06	1.46e-05	-	-	-	6.21	
	8	5.75e-07	7.01e-07	1.49e-06	3.8	3.7	3.3	14.84	3.22e-04
	16	7.24e-08	8.98e-08	2.00e-07	3.0	3.0	2.9	32.91	2.58e-03
	32	9.58e-09	1.16e-08	2.59e-08	2.9	2.9	3.0	70.57	2.06e-02
	64	1.20e-09	1.47e-09	3.40e-09	3.0	3.0	2.9	175.85	1.65e-01
	128	1.50e-10	1.84e-10	4.54e-10	3.0	3.0	2.9	491.91	1.32e+00
	256	2.25e-11	2.72e-11	6.47e-11	2.7	2.8	2.8	1674.83	1.06e+01
	512	1.50e-11	1.68e-11	2.90e-11	0.6	0.7	1.2	4963.15	8.44e+01

TABLE 4.2: Empirical convergence rates for a third order ADER scheme with several relaxation times ε. N is the number of cells. Errors are computed for variable A. CPU times are reported for all tests. The highlighted row corresponds to the largest number of cells N for which, according to proposition 2.3, the theoretical convergence rate is expected to be achieved.

ADER-O4

ε	N	L^1	L^2	L^∞	$\mathcal{O}(L^1)$	$\mathcal{O}(L^2)$	$\mathcal{O}(L^\infty)$	$t_{CPU}\,[s]$	$\triangle_4$
10^{-2}	4	6.73e-06	7.68e-06	1.64e-05	-	-	-	0.81	
	8	3.94e-07	4.83e-07	1.21e-06	4.1	4.0	3.8	1.62	1.16e+00
	16	2.18e-08	2.47e-08	5.65e-08	4.2	4.3	4.4	3.66	1.86e+01
	32	1.49e-08	1.65e-08	2.55e-08	0.6	0.6	1.1	10.42	2.98e+02
10^{-3}	4	5.91e-06	7.80e-06	1.89e-05	-	-	-	1.11	
	8	4.94e-07	6.09e-07	1.55e-06	3.6	3.7	3.6	2.52	1.16e-01
	16	2.80e-08	3.56e-08	9.79e-08	4.1	4.1	4.0	6.02	1.86e+00
	32	9.59e-10	1.22e-09	4.02e-09	4.9	4.9	4.6	16.06	2.98e+01
	64	1.44e-09	1.60e-09	2.44e-09	-0.6	-0.4	0.7	40.93	4.76e+02
10^{-4}	4	6.27e-06	7.49e-06	1.74e-05	-	-	-	2.43	
	8	6.80e-07	8.16e-07	1.85e-06	3.2	3.2	3.2	6.32	1.16e-02
	16	4.00e-08	4.78e-08	1.18e-07	4.1	4.1	4.0	15.28	1.86e-01
	32	2.29e-09	2.77e-09	7.21e-09	4.1	4.1	4.0	39.87	2.98e+00
	64	5.79e-11	7.43e-11	2.61e-10	5.3	5.2	4.8	107.24	4.76e+01
	128	1.44e-10	1.61e-10	2.55e-10	-1.3	-1.1	0.0	335.48	7.62e+02
10^{-5}	4	1.57e-05	1.81e-05	2.64e-05	-	-	-	8.23	
	8	5.50e-07	6.73e-07	1.66e-06	4.8	4.7	4.0	18.71	1.16e-03
	16	4.53e-08	5.33e-08	1.26e-07	3.6	3.7	3.7	44.81	1.86e-02
	32	2.64e-09	3.12e-09	7.74e-09	4.1	4.1	4.0	113.75	2.98e-01
	64	1.46e-10	1.78e-10	4.89e-10	4.2	4.1	4.0	344.79	4.76e+00
	128	2.06e-11	2.24e-11	4.12e-11	2.8	3.0	3.6	1068.13	7.62e+01

TABLE 4.3: Empirical convergence rates for a fourth order ADER scheme with several relaxation times ε. N is the number of cells. Errors are computed for variable A. CPU times are reported for all tests. The highlighted row corresponds to the largest number of cells N for which, according to proposition 2.3, the theoretical convergence rate is expected to be achieved.

ADER-O5

ε	N	L^1	L^2	L^∞	$\mathcal{O}(L^1)$	$\mathcal{O}(L^2)$	$\mathcal{O}(L^\infty)$	$t_{CPU}\,[s]$	$\triangle_5$
10^{-2}	4	1.88e-06	2.10e-06	3.37e-06	-	-	-	1.08	
	8	7.88e-08	9.43e-08	1.90e-07	4.6	4.5	4.1	2.60	4.44e+00
	16	1.58e-08	1.75e-08	2.57e-08	2.3	2.4	2.9	6.75	1.42e+02
	32	1.54e-08	1.71e-08	2.47e-08	0.0	0.0	0.1	19.59	4.54e+03
10^{-3}	4	1.61e-06	1.88e-06	3.48e-06	-	-	-	1.32	
	8	6.71e-08	8.22e-08	1.71e-07	4.6	4.5	4.3	3.80	4.44e-01
	16	2.71e-09	3.21e-09	6.61e-09	4.6	4.7	4.7	10.52	1.42e+01
	32	1.54e-09	1.72e-09	2.49e-09	0.8	0.9	1.4	29.37	4.54e+02
10^{-4}	4	1.57e-06	1.94e-06	3.55e-06	-	-	-	3.51	
	8	6.90e-08	8.41e-08	1.73e-07	4.5	4.5	4.4	9.45	4.44e-02
	16	2.29e-09	2.83e-09	6.02e-09	4.9	4.9	4.8	25.46	1.42e+00
	32	1.66e-10	1.86e-10	3.08e-10	3.8	3.9	4.3	77.60	4.54e+01
10^{-5}	4	2.00e-06	2.24e-06	3.34e-06	-	-	-	10.37	
	8	6.93e-08	8.44e-08	1.74e-07	4.8	4.7	4.3	27.91	4.44e-03
	16	2.46e-09	2.92e-09	6.00e-09	4.8	4.9	4.9	78.60	1.42e-01
	32	7.24e-11	9.00e-11	1.95e-10	5.1	5.0	4.9	215.37	4.54e+00
	64	1.71e-11	1.90e-11	3.01e-11	2.1	2.2	2.7	724.42	1.54e+02

TABLE 4.4: Empirical convergence rates for a fifth order ADER scheme with several relaxation times ε. N is the number of cells. Errors are computed for variable A. CPU times are reported for all tests. The highlighted row corresponds to the largest number of cells N for which, according to proposition 2.3, the theoretical convergence rate is expected to be achieved.
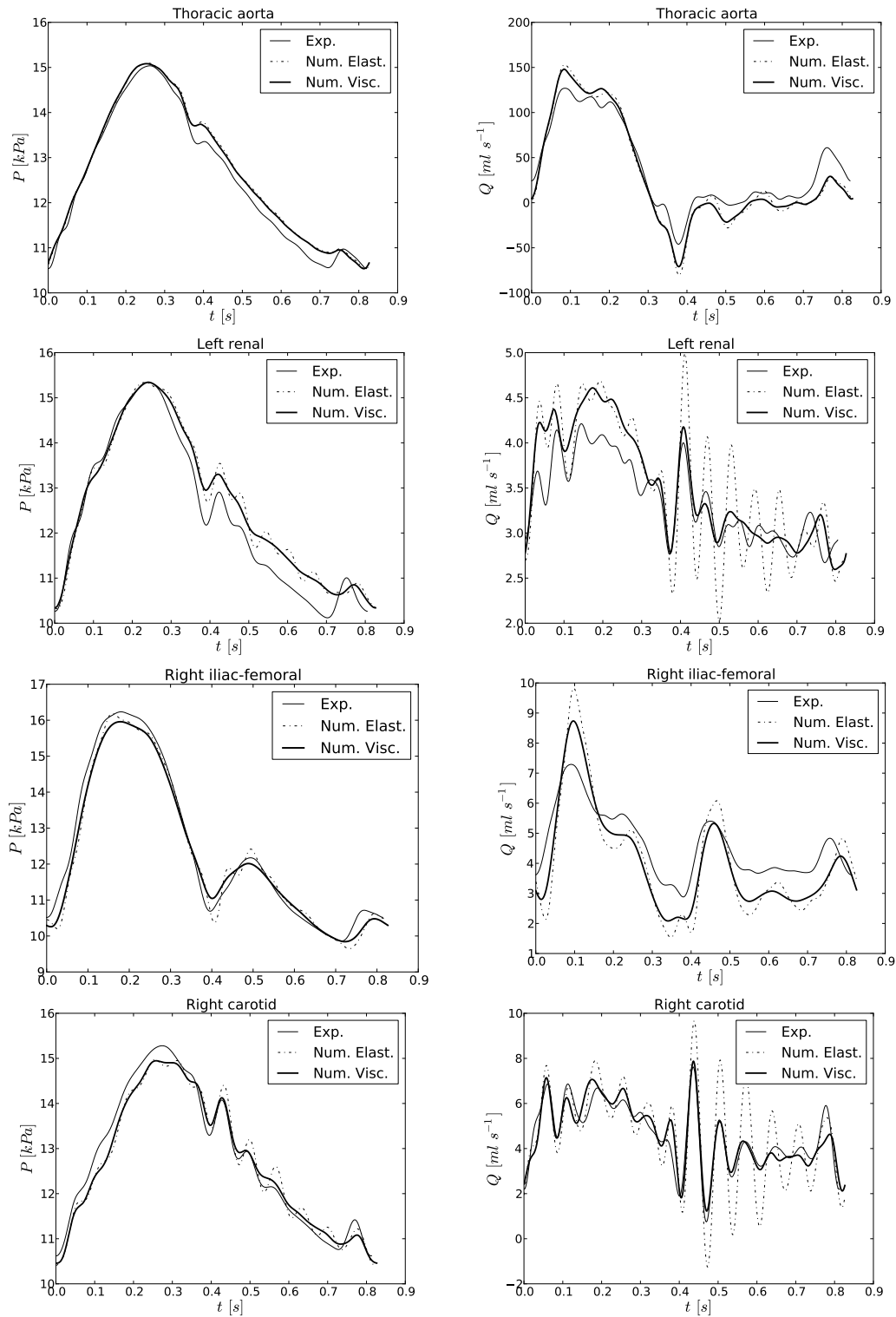
FIGURE 4.1: Comparison of numerical results obtained with a third order numerical scheme for the elastic model (dashed line) and the viscoelastic model with a relaxation time $\varepsilon = 10^{-3} s$ (thick continuous line) and experimental measurements (thin continuous line) reported in [2].
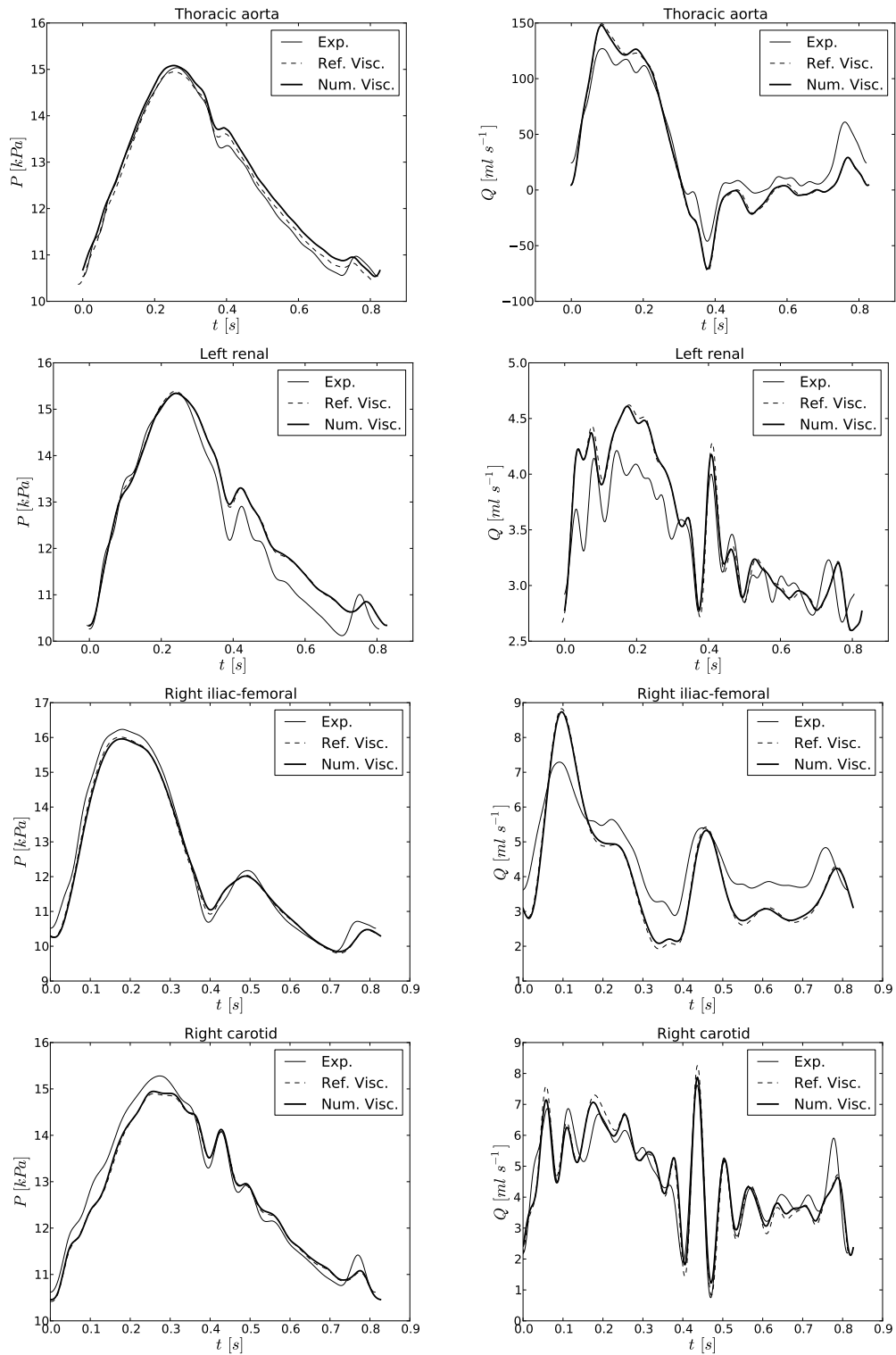
FIGURE 4.2: Comparison of numerical results obtained with our third order numerical scheme for the viscoelastic model with a relaxation time $\varepsilon = 10^{-3}\,s$ (thick continuous line), reference numerical results (dashed line) and experimental measurements (thin continuous line), both reported in [2].
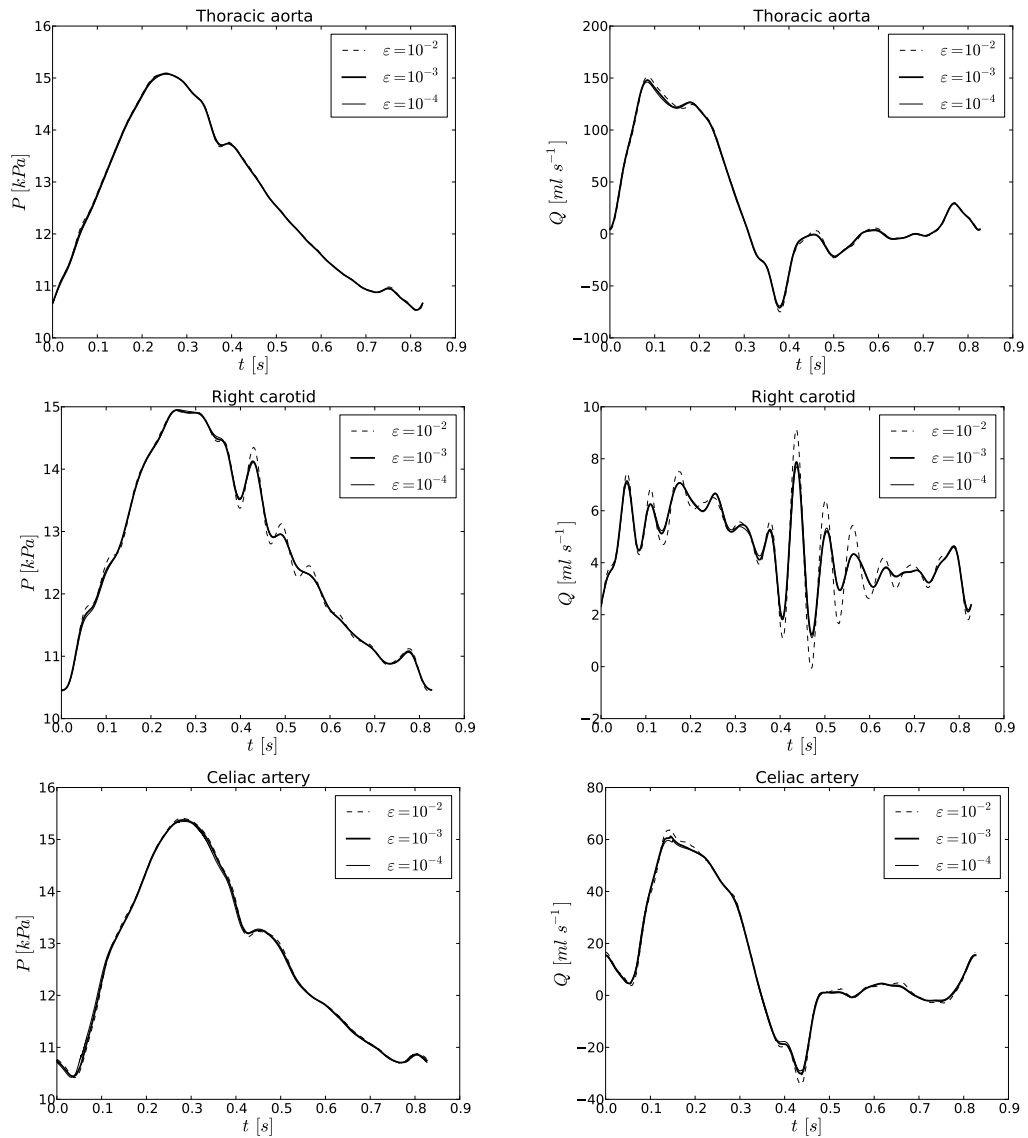
FIGURE 4.3: Comparison of numerical results obtained with our third order numerical scheme for the viscoelastic model with relaxation times $\varepsilon = 10^{-2}\, s$ (dashed line), $\varepsilon = 10^{-3}\, s$ (thick continuous line) and $\varepsilon = 10^{-4}\, s$ (thin continuous line).

Chapter 5

Computational Haemodynamics in Stenotic Internal Jugular Veins

5.1 Introduction

Internal jugular veins (IJVs) are the main paths of discharge of blood from brain towards the heart for most subjects in supine position. When these paths are perturbed, cerebral venous drainage is assured by collateral circles. The potential higher pressures and consequences on cerebral blood flow still need to be fully understood. Chronic CerebroSpinal Venous Insufficiency (CCSVI) is a recently described vascular condition [165, 166] which is characterized by an anomalous cerebral venous drainage. This discovery has given rise to the still controversial hypothesis that such venous pathology can have a role in the aetiology of Multiple Sclerosis [165, 167]. IJV stenoses, defined as occlusions of the blood vessel, represent one of the diagnosis criteria of CCSVI. In this context, stenoses, as other venous anomalies, are assessed *non-invasively* through MRI and Echo-Colour Doppler imaging, which allows visualisation of the morphology of head and neck veins, as well as their haemodynamics. These criteria, however, are strongly dependent on subjective evaluation and often do not take into account specific anatomical features of patients. In particular, stenoses are mainly diagnosed based on the reduction in the cross-sectional area. For example in [165] an IJV is considered stenotic if its area is smaller than 0.3 cm^2 .

In recent years, computational haemodynamics has become a valuable, non-invasive alternative tool for gaining additional insight on patient haemodynamics, in terms of flow patterns, pressure, wall shear stress (see, *e.g.*,[82, 87, 156, 164]), as well as for computing clinically relevant indicators [62, 85].

However, the feasibility of detailed computer simulation is still limited by the prohibitive computational cost, especially when considering a large number of blood vessels and complex topologies. This issue is particularly important when modelling the haemodynamics of veins, as small vessels and minor collaterals (which are usually neglected in arterial blood flow modelling) might be determinant for the physiological flow conditions. In order to reduce the model complexity, 3D models are often used in combination with reduced one-dimensional (1D) models, to simulate haemodynamics in large vessel networks (see *e.g.* [15, 49, 50, 92, 119]), and *lumped parameter* or zero-dimensional (0D) models, which are introduced to take into account the influence of smaller and terminal vessels (see, *e.g.*, [161, 162]). A further application of these reduced models is the simulation of one-dimensional stenoses, modelled as a reduction of vessel cross sectional area [106, 134].

In this chapter we propose a multiscale computational framework to support the diagnosis and the characterization of internal jugular vein stenoses. To this end we will first construct a model of IJV stenosis in a realistic context, by deforming locally a patient-specific geometry, obtained from medical imaging. Through a geometrical multiscale model, taking into account realistic flow rates profiles for the straight sinuses and brachiocephalic veins, we investigate different scenarios involving *occlusions of the IJVs of different severity* and *different morphologies of cerebral veins*. Computationally, stenoses will be characterised through the perturbation of cerebral haemodynamics as function of the reduction of cross sectional area of the jugular veins. Haemodynamics quantities to monitor include pressure increase across the stenosis (a criteria used for diagnosis in *e.g.* [157, 165]), peak velocity increase [86] and wall shear stress. As a result, our study provides the possibility of improving these diagnosis criteria, through a detailed investigation of flow field perturbation and considering variable veins morphology.

The rest of the chapter is organized as follows. In Section 5.2 we describe the tools and the algorithms used for the setup of our *in-silico* stenotic vein model, while the methodologies for the numerical simulations of stenotic jugular veins is described in Section 5.3. Section 5.4 describes the setup of the computational study, while results are presented in Section 5.5 and discussed in detail in Section 5.6. Finally, conclusions are drawn in Section 5.7.

5.2   Anatomical model set up

5.2.1   Data acquisition

Patients data and medical images used in this study have been obtained from the Detroit MR Imaging Center (Wayne State University, Detroit, MI, USA). Data were obtained following the MRI protocols described in [157], specifically designed to assess CCSVI, with particular focus on the imaging of head, neck, and spine (to image the azygos system). The veins of interest for the present study were imaged using *2D time-of-flight MR venography* and *3D contrast-enhanced MR angiography/venography*. Imaged vessels include the superior vena cava, brachiocephalic veins, internal jugular veins and dural sinuses. These vessels are responsible for almost the totality of cerebral venous drainage towards the heart in supine position. Besides anatomical images, 2D phase-contrast MRI (PC-MRI) flow acquisitions have been collected in the neck, positioned at the level of the second and third vertebrae of the cervical spine (C2/C3). Manually defined contours on PC-MRI allowed for quantification of flow variables, including average velocity, positive (toward the brain), negative (toward the heart), and combined volume flow rates [157].

5.2.2   Image segmentation

MRI data has been segmented using the open-source software VMTK (*Vascular Modeling ToolKit*, [6, 143]). In particular, we extracted the surface representation of the two IJVs, right and left brachiocephalic veins, up to the superior vena cava and the subclavian veins (Figure 5.1, left). From the triangulated surface geometries, three-dimensional meshes for computational analysis were obtained using the open-source mesh generator TetGen [138].

5.2.3   Mathematical model of a stenosis

Our goal is to set up a model for blood flow in stenotic veins, able to take into account realistic flow conditions as well as the realistic patients anatomies. To this end we adopted a computational procedure to create *stenotic IJVs* artificially, starting from the geometry of a healthy (i.e. non stenotic) patient. Let us denote with $\mathcal{S}$ a given patient surface geometry (see Figure 5.1, left) obtained from medical imaging, and with Ω the corresponding three-dimensional computational domain. In order to obtain a stenotic geometry, we consider the computational domain Ω as it would be filled with an ideal elastic material at rest. The narrowing of cross sectional area, defining the stenosis,
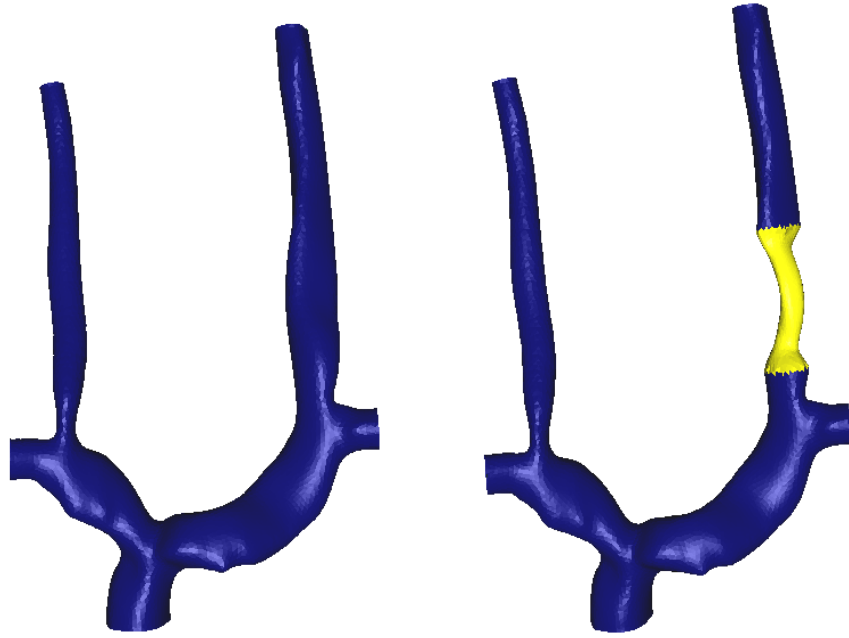
FIGURE 5.1: **Left:** View of a patient surface geometry after segmentation. **Right:** Stenotic geometry, with a local CSA reduction of 77% along the left IJV (in yellow).

is then created applying an external compression force on a small subset Γ_sten of the surface $\mathcal{S}$.

In practice, a stenotic mesh is obtained by deforming the original mesh through a displacement field $\mathbf{d} : \Omega \to \mathbb{R}^3$, solution of the partial differential equation give by

$$\begin{cases} \nabla \cdot \sigma_e(\mathbf{d}) = 0, \text{ on } \Omega\ , \\ \qquad\quad \mathbf{d} = \mathbf{0}, \text{ on } \partial\Omega/\Gamma_\text{sten}\ , \\ \sigma_e(\mathbf{d})\mathbf{n} = -\mathbf{f_n}, \text{ on } \Gamma_\text{sten}\ , \end{cases} \qquad (5.1)$$

where $\sigma_e(\mathbf{d})$ plays the role of the second Piola-Kirchhoff stress tensor for an elastic material, related to the $\boldsymbol{\nabla}\mathbf{d}$ through a constitutive law, *e.g.*

$$\sigma_e(\mathbf{d}) = \kappa \left(\boldsymbol{\nabla}\mathbf{d} + \boldsymbol{\nabla}\mathbf{d}^T\right), \ \kappa > 0$$

(for a linear elastic model). In (5.1), $\mathbf{f_n}$ is a normal force, whose entity (to be tuned according to the particular geometry) defines the reduction of the cross sectional area, while κ is a free parameter which corresponds to the elastic modulus of the ideal material.

Equation (5.1) is solved numerically using piecewise linear finite elements in a preprocessing step. From the solution of (5.1), the deformed surface is recovered adding the displacement $\mathbf{d}$ to the original mesh. Figure 5.1 (right) shows the result of this procedure for a CSA reduction of 77%.

5.3   Computational haemodynamics

5.3.1   Three-dimensional blood flow modelling

In order to simulate the blood flow in internal jugular veins, we consider the boundary of the computational domain Ω partitioned as

$$\partial\Omega = \Gamma_{\text{in}} \cup \Gamma_{\text{wall}} \cup \Gamma_{\text{out}},$$

denoting, respectively, the *inflow* boundaries, the *vessel wall* and the *outflow* boundaries.

The images have been acquired in supine position, when the internal jugular veins represent the main discharge path for cerebral blood flow, and have relatively low volume changes during the cardiac cycle. Hence, as a first approximation, we consider the domain Ω to be constant in time. Furthermore, as MRI-derived flow rate wave forms exhibited a marked pulsatility in phase with the cardiac cycle (time scale less than one second), the blood flow within the domain of interests can be assumed to behave as a Newtonian fluid (see e.g. the discussion in [49, chapter 6] and [51])[1]

Thus, we describe the blood flow in Ω in terms of the velocity $\mathbf{u} : \Omega \times \mathbb{R}^+ \to \mathbb{R}^3$ and the pressure $p : \Omega \times \mathbb{R}^+ \to \mathbb{R}$ solution of the incompressible Navier-Stokes equations

$$\begin{cases} \rho\partial_t\mathbf{u} + \rho\mathbf{u} \cdot \nabla\mathbf{u} + \nabla p - 2\mu\,\text{div}\,\boldsymbol{\epsilon}(\mathbf{u}) = 0 & \text{in} \quad \Omega, \\ \text{div}\,\mathbf{u} = 0 & \text{in} \quad \Omega, \\ \mathbf{u} = \mathbf{u}_{\text{in}} & \text{on} \quad \Gamma_{\text{in}}, \\ \mathbf{u} = 0 & \text{on} \quad \Gamma_{\text{wall}}, \\ \boldsymbol{\sigma}(\mathbf{u}, p)\mathbf{n} = p_{\text{out}} & \text{on} \quad \Gamma_{\text{out}}. \end{cases} \qquad (5.2)$$

In (5.2) ρ stands for the density of the fluid ($1060\,\text{Kg/m}^3$) and the fluid Cauchy-stress tensor is given by

$$\boldsymbol{\sigma}(\mathbf{u}, p) = -p\mathbf{I} + 2\mu\epsilon(\mathbf{u}), \quad \boldsymbol{\epsilon}(\mathbf{u}) \overset{\text{def}}{=} \frac{1}{2}\left(\boldsymbol{\nabla}\mathbf{u} + \boldsymbol{\nabla}\mathbf{u}^{\mathsf{T}}\right),$$

μ being the dynamic viscosity of the fluid ($4 \cdot 10^{-3}\,\text{Pa} \cdot \text{s}$).

Moreover, $\mathbf{u}_{\text{in}}$ and p_{out} represent a given inlet velocity and a given outlet pressure, imposed at inflow and outflow boundaries, respectively. In order to simulate a physiologic regime, these values have been prescribed based on realistic flow rate and pressure profiles (see Section 5.4.1).

---

[1] This assumption was also verified *a posteriori*, computing the value of shear rates from the numerical results of exploratory simulations, which resulted to be always larger than $1\,s^{-1}$, below which non-Newtonian effects becomes important [49, chapter 6].

5.3.1.1   Numerical solution

In order to numerically solve problem (5.2), we consider first a time-discretization based on a Chorin-Temam projection scheme [27, 61, 142]. In this approach, velocity and pressure are computed separately in two sub-steps. Let t_n denote the time at the n-th time step performed with an uniform time step τ. For a given initial condition $\mathbf{u}^0 = \mathbf{u}_0$, each time iteration consists of solving the two problems:

- an advection-diffusion problem for the velocity $\mathbf{u}^{n+1}$, obtained by relaxing the incompressibility constrain

$$
\begin{cases}
\rho\dfrac{\mathbf{u}^{n+1} - \mathbf{u}^n}{\tau} + \rho\mathbf{u}^n \cdot \boldsymbol{\nabla}\mathbf{u}^{n+1} - 2\mu\boldsymbol{\nabla} \cdot \boldsymbol{\epsilon}(\mathbf{u}^{n+1}) + \nabla p^n = \mathbf{0} & \text{in} \quad \widehat{\Omega}, \\
\mathbf{u}^n = \mathbf{u}_{\text{in}}(t_{n+1}) & \text{on} \quad \Gamma_{\text{in}}, \\
2\mu\epsilon(\mathbf{u}^{n+1})\mathbf{n} = \mathbf{0} & \text{on} \quad \Gamma_{\text{out}}, \\
\mathbf{u}^n = \mathbf{0} & \text{on} \quad \Gamma_{\text{wall}}.
\end{cases}
\tag{5.3}
$$

- a Poisson problem for the pressure p^{n+1}, obtained by projecting the velocity onto a divergence-free space

$$
\begin{cases}
-\dfrac{\tau}{\rho}\Delta p^{n+1} = -\boldsymbol{\nabla} \cdot \mathbf{u}^{n+1} & \text{in} \quad \widehat{\Omega}, \\
\dfrac{\tau}{\rho}\dfrac{\partial p^{n+1}}{\partial \mathbf{n}} = 0 & \text{on} \quad \Gamma_{\text{in}} \cup \Gamma_{\text{wall}}, \\
p^{n+1} = p_{\text{out}}^{n+1} & \text{on} \quad \Gamma_{\text{out}}.
\end{cases}
\tag{5.4}
$$

Problems (5.3)-(5.4) are solved using continuous piece-wise linear finite elements on the tetrahedral mesh.

5.3.1.2   Boundary conditions of the 3D model

In the numerical studies presented in Section 5.4–5.5, the inlet boundary Γ_{in} is composed by the (left and right) internal jugular veins and by the (left and right) subclavian veins (see also Figure 5.2, left). At these locations we impose flow rates via prescribing in (5.3) a *plug* velocity profile $\mathbf{u}_{\text{in}}$. At the outflow boundary (superior vena cava), we prescribe a given pressure profile, which is imposed through a Dirichlet boundary condition on the pressure in equation (5.4). Further details on the physiological inlet flow rates and outlet pressure profiles used in the simulation will be provided in Section 5.4.1. Additionally, a recently proposed regularization method [13] for backflow stabilization has been used, in order to prevent numerical instability at the outflow boundary.

5.3.2 One-dimensional blood-flow model

Due to their relatively high computational cost, full 3D fluid models can be currently used to resolve the blood flow only *locally*, i.e. focusing on a limited number of vessels. In order to investigate the cerebral haemodynamics from a more general point of view, one has to reduce the complexity of the original Navier-Stokes equations (5.2). This can be done considering the cardiovascular system as a network of interconnected and compliant vessels, in which the flow is assumed to be one-dimensional. Integrating the mass and momentum conservation equations (5.2) over each pipe cross section one obtains (see, *e.g.*, [124])

$$
\begin{cases}
\dfrac{\partial A}{\partial t} + \dfrac{\partial}{\partial x}\left(uA\right) = 0, \\
\dfrac{\partial(uA)}{\partial t} + \dfrac{\partial}{\partial x}\left(\hat{\alpha}u^2 A\right) + \dfrac{A}{\rho}\dfrac{\partial p}{\partial x} = f,
\end{cases}
\tag{5.5}
$$

where $A(x,t)$ is the cross sectional area along the longitudinal axis, $u(x,t)$ the cross-sectional averaged axial velocity, $p(x,t)$ the average internal pressure over the cross-section, $f(x,t)$ stands for the friction force per unit length, and the parameter $\hat{\alpha}$ depends on the shape of the velocity profile along the cross section (usually assumed equal to 1, which corresponds to a constant velocity over the cross section). As in (5.2), ρ denotes the blood density.

System (5.5) for the three unknowns A, u and p requires a closure condition. This is usually accomplished via a *tube law* involving a pressure-area relation. In this manner the vessel deformation is related to changes in transmural pressure [121], namely

$$
p(x,t) = p_e(x,t) + K(x)\phi(A(x,t), A_0(x)),
\tag{5.6}
$$

with

$$
\phi(A, A_0) = \left(\frac{A}{A_0}\right)^m - \left(\frac{A}{A_0}\right)^n.
\tag{5.7}
$$

Here $p_e(x,t)$ denotes the external pressure, $K(x)$ is the bending stiffness of the vessel wall (related the Young modulus, the wall thickness, and the vessel radius in an unloaded reference configuration), while $A_0(x)$ denotes the cross-sectional area at reference pressure.

5.3.2.1 Numerical scheme for the 1D model

We reformulate (5.5) in quasilinear form as proposed in [151]:

$$
\partial_t \mathbf{Q} + \mathbf{A}(\mathbf{Q})\partial_x \mathbf{Q} = \mathbf{S}(\mathbf{Q}),
\tag{5.8}
$$

in terms of the unknowns

$$\mathbf{Q} = \left[A, q, K, A_0, p_e\right]^T,$$ (5.9)

where $q = Au$ is the mass flow rate. Now the source term vector in (5.8) is

$$\mathbf{S}(\mathbf{Q}) = [0, -f, 0, 0, 0]^T$$ (5.10)

and the coefficient matrix $\mathbf{A}(\mathbf{Q})$ is given by

$$\mathbf{A}(\mathbf{Q}) = \begin{bmatrix} 0 & 1 & 0 & 0 & 0 \\ c^2 - u^2 & 2u & \frac{A}{\rho}\phi & K\frac{A}{\rho}\frac{\partial\phi}{\partial A_0} & \frac{A}{\rho} \\ 0 & 0 & 0 & 0 & 0 \\ 0 & 0 & 0 & 0 & 0 \\ 0 & 0 & 0 & 0 & 0 \end{bmatrix},$$ (5.11)

$c = \sqrt{\frac{A}{\rho}K\frac{\partial\phi}{\partial A}}$ being the wave speed. See [151] for the details of the derivation and for a detailed mathematical analysis of the system.

We solve numerically system (5.8) using a high-order ADER finite volume scheme [150], with the DET solver for the generalised Riemann problem [41]. As is well known, all GRP solvers require in addition a classical Riemann solver (piece-wise constant data), see [100]; to this end here we adopt the Dumber-Osher-Toro (DOT) scheme [46] a modification described in [104]. For a full description of the global, closed-loop multi-scale model see [105]. For background on the ADER approach and recent developments see [147] (Chapters 19 and 20) and references therein.

5.3.3 Geometrical multiscale model

To take into account the effect of the upstream veins on the haemodynamics of stenotic IJVs, we consider a multi-scale model combining the local three-dimensional finite element solver for stenotic IJVs with a one-dimensional network containing the sigmoid sinuses, the transverse sinuses, the straight and the sagittal sinuses (see Figure 5.2).

From the computational point of view, the coupled model consists of solving equations (5.2) and equations (5.8) on two separate domains. The outgoing fluxes from the one-dimensional model, at each 3D-1D interface, are used to impose inlet boundary conditions for the velocity in (5.2), prescribing a 3D velocity profile satisfying

$$q_{3D}^{n+1} = q_{1D}^{n+1},$$
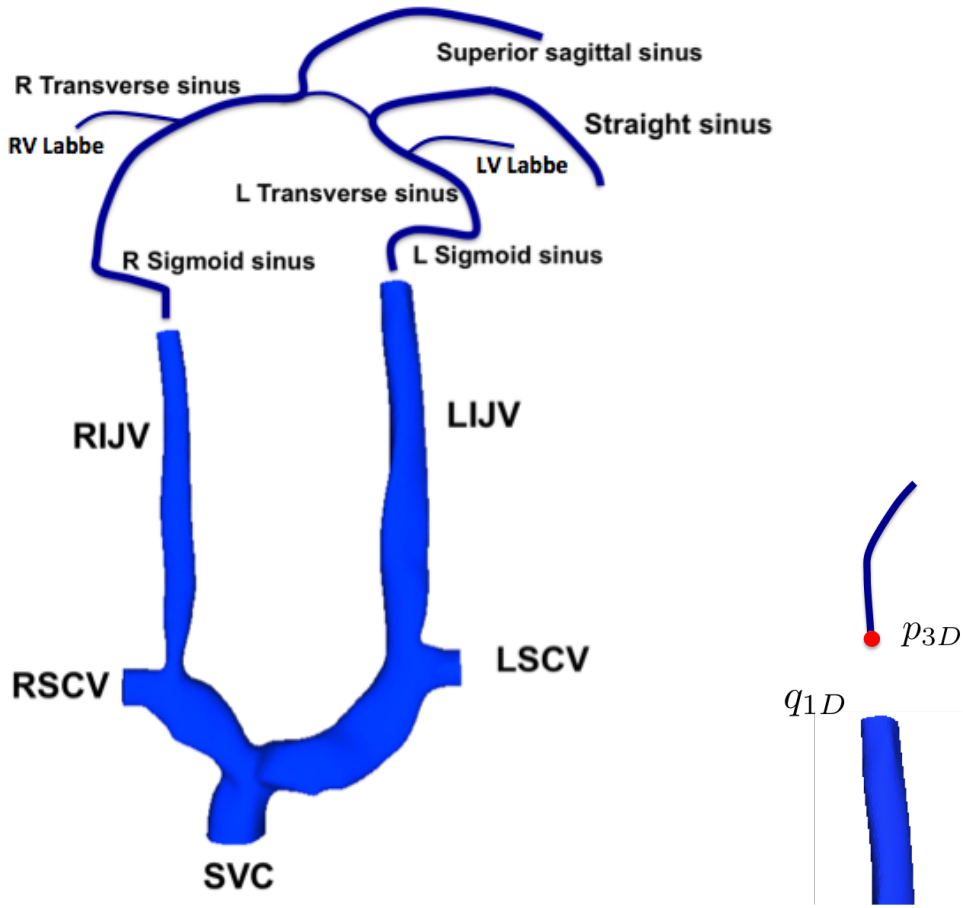
FIGURE 5.2: **Left.** A sketch of the multiscale 3D-1D model. Fluid 3D simulations are used for the left and right internal jugular veins, denoted by LIJV and RIJV respectively, up to the left and right subclavian veins (LSCV and RSCV respectively) and the superior vena cava (SVC), while a 1D network takes into account the response up to the level of traight and superior sagittal sinuses. **Right.** The coupling between dimensionally heterogeneous models is acomplished by imposing the outgoing 1D flow to the 3D model (5.2), and imposing the resulting pressure as boundary condition for (5.8), at terminal segments of the 1D network.

while the resulting 3D pressures are used to modify the boundary conditions of problem (5.8) at the end of the network (Figure 5.2, right). The pressure coupling is implemented following the approach proposed in [119] (in the form of a preconditioned Richardson iteration), setting the 1D pressure as

$$p_{1D}^{n+1} = \gamma p_{3D}^{n+1} + (1 - \gamma)p_{1D}^{n}$$

for a parameter $\gamma \in (0, 1]$.

5.3.4   Computation of Wall Shear Stress

Besides the velocity and pressure fields, another quantity of clinical relevance is the Wall Shear Stress (WSS), defined as the tangential component of the normal shear stress at the vessel wall:

$$\tau_{\text{WSS}} \overset{\text{def}}{=} \tau_{\mathbf{n}} - (\tau_{\mathbf{n}} \cdot \mathbf{n})\mathbf{n} \tag{5.12}$$

(where $\tau_{\mathbf{n}} = \mathbf{n}^T \nabla \mathbf{u}$ denotes the normal shear stress).

In fact, it has been shown that an abnormal WSS might affect the biology of endothelial cells, playing a relevant role in the development of pathologies and in the triggering of inflammatory responses (see, *e.g.*, [11, 82, 116]).

In this context, an important mechanical indicator, monitoring the oscillatory behaviour in time of WSS, is the so-called Oscillatory Stress Index (OSI), defined as

$$\text{OSI}_{\text{WSS}} \overset{\text{def}}{=} \frac{1}{2} \left(1 - \frac{\|\langle \tau_{\text{WSS}} \rangle\|}{\langle \|\tau_{\text{WSS}}\| \rangle} \right) , \tag{5.13}$$

where $\langle \cdot \rangle$ stands for the average value over a period (cardiac cycle). Namely, the OSI quantifies the WSS vector deflection from blood flow predominant direction (varying from 0.0, for no-cyclic variation of WSS vector, to 0.5, for 180 degrees deflection of WSS direction).

In computational haemodynamics, the calculation of accurate wall shear stresses is a relatively complex issue, as it strongly depends on the level of approximation of the surface geometry (hence on the quality of the medical images). Using piecewise linear finite elements for the three-dimensional fluid solutions (Section 5.3.1.1), the velocity on the surface is approximated by linear polynomials, which results in a piecewise constant distribution of gradients. In order to reconstruct a smoother stress distribution at the surface nodes, we have computed nodal approximations of the velocity gradient considering all the neighbouring mesh points using then the smoothing and approximation procedure recently described in [32].

5.4   Case studies

Starting from a patient-specific reference domain for a healthy subject (not diagnosed as having a stenosis), we consider different set-ups of the computational model, which are depicted in Figure 5.3. First, we create artificial stenosis of increasing severity, using the procedure described in Section 5.2.3, obtaining CSA reductions from 20% up to 77% at the bottom of the left IJV (Figure 5.3, bottom). At the same time, in
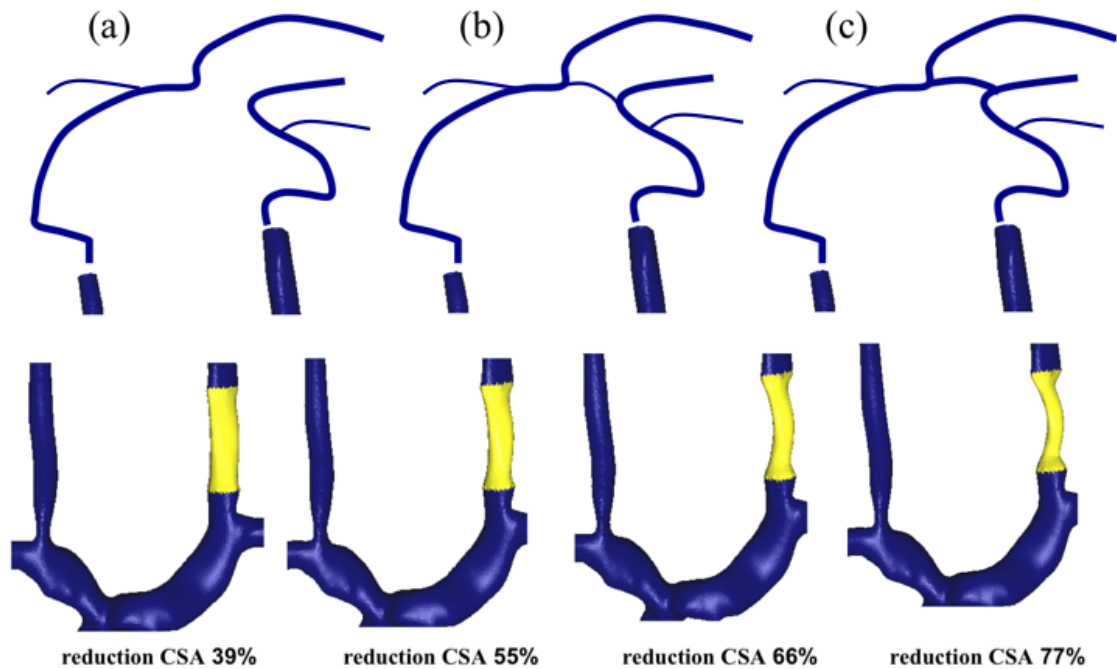
FIGURE 5.3: Model setups considered in our study. At the top, the different one-dimensional networks modelling the cerebral veins up to the straight and superior sagittal sinuses, considering the cases of disconnected, weakly connected and strongly connected sinuses (a, b and c, respectively). At the bottom, different stenotic geometries (with reduction of CSA of 39%, 55%, 66% and 77%, respectively) obtained perturbing the original patient-specific mesh at the bottom of the left IJV.

order to take into account the effect of upstream veins, we coupled the computational 3D domain to a 1D network of compliant vessels up to the Straight Sinus (STS) and Superior Sagittal Sinus (SSS), through the geometrical multiscale method described in Section 5.3.3. Anatomical studies have shown that in about 50% of the population the SSS is drained by both transverse sinuses, whereas in the remaining cases drainage is unilateral [54]. This aspect might play a relevant role in the presence of a stenosis, as the connection between sinuses represents an important alternative discharge path in case of stenosis (as will be illustrated in Sections 5.5.2–5.5.3). Hence, in order to account for the variability of the intracranial venous network topology, three different versions of the multi-scale model have been considered:

- no connection between transverse sinuses (Figure 5.3a);

- weak connection (Figure 5.3b);

- strong connection (Figure 5.3c).

These different upstream models have been investigated in combination with all the different stenotic configurations.

5.4.1   Physiological boundary conditions

On each computational (3D-1D) domain, blood flow has been simulated through the coupled approach described in Section 5.3. Flow rates at inlet boundaries of the one-dimensional network, that is at the inlet of STS, SSS, VLs and SCVs, and pressure at the SVC outlet boundary (depicted in Figure 5.4) have been prescribed using values obtained from a closed-loop one-dimensional model of the cardiovascular system [105]. See [4, 137] for more details about settings of the network solver regarding the treatment of junctions and boundary conditions.

5.5   Simulation results

This section presents the outcome of our computational study on the effect of a progressive IJV stenosis. In particular, we assessed the impact of an IJV stenosis according to

- the maximum pressure drop, defined as the pressure difference between IJV inlet and SVC outlet, as measured in [166],

- the peak velocity ratio, which refers to the ratio between the maximum pre-stenotic and post-stenotic velocities [86],

- the perturbation induced on the flow, in terms of WSS and OSI.

Finally, we provide computational evidence on the mesh independence of reported numerical results.

5.5.1   Computational results *vs* MRI-derived flow rate measurements

In Figure 5.5, we compare numerically computed flow rates at C2/C3 level for the *weak confluence* configuration (without stenosis) *vs* PC-MRI flow quantification data for the same patient. The qualitative and quantitative agreement for the left IJV is very satisfactory, both for the average flow (computed value of 6.68 ml/s versus a measured flow of 6.98 ml/s) and for the pulsatility. In the case of the right IJV we obtain a computed average flow rate of 2.94 ml/s versus a measured average flow of 4.18 ml/s. Moreover the computed flow rate pulsatility for this vessel is lower than the one obtained from PC-MRI measurements. This mismatch can be explained by the fact that the mass entering the domain is given by prescribed boundary conditions in intracranial 1D vessels and SCVs. In reality, many small collaterals, not considered in this model, contribute
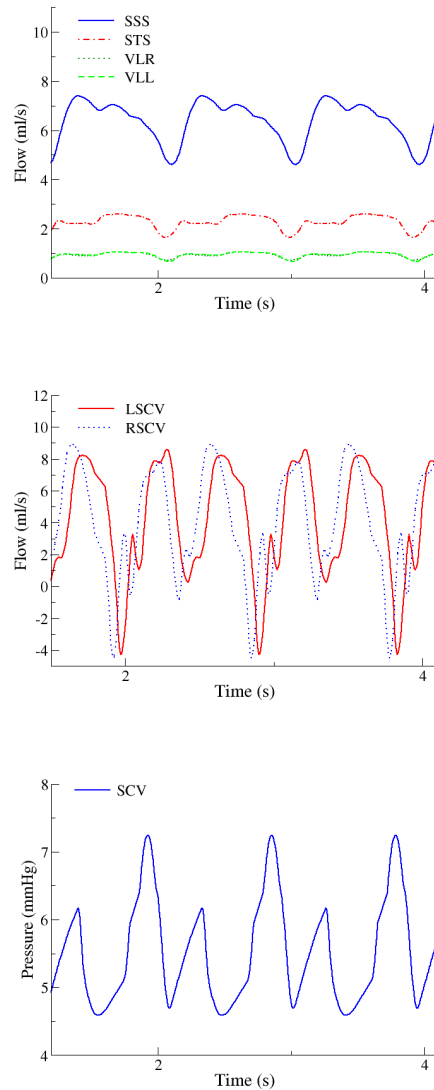
FIGURE 5.4: Flow rates and pressure used as boundary conditions for the 3D-1D computational model [105]. **Top:** Flow rates for the SSS, STS, left Vein of Labbe (VLL) and right Vein of Labbe (VLR). **Middle:** Flow rates for the left Subclavian Vein (LSCV) and right Subclavian Veins (RSCV). **Bottom:** Pressure profile imposed at the Superior Vena Cava (SVC).

to an increase of flow rate along the IJV as one moves towards the heart. In any case, due to the simplifications adopted in this model and to the absence of patient-specific boundary conditions, we consider the agreement between MRI-derived and computed flow rates as satisfactory for the purposes of this work.
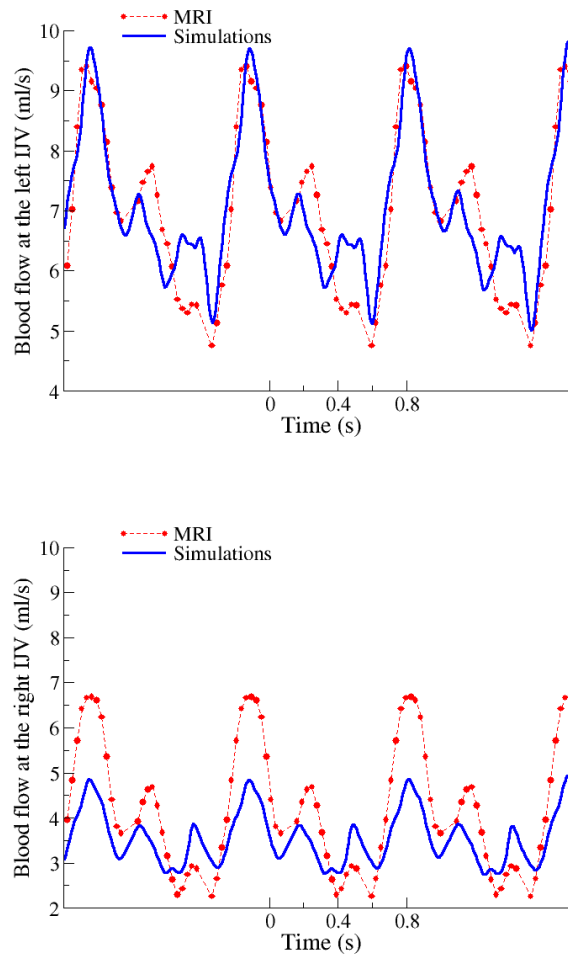
FIGURE 5.5: **Top:** Comparison of numerically computed flow rate (Simulation, full line) and PC-MRI measurements (MRI, dashed line) for the left IJV at C2/C3 level. **Bottom:** Comparison of computed flow rate (Simulation, full line) and PC-MRI measurements (MRI, dashed line) for the right IJV at C2/C3 level.

5.5.2   Intracranial venous pressure increase

Figure 5.6 shows the maximum pressure drop across the stenotic vein, throughout one cardiac cycle, as function of the variation of the CSA, which represents the variation of the severity of the left IJV stenosis; results are shown for all three configurations of the confluence of sinuses considered. Computed pressure drop is in agreement with results reported in [166], with pressure drops larger than 1.3 mmHg for a CSA reduction higher than 50%, and with maximum values of about 2.5 mmHg. We note that in a normal subject the reported pressure drop is about 1 mmHg.

However, the result is highly depending on the morphology of cerebral veins. We remark that strongly connected left and right transverse sinuses have regulatory effects, allowing
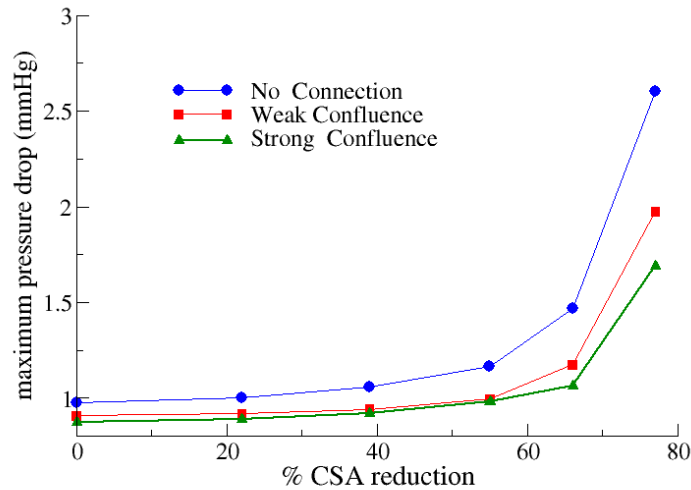
FIGURE 5.6: Maximum pressure drop (mmHg) across the stenotic IJV versus the reduction (in %) of CSA.

a redistribution of flow between the two IJVs. This aspect is further evidenced in Figure 5.7 (right). While flow is deviated from the left to the right IJV, pressure drop decreases in the stenotic left IJV (LIJV) due to the collateral path, and increases in the stenotic right IJV (RIJV), which is receiving more flow. For comparison, we simulated a pathological case where stenoses are present in both right and left IJVs (Figure 5.7, left), with CSA reductions of 77% (from 105 mm^2 to 24 mm^2) and 50% (from 40 mm^2 to 20 mm^2), respectively (Figure 5.7, left). The results are shown in Figure 5.7 (right). In this situation, the augmented resistance of the right IJV reduces the regulatory effect of the confluence of sinuses yielding a higher pressure also in the right IJV.

Finally, Figures 5.8 and 5.9 depict the computed pressures in the SSS and STS for the non-stenotic case, and for the case of stenoses in both IJVs. The maximum pressure increase in the SSS reaches 4 mmHg (from 9 mmHg to 13 mmHg) in the morphology without connection, while it remains relatively constant when transverse sinuses are connected. On the other hand, one can observe that a strong transverse sinuses connection, while reducing the pressure in the SSS, yields a pressure increases in the STS.

5.5.3   Flow perturbation

The perturbation of the flow field (upstream and downstream) due to the stenosis is also a relevant aspect, which might have clinical implications. In Figure 5.10 (top) we show the peak velocity ratio, i.e. the ratio between pre-stenotic and post-stenotic velocity,
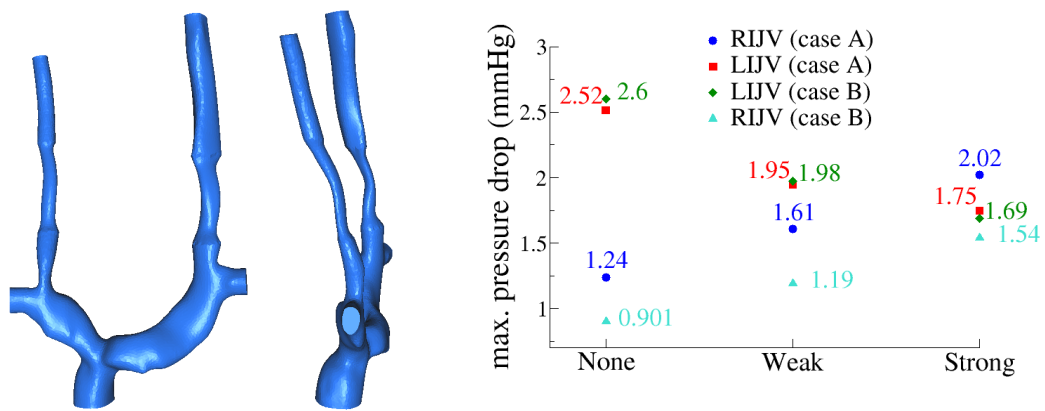
FIGURE 5.7: **Left:** Configuration with stenoses in both IJVs (frontal and lateral views). CSA reduction: 50% (right IJV) and 77% (left IJV). **Right:** Maximum pressure drop (for both left and right IJVs) depending on the degree of connection of confluence of sinuses, comparing the case of a single stenosis, case A (left IJV, CSA reduction of 77%) and stenoses in both IJVs, case B (CSA reduction of 50% – right IJV – and 77% – left IJV).
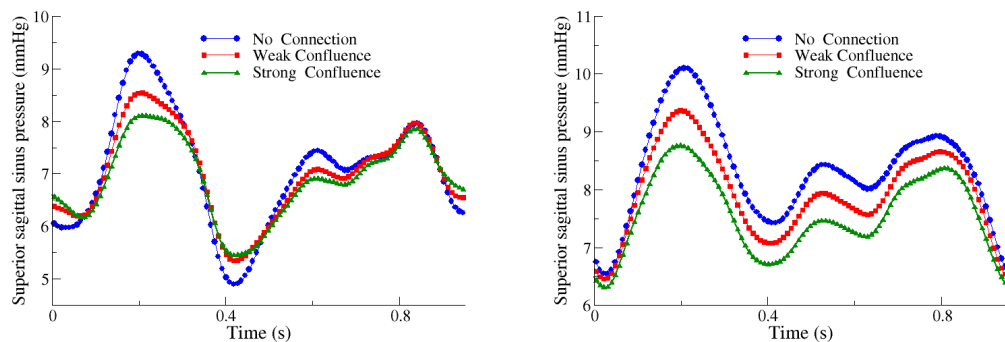
FIGURE 5.8: Computed pressure (in mmHg) in the SSS for different configurations of the confluence of sinuses. **Left:** Original geometry (no CSA reduction). **Right:** Left IJV CSA reduction of 77%.

for the different stenotic configuration and for the different considered topologies. In all cases, values are larger than 2.5 for CSA reduction higher than 60%. These values are in agreement with the results of [86], where a peak velocity ratio of 2.5 was used to characterise stenosis in the SVC. On the other hand, the behaviour is almost independent from the existence of sinuses connection. In fact the peak velocity ratio is not very sensitive to maximum pressure drop magnitude for different configurations of dural sinuses, as we can see in Figure 5.10 (bottom).

Next, Figure 5.11 shows a snapshot of the streamlines near the stenotic region. One can clearly observe flow disturbances in the post-stenotic region, which, for severe stenosis degree, might lead to flow recirculation. A further quantity that might be perturbed by
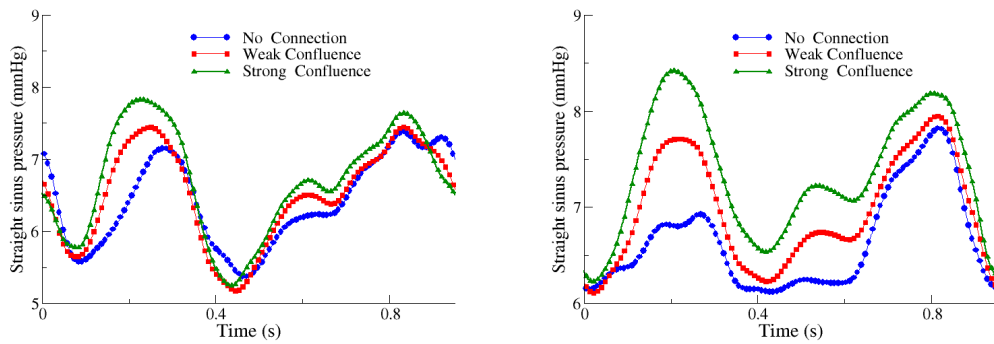
FIGURE 5.9: Computed pressure (in mmHg) in the STS for different configurations of the confluence of sinuses. **Left:** Original geometry (no CSA reduction). **Right:** Left IJV CSA reduction of 77%.

the presence of a stenosis is the WSS, depicted in Figures 5.12 to 5.14 for three selected points in space, located before, within and after the stenosis, respectively. While inside the stenotic area the WSS increases accordingly to the reduction of CSA (expected, as a consequence of higher peak velocity), one can observe an irregular behaviour when the occlusion reaches 50%, which results in a lower post-stenosis WSS.

The same effect can be observed from a different perspective in Figure 5.15, which shows the WSS over the surface of the 3D domain at time 0.2 s (corresponding to the maximum WSS in the non-stenotic configuration). Furthermore, Figure 5.16 depicts the surface OSI, an indicator of WSS perturbation, which quantifyies the change in the periodic behaviour of shear stresses. Although the stenosis seems to have a moderate influence, due to the fact that the flow in the IJVs is mainly unidirectional, the area of highest perturbation is the one immediately after the stenosis and includes the brachiocephalic vein.

5.5.4   Computational domain and mesh independence study

Here we carry out a mesh refinement exercise by considering a sequence of three dimensional meshes: *Mesh 1* (66K tetrahedra), *Mesh 2* (135 K tetrahedra) and *Mesh 3* (240K tetrahedra). The corresponding results show that the change in the solution from *Mesh 2* to *Mesh 3* is virtually negligible. Computations are carried out for the stenotic geometry with a 66% CSA reduction and weakly connected transverse sinuses.

Figure 5.17 shows the result for all three meshes, for the pressure at the inlet of the left and right internal jugular veins. It is clearly seen that the computational results from *Mesh 2* and *Mesh 3* are almost indistinguishable. Most results in this chapter are from
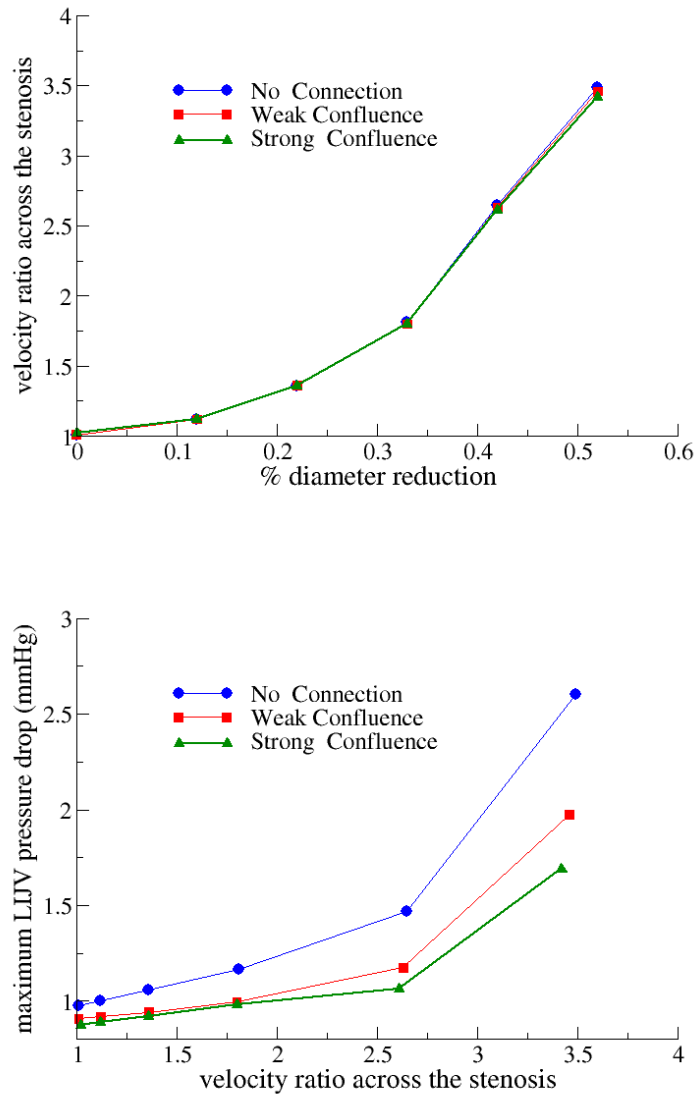
FIGURE 5.10: **Top:** Peak velocity ratio across the stenosis as function of relative reduction of its diameter. **Bottom:** Maximum pressure drop on LIJV as function of peak velocity ratio.

Mesh 2 and note that the pressure at the inlet plays a key role in our study. Moreover, figure 5.18 shows the pressure history at the point of coordinates (13.1, 13.7, 13.0), close to the pre-stenotic zone. Again the results support our observation that the spatial discretization of *Mesh 2* implies reliable solutions of the partial differential equation.
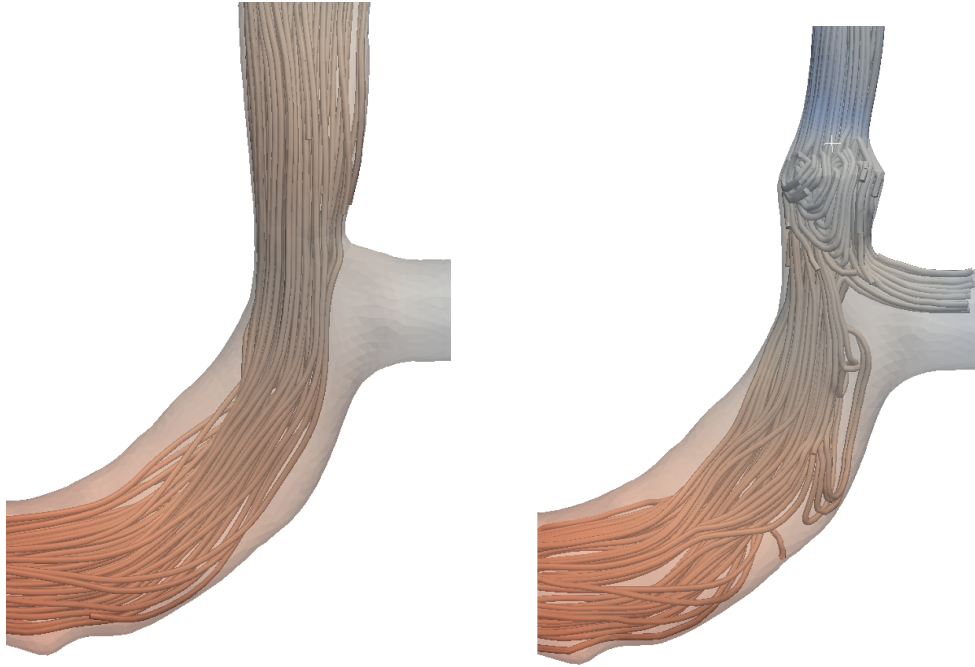
FIGURE 5.11: Snapshot of the streamlines near the stenotic area (time 0.2 s) for the simulation without confluence of transverse sinuses. **Left:** Non-stenotic configuration (CSA = 105 mm^2). **Right:** Configuration with the largest occlusion (reduction of 77%, CSA = 35 mm^2).

5.6   Discussion

5.6.1   General remarks

Despite the several simplifications at the base of our computational model, we obtain a satisfactory agreement between computed IJV flow rates and patient-specific PC-MRI measurements (see Figure 5.5). The best match has been obtained for the left IJV flow rate for a *weak connection* of both transverse sinuses, which in this case corresponds to the patient morphology observed in the MRI images. It is worth noticing that this vein is the one where we focus our attention throughout this study. On the other hand, since many tributaries and collaterals that might contribute to cerebral venous flow are not taken into account in the present study, the model seems to underestimate flow in the right IJV. Moreover, as the following sections will show, we note that for stenotic IJVs our computational results are in agreement with reported values for pressure drop [166] and peak velocity ratio [86].
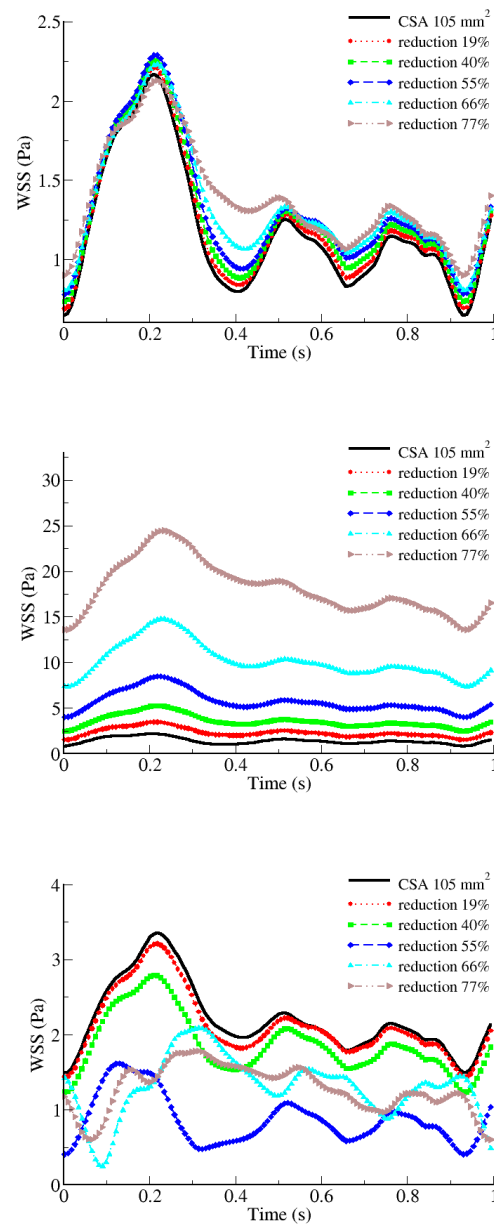
FIGURE 5.12: Behaviour in time of WSS at three selected points for the *no connection* confluence of sinuses configuration. **Top:** before; **Middle:** inside and **Bottom:** after the stenotic region.

5.6.2   Pressure increase and importance of intracranial venous topology

The relation between CSA reduction and maximum pressure drop appears to behave exponentially when the CSA reduction is larger than 60% (Figure 5.6). This finding supports the indications given in a recent clinical study based on ultrasound imaging
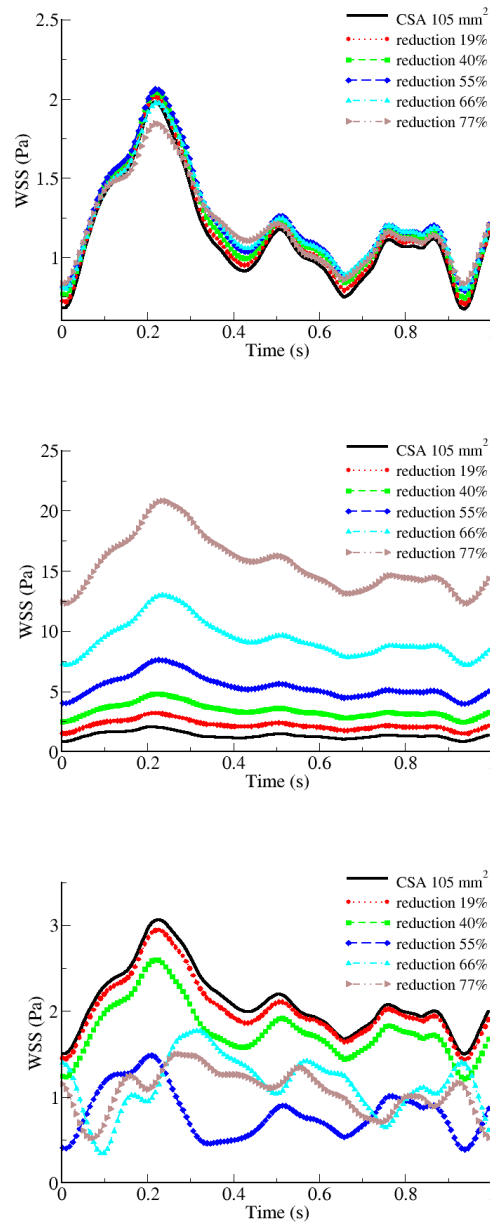
FIGURE 5.13: Behaviour in time of WSS at three selected points for the *weak connection* confluence of sinuses configuration. **Top:** before; **Middle:** inside and **Bottom:** after the stenotic region.

[86], in which only a CSA reduction higher than 75% was considered to be clinically significant.

On the other hand, we observe that the magnitude of the maximum pressure drop appears to be strongly correlated to the intracranial venous configuration. This is an aspect that, due to the technical complications in imaging minor veins, makes their investigation difficult, from an experimental point of view. The *no connection* configuration yields the most pronounced pressure increase (Figure 5.6). For instance, a CSA
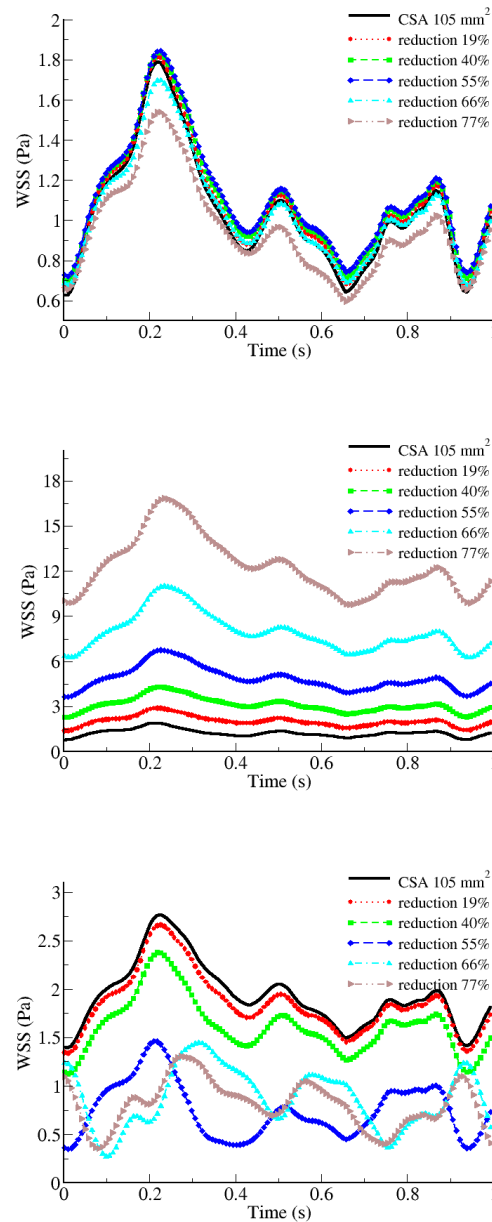
FIGURE 5.14: Behaviour in time of WSS at three selected points for the *strong connection* confluence of sinuses configuration. **Top:** before; **Middle:** inside and **Bottom:** after the stenotic region.

reduction of 66% leads to a maximum pressure drops of 1.06, 1.17 and 1.47 (mmHg), for confluence of sinuses with *strong connection*, *weak connection* and *no connection*, respectively. This behaviour is, to some extent, to be expected, as in the *no connection* configuration the intracranial venous systems are separated circuits and the regulatory mechanism can not take place. However, it is interesting to see that a *weak connection* might already be able to bring the pressure to a normal value.

The effect of the morphology of the confluence of sinuses can also be seen in Figures
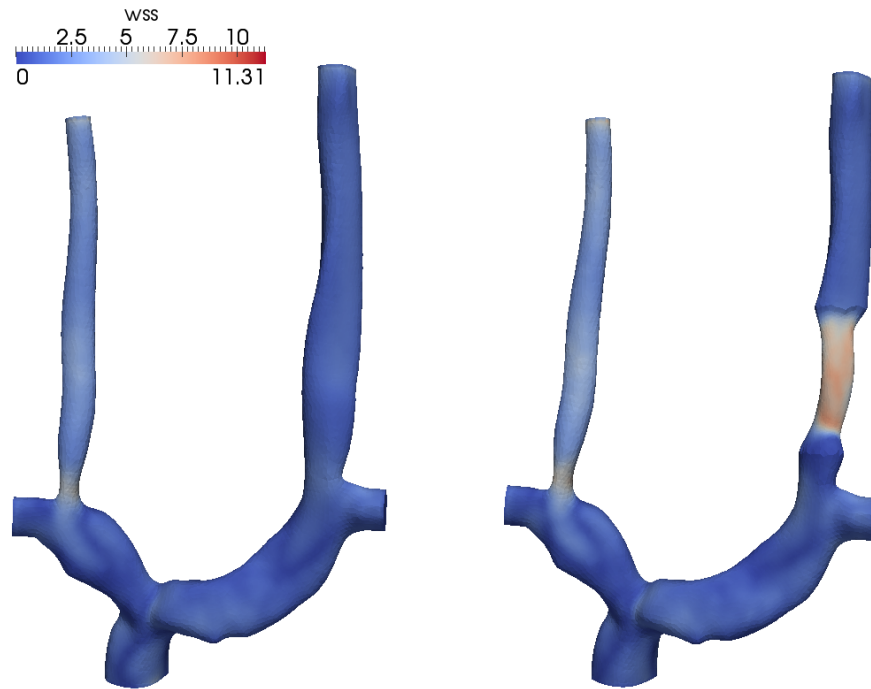
FIGURE 5.15: WSS magnitude on neck veins for the *strong confluence* configuration, at time t=0.2. **Left:** Non-stenotic configuration (CSA = 105 mm^2). **Right:** Large occlusion (reduction of 66%, CSA = 35 mm^2).

5.8 and 5.9. Comparing pressures in the SSS and STS, for non-stenotic and stenotic IJVs, we obtained higher dural sinuses pressures for the *no connection* case. For the non-stenotic case, peak pressures in SSS and STS are 9.3 vs 7.0 mmHg, for the *no connection* configuration and 8.0 vs 7.8 mmHg for the *strong connection* configuration. Similarly, for the stenotic case, pressures in SSS and STS are 11.0 vs 7.8 mmHg, for the *no connection* configuration and 8.7 vs 8.5 mmHg for the *strong connection* configuration. In the presence of well connected transverse sinuses, flow distribution can easily take place, yielding similar pressures in SSS and STS and lowering peak pressure values.

5.6.3 Flow field perturbation

The oscillatory behaviour of WSS, as well as abnormal WSS intensity have been reported as key factors influencing the morphology and disposition of endothelial cells [65]. There is medical evidence that pathological conditions are caused by low or highly oscillatory shear stress. In the context of our study, this potentially pathological condition can be observed in the post-stenotic area for all considered confluence of sinuses (see, *e.g*, Figure 5.13). As expected, WSS inside the stenotic area is considerably higher than in pre- and post stenotic regions (Figures 5.12 to 5.14). As reported in [30], this higher
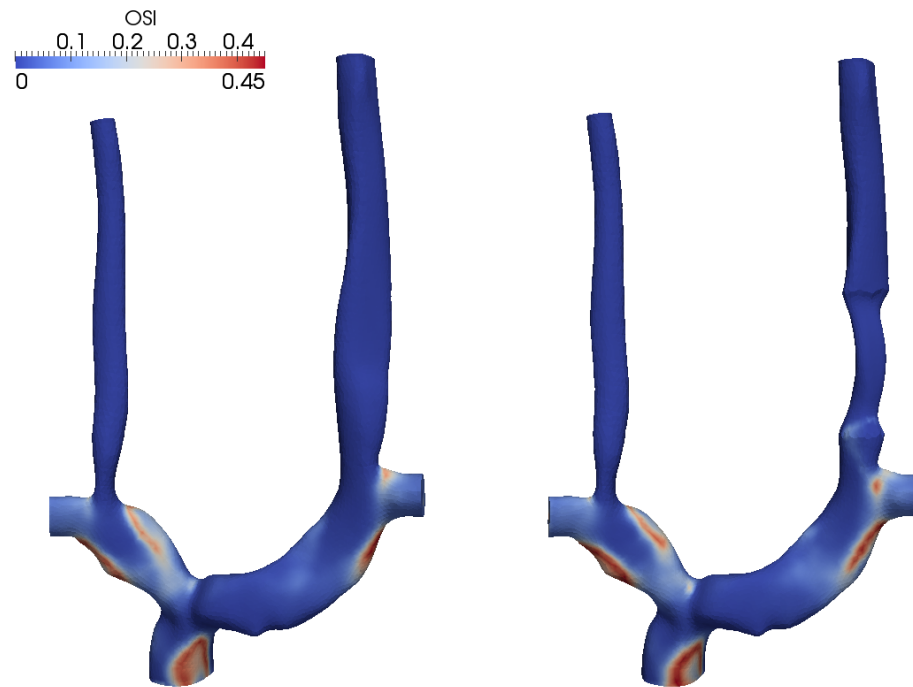
FIGURE 5.16: OSI near the stenosis for the case of sinuses without confluence. **Left:** Non-stenotic configuration (CSA = 105 mm^2). **Right:** Configuration with the largest occlusion (reduction of 66%, CSA = 35 mm^2).
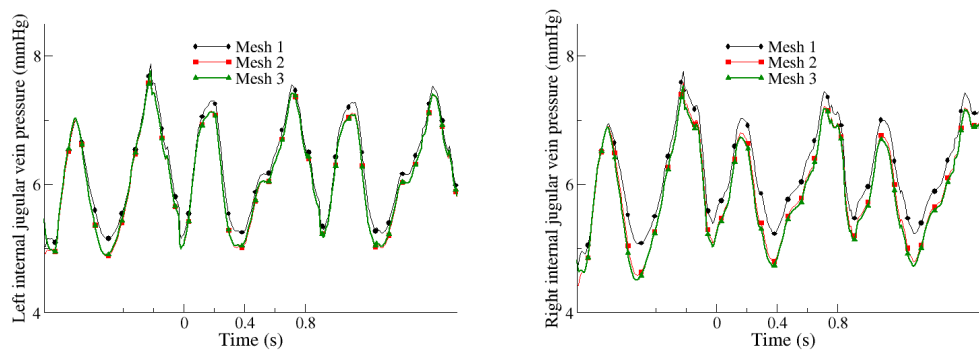
FIGURE 5.17: Pressure history for the stenotic geometry with a 66% CSA reduction for three different 3D meshes. (**Left**) Pressure at the LIJV inlet. (**Right**) Pressure at the RIJV inlet.
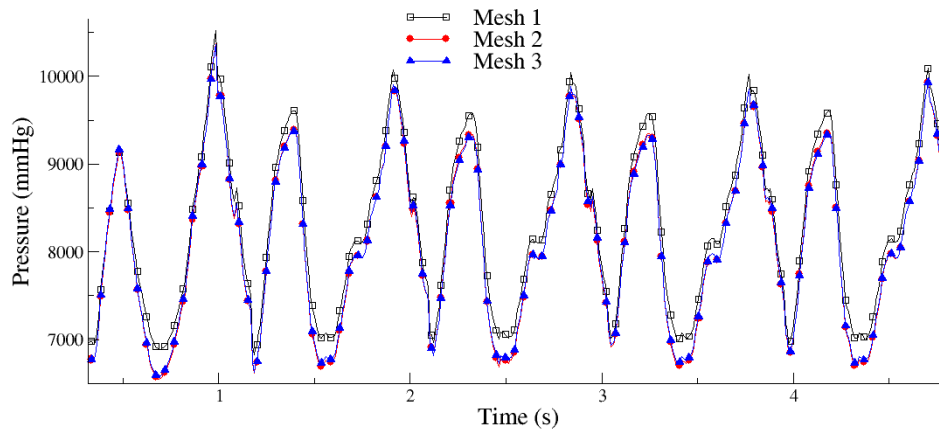
FIGURE 5.18: Pressure history at a fixed point in the pre-stenotic zone, for the stenotic geometry with a 66% CSA reduction for three different 3D meshes and weakly connected transverse sinuses. Note that results from meshes *Mesh 2* and *Mesh 3* are almost indistinguishable.

shear stresses might induce morphological and histological changes in the affected IJVs. On the other hand, it is important to notice that the venous outflow in the IJV is mainly unidirectional, and reflux, which might take place for very short times in the case of strong CSA reduction (Figures 5.12 to 5.14) is limited to portions of the vessel after the stenosis.

We note that although WSS can also be computed using 1D models, these have serious limitations for producing physically meaningful results [82]. One limitation is to have to assume a velocity profile. The main motivation of the work presented in this chapter, is to locally resolve the flow in 3 space dimensions so that computation of WSS and other physical quantities is physically more correct.

5.6.4 Diagnosis criteria for IJV stenosis

Criteria for assessing the presence of a stenosis are currently defined according to the severity of the venous occlusion, i.e. based on the reduction of CSA below a fixed threshold [157, 166], or on the post- vs pre-stenotic peak velocities ratio [86]. Our computational results show that the peak velocity ratio criteria proposed in [86] is able to accurately identify a significant reduction of CSA, while it is not a relevant indicator for a pathological pressure drop, since peak velocity ratio for different intracranial venous configurations is almost identical (Figure 5.10), while pressure drops vary considerably

(Figure 5.6). In the extreme cases considered, for a CSA reduction of 77%, peak velocity ratios for *no connection* and *strong connection* configurations are identical, while maximum pressure drops are 2.60 mmHg and 1.69 mmHg, respectively.

Another outcome of our study is that the criterion of a fixed threshold value of CSA, to identify clinically relevant stenoses, must be applied very carefully. For the particular configuration studied in this chapter, the right IJV would have been considered a stenotic vein, even in its physiological (sane) configuration. In fact, the impact of a stenosis in terms of pressure increase, which might yield pathological conditions in the cerebral venous system, is related not only to geometrical aspects (such as CSA reduction and, consequently high peak velocity ratio), but also to the flow rate across the stenosis. This aspect has been clearly shown for blood flow in different configurations of the confluence of sinuses (as discussed in Section 5.6.2). While CSA reduction and peak velocity ratio were identical for all intracranial venous morphologies, the related pressure increases differed considerably from case to case.

5.6.5   Model limitations

Although our model is based on patient-specific geometries and we achieve a satisfactory agreement with patient-measured flow data, some of the simplifications made in this study must be underlined. In this study we have considered rigid vessel walls for the local 3D domain (IJVs). Although veins typically have a relatively high compliance, this simplification might be acceptable for a subject in supine position. In the case of a stenotic vessel, a compliant IJV would compensate a pressure increase by a volume change. In order to take this aspect into account, we introduced compliant intracranial vessels, modelled through a one-dimensional network, which allows to significantly reduce the computational complexity of the simulation. On the other hand, it is well known that these vessels are stiffer than neck veins, and, therefore, pressure changes must be considered as an upper-bound of a realistic situation. Another important aspect to be explored in future studies is the influence of alternative cerebral drainage pathways, such as vertebral veins, deep cervical veins, vertebral venous plexus and anastomoses between IJVs and external jugular veins. The presence of well developed collaterals might reduce the impact of a stenotic IJV on cerebral venous drainage.

5.7   Conclusions

We have developed a computational framework to study, in a patient-specific setting, the effect of a stenosis of IJVs on cerebral haemodynamics. In particular, starting

from individual images of the head and neck veins and using patient-specific measured blood flow rates, we have investigated the perturbation induced by stenoses of increasing severity in terms of *extracranial* (IJVs) and *intracranial venous pressure increase* as well as *flow disturbances*. We have assessed our results utilizing widely used clinical criteria for the diagnosis of stenoses.

Furthermore, using a multi-scale mathematical blood flow model we have been able to investigate *different topologies of intracranial veins*. Our computational study shows that currently used diagnosis criteria should be applied cautiously. In particular, a purely geometric criterion such as absolute CSA might be misleading, whilst a *local criterion*, such as the CSA ratio between pre- and stenotic portions of the veins (equivalent, to some extent, to a peak velocity ratio criterion) would be more significant. Moreover, we have illustrated the relevance of cerebral venous topology in relation to considerable pressure increments caused by stenotic IJVs. Note the important fact that the size of the pressure changes are no to be judged in absolute terms, but relative to the usual venous pressures. This means that the computed pressure drops are, percentage wise, actually quite high. We have observed that venous configurations with well-connected transverse sinuses are much less sensitive to IJV stenoses than weakly connected ones. This suggests that the morphology of the cerebral venous system should also be taken into account as a relevant aspect, when diagnosing an IJV stenosis.

The work presented in this chapter, represents a first step towards a computer aided diagnosis of venous anomalies and venous insufficiencies. These pathologies are currently assessed through criteria that do not consider patient specific anatomies. Further studies will extend the computational analysis to take into account anatomical data of a large set of individual geometries, in order to provide statistically significant trends. The coupling of the local three-dimensional stenotic model to a closed-loop, global one-dimensional model will be the subject of future investigations.

Chapter 6

Summary of the thesis

In this thesis two topics have been considered, firstly, the study of the Cattaneo relaxation procedure for numerically solving advection-diffusion-reaction equations, and secondly, a medical application of current interest.

Concerning the first topic, we have extended the applicability of the Cattaneo relaxation approach to reformulate time-dependent advection-diffusion-reaction equations. Based on the approach of Cattaneo two new relaxations have been proposed, the *canonical relaxation formulation* and the *the ad-hoc relaxation formulation*. We have presented an strategy to choose the relaxation parameter which is independent of model equations and numerical methodologies. This strategy relates the mesh spacing Δx, an order of accuracy r and the relaxation parameter ε. So, an optimal ε can be chosen in terms of Δx and ε. This results in a more generous time step restriction than some conventional numerical schemes with parabolic stability constraint.

The ADER methodology has been extended to solve advection-diffusion-reaction equations. Furthermore, a new locally implicit generalized Riemann problem has been presented, which is based on the implicit Taylor expansion and the Cauchy-Kowalewski procedure. The ADER method resulting from this new solver, is able to solve balance laws with stiff source terms. Only the second-order version has been implemented in this thesis. However, the basis for constructing high order schemes has been presented.

We have solved selected model equations and convergence rate assessments have been carried out for some of them. Additionally, a blood flow model for a network of viscoelastic vessels has been solved and the results have been compared with existing experimental measurements and reference numerical solutions.

Regarding the second topic of this thesis, a numerical study of the haemodynamics impact of stenoses in the internal jugular veins has been carried out. A 3D/1D multi

scale flow model has been used in this study. MRI imaging has provided patient-specific information for the multi-scale model, as well as, the three-dimensional geometry and blood flow rates. Different topologies of intracranial veins have considered as 1D models. Using this mathematical framework, several degrees of stenoses have been investigated in terms of *extracranial* (IJVs) and *intracranial venous pressure increase* as well as *flow disturbances*.

We have assessed some conventional clinical criteria for the diagnosis of stenoses. We have observed that topologies of intracranial veins result in considerable pressure increments caused by stenotic IJVs, which suggested that the morphology of the cerebral venous system should also be taken into account as a relevant aspect, when diagnosing an IJV stenosis.

Appendix A

Linear advection-diffusion-reaction partial differential equations

Here, via an example, we compare our approach to an existing approach to calculate the eigenvalues of relaxation systems. The relevance of this concerns the efficiency of the time marching procedure, as the time step is computed from a CFL condition involving an estimate for the maximum signal speed.

Consider the linear *adrPDE* system

$$\partial_t \mathbf{Q} + \partial_x (\mathbf{AQ}) = \partial_x \mathbf{G}(\mathbf{Q}, \partial_x \mathbf{Q}) , \tag{A.1}$$

with $\mathbf{Q} = [q_1, q_2]^T$ and $\mathbf{G}(\mathbf{Q}, \partial_x \mathbf{Q}) = (\mathbf{BQ} + \mathbf{D}\partial_x \mathbf{Q})$ where

$$\mathbf{A} = \begin{bmatrix} 2 & -1 \\ 4 & -2 \end{bmatrix} , \quad \mathbf{B} = \begin{bmatrix} -1 & 0 \\ 3 & -7 \end{bmatrix} , \quad \mathbf{D} = \begin{bmatrix} 1 & 0 \\ 1 & 2 \end{bmatrix} . \tag{A.2}$$

We shall consider the following:

- Verify if conditions of Proposition (3.3) apply and;

- Compare the eigenvalues from existing splitting operator procedure and the present approach.

To assess the conditions of Proposition (3.3), we must check that $\mathbf{D}$ is similar to a semi positive definite matrix and that $\mathbf{A} - \mathbf{B}$ has real eigenvalues only. The eigenvalues of

D are $\delta_1 := 1$ $\delta_2 := 2$ and it is similar to the diagonal matrix formed by δ_1 and δ_2. In addition, the eigenvalues of $\mathbf{A} - \mathbf{B}$ are $\mu_1 = \mu_2 = 4$, which are real. Thus, the requirements of Proposition (3.3) are satisfied.

A canonical relaxation formulation of the system under consideration is

$$
\begin{aligned}
\partial_t \mathbf{Q} + \partial_x \left((\mathbf{A} - \mathbf{B}) \, \mathbf{Q} - \mathbf{D}\mathbf{U} \right) &= \mathbf{0} \,, \\
\partial_t \mathbf{U} + \partial_x \left(-\tfrac{1}{\varepsilon} \mathbf{Q} \right) &= \tfrac{1}{\varepsilon} \mathbf{U} \,,
\end{aligned}
\tag{A.3}
$$

with $\mathbf{U} = [u_1, u_2]^T$. The Jacobian of this system with respect to $\mathbf{W} = [\mathbf{Q}, \mathbf{U}]^T$ is

$$
\mathbf{J} = \begin{bmatrix} \mathbf{A} - \mathbf{B} & -\mathbf{D} \\ -\tfrac{1}{\varepsilon}\mathbf{I} & \mathbf{0} \end{bmatrix} = \begin{bmatrix} 3 & -1 & -1 & 0 \\ 1 & 5 & -1 & -2 \\ -\tfrac{1}{\varepsilon} & 0 & 0 & 0 \\ 0 & -\tfrac{1}{\varepsilon} & 0 & 0 \end{bmatrix}
\tag{A.4}
$$

and its eigenvalues are given by

$$
\lambda_1 = \tfrac{1}{2}\left\{ 4 - \sqrt{16 + \tfrac{4}{\varepsilon}} \right\} \,, \quad \lambda_2 = \tfrac{1}{2}\left\{ 4 + \sqrt{16 + \tfrac{4}{\varepsilon}} \right\} \,,
$$
$$
\lambda_3 = \tfrac{1}{2}\left\{ 4 - \sqrt{16 + \tfrac{8}{\varepsilon}} \right\} \,, \quad \lambda_4 = \tfrac{1}{2}\left\{ 4 + \sqrt{16 + \tfrac{8}{\varepsilon}} \right\} \,.
\tag{A.5}
$$

As predicted by proposition (3.3) they have the form

$$
\lambda_i^{\pm} = \frac{1}{2}\left\{ \mu_i \pm \sqrt{\mu_i^2 + \frac{4}{\varepsilon}\delta_i} \right\} \,.
\tag{A.6}
$$

Note that this system has distinct eigenvalues and is therefore hyperbolic, even if the advective part in the original system is not hyperbolic (eigenvectors of $\mathbf{A}$ do not form a set on two linearly independent vectors. $\mathbf{A}$ only contains one eigenvector).

On the other hand, following a splitting operator procedure to approximate eigenvalues of $\mathbf{J}$. As for example such of Nishikawa [113], the eigenvalues λ_i derive from the viscous part $\mathbf{F}^v$ and the inviscid part $\mathbf{F}^i$

$$
\mathbf{F}^i = \begin{bmatrix} \mathbf{A}\mathbf{Q} \\ \mathbf{0} \end{bmatrix} \,, \quad \mathbf{F}^v = \begin{bmatrix} -\mathbf{B}\mathbf{Q} - \mathbf{D}\mathbf{U} \\ -\tfrac{1}{\varepsilon}\mathbf{Q} \end{bmatrix} \,.
\tag{A.7}
$$

The eigenvalues of the viscous and inviscid part are computed with respect to $\mathbf{W}$. If we denote by λ_j^i the eigenvalues of the inviscid part and by λ_j^v the eigenvalues of the viscous part, with $j = 1, 2, 3, 4$. Then the splitting operator procedure suggest that the maximum eigenvalue of $\mathbf{J}$ is approximated by $\lambda_{max}^s := max\{|\lambda_j^i|\} + max\{|\lambda_j^v|\}$.

On the other hand, the eigenvalues for the inviscid part are $\lambda_1^i = \lambda_2^i = \lambda_3^i = \lambda_4^i = 0$ and for the viscous part are

$$\lambda_1^v = \tfrac{1}{2}\left\{1 - \sqrt{1 + \tfrac{4}{\varepsilon}}\right\} , \qquad \lambda_2^v = \tfrac{1}{2}\left\{1 + \sqrt{1 + \tfrac{4}{\varepsilon}}\right\} ,$$

$$\lambda_3^v = \tfrac{1}{2}\left\{7 - \sqrt{49 + \tfrac{8}{\varepsilon}}\right\} , \qquad \lambda_4^v = \tfrac{1}{2}\left\{7 + \sqrt{49 + \tfrac{8}{\varepsilon}}\right\} . \tag{A.8}$$

Therefore, the approximation to the maximum wave speed is $\lambda_{max}^s = \tfrac{1}{2}\left\{7 + \sqrt{49 + \tfrac{8}{\varepsilon}}\right\}$, whereas the maximum exact wave speed is $\lambda_{max} = \tfrac{1}{2}\left\{4 + \sqrt{16 + \tfrac{8}{\varepsilon}}\right\}$. Consequently, the splitting approach overestimates the signal speed and thus underestimates the time step, making it more inefficient.

Appendix B

Junctions and boundary conditions

While blood flow within each vessel is modelled using equations (4.20), we still need to treat boundary conditions arising from measurements to be prescribed or from the interaction of one-dimensional vessels with lumped parameter models [4]. Here we briefly explain how to treat junction and to assign boundary conditions for the one-dimensional model. Details on the numerical treatment of lumped parameter models can be found in [4, 96].

B.1 Junction treatments

Let us consider a junction to be the point where J+1 vessels are confluent, where $\mathbf{Q}_j$ is the state vector associated to vessel j-th, with $j = 0, \ldots, J$. We assume that at the junction

$$dA_0 = dK = dp_e = 0 \tag{B.1}$$

and that the vessel wall has elastic properties, as proposed in [96]. We want to find state vectors $\mathbf{Q}_j^* = [A_j^*, q_j^*]$ to be used as boundary conditions for each vessel. Therefore, for $J + 1$ vessels we need to compute $2(J + 1)$ unknowns. $J + 1$ equations are provided by requiring mass conservation

$$\sum_{j=0}^{J} g_j \, q_j^* = 0 \tag{B.2}$$

and continuity of total pressure

$$\tilde{p}_0^* + \frac{1}{2}\rho \left(\frac{q_0^*}{A_0^*}\right)^2 - \tilde{p}_j - \frac{1}{2}\rho \left(\frac{q_j}{A_j}\right)^2 = 0, \quad j = 1, ..., J \,. \tag{B.3}$$

In (B.2) g_j is given as

$$g_j(I_j) = \begin{cases} 1, & \text{if } I_j = N_j \,, \\ -1, & \text{if } I_j = 1 \,, \end{cases} \tag{B.4}$$

where I_j is the index of the computational cell of the j-th vessel that shares an interface with the junction and N_j is the number of computational cells of vessel j. Finally, the missing $J+1$ equations are provided by Riemann invariants for waves leaving the one-dimensional domain

$$\frac{q_j^*}{A_j^*} + g_j \int_{A_0}^{A_j^*} \frac{c(A)}{A} dA - \frac{q_j}{A_j} - g_j \int_{A_0}^{A_j} \frac{c(A)}{A} dA = 0 \quad j = 0, ..., J \,. \tag{B.5}$$

Equations (B.2), (B.3) and (B.5) constitute a non-linear system with $2(J+1)$ equations and $2(J+1)$ unknowns and is solved using a Newton method. For further details on this methodology see [137].

B.2   Assigning boundary conditions for the one-dimensional model

Let $\mathbf{Q} = [A_{1D}, q_{1D}]^T$ be the state of a computational cell at the extremity of a one-dimensional vessel sharing a boundary, where we want to prescribe the cross-sectional area A_{bc}, the flow rate q_{bc}, or both of them. These quantities might arise from lumped parameter models, from measurements or from coupling conditions at junctions. If only one component of $\mathbf{Q}$ is known we compute the value of the remaining component by solving the following equation

$$\frac{q_{1D}}{A_{1D}} + g_{1D} \int_{A_0}^{A_{1D}} \frac{c(A)}{A} dA - \frac{q_{bc}}{A_{bc}} - g_{1D} \int_{A_0}^{A_{bc}} \frac{c(A)}{A} dA = 0 \tag{B.6}$$

for the unknown quantity. Here, g_{1D} plays the role of g_j in (B.4), i.e. it identifies if computational cell at the extremity corresponds to the beginning or to the end of the vessel.

We denote by $\mathbf{Q}_{bc}^L = [A_{bc}^L, q_{bc}^L]^T$ and $\mathbf{Q}_{bc}^R = [A_{bc}^R, q_{bc}^R]^T$ the state vectors for boundary conditions on the left and right boundaries of the vessel, obtained from (B.6). To

prescribe these values at the vessel extremities, we use the fluctuations

$$\mathcal{D}^+_{1-\frac{1}{2}} = f(\mathbf{Q}^L_{1D}) - f(\mathbf{Q}^L_{bc}), \qquad \mathcal{D}^-_{N+\frac{1}{2}} = f(\mathbf{Q}^R_{bc}) - f(\mathbf{Q}^R_{1D}), \tag{B.7}$$

where f is a flux to be determined, N is the total number of cells of the vessel and $\mathbf{Q}^{L,R}_{1D}$ are the state vectors inside the computational domain for the left and right boundaries, respectively. Moreover, assuming

$$dA_0 = dK = dp_e = d\Psi = 0, \tag{B.8}$$

from the momentum equation in (4.20) f must satisfy

$$f_A \partial_x A + f_q \partial_x q = \left(c^2 - u^2 + \frac{a_\Gamma}{2} \right) \partial_x A + \left(2u \right) \partial_x q = 0. \tag{B.9}$$

The reader can check that this is an exact differential equation. Therefore, flux f is found simply from integration of (B.9), yielding

$$f(A, q) = A \left[\frac{K}{\rho} \left(\frac{m}{m+1} \left(\frac{A}{A_0} \right)^m - \frac{n}{n+1} \left(\frac{A}{A_0} \right)^n \right) + u^2 + a_\Gamma \right]. \tag{B.10}$$

This procedure ensures exact mass conservation over the network at a discrete level.

Bibliography

[1] R. Abgrall and S. Karni. Two-layer shallow water system: A relaxation approach. *SIAM Journal on Scientific Computing*, 31(3):1603–1627, 2009.

[2] J. Alastruey, A. W. Khir, K. S. Matthys, P. Segers, S. J. Sherwin, P. R. Verdonck, K. H. Parker, and J. Peiró. Pulse wave propagation in a model human arterial network: Assessment of 1-D visco-elastic simulations against in vitro measurements . *Journal of Biomechanics*, 44(12):2250 – 2258, 2011.

[3] J. Alastruey, K. H. Parker, J. Peiró, S. M. Byrd, and S. J. Sherwin. Modelling the circle of Willis to assess the effects of anatomical variations and occlusions on cerebral flows. *Journal of Biomechanics*, 40:1794–1805, 2007.

[4] J. Alastruey, K. H. Parker, J. Peiró, and S. J. Sherwin. Lumped parameter outflow models for 1-D blood flow simulations: Effect on pulse waves and parameter estimation. *Communications in Computational Physics*, 4(2):317–336, 2008.

[5] R. Anguelov, J. M. S. Lubuma, and S. K. Mahudu. Qualitatively stable finite difference schemes for advection-reaction equations. *Journal of Computational and Applied Mathematics*, 158(1):19–30, 2003.

[6] L. Antiga and D. A. Steinman. Robust and objective decomposition and mapping of bifurcating vessels. *IEEE Transactions on Medical Imaging*, 23(6):704–713, 2004.

[7] R. Araya, E. Behrens, and R. Rodriguez. An adaptive stabilized finite element scheme for the advection-reaction-diffusion equation. *Applied Numerical Mathematics*, 54:491–503, 2005.

[8] R. Araya, E. Behrens, and R. Rodriguez. Error estimators for advection-reaction-diffusion equations based on the solution of local problems. *Journal of Computational and Applied Mathematics*, 206:440–453, 2007.

[9] M. Arora and P. L. Roe. *Issues and Strategies for Hyperbolic Problems with Stiff Source Terms*, volume 6 of *ICASE/LaRC Interdisciplinary Series in Science and Engineering*. Springer Netherlands, 1998.

[10] M. Ben-Artzi and J. Falcovitz. A second order Godunov–type scheme for compressible fluid dynamics. *Journal of Computational Physics*, 55(1):1–32, 1984.

[11] S. A. Berger and L. D. Jou. Flow in stenotic vessels. *Annual Review of Fluid Mechanics*, 32:347–382, 2000.

[12] J. G. Berryman and C. J. Holland. Nonlinear diffusion problems arising in plasma physics. *Physical Review Letters*, 40 (26):1720–1722, 1978.

[13] C. Bertoglio and A. Caiazzo. A tangential regularization method for backflow stabilization in hemodynamics. *Journal of Computational Physics*, 261(0):162 – 171, 2014.

[14] M. Bertsch. Asymptotic behavior of solutions of a nonlinear diffusion equation. *SIAM Journal on Applied Mathematics*, 42 (1):66–76, 1982.

[15] P. J. Blanco, M. R. Pivello, S. A. Urquiza, and R. A. Feijóo. On the potentialities of 3D-1D coupled models in hemodynamics simulations. *Journal of Biomechanics*, 42:919–930, 2009.

[16] T. Bodnar and A. Sequeira. Numerical simulation of the coagulation dynamics of blood. *Computational and Mathematical Methods in Medicine*, 9(2):83–104, 2008.

[17] S. Boscarino, L. Pareschi, and G. Russo. Implicit–explicit Runge-Kutta schemes for hyperbolic systems and kinetic equations in the diffusion limit. *SIAM Journal on Scientific Computing*, 35:22–51, 2013.

[18] S. Boscarino and G. Russo. Flux–explicit IMEX Runge-Kutta schemes for hyperbolic to parabolic relaxation problems. *SIAM Journal on Numerical Analysis*, 51(1):163–190, 2013.

[19] B. S. Brook, S. A. E. G. Falle, and T. J. Pedley. Numerical solutions for unsteady gravity-driven flows in collapsible tubes: evolution and roll-wave instability of a steady state. *Journal of Fluid Mechanics*, 396:223–256, 1999.

[20] A. Canestrelli, A. Siviglia, M. Dumbser, and E. F. Toro. Well-balanced high-order centred schemes for non-conservative hyperbolic systems. Applications to shallow water equations with fixed and mobile bed. *Advances in Water Resources*, 32(6):834 – 844, 2009.

[21] C. E. Castro. *High–order ADER FV/DG numerical methods for hyperbolic equations*. PhD thesis, Department of Civil and Environmental Engineering, University of Trento, Italy, 2007.

[22] C. E. Castro and E. F. Toro. Solvers for the high–order Riemann problem for hyperbolic balance laws. *Journal of Computational Physics*, 227:2481–2513, 2008.

[23] V. Casulli and P. Zanolli. A Nested Newton-Type Algorithm for Finite Volume Methods Solving Richards' Equation in Mixed Form. *SIAM Journal on Scientific Computing*, 32(4):2255–2273, 2010.

[24] C. Cattaneo. Sulla conduzione del calore. *Atti del Seminario Matematico e Fisico dell'Universita di Modena*, 3:83–101, 1948.

[25] C. Cattaneo. A form of heat-conduction equations which eliminates the paradox of instantaneous propagation. *Comptes Rendus de l'Académie des Sciences, Paris*, 247:431–433, 1958.

[26] G. Q. Chen, C. D. Levermore, and T. P. Liu. Hyperbolic conservation laws with stiff relaxation terms and entropy. *Communications on Pure and Applied Mathematics*, 47(6):787–830, 1994.

[27] A. J. Chorin. Numerical solution of the Navier-Stokes equations. *Mathematics of Computation*, 22:745–768, 1968.

[28] C. Clavero, J. L. Gracia, and J. C. Jorge. High-order numerical methods for one-dimensional parabolic singularly perturbed problems with regular layers. *Numerical Methods for Partial Differential Equations*, 21:148–169, 2005.

[29] R. H. Clayton. Computational models of normal and abnormal action potential propagation in cardiac tissue: linking experimental and clinical cardiology. *Physiological Measuremen*, 22(3):0967–3334, 2001.

[30] M. Coen, E. Menegatti, F. Salvi, F. Mascoli, P. Zamboni, G. Gabbiani, and M. L. Bochaton-Piallat. Altered collagen expression in jugular veins in multiple sclerosis. *Cardiovascular Pathology*, 22(1):33–38, 2013.

[31] J. Colliander, M. Keel, G. Staffilani, H. Takaoka, and T. Tao. Multilinear estimates for periodic KdV equations, and applications. *Journal of Functional Analysis*, 211:173–218, 2004.

[32] C. D. Correa, R. Hero, and K. L. Ma. A comparison of gradient estimation methods for volume rendering on unstructured meshes. *IEEE Transactions on Visualization and Computer Graphics*, 17(3):305–319, 2011.

[33] G. Dal Maso, P. G. LeFloch, and F. Murat. Definition and weak stability of nonconservative products. *Journal de Mathématiques Pures et Appliquées*, 74:483–548, 1995.

[34] H. Do, A. A. Owida, W. Yang, and Y. S. Morsi. Numerical simulation of the haemodynamics in end-to-side anastomoses. *International Journal for Numerical Methods in Fluids*, 67(5):638–650, 2011.

[35] M. Dumbser. *Arbitrary high order schemes for the solution of hyperbolic conservation laws in complex domains*. PhD thesis, Institut für Aero- un Gasdynamik, Universität Stuttgart, Germany, 2005.

[36] M. Dumbser. Building blocks for arbitrary high order discontinuous Galerkin schemes. *Journal of Scientific Computing*, 27:215–230, 2006.

[37] M. Dumbser. Arbitrary high order PNPM schemes on unstructured meshes for the compressible Navier-Stokes equations. *Computers & Fluids*, 39:60–76, 2010.

[38] M. Dumbser, D. Balsara, E. F. Toro, and C. D. Munz. A unified framework for the construction of one-step finite volume and discontinuous Galerkin schemes on unstructured meshes. *Journal of Computational Physics*, 227:8209–8253, 2008.

[39] M. Dumbser and D. S. Balsara. High-order unstructured one-step PNPM schemes for the viscous and resistive MHD equations. *Computer Modeling in Engineering and Sciences*, 54:301–333, 2009.

[40] M. Dumbser, M. J. Castro, C. Parés, and E. F. Toro. ADER schemes on unstructured meshes for nonconservative hyperbolic systems: Applications to geophysical flows. *Computers & Fluids*, 38(9):1731–1748, 2009.

[41] M. Dumbser, C. Enaux, and E. F. Toro. Finite volume schemes of very high order of accuracy for stiff hyperbolic balance laws. *Journal of Computational Physics*, 227(8):3971–4001, 2008.

[42] M. Dumbser, A. Hidalgo, M. Castro, C. Parés, and E. F. Toro. FORCE schemes on unstructured meshes II: Non-conservative hyperbolic systems. *Computer Methods in Applied Mechanics and Engineering*, 199(9–12):625–647, 2010.

[43] M. Dumbser and M. Käser. Arbitrary high order non-oscillatory finite volume schemes on unstructured meshes for linear hyperbolic systems. *Journal of Computational Physics*, 221(2):693–723, 2007.

[44] M. Dumbser, M. Käser, and E. F. Toro. An arbitrary high order discontinuous Galerkin method for elastic waves on unstructured meshes V: Local time stepping and *p*–adaptivity. *Geophysical Journal International*, 171:695–717, 2007.

[45] M. Dumbser and C. D. Munz. ADER Discontinuous Galerkin Schemes for Aeroacoustics. *Comptes Rendus Mécanique*, 333:683–687, 2005.

[46] M. Dumbser and E. F. Toro. A simple extension of the Osher Riemann solver to non-conservative hyperbolic systems. *Journal of Scientific Computing*, 48:70–88, 2010.

[47] M. Dumbser and E. F. Toro. On universal Osher-type schemes for general non-linear hyperbolic conservation laws. *Communications in Computational Physics*, 10(3):635–671, 2011.

[48] N. El Khatib, S. Genieys, and V. Volpert. Atherosclerosis initiation modeled as an inflammatory disease. *Mathematical Modelling of Natural Phenomena*, 2(2):126–141, 2007.

[49] L. Formaggia, J. F. Gerbeau, F. Nobile, and A. Quarteroni. On the coupling of 3D and 1D Navier-Stokes equations for flow problems in compliant vessels. *Computer Methods in Applied Mechanics and Engineering*, 191(6-7):561–582, 2001.

[50] L. Formaggia, J. F. Gerbeau, F. Nobile, and A. Quarteroni. Numerical treatment of defective boundary conditions for the Navier-Stokes equations. *SIAM Journal on Numerical Analysis*, 40(1):376–401, 2002.

[51] L. Formaggia, A. Quarteroni, and A. Veneziani. *Cardiovascular Mathematics: Modeling and simulation of the circulatory system.* Springer-Verlag Italia, Milano, 2009.

[52] L. P. Franca and F. Valentin. On an improved unusual stabilized finite element method for the advective-reactive-diffusive equation. *Computer Methods in Applied Mechanics and Engineering*, 190:1785–1800, 2000.

[53] A. Friedman. *Partial differential equations of parabolic type.* Dover Books on Mathematics Series. DOVER PUBN Incorporated, 2008.

[54] A. Fukusumi, T. Okudera, S. Takahashi, T. Taoka, M. Sakamoto, H. Nakagawa, K. Takayama, K. Kichikawa, and S. Iwasaki. Anatomical Evaluation of the Dural Sinuses in the Region of the Torcular Herophili Using Three Dimensional CT Venography. *Academic Radiology*, 17:1103–1111, 2010.

[55] S. K. Godunov. A Finite Difference Method for the Computation of Discontinuous Solutions of the Equations of Fluid Dynamics. *Matematicheskii Sbornik*, 47:357–393, 1959.

[56] D. Goldman and T. J. Kaper. Nth-order operator splitting schemes and nonreversible systems. *SIAM Journal on Numerical Analysis*, 33:349–367, 1996.

[57] H. Gómez, I. Colominas, F. Navarrina, and M. Casteleiro. A Generalized Method for Advective-diffusive Computations in Engineering. In *Fluid Structure Interaction and Moving Boundary Problems*, pages 563–572. Chakrabarti S. K., Hernández S., Brebbia C.A., Southampton, UK., 2005.

[58] H. Gómez, I. Colominas, F. Navarrina, and M. Casteleiro. A finite element formulation for a convection–diffusion equation based on Cattaneo's law. *Computer Methods in Applied Mechanics and Engineering*, 196:1757–1766, 2007.

[59] H. Gómez, I. Colominas, F. Navarrina, and M. Casteleiro. Un nuevo enfoque para el tratamiento de los términos difusivos de la ecuación de convección–difusión en el método de Galerkin discontinuo. *Revista Internacional de Métodos Numéricos para Cálculo y Diseño en Ingeniería*, 23(4):343–362, 2007.

[60] L. Grinberg, E. Cheever, T. Anor, J. R. Madsen, and G. E. Karniadakis. Modeling blood flow circulation in intracranial arterial networks: A comparative 3d/1d simulation study. *Annals of Biomedical Engineering*, 39(1):297–309, 2011.

[61] J. L. Guermond, P. Minev, and J. Shen. An overview of projection methods for incompressible flows. *Computer Methods in Applied Mechanics and Engineering*, 195:6011–6045, 2006.

[62] R. Guibert, K. McLeod, A. Caiazzo, T. Mansi, M. A. Fernández, M. Sermesant, X. Pennec, I. E. Vignon-Clementel, Y. Boudjemline, and J. F. Gerbeau. Groupwise Construction of Reduced Models for Understanding and Characterization of Pulmonary Blood Flows from Medical Images . *Medical Image Analysis*, 18(1):63–82, 2014.

[63] C. H. Guo. On quadratic matrix equation associated with a m-matrix. *IMA Journal of Numerical Analysis*, 23(1):11–27, 2003.

[64] G. H. Guo and A. J. Laub. On the iterative solution of a class of Nonsymmetric algebraic Riccati equations. *SIAM Journal on Matrix Analysis and Applications*, 22(2):376–391, 2000.

[65] C. Haond, C. Ribreau, O. Boutherin-Falson, and M. Finet. Laminar flow through a model of collapsed veins. Morphometric response of endothelial vascular cells to a longitudinal shear stress non uniform cross-wise. *European Journal of Applied Physiology*, 8:87–96, 1999.

[66] A. Harten, B. Engquist, S. Osher, and S. R. Chakravarthy. Uniformly high order accuracy essentially non–oscillatory schemes III. *Journal of Computational Physics*, 71:231–303, 1987.

[67] A. Hidalgo and M. Dumbser. ADER schemes for nonlinear systems of stiff advection-diffusion-reaction equations. *Journal of Scientific Computing*, 48:173–189, 2011.

[68] A. Hidalgo, L. Tello, and E. F. Toro. Numerical and analytical study of an atherosclerosis inflammatory disease model. *Journal of Mathematical Biology*, pages 1–30, 2013.

[69] J. A. Hittinger. *Foundations for the generalization of the Godunov method to hyperbolic systems with stiff relaxation source terms*. PhD thesis, University of Michigan, 2000.

[70] J. A. Hittinger, Y. Suzuki, and B. van Leer. Investigation of the discontinuous Galerkin method for first-order PDE approaches to CFD. In *17th AIAA Computational Fluid Dynamics Conference, 6 - 9 June, Toronto, Ontario Canada, 2005*, 2005.

[71] S. Idelsohn, N. Nigro, and G. Buscaglia. A Petrov-Galerkin formulation for advection-reaction-diffusion problems. *Computer Methods in Applied Mechanics and Engineering*, 136(27):27–46, 1996.

[72] G. S. Jiang and C. W. Shu. Efficient Implementation of Weighted ENO Schemes. *Journal of Computational Physics*, 126:202–228, 1996.

[73] S. Jin. A convex entropy for a hyperbolic system with relaxation. *Journal of Differential Equations*, 127(1):97–109, 1996.

[74] S. Jin and C. D. Levermore. Numerical schemes for hyperbolic conservation laws with stiff relaxation terms. *Journal of Computational Physics*, 126 (2):449–467, 1996.

[75] S. Jin and H. Liu. A diffusive subcharacteristic condition for hyperbolic systems with diffusive relaxation. *Transport Theory and Statistical Physics*, 29(3-5):583–593, 2000.

[76] S. Jin, L. Pareschi, and G. Toscani. Diffusive relaxation schemes for multi-scale discrete-velocity kinetic equations. *SIAM Journal on Numerical Analysis*, 35(6):2405–2439, 1998.

[77] S. Jin and Z. Xin. The relaxation schemes for systems of conservation laws in arbitrary space dimensions. *Communications on Pure and Applied Mathematics*, 48:235–277, 1995.

[78] F. John. *Partial Differential Equations*. Number v. 1 in Applied Mathematical Sciences. Springer, 1982.

[79] M. Käser. *Adaptive methods for the numerical simulation of transport processes.* PhD thesis, Institute of Numerical Mathematics and Scientific Computing, University of Munich, Germany, 2003.

[80] M. Käser. ADER schemes for the solution of conservation laws on adaptive triangulations. Mathematical Methods and Modelling in Hydrocarbon Exploration and Production. Springer–Verlag, Vol. 7, 2004.

[81] M. Käser and A. Iske. Adaptive ADER schemes for the solution of scalar non–linear hyperbolic problems. *Journal of Computational Physics*, 205:489–508, 2005.

[82] D. Katritsis, L Kaiktsis, A. Chaniotis, J. Pantos, E. P. Efstathopoulos, and V. Marmarelis. Wall shear stress: Theoretical considerations and methods of measurement. *Progress in Cardiovascular Diseases*, 49(5):307–329, 2007.

[83] L. A. Khan and P. L. Liu. An operator splitting algorithm for coupled one-dimensional advection-diffusion-reaction equations. *Computer Methods in Applied Mechanics and Engineering*, 127(1–4):181–201, 1995.

[84] H. V. Kojouharov and B. M. Chen. *Nonstandard methods for advection-diffusion-reaction equations.* R. E. Mickens, editor, Applications of nonstandard finite difference schemes, World Scientific, Singapore, 2000.

[85] B. K. Koo, A. Erglis, J. H. Doh, D. V. Daniels, S. Jegere, H. S. Kim, A. Dunning, T. DeFrance, A. Lansky, J. Leipsic, and J. K. Min. Diagnosis of ischemia-causing coronary stenoses by noninvasive fractional flow reserve computed from coronary computed tomographic angiograms. Results from the prospective multi-center DISCOVER-FLOW (Diagnosis of Ischemia-Causing Stenoses Obtained Via Noninvasive Fractional Flow Reserve) study. *Journal of the American College of Cardiology*, 58(19):1989–1997, 2011.

[86] N. Labropoulos, M. Borge, K. Pierce, and P. J. Pappas. Criteria for defining significant central vein stenosis with duplex ultrasound. *Journal of Vascular surgery*, 46(1):101–107, 2007.

[87] J. F. LaDisa, R. J. Dholakia, C. A. Figueroa, I. E. Vignon-Clementel, F. P. Chan, M. M. Samyn, J. R. Cava, C. A. Taylor, and J. A. Feinstein. Computational simulations demonstrate altered wall shear stress in aortic coarctation patients treated by resection with end-to-end anastomosis. *Congenital heart disease*, 6(5):432–43, 2011.

[88] J. Lawson and Y. Lim. A Birkhoff contraction formula with applications to Riccati equations. *SIAM Journal on Control and Optimization*, 46:930–951, 2007.

[89] E. W. Lemmon and R. T. Jacobsen. Viscosity and thermal conductivity equations for Nitrogen, Oxygen, Argon, and Air. *International Journal of Thermophysics*, 25(1):21–69, 2004.

[90] R. J. LeVeque and H. C. Yee. A study of numerical methods for hyperbolic conservation laws with stiff source terms. *Journal of Computational Physics*, 86:187–210, 1990.

[91] J. R. Levick. *Introduction to cardiovascular physiology. Fifth Edition.* Hodder Arnold, 2010.

[92] F. Y. Liang, S. Takagi, R. Himeno, and H. Liu. Multi-scale modeling of the human cardiovascular system with applications to aortic valvular and arterial stenoses. *Medical and Biological Engineering and Computing*, 47:743–755, 2009.

[93] T. P. Liu. Nonlinear stability of shock waves for viscous conservation laws. *Bulletin of the American Mathematical Society (N.S.)*, 12(5):233–236, 1985.

[94] T. P. Liu. Hyperbolic conservation laws with relaxation. *Communications in Mathematical Physics*, 108:153–175, 1987.

[95] R. B. Lowrie and J. E. Morel. Methods for hyperbolic systems with stiff relaxation. *International Journal for Numerical Methods in Fluids*, 40:413–423, 2002.

[96] K. S. Matthys, J. Alastruey, J. Peiró, A. W. Khir, P. Segers, P. R. Verdonck, K. H. Parker, and S. J. Sherwin. Pulse wave propagation in a model human arterial network: Assessment of 1-D numerical simulations against *in vitro* measurements. *Journal of Biomechanics*, 40:3476–3486, 2007.

[97] R. E. Mickens. *Nonstandard finite difference models of differential equations.* World Scientific, 1994.

[98] R. E. Mickens. Analysis of a finite-difference scheme for a linear advetion-diffusion-reaction equation. *Journal of Sound and Vibration*, 236(5):901–903, 2000.

[99] R. Miura. The Korteweg–deVries Equation: A Survey of Results. *SIAM Review*, 18(3):412–459, 1976.

[100] G. Montecinos, C. E. Castro, M. Dumbser, and E. F. Toro. Comparison of solvers for the generalized Riemann problem for hyperbolic systems with source terms. *Journal of Computational Physics*, 231:6472–6494, 2012.

[101] G. Montecinos and E. F. Toro. Solver for the generalized Riemann problem for balance laws with stiff source terms: The scalar case. In *Hyperbolic problems. Theory, numerics and applications. Vol. 2. Proceedings of the 13th international*

conference on hyperbolic problems, HYP 2010, Beijing, China, June 15–19, 2010, pages 576–583. Hackensack, NJ: World Scientific; Beijing: Higher Education Press, 2012.

[102] K. Mukherjee and S. Natesan. Parameter-uniform hybrid numerical scheme for time-dependent convection-dominated initial-boundary-value problems. *Computing*, 84:209–230, 2009.

[103] L. O. Müller, C. Parés, and E. F. Toro. Well-balanced high-order numerical schemes for one-dimensional blood flow in vessels with varying mechanical properties. *Journal of Computational Physics*, 242:53–85, 2013.

[104] L. O. Müller and E. F. Toro. Well-balanced high-order solver for blood flow in networks of vessels with variable properties. *International Journal for Numerical Methods in Biomedical Engineering*, 29(12):1388–1411, 2013.

[105] L. O. Müller and E. F. Toro. A global multiscale mathematical model for the human circulation with emphasis on the venous system. *International Journal for Numerical Methods in Biomedical Engineering*, pages n/a–n/a, 2014.

[106] B. R. Munson, D. F. Young, T. H. Okiishi, and B. W. Huebsch. *Fundamentals Of Fluid Mechanics. Sixth Edition*. Wiley India Pvt. Ltd., 2009.

[107] G. B. Nagy, O. E. Ortiz, and O. A. Reula. The behaviour of hyperbolic heat equations solutions near their parabolic limit. *Journal of Mathematical Physics*, 8:4334–4356, 1994.

[108] G. Naldi and L. Pareschi. Numerical schemes for hyperbolic systems of conservation laws with stiff diffusive relaxation. *SIAM Journal on Numerical Analysis*, 37(4):1246–1270, 2000.

[109] R. Natalini. Convergence to equilibrium for the relaxation approximations of conservation laws. *Communications on Pure and Applied Mathematics*, 49:795–823, 1996.

[110] R. W. D. Nickalls. A new approach to solving the cubic: Cardan's solution revealed. *The Mathematical Gazette*, 77(480):354–359, 1993.

[111] H. Nishikawa. A first-order system approach for diffusion equation. I: Second-order residual-distribution schemes. *Journal of Computational Physics*, 227:315–352, 2007.

[112] H. Nishikawa. A first-order system approach for diffusion equation. II: Unification of advection and diffusion. *Journal of Computational Physics*, 229:3989–4016, 2010.

[113] H. Nishikawa. New-generation hyperbolic Navier-Stokes schemes: O(1/h) Speed-up and accurate viscous/heat fluxes. In *20th AIAA Computational Fluid Dynamics Conference, 27 - 30 June, Honolulu, Hawaii, 2011*, 2011.

[114] H. Nishikawa and P. L. Roe. Towards High-Order Fluctuation-Splitting Schemes for Navier-Stokes Equations. In *17th AIAA Computational Fluid Dynamics Conference, 6 - 9 June, Toronto, Ontario Canada, 2005*, 2005.

[115] H. Nishikawa and P. L. Roe. On High-Order Fluctuation-Splitting Schemes for Navier-Stokes Equations. In Clinton Groth and DavidW. Zingg, editors, *Computational Fluid Dynamics 2004*, pages 799–804. Springer Berlin Heidelberg, 2006.

[116] T. Papaioannou and C. Stefanadis. Vascular wall shear stress: Basic principles and methods. *The Hellenic Journal of Cardiology*, 46:9–15, 2005.

[117] C. Parés. Numerical methods for nonconservative hyperbolic systems: a theoretical framework. *SIAM Journal on Numerical Analysis*, 44:300–321, 2006.

[118] L. Pareschi and G. Russo. Implicit–explicit Runge–Kutta schemes and applications to hyperbolic systems with relaxation. *Journal of Scientific Computing*, 25:129–155, 2005.

[119] T. Passerini, M. De Luca, L. Formaggia, A. Quarteroni, and A. Veneziani. A 3D/1D geometrical multiscale model of cerebral vasculature. *Journal of Engineering Mathematics*, 64:319–330, 2009.

[120] R. Patterson and W. Wagner. A Stochastic Weighted Particle Method for Coagulation–Advection Problems. *SIAM Journal on Scientific Computing*, 34(3):290–311, 2012.

[121] T. J. Pedley, B. S. Brook, and R. S. Seymour. Blood pressure and flow rate in the giraffe jugular vein. *Philosophical Transactions of the Royal Society of London. Series B, Biological sciences*, 351:855–866, 2004.

[122] R. B. Pember. Numerical Methods for Hyperbolic Conservation Laws with Stiff Relaxation I: Spurious Solutions. *SIAM Journal on Applied Mathematics*, 53:1293–1330, 1993.

[123] R. B. Pember. Numerical methods for hyperbolic conservation laws with stiff relaxation II. Higher-order Godunov methods. *SIAM Journal on Scientific Computing*, 14(4):824–859, 1993.

[124] A. Quarteroni and L. Formaggia. Mathematical modelling and numerical simulation of the cardiovascular system. *Handbook of Numerical Analysis*, 12:31–127, 2004.

[125] P. Reymond, F. Merenda, F. Perren, D. Rüfenacht, and N. Stergiopulos. Validation of a one-dimensional model of the systemic arterial tree. *American Journal of Physiology - Heart and Circulatory Physiology*, 297:208–222, 2009.

[126] P. L. Roe. Approximate riemann solver, parameter vectors and difference schemes. *Journal of Computational Physics*, 43:357–372, 1981.

[127] P. L. Roe. Characteristic-based schemes for the Euler equations. *Annual Review of Fluid Mechanics*, 18:337–365, 1986.

[128] P. L. Roe and M. Arora. Characteristic-based schemes for dispersive waves I. The method of characteristics for smooth solutions. *Numerical Methods for Partial Differential Equations*, 9:459–505, 1993.

[129] W. Roetzel, N. Putra, and S. K. Das. Experiment and analysis for non-Fourier conduction in materials with non-homogeneous inner structure. *International Journal of Thermal Sciences*, 42:541–552, 2003.

[130] S. Sajjadi, G. B. Nash, M. W. Rampling, and M. W. Rampling. *Cardiovascular Flow Modelling and Measurement with Application to Clinical Medicine*. Institute of Mathematics and its Applications Conference Series. OUP Oxford, 1999.

[131] S. Scarle. Implications of the Turing completeness of reaction-diffusion models, informed by GPGPU simulations on an XBox 360: Cardiac arrhythmias, re-entry and the Halting problem. *Computational Biology and Chemistry*, 33(4):253–260, 2009.

[132] T. Schwartzkopff, C. D. Munz, and E. F. Toro. ADER: High–order approach for linear hyperbolic systems in 2D. *Journal of Scientific Computing*, 17:231–240, 2002.

[133] J. R. Scott. Solving ODE initial value problems with implicit Taylor series methods. *Glenn Research Center, Cleveland, Ohio. NASA/TM–2000-209400*, 2000.

[134] B .D. Seeley and D. F. Young. Effect of geometry on pressure losses across models of arterial stenoses. *Journal of Biomechanics*, 9:439–448, 1976.

[135] Q. Sheng. Solving partial differential equations by exponential splittings. *IMA Journal of Numerical Analysis*, 9:199–212, 1989.

[136] S. J. Sherwin. *Computational Haemodynamics: Geometry and Non-Newtonian Modelling Using Spectral/hp Element Methods*. IC aero report. Imperial College of Science, Technology & Medicine, Department of Aeronautics, 1998.

[137] S. J. Sherwin, V. Franke, J. Peiró, and K. Parker. One-dimensional modelling of a vascular network in space-time variables. *Journal of Engineering Mathematics*, 47(3-4):217–250, 2003.

[138] H. Si. TetGen: A Quality Tetrahedral Mesh Generator and a 3D Delaunay Triangulator. Technical Report 1762, WIAS, Berlin, 2013.

[139] B. N. Steele, J. Wan, P. Ku, J, T. J. Hughes, and C. A. taylor. In vivo validation of a one-dimensional finite-element method for predicting blood flow in cardiovascular bypass grafts. *IEEE Transactions on Biomedical Engineering*, 50:649–655, 2003.

[140] G. I. Surbet, T. O. Lewis, and T. L. Boullin. Quadratic matrix equations. *The Ohio Journal of Science*, 74(5):273–277, 1974.

[141] Y. Takakura and E. F. Toro. Arbitrarily Accurate Non–Oscillatory Schemes for a Non–Linear Conservation Law. *Computational Fluid Dynamics*, 11:7–18, 2002.

[142] R. Temam. *The Navier-Stokes equations, theory and numerical analysis*. Amsterdam-New York-Oxford, 1977.

[143] J. B. Thomas, L. Antiga, S. Che, J. S. Milner, D. A. Hangan Steinman, J. D. Spence, B. K. Rutt, and D. A. Steinman. Variation in the carotid bifurcation geometry of young versus older adults: Implications forgeometric risk of atherosclerosis. *Stroke*, 36(11):2450–2456, 2005.

[144] V. A. Titarev and E. F. Toro. ADER: Arbitrary high order Godunov approach. *Journal of Scientific Computing*, 17:609–618, 2002.

[145] V. A. Titarev and E. F. Toro. High–order ADER schemes for scalar advection–reaction–diffusion equations. *CFD Journal*, 12(1):1–6, 2003.

[146] V. A. Titarev and E. F. Toro. ADER schemes for three–dimensional hyperbolic systems. *Journal of Computational Physics*, 204:715–736, 2005.

[147] E. F. Toro. *Riemann Solvers and Numerical Methods for Fluid Dynamics: A Practical Introduction*. Springer-Verlag, third edition, 2009. ISBN 978-3-540-25202-3.

[148] E. F. Toro and A. Hidalgo. ADER finite volume schemes for nonlinear diffusion–reaction equations. Technical Report Preprint NI07007–NPA, Newton Institute for Mathematical Sciences, University of Cambridge, UK, 2007.

[149] E. F. Toro and A. Hidalgo. ADER finite volume schemes for diffusion–reaction equations. *Applied Numerical Mathematics*, 59:73–100, 2009.

[150] E. F. Toro, R. C. Millington, and L. A. M. Nejad. Towards very high–order Godunov schemes. In *Godunov Methods: Theory and Applications. Edited Review, E. F. Toro (Editor)*, pages 905–937. Kluwer Academic/Plenum Publishers, 2001.

[151] E. F. Toro and A. Siviglia. Simplified blood flow model with discontinuous vessel properties: Analysis and exact solutions. 5:19–39, 2012.

[152] E. F. Toro and A. Siviglia. Flow in collapsible tubes with discontinuous mechanical properties: mathematical model and exact solutions. *Communications in Computational Physics*, 13(2):361–385, 2013.

[153] E. F Toro and V. A. Titarev. ADER: Towards arbitrary–order non–oscillatory schemes for advection–diffusion–reaction. In *Proc. 8th National Conference on Computational Fluid Dynamics, E-Land, Taiwan, August 18–20, 2001*, pages 8–23, 2001.

[154] E. F. Toro and V. A. Titarev. Solution of the generalised Riemann problem for advection–reaction equations. *Proceedings of the Royal Society of London A*, 458:271–281, 2002.

[155] E. F. Toro and V. A. Titarev. ADER schemes for scalar non-linear hyperbolic conservation laws with source terms in three-space dimensions. *Journal of Computational Physics*, 202(1):196–215, 2005.

[156] G. Troianowski, C. A. Taylor, J. A. Feinstein, and I. E. Vignon-Clementel. Three-Dimensional Simulations in Glenn Patients: Clinically Based Boundary Conditions, Hemodynamic Results and Sensitivity to Input Data. *Journal of Biomechanical Engineering-Transactions of the Asme*, 133(11), 2011.

[157] D. Utriainen, W. Feng, S. Elias, Z. Latif, D. Hubbard, and E. M. Haacke. Using magnetic resonance imaging as a means to study chronic cerebral spinal venous insufficiency in multiple sclerosis patients. *Techniques in Vascular and Interventional Radiology*, 15:101–112, 2012.

[158] J. J. W. van der Vegt and H. van der Ven. Space-Time Discontinuous Galerkin Finite Element Method with Dynamic Grid Motion for Inviscid Compressible Flows: I. General Formulation. *Journal of Computational Physics*, 182(2):546–585, 2002.

[159] H. van der Ven and J. J. W. van der Vegt. Space-time discontinuous Galerkin finite element method with dynamic grid motion for inviscid compressible flows: II. Efficient flux quadrature. *Computer Methods in Applied Mechanics and Engineering*, 191(41–42):4747–4780, 2002.

[160] P. Vernotte. Les paradoxes de la theorie continue de lequation de la chaleur. *Comptes rendus de l'Académie des sciences*, 246:3154–3155, 1958.

[161] I. E. Vignon-Clementel, C. A. Figueroa, K. E. Jansen, and C. A. Taylor. Outflow boundary conditions for 3D simulations of non-periodic blood flow and pressure fields in deformable arteries. *Computer Methods in Biomechanics and Biomedical Engineering*, 111(3):502–513, 2010.

[162] N. Westerhof, F. Bosman, C. J. DeVries, and A. Noordergraaf. Analogue studies of the human systemic arterial tree. *Journal of Biomechanics*, 2:121–143, 1969.

[163] N. Xiao, J. Alastruey, and C. Alberto Figueroa. A systematic comparison between 1-D and 3-D hemodynamics in compliant arterial models. *International Journal for Numerical Methods in Biomedical Engineering*, pages n/a–n/a, 2013.

[164] J. J. Yeung, H. J. Kim, T. A. Abbruzzese, I. E. Vignon-Clementel, M. T. Draney-Blomme, K. K. Yeung, I. Perkash, R. J. Herfkens, C. A. Taylor, and R. L. Dalman. Aortoiliac hemodynamic and morphologic adaptation to chronic spinal cord injury. *Journal of Vascular Surgery*, 44(6):1254–1265, 2006.

[165] P. Zamboni and R. Galeotti. The chronic cerebrospinal venous insufficiency syndrome. *Phlebology*, 25:269–279, 2010.

[166] P. Zamboni, R. Galeotti, E. Menegatti, A. M. Malagoni, G. Tacconi, S. Dall'Ara, I. Bartolomei, and F. Salvi. Chronic cerebrospinal venous insufficiency in patients with multiple sclerosis. *Journal of Neurology, Neurosurgery, and Psychiatry*, 80:392–399, 2009.

[167] P. Zamboni, E. Menegatti, I. Bartolomei, R. Galeotti, A. M. Malagoni, G. Tacconi, and F. Salvi. Intracranial Venous Haemodynamics in Multiple Sclerosis. *Current Neurovascular Research*, 4:252–258, 2007.

[168] C. E. Zambra, M. Dumbser, E. F. Toro, and N. O. Moraga. A novel numerical method of high-order accuracy for flow in unsaturated porous media. *International Journal for Numerical Methods in Engineering*, 89(2):227–240, 2012.

[169] C. Zhixian and W. Liangyan. Operator-splitting algorithm for advection-diffusion-reaction equation. *Journal of Hydrodynamics*, 4(1):65–73, 1992.